

BRUNEL UNIVERSITY LONDON

---

**Alternative Plate Deformation  
Phenomenon for Squeeze Film  
Levitation**

---

*Author: Ahmed Almurshedi*

*A thesis submitted in fulfilment of the requirements  
for the degree of Doctor of Philosophy*

*Supervisor: Prof. Mark Atherton*

*Department of Mechanical and Aerospace Engineering,  
College of Engineering, Design and Physical Sciences,  
Brunel University London,  
UK.*

November, 2018



# Declaration of Authorship

I declare that this thesis is my own work and is submitted for the first time to the Post-Graduate Research Office. The study was originated, composed and reviewed by myself and my supervisors in the Department of Mechanical and Aerospace Engineering, College of Engineering, Design and Physical Sciences, Brunel University London, UK. All the information derived from other works has been properly referenced and acknowledged.

Ahmed Almurshedi

Thursday 1<sup>st</sup> November, 2018



## *Abstract*

This thesis deals with a theoretical and an experimental exploration of squeeze film levitation (SFL) of light objects. The investigations aimed to find the important design parameters controlling this levitation mechanism and also to suggest an alternative way to implement SFL. The study, through computer modelling and experimental validation, focused on Poisson's contraction effect for generating SFL. A finite element model (ANSYS) was verified by experimental testing of five different plate designs. Each plate was subjected to a uniaxial plain stress by an arrangement of two hard piezoelectric actuators (PZT) bonded to the bottom of the plate and driven with DC or AC voltages. It was observed that pulsation of a dimple or crest shaped elastic deformation along the longitudinal axis in the central area of the plate was created because of Poisson's contraction. This Poisson's effect generated the squeeze-film between the plate and the levitated object. The separation distance between a floating lightweight object and the plate was analysed using computational fluid dynamics (ANSYS CFX) through creation of a modelling model for the air-film entrapped between the two interacting surfaces – a typical three-dimensional fluid-solid interaction system (FSI). Additionally, the levitation distance has been experimentally measured by a Laser Sensor. A satisfactory agreement has been found between model predictions and experimental results. Two levitation systems, one based on a horn transducer (Langevin type) and the other one in the form of a plain rectangular plate made of Aluminium and firmly fastened at both ends with a surface-mounted piezoelectric actuator, were compared in this thesis. Both devices were based on SFL mechanism. Evidently, the performances of both designs were greatly influenced by the design structure and in particular by the driving plate characteristics such as plate size and geometry as well as the driving boundary conditions. To this end, physical experiments were carried out and it was found that the device utilising horn-type transducer yields better levitation performance. Ultimately, the research explained the confusion between three

approaches to non-contact levitation through literature review and also pointed out some essential parameters like piezoelectric actuators location, material of the driving structure, coupled-field between the actuators and the driving structure and the fluid-solid interface that was existed between the excited plate and the levitated object.



## *Acknowledgements*

Firstly, I would like to express my sincere gratitude to my supervisor Professor Mark Atherton for the continuous support of my Ph.D study, for his patience, motivation, and immense knowledge. His guidance helped me in all the time of research and writing of this thesis, and also for his insightful comments and encouragement.

I would like to extend my appreciation and thanks to Dr. Cristinel Mares for his encouragement and supervisory role and also Professor Tadeusz Stolarski for all the help and support he provided.

Many thanks to Mr. Guillermo Schkzhamian (William) and Mr. Ali Ahmadnia for their help and advices at the Laboratory.

I gratefully acknowledge the funding received towards my PhD from the Iraqi Ministry of Higher education and Scientific Research, Iraqi Cultural Attache and also Al-Furat Al-Awsat Technical University.

Last but not the least, I would like to thank my family (my wife, Asraa Alhar and my daughter, Noor) for all their love and encouragement. For my parents who raised me with a love of science and supported me in all my pursuits.



# Contents

<b>List of Abbreviations</b>	<b>xvii</b>
<b>1 Introduction</b>	<b>1</b>
1.1 Introduction . . . . .	1
1.1.1 Motivation . . . . .	1
1.2 Background . . . . .	2
1.2.1 Aim and Objectives . . . . .	3
1.2.2 Thesis Framework . . . . .	3
1.3 Published and Submitted Work . . . . .	6
1.3.1 Research Journal Paper . . . . .	6
1.3.2 Conference Papers . . . . .	6
<b>2 Literature Review</b>	<b>7</b>
2.1 Literature review . . . . .	7
2.2 Differences between OAPL Approches . . . . .	7
2.2.1 Standing Wave Acoustic Levitation (SWAL) . . . . .	7
2.2.2 Near-Field Acoustic Levitation (NFAL) . . . . .	12
2.2.3 Squeeze Film Levitation (SFL) . . . . .	15
2.3 Levitating Characteristics of OAPL Bearing . . . . .	18
2.3.1 Levitating Features of SFL Journal Bearing . . . . .	20
2.3.2 SFL characteristics . . . . .	23
2.3.3 NFAL Influence and Load-Carrying Capacity . . . . .	27
2.3.4 Conclusion . . . . .	33

<b>3</b>	<b>Driving Unit – Piezoelectric Actuators</b>	<b>35</b>
3.1	Introduction . . . . .	35
	Piezoelectric History . . . . .	35
3.2	Piezoelectric ceramics overview . . . . .	36
3.3	Dynamics of Piezoelectricity . . . . .	37
	Introduction . . . . .	37
	Piezoelectric working principles . . . . .	38
3.4	Piezoelectric Coefficients . . . . .	40
3.5	Piezoelectric Performance . . . . .	44
3.6	Piezoelectric Mechanical and Electrical Modelling . . . . .	45
	Piezoelectric drawbacks . . . . .	47
	Transducer Design and Performance . . . . .	48
	Transducer Characteristics . . . . .	49
	Efficiency and power efficiency . . . . .	51
	Mechanical quality factor . . . . .	51
	Piezoelectric quality number ( $M$ ) . . . . .	52
	Actuator Operating Approaches . . . . .	52
	Self-Vibrating Circuit (SVC) . . . . .	53
	Phase-Locked-Loop (PLL) Technique . . . . .	54
	Piezoelectric Mathematical Description . . . . .	56
	Piezoelectric Finite Element Method Formulation . . . . .	58
3.7	Conclusion . . . . .	60
<b>4</b>	<b>Mathematical Modelling of Thin Plate.</b>	<b>61</b>
4.1	Introduction . . . . .	61
4.2	Plate under Concentrated Load . . . . .	61
4.2.1	Rectangular Plate Simply Supported . . . . .	61
	Navier Solution Approach for Simply Supported Rectangular Plates . . . . .	63

Concentrated Load on a Plate . . . . .	65
4.2.2 Dynamic Plate Theory . . . . .	68
4.3 Plate Deformation Measurements . . . . .	76
<b>5 Influence of design embodiment on the performance of SFL</b>	<b>81</b>
5.1 Introduction . . . . .	81
5.1.1 Squeeze Film Levitation (SFL) Approach . . . . .	82
5.1.2 Configuration of Horn-Transducer (Design A) . . . . .	84
5.1.3 Horn Design . . . . .	84
5.1.4 Experimental Method for Design A . . . . .	86
5.2 Results and Discussion for Horn-Transducer Designs (A1 and A2) . .	88
5.3 Configuration of Actuated Plate (Design B) . . . . .	92
5.4 Experimental Method for Design B . . . . .	93
5.5 Results and Discussion for Design B . . . . .	94
5.6 Conclusion . . . . .	97
<b>6 Alternative Plate Deformation Phenomenon for SFL</b>	<b>99</b>
6.1 Introduction . . . . .	99
6.2 Method . . . . .	100
6.2.1 Theoretical Modelling . . . . .	100
6.2.2 Poisson's Ratio Plate Deformation for SFL . . . . .	101
6.2.3 Forced Plate Design and Statement of the Problem . . . . .	105
6.2.4 Finite Element Modelling (FEM) . . . . .	106
6.2.5 Dynamic Analysis . . . . .	109
Structural Dynamics . . . . .	109
Squeeze-Film Levitation Modelling . . . . .	109
Squeeze-Film Action . . . . .	113
Model of Squeeze Air-Film in ANSYS CFX . . . . .	114
6.3 Experimental Method . . . . .	117
6.3.1 Configuration Study . . . . .	117

6.4	Results and Discussion . . . . .	120
6.4.1	The Dynamic performance of the squeeze-film levitation . . . . .	129
6.5	Concluding Remarks . . . . .	131
<b>7</b>	<b>Summary of Findings and Concluding</b>	<b>133</b>
7.1	Summary of Findings . . . . .	133
7.2	Concluding Remarks . . . . .	135
7.3	Contributions to Knowledge . . . . .	136
7.4	Future Work Recommendations . . . . .	138
	<b>References</b>	<b>141</b>
<b>A</b>	<b>Appendix A</b>	<b>149</b>
A.1	Published Research Paper . . . . .	149
<b>B</b>	<b>Appendix B</b>	<b>161</b>
B.1	Digital Image Correlation system overview . . . . .	161
B.1.1	Calibration of Cameras . . . . .	162
B.1.2	Utilize of Digital Image Correlation and Restrictions . . . . .	163
<b>C</b>	<b>Appendix C</b>	<b>167</b>
C.1	Reynolds Equation: . . . . .	167
C.1.1	Analytical solution for Force and Pressure . . . . .	169

# List of Figures

1.1	: Bearing and conveying types. . . . .	2
1.2	: Thesis organisation . . . . .	5
2.1	: A levitating system using standing wave . . . . .	9
2.2	: Schematic layout of SWAL design (Whymark, 1975). . . . .	11
2.3	: NFAL schematic design. . . . .	13
2.4	: Schematic layout of NFAL design (Ueha, Hashimoto, and Koike, 2000) . . . . .	15
2.5	: The non-harmonic pressure vibration as a result of a harmonic motion . . . . .	17
2.6	: Linear SFL bearing with piezoelectric actuators attached (Stolarski and Woolliscroft, 2007). . . . .	19
2.7	: Linear SFL bearing design (Yoshimoto, Kobayashi, and Miyatake, 2007). . . . .	20
2.8	: Experimental set up of SFL journal bearing (Wang and Au, 2011). . . . .	21
2.9	: Modal shape of squeeze-film journal bearing (Wang and Au, 2012). . . . .	22
2.10	: Squeeze-film design (Minikes and Bucher, 2003). . . . .	23
2.11	: Squeeze-film design (Minikes and Bucher, 2006). . . . .	24
2.12	: a-Schematic layout of transducer design, b-the former transducer design, c-the optimal transducer design (Ilssar, Bucher, and Cohen, 2014) . . . . .	25
2.13	: Wafer aligner design; arrows show the direction of forces / torqus Bucher et al., 2016 . . . . .	26
2.14	: Setup diagram of NFAL Kim and Ih, 2007. . . . .	27
2.15	: Design of NFAL (Ishii et al., 2014). . . . .	29

2.16	: SFL design (Ilssar and Bucher, 2015).	30
2.17	: NFAL design (Ilssar, Bucher, and Flashner, 2017).	31
2.18	: <b>Left</b> -deflection angle; <b>Right</b> - Experimental set up for a non-parallel SFL design (Wei, Shaham, and Bucher, 2018).	32
2.19	: <b>Left</b> -engraved levitating disc configuration; <b>Right</b> - Experimental set up (Li, Liu, and Feng, 2017).	32
3.1	: Direction of piezoelectric element axes.	38
3.2	: Direct and indirect piezoelectric material effects, voltage gained and shape change.	39
3.3	: Basic Piezoelectric modes: (a) Longitudinal Mode; (b) Shear Mode and (c) Transverse Mode ( <i>purple area shows the electrodes</i> ).	43
3.4	: Force versus displacement for a piezoelectric actuator (Ghodssi and Lin, 2011).	45
3.5	: Equivalent mechanical state of piezoelectric element.	47
3.6	: Equivalent electrical state of piezoelectric element.	47
3.7	: Design of a Langevin type ultrasonic transducer.	49
3.8	: Design ultrasonic transducer.	49
3.9	: Piezoelectric frequency response.	54
3.10	: Self-vibrating circuit (SVC) layout.	54
3.11	: Phase-locked-loop.	55
4.1	: Plate under concentrated load distributed as a rectangular.	64
4.2	: Plate under concentrated load and axis of deformation	67
4.3	: Plate coordinates and dimensions.	69
4.4	: Plate boundary conditions signs used in Table 4.3.	74
4.5	: INSTRON machine and plate under a concentrated load.	77
4.6	: Comparison of analytical and measurement results for various plate cases (Table 4.5).	79

4.7	: Plate deformation measurement result versus plate thickness for various plate cases (Table 4.5). . . . .	80
4.8	: Plate deformation measurement result versus Poisson's Ratio for various plate cases (Table 4.5). . . . .	80
5.1	: Types of horn design. . . . .	85
5.2	: Conical horn configuration. . . . .	86
5.3	: Schematic and experimental layout of SFL design A ( <i>Tokyo University of Science</i> ). . . . .	87
5.4	: Experimental set-up of SFL design A ( <i>Tokyo University of Science</i> ). . . . .	87
5.5	: Experimental actuated plate set-up design A1 at 26.4 kHz ( <i>Tokyo University of Science</i> ). . . . .	89
5.6	: Experimental dynamic plate deformation (Design A1) at resonance frequency of 25.8 [kHz]. . . . .	90
5.7	: Experimental separation distance for various weights (Wafer) at different driving voltages for (Design A1). . . . .	90
5.8	: Experimental dynamic plate deformation (Design A2) at 26.4 [kHz]. . . . .	91
5.9	: Experimental of separation distance for various weights (wafer) at different driving voltages for Design A2. . . . .	91
5.10	: CAD model of design B (all units in <i>mm</i> ). . . . .	93
5.11	: Experimental set-up measurements (Design B). . . . .	94
5.12	: Design B and DIC system features and experimental set-up. . . . .	95
5.13	: Experimental measurements using DIC system for dynamic plate deformation of design B at a resonance frequency of 0.339 kHz: A- plate modal shape; B- plate centre point deformation; C- plate section or lengthwise deformation. . . . .	95
5.14	: Design B and levitating disc under DIC system. . . . .	96
5.15	: Separation distance for a disc of 5 g levitating on Design B at 339 Hz. . . . .	96

6.1	: A- Side view of SFL schematic design, B- Bottom view of the plate design and Sine wave voltage excitation; all dimensions in [mm]. . .	101
6.2	: A- Side view of SFL generated by oscillating dimple due to Poisson's Ratio effect, B- Bottom view of the plate design and Square wave voltage excitation; all dimensions in [mm]. . . . .	102
6.3	: Oscillating dimple due to Poisson's Ratio effect based on Square wave voltage excitation . . . . .	103
6.4	: Finite element analysis simulation of plate dimple due to Poisson's Ratio effect. . . . .	103
6.5	: Top view of the plate design and lengthwise segment; all dimensions in mm. . . . .	105
6.6	: Square wave voltage signal to drive the PZTs. . . . .	107
6.7	: Mesh of a forced plate (Design A1), bottom view. . . . .	109
6.8	: Schematic design of the OAPL (SFL); A- Rig design; B- Air film modelling (ANSYS-CFX); C-Design free body diagram. . . . .	112
6.9	: Squeeze film Modelling with ANSYS-CFD. . . . .	115
6.10	: Theoretical method flowchart. . . . .	116
6.11	: Experimental devices used for the measurements. . . . .	118
6.12	: Top view for floating design with lifted metal ring. . . . .	119
6.13	: Layout of the measurement work. . . . .	119
6.14	: Static deformation (Design A1). . . . .	121
6.15	: Dynamic deformation (Design A1). . . . .	121
6.16	: Measurement and simulation of static deformation (Design A1). . .	122
6.17	: Measurement and simulation of static deformation (Design A2). . .	122
6.18	: Measurement and simulation of static deformation (Design A3). . .	123
6.19	: Measurement and simulation of static deformation (Design B). . . .	123
6.20	: Measurement and simulation of static deformation (Design C). . . .	124
6.21	: Measurement and simulation of dynamic deformation (Design A1). .	124
6.22	: Measurement and simulation of dynamic deformation (Design A2). .	125



6.23	: Measurement and simulation of dynamic deformation (Design A3).	125
6.24	: Measurement and simulation of dynamic deformation (Design B).	126
6.25	: Measurement and simulation of dynamic deformation (Design C).	126
6.26	: Measurement and simulation of dynamic levitation (Design A3).	127
6.27	: Measurement and simulation of dynamic levitation (Design C).	127
6.28	: Measurement of dynamic levitation for various designs.	128
B.1	: Photogrammetric standard and calculation of 3-D translation vector (Hagara et al., 2014).	161
B.2	: Calibration Live Image (Dantec Dynamic 2016).	163



# List of Tables

4.1	: Factor $\alpha$ values for different ratio of $b/a$ . . . . .	68
4.2	: The numerical values of $\alpha$ at various plate dimensions (Timoshenko and Woinowsky-Krieger, 1959). . . . .	70
4.3	: Boundary conditions (B.C) and parameters of Plate in dynamic approaches (Leissa, 1969; Venstel and Krauthammer, 2001). . . . .	73
4.4	: Boundary conditions and parameters under plate dynamic theories (Leissa, 1969). . . . .	75
4.5	: Various plate cases, the plate is simply supported and subjected to a central point load of 5 N. . . . .	78
5.1	: Plate designs sizes and material properties. . . . .	82
6.1	: Plates design configurations (Callister Jr and Rethwisch, 2012). . . . .	106
6.2	: AC voltage amplifier specifications. . . . .	120



# List of Abbreviations

$a$	length dimension
$\alpha_0$	vibration amplitude
$A$	Area
$ A $	amplitude
$BD$	bulk density
$B_d$	structural damping
$c_a$	speed in air
$C$	electrical capacitance
$c_E$	stiffness quantities under constant electric field
$c$	sound speed in air
$d$	modal damping
$D$	flexural rigidity
$D_e$	electric displacement
$d_{3i}$	charge constant [ $m/V$ ]
$\delta$	specific heat ratio
$d_{ip}$	vector involving of piezoelectric charge constants
$d_0$	space between the stator and plate
$\epsilon$	Dimensionless amplitude
$e_p$	piezoelectric coupling coefficient in the stress–charge system
$E_3$	applied electrical field

$E_s$	stored energy
$E_{loss}$	losses energy
$E_T$	kinetic energy
$E_A$	dissipated energy
$E_e$	electric field strength
$E$	plate Young's modulus
$E_{pe}$	piezoelectric Young's modulus
$\varepsilon_S$	electric permittivity matrix under constant stain
$F_e$	electrostatic force of attraction in the vertical path
$F$	Dimensionless bearing force / Radiation force
$F_f$	Fluid flow force [ $N$ ]
$F_m$	weight of the top surface [ $N$ ]
$g_{ij}$	Piezoelectric Voltage Coefficient
$H$	Dimensionless film thickness
$h$	Film thickness [ $m$ ]
$h_0$	Initial film thickness
$I(t)$	current
$K_p$	anisotropic permittivity
$K_s$	anisotropic stiffness
$K_z$	piezoelectric effect
$k$	wave number
$L$	Length variable [ $m$ ]
$\lambda$	London penetration depth
$M$	mass matrix

$m$	modal mass
$\phi_m$	phase variance between $F(t)$ and $v(t)$
$\mu$	Dynamic viscosity <i>Pas</i>
$m$ and $n$	integer numbers
$M_x$ and $M_y$	moments
$\dot{M}$	linear flow rate of material
NFAL	Near-Field Acoustic Levitation
$\nu$	Poisson's Ratio
OAPL	Oscillating Air Pressure Levitation
$\omega$	Angular frequency [rad/s]
$\Pi$	Radiation pressure
$P$	Normalized pressure $p/p_0$ [Pa]
$p_0$	Ambient pressure
$p_{e(t)}$	transducer input power
$p_i$	pressure of grid
$\hat{P}_e$	apparent power
$p_e$	refer to Piezoelectric material
$\pi_a$	strain energy of the plate
$\pi_b$	strain energy of the Piezoelectric
$q$	load intensity
$Q_m$	mechanical quality factor
$R_s$	sphere radius
$R$	Dimensionless floating disc radius $m$
$r_o$	Radius of floating object $m$
$r_p$	piezoelectric radius
$\rho_o$	surrounding medium density
$\rho_a$	Air Density [kg/m <sup>3</sup> ]

$\alpha$	electromechanical conversion parameter
$U, Q, u$ and $F$	input voltage, charge, modal displacement and mechanical load
$\epsilon_\sigma$	permittivity
$S$	strain
$S_E$	compliance matrix
$\sigma$	Squeeze Number
$S_{pq}^E$	elastic compliance matrix
SWAL	Standing Wave Acoustic Levitation
SFL	Squeeze film levitation
$T_b$	belt tension
$T_a$	Air Temperature [K]
$\tau$	Dimensionless time [s]
$\bar{V}_c^2$	root mean square voltage
$\theta$ and $\Delta r$	grid width
$u_x, u_y$ and $u'_x, u'_y$	Surface velocity
$V_b$	belt speed
$V$	velocity $m/s$
$W_p$	plate weight
$w$	trough width
$w_s$	piezoelectric material thickness in the poling direction
$\xi_{ij}$	vector containing permittivity constants
$\zeta_0$	Amplitude of oscillation
$X$	Dimensionless form of $x$ direction
$Y$	Dimensionless form of $y$ direction
$Z$	Dimensionless floating disc displacement
$z_l$	Levitating height of disc [m]
$Z_0$	Initial displacement



# Chapter 1

## Introduction

### 1.1 Introduction

#### 1.1.1 Motivation

Conventional contact methods of manufacturing conveying are sometimes not suitable where there are rapidly changing demands for product variety and special stringent operating conditions, such as for food, drug and semiconductor chip manufacture. Problems with contact conveying include conveying rough materials that can reduce the life of the conveyor. Corrosive items should be conveyed on special corrosion-resistant belts and elaborate belt cleaning design may be necessary. Any additional mechanisms added to deal with the problems described above will add cost to a contact conveying system (Thangali, 1991; Fayed and Skocir, 1996; McGuire, 2009)

Wear can occur at conveyor loading points, which creates trace quantities of substances like metal from abrasion or friction. When conveying high-purity materials or delicate objects such as pharmaceuticals or electronic parts the acceptable levels of contamination are very low. Thus, the conveying of such material in industry requires rigorous cleaning and sterilisation processes. For example, in semiconductor technologies, it is challenging to convey a component of a Micro- Electromechanical System (MEMS) due to their delicate surface characteristics and fragility (Reinhart and Hoepfner, 2000; Vandaele, Lambert, and Delchambre, 2005).

## 1.2 Background

Products are conventionally transported utilising rollers, belts and chains in contact conveyors; and magnetic, electrostatic and aerodynamic levitation in non-contact industrial conveying. They sometimes cause damage to the conveyed item. Based on the field of tribology (Jost, 1976), figure 1.1 shows a basic classification of most commonly utilised bearing and conveying configurations, which includes relevant developments in bearings. Tribology research has developed several kinds of conveying to reduce frictional losses, including a range of non-contact conveyors, the most common of which are porous-walled air film and electromagnetic conveyors (McGuire, 2009; Brandt, 1989).

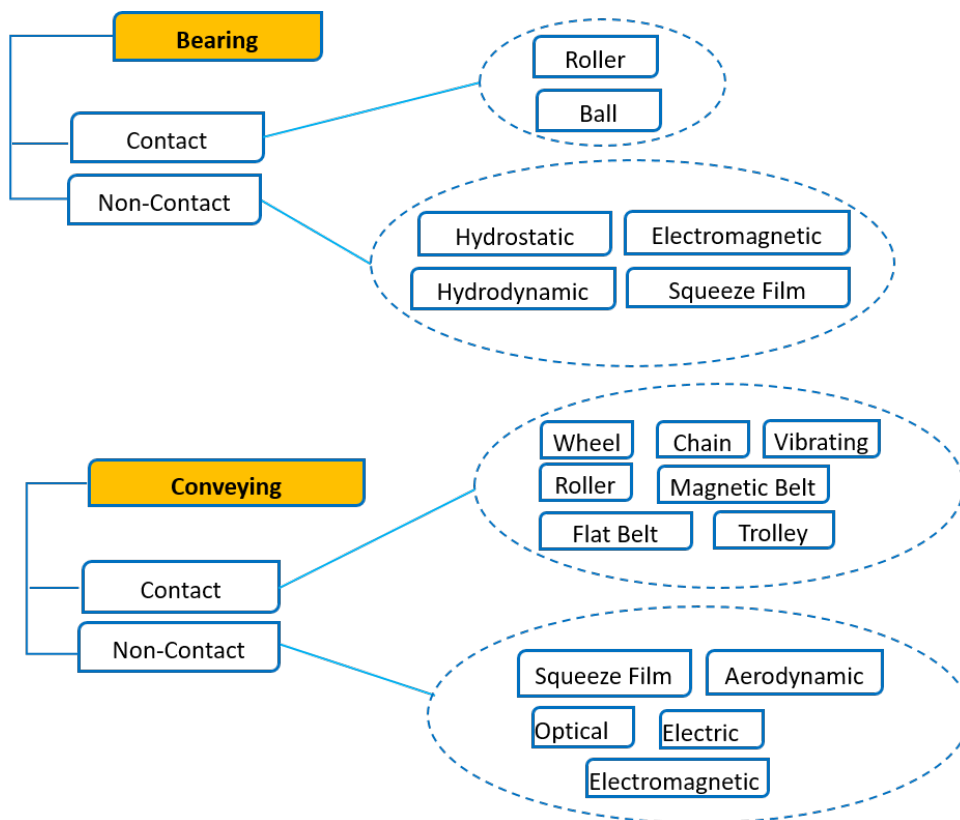


FIGURE 1.1 : Bearing and conveying types.

Squeeze film levitation (SFL) is one of the most appropriate approaches for a wide kind of conveying applications, as it is an inexpensive non-contact technique, and has suitable characteristics for clean-room and precision conveying (Stolarski

and Chai, 2006; Liu et al., 2009; Vandaele, Lambert, and Delchambre, 2005; Atherton, Mares, and Stolarski, 2014). The main advantage is that any conductor, insulator, magnetic or non-magnetic material, can be handled by SFL without tactile contact.

### 1.2.1 Aim and Objectives

The aim of this research is to design a new system of levitation for lightweight objects using an alternative plate actuation technique for generating squeeze film levitation (SFL). The following objectives will be addressed:

1. Conduct an in-depth literature review of SFL.
2. Simulate Fluid-Structure Interaction (FSI) between the air-layer (clearance) trapped between the driving surface and the levitating object in order to determine the pressure distribution.
3. Conduct experimental measurements to determine the static and dynamic characteristics of the forced plate designs, and the SFL performance in order to validate the theoretical work.

### 1.2.2 Thesis Framework

This thesis is composed of 7 chapters. Chapter 1 provides the background and motivation for seeking novel methods of non-contact levitation. In addition, the purposes, aims and goals for the research are clarified.

Chapter 2 critically reviews the literature for non-contact conveying based on several approaches and in particular in relation to the squeeze-film method. In addition, the pros and cons of the current squeeze-film levitation designs for linear, sliding and journal bearings are explained.

In Chapter 3, the electrical and mechanical characteristics of single layer piezoelectric actuators and ultrasonic transducers are described. Moreover, the mathematical description of piezoelectric effect and the finite element method formulation

that is used to find out the electrical and mechanical characteristics of piezoelectric actuators are also presented.

Chapter 4 presents thin plate theories and their mathematical modelling.

Chapter 5 presents the physical experimental design, testing set-up and experimental measurements process for two different SFL designs, including forced plate characteristics and levitating performance. In addition, a comparison between the designs will be provided, plus discussion of the experimental outcomes.

Chapter 6 proposes an alternative SFL design that includes an explanation of the compressible Reynold's equation derivation and solution. Moreover, a simulation of SFL utilising computational fluid dynamics (CFX) to determine pressure and lift is outlined. With the comprehension acquired from Chapter 3 and Chapter 4, there is reflection on how to utilise the results of the SFL method to build a realistic design of non-contact conveying.

Chapter 7 reports the conclusions in relation to the stated objectives, together with recommendations for future work. Figure 1.2 presented the outline of thesis contents.

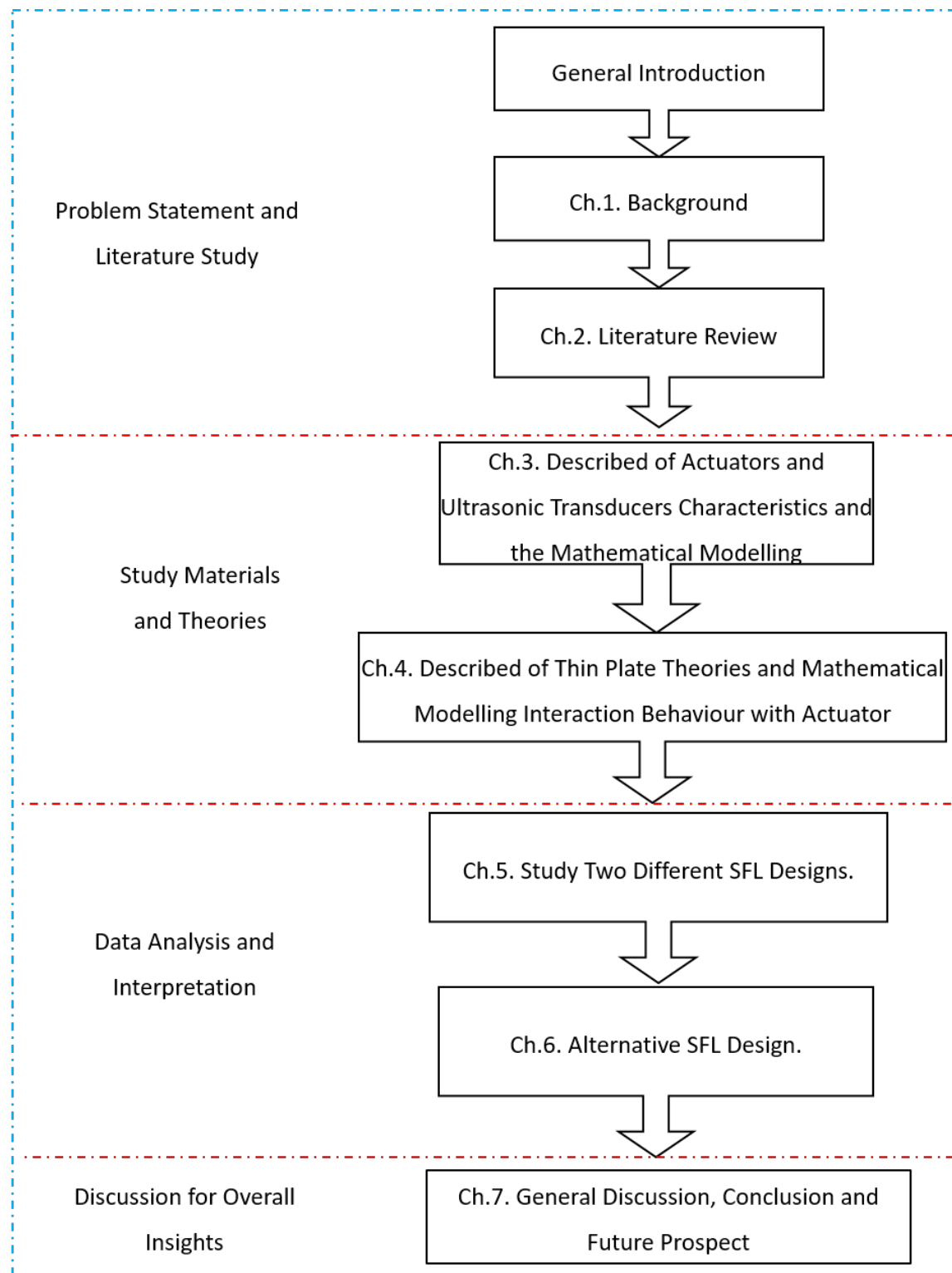


FIGURE 1.2 : Thesis organisation

## 1.3 Published and Submitted Work

### 1.3.1 Research Journal Paper

#### *Published*

Chang, X., Wei, B., Atherton, M., Mares, C., Stolarski, T. and Almurshedi, A., 2016. NFAL prototype design and feasibility analysis for self-levitated conveying. *Tribology Transactions*, 59(5), pp.957-968, DOI:10.1080/10402004.2015.1124306. See, Appendix [A](#).

#### *Submitted*

Almurshedi, A., Atherton, M., Mares, C., Stolarski, T., 2018. Alternative Plate Deformation Phenomenon for Squeeze Film Levitation. *Journal of Applied Physics*.

Almurshedi, A., Atherton, M., Mares, C., Stolarski, T., 2018. Influence of design embodiment on the performance of squeeze-film levitation contacts. *IMEchE, Journal of Engineering Tribology*.

### 1.3.2 Conference Papers

Almurshedi, A., Atherton, M. and Mares, C., 2015. Plate vibration characteristics for squeeze film levitation. 10 th International Conference on Advances in Experimental Mechanics, Heriot-Watt University, Edinburgh, 1-3 September 2015.

Almurshedi, A., Atherton, M., Mares, C., Stolarski, T., Wei, B. and Wang, Y., 2015. Plate actuator vibration modes for levitation. International Tribology Conference, Tokyo, Japan, 16-20 September 2015.

Almurshedi, A., Atherton, M., Stolarski, T., Mares, C., 2018. Investigation into Squeeze-Film Induced Levitation of Light Objects. IOP Conference Series, Modern Practice in Stress and Vibration Analysis, 2-4th July 2018, Clare College, Cambridge, UK.

## Chapter 2

# Literature Review

### 2.1 Literature review

In this chapter, the literature dealing with a standing wave acoustic levitation (SWAL), near-field acoustic levitation (NFAL) and squeeze film levitation (SFL) approaches will be summarised, reviewed and discussed. As a result the authors proposed that a suitable term to describe all three approaches is "Oscillating Air pressure Levitation" or OAPL. In addition, studies of OAPL pertaining to oscillation and modal shape analyses are reviewed in order to understand the significant characteristics of OAPL and to identify matters for further consideration.

### 2.2 Differences between OAPL Approches

#### 2.2.1 Standing Wave Acoustic Levitation (SWAL)

The theory of generating standing wave is important to calm acoustic levitation. In comparison with ordinary waves vibrating as they travel through the air, a standing wave is fundamentally stationary with the waveform forced to stay in one position. The delusion of immobility of the standing waves which seem to have the same location at any time or in other words, do not mobile from place to place is what offers their label "standing" (Vandaele, Delchambre, and Lambert, 2011). Originated

on sound physics, the distance between the sound radiator (transducer) and reflector should be a multiple of half of the sound wavelength generated through the transducer. This will create a standing wave with stable nodes (areas of minimum pressure) and antinodes (areas of maximum pressure) (Vandaele, Delchambre, and Lambert, 2011; Yarin, Pfaffenlehner, and Tropea, 1998). Two conflicting forces acting on a sample that is subjected to the SWAL are gravitational force and a rising pull through the sound wave. When the forces are balanced, the sample are confined in the stable positions of the energy field that is nodes in which they start to levitate in air. If a wave positioning is parallel to a pull force (gravity), parts of the standing wave reveal a constant downward pressure and others expose a constant upward pressure. The nodes locations have slight pressure. Samples can be gathered just below the nodes, since the acoustic radiation pressure that a sound wave can exert on the sample in equilibrium with the pull force (Vandaele, Delchambre, and Lambert, 2011; Yarin, Pfaffenlehner, and Tropea, 1998). Any sample of appropriate size and weight will have more accidental to lift in the comparatively calm locations of nodes rather than the great pressure, excessive vibration “turbulant” regions of antinodes (Figure 2.1). The first investigation into the standing wave levitation (SWL) technique was implemented by Kundt in 1866, in which transportation of small dust particles in a horizontal tube were carried by pressure nodes of a standing wave formed in the tube. A common fundamental operation arrangement of standing wave levitation (SWL) is shown in Figure 2.1, depending on compound reflection through an ultrasonic radiator and a reflector (solid flat or concave shape), SWL, with uniformly spaced nodes and anti-nodes of the velocity amplitude and sound pressure, will be created. Various particles with operative diameters of less than the wavelength can be transported below the pressure nodes through SWL. The influence of the sound radiation pressure in SWL can hold-up the particles in an axial position. King in 1934, was the first to investigate standing wave levitation theoretically. His work was built upon by Hasegawa and Yosioka who incorporated the action of compressibility within the SWL approach. Westervelt in 1950



created a universal formula for a force, according to a radiation pressure effect, on an item of normal boundary impedance utilising SWL. Moreover, he explained that a boundary film with a high internal loss can cause forces that are several orders of magnitude larger than those of the standard radiation pressure concept.

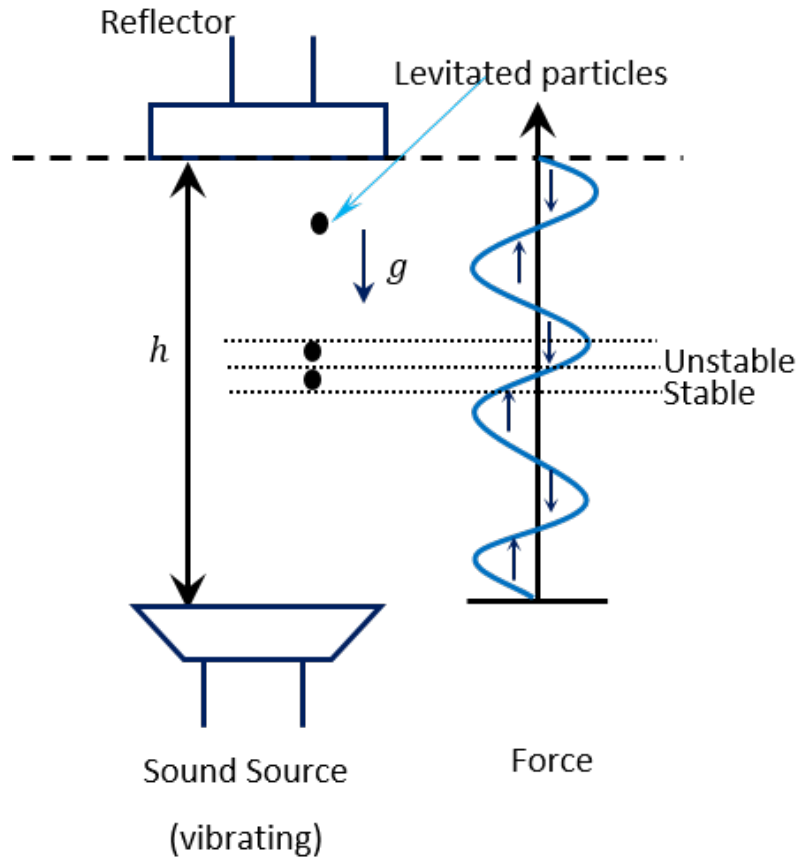


FIGURE 2.1 : A levitating system using standing wave

The fundamental operation of the SWL approach can be theoretically explained based on King's illustration, supposing that the fluid being studied is adiabatic, so, the motion equation can be expressed as:

$$\rho \frac{du}{dt} = -\frac{\partial p}{\partial x} \quad (2.1)$$

$$\rho \frac{dv}{dt} = -\frac{\partial p}{\partial y} \quad (2.2)$$

where, the absolute derivative is:

$$\frac{d}{dt} = \frac{\partial}{\partial t} + u \frac{\partial}{\partial x} + v \frac{\partial}{\partial y} + w \frac{\partial}{\partial z} \quad (2.3)$$

where,  $\rho$  is medium density,  $p$  is pressure, and  $(u, v, w)$  are the Cartesian velocity components. By taking  $\psi = \frac{dp}{\rho}$  then the equation of motion can be altered as:

$$\frac{du}{dt} = -\frac{\partial \psi}{\partial x'} \frac{dv}{dt} = -\frac{\partial \psi}{\partial y'} \frac{dw}{dt} = -\frac{\partial \psi}{\partial z} \quad (2.4)$$

The approximate linear wave equation can represent the velocity potential when the medium is an air and expressed as follows:

$$\nabla^2 \omega = \frac{1}{c^2} \frac{\partial^2 \omega}{\partial t^2} \quad (2.5)$$

Utilising a second order calculation, equation 2.5 can be simplified to represent the equation of continuity:

$$\frac{\partial \rho}{\partial t} + \frac{\partial}{\partial x} (\rho u) + \frac{\partial}{\partial y} (\rho v) + \frac{\partial}{\partial z} (\rho w) = 0 \quad (2.6)$$

Thus, the pressure variation  $\Delta p$  can be derived from equation 2.6 as:

$$\Delta p = p_0 \frac{\partial \psi}{\partial t} + \frac{1}{2} \frac{\rho_0}{c^2} \left( \frac{\partial \psi}{\partial t} \right)^2 - \frac{1}{2} \rho_0 q^2 \quad (2.7)$$

where,  $\rho_0$  is the surrounding medium density,  $c$  is the sound speed in air and  $q$  is the velocity amplitude, which has the value  $\sqrt{u^2 + v^2 + w^2}$ . Integrating the acoustic pressures impacting on the surface of a levitated item, the time averaged acoustic pressure can be calculated. The velocity potential of a plane standing wave can be written as:  $\psi_s = |A| \cos kh \cos \omega t$  where,  $|A|$  is the amplitude, the wave number is  $k = \frac{2\pi}{\lambda}$ ,  $h$  is the levitating item position and  $R_s$  is the sphere radius. The force of

acoustic radiation on a rigid sphere can be expressed as:

$$F = -\frac{5}{6}\pi\rho_o |A|^2 (kR_s)^3 \sin(2kh) \quad (2.8)$$

Whymark, 1975, suggested a design of a levitator for standing of materials in space utilising a single source of sound. The author showed that regulating the reflector motion can lead to fine control of a levitating object's position. (Otsuka, Higuchi, and Seya, 1990), utilised a stepped rounded oscillating plate work as a radiator, which could produce a high strength ultrasound effect to levitate different sample shapes based on the SWAL approach. The plate design consisted of concave and convex channels (Figure 2.2), with the former having a fixed depth equivalent to half the sound wavelength in air. This technique involved applying a flexural vibration mode for the oscillating plate, with two nodal rings to attain better oscillation amplitude. Hence, the author with that driving design produced a different form of conventional piston-like vibration source.

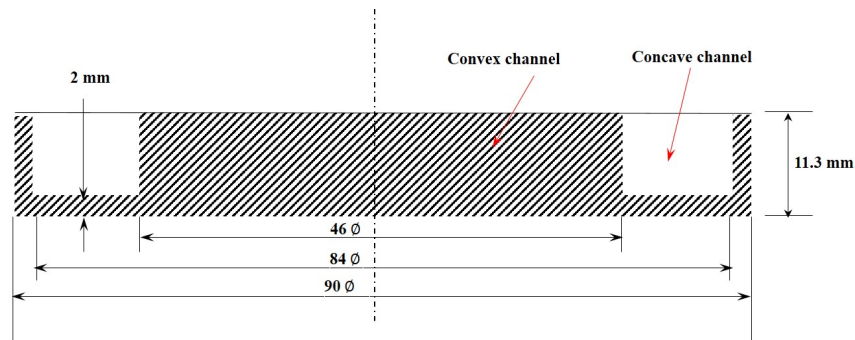


FIGURE 2.2 : Schematic layout of SWAL design (Whymark, 1975).

In 2004, Xie and Wei, studied a force of levitation applied to disc samples and water drops in a standing wave by analysing a wave propagation by including the method of boundary element. The investigations revealed, physically, that an essential condition of the standing wave for the steady levitating of a water drop is to regulate the reflector-emitter, and they also showed that a higher force can be gained

for a thin levitating disc. The above standing wave levitation designs involved utilising the classic radiator-reflector configuration. The applications of such systems of levitation were restricted to the levitating of small particles, the sizes of which were not larger than the wavelength of the executed sound wave. Hence, the levitating force that can be acquired from the standing wave system is inadequate.

### 2.2.2 Near-Field Acoustic Levitation (NFAL)

This method has a similar principle operation to the SWL technique, but there is no reflector required to perform a mission of levitation. The levitating object will represent the reflector, so, the levitating with this method is based on the pressure radiation created by a driving surface that is supposed to be excited in a harmonic mode (Ueha, Hashimoto, and Koike, 2000). A travelling sound in the clearance entrapped between the two surfaces (top of the driving structure and bottom of the levitating item) yields two forces, one of which can raise a levitating item in a normal direction, whilst the other, makes a near-boundary flowing in a circumferential path near to the surface of the levitating item. A velocity gradient of that boundary can generate a viscous force, which leads to the levitated object being transported on a horizontal path. Additionally, the theoretical analysis of this approach is based on a vibrational frequency, an acoustic wave and the sound velocity in the air. Hashimoto, Koike, and Ueha, 1996, expressed a basic equation to represent the radiation pressure based on NFAL principle obtained by Chu and Apfel, 1982. They proposed the Rayleigh radiation pressure in an ideal gas on a reflecting structure as:

$$\Pi = \frac{1 + \delta}{2} \left( 1 + \frac{\sin(2kh)}{2kh} \right) E \quad (2.9)$$

In which,  $E$  is the energy density, which is equal to:  $\frac{\alpha_0^2}{4} \left( \frac{\rho_0 \omega^2}{\sin^2 kh} \right)$  where,  $k$  is the wave number,  $\delta$  is the specific heat ratio,  $\omega$  is the wave angular velocity,  $h$  is the height between the driving source and the levitating item. As the levitating height at the micrometre level, then  $\sin(kh) \approx kh$ . Equation 2.9 was shortened to being a linear

equation that describes radiation pressure in NFAL:

$$\Pi = \frac{1 + \delta}{4} \rho_0 c^2 \frac{\alpha_0^2}{h^2} \quad (2.10)$$

The radiation pressure  $\Pi$  in NFAL is oppositely proportional to the square of the levitating height and directly proportional to the square of the vibration amplitude  $\alpha_0$ . Physical measurements was undertaken by Hashimoto, Koike, and Ueha, 1996, to validate equation (2.10) and the outcomes revealed a variation in the levitating force of about. The authors surmised that the result differences might be due to the finite size of the surfaces and non-uniformity of the amplitude of the radiation source.

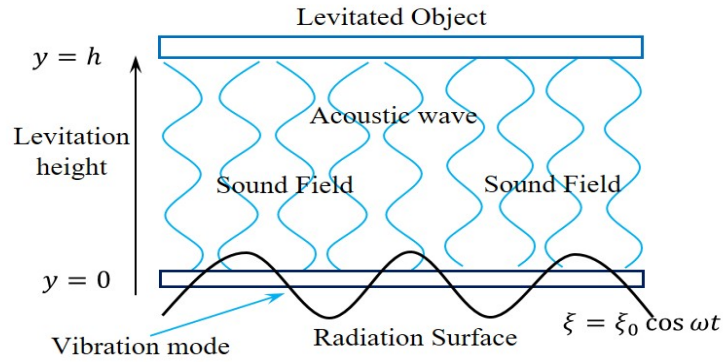


FIGURE 2.3 : NFAL schematic design.

In addition, the NFAL displacement of a floating item based on wave number and sound radiation was proposed by (Hashimoto, Koike, and Ueha, 1996) as;

$$\zeta(y, t) = \zeta_0 \frac{\sin(h - y)}{\sin kh} \cos \omega t \quad (2.11)$$

Where,  $\zeta(y, t)$  is the displacement,  $a$  is the direction of acoustic wave propagation from the radiating plane,  $k$  is the wave number in levitation domain,  $\omega$  is the angular frequency of oscillation,  $\zeta_0$  is the amplitude of oscillating at the driving plane, and  $h$  is the mean height between the floating item and the driving surface. The radiation

pressure  $p$  is equal to floating object weight  $F$  per unit area  $A$ , see equation (2.12).

$$F = \frac{1}{2} \rho_a c_a^2 \frac{\xi_0^2}{h^2} A \quad (2.12)$$

Where,  $\rho_a$  refers to the air density,  $c_a$  is the velocity of sound in air. Hashimoto and Ueha, 1998, described the fundamentals and design of an oscillating plate, which is essential for the stable conveying of levitated items as well as provided data measured for several levitated features. Based on NFAL approach, an association among levitated height, oscillation amplitude, and weight per unit area for two of the oscillation modes was experimentally investigated. The design of the OAPL consisted of a rectangular thin plate excited with flexural oscillation (Figure 2.4). The authors proposed that the driving surface (a thin plate) should have a piston motion and various types of flexural oscillation. So as to acquire a flexural travelling wave, the design included a pair of longitudinal transducers located at right angles, close to the plate ends. One of these transducers operated as a generator for the wave, whilst the other one operated as a receiver for it. The receiver transducer was linked to a matching load comprising a resistor and an inductance. The path of a moving object could be altered through reversing the matching load and the oscillator.

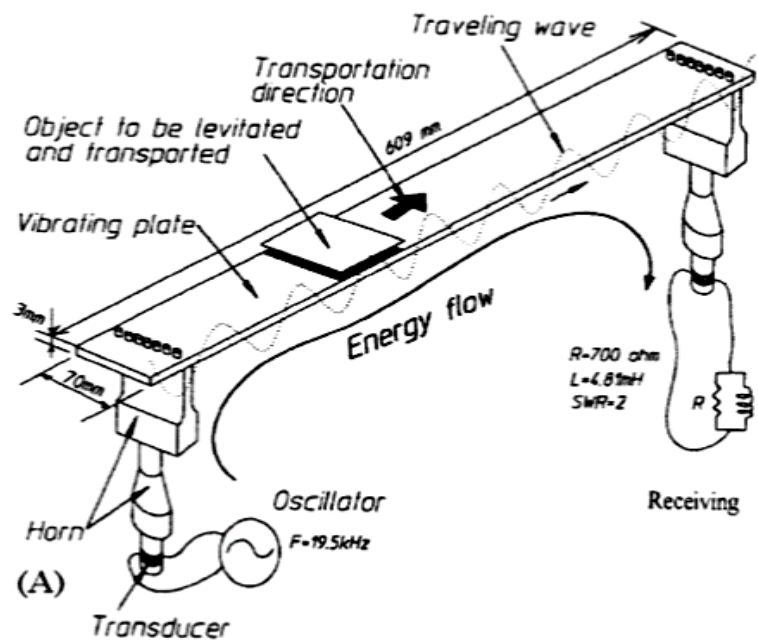


FIGURE 2.4 : Schematic layout of NFAL design (Ueha, Hashimoto, and Koike, 2000)

### 2.2.3 Squeeze Film Levitation (SFL)

It is not known when the squeeze-film levitation (SFL) approach was first proposed; however, experiments on squeeze-film air were illustrated by Langlois in 1962 and Salbu in 1964. Under this method, it is held that a time- average pressure in a clearance or between surfaces (driving and levitating) has a value which is greater than the ambient pressure, caused by the second-order influences possessed by a quickly compressed and released gas film between the surfaces. Two distinct properties distinguish the SFL design. First, it is unlike the SWL design as a reflector is no longer required and instead the levitating object itself acts as an obstacle for free circulation of the squeezed gas (air). Second, rather than the standing wave proposed for the SWL process, a thin gas film or air layer is assumed to be created between the top surface of driving structure and the bottom surface of the levitated item when the SFL is utilised, with the air-film being quickly compressed and decompressed as a result of the driving surface movement. Moreover, the theoretical analysis of

this method is based on the Reynolds equation unlike the SWAL or NFAL methods, which are both theoretically based on the acoustic radiation and sound velocity in air. In 1975, Whymark described a squeeze-film levitation design comprising a piston vibration source model, operated at an ultrasonic frequency of 20 kHz in order to levitate a flat brass disc of size  $50 \times 0.5$  [mm]. Wiesendanger, 2001, proposed a simple model that describes the basic idea of SFL performance. He only considered an entrapped gas between two surfaces that is quickly compressed and decompressed, thus ignoring the leaking and thrusting at the boundary. Hence, the total mass of air in a fixed volume remains constant, resulting in:

$$pV^n \sim ph^n = \text{const.} \quad (2.13)$$

where,  $p$  denotes the pressure,  $V$  is the entrapped gas volume,  $h$  is the gap height and  $n$  is the polytropic constant (isothermal  $n = 1$  and  $n = k \approx 1.4$  for adiabatic air). The relation between pressure and levitating separation is non-linear, which creates a time-averaged pressure  $\bar{p}(t)$  as a result of the imposed periodic gap distance  $h(t)$  (Wiesendanger, 2001). In view of the situation revealed in Figure 2.5, the gap fluctuates harmonically close to an equilibrium height  $h_0$ , i.e.  $h(t) = h_0(1 + \varepsilon \sin \omega t)$

where,  $\omega$  is the fluctuation's angular frequency,  $\varepsilon$  is the excursion ratio  $= a_0/h_0$ . The excursion ratio represents the vibration amplitude  $a_0$  to the average gap distance  $h_0$  and thus, the average pressure under the isothermal condition can be presented as:

$$\bar{p} = \frac{p_0 h_0}{2\pi} \int_0^{2\pi} \frac{1}{h(t)} d(\omega t) = \frac{p_0}{\sqrt{1 - \varepsilon^2}} \quad (2.14)$$

The harmonic motion of the driving surface yields a non-harmonic pressure vibration, the average value of which greater than the ambient pressure  $p_0$  (Figure 2.5). The analysis shows that the positive average pressure  $\bar{p}$  is greater than the ambient pressure  $p_0$ .



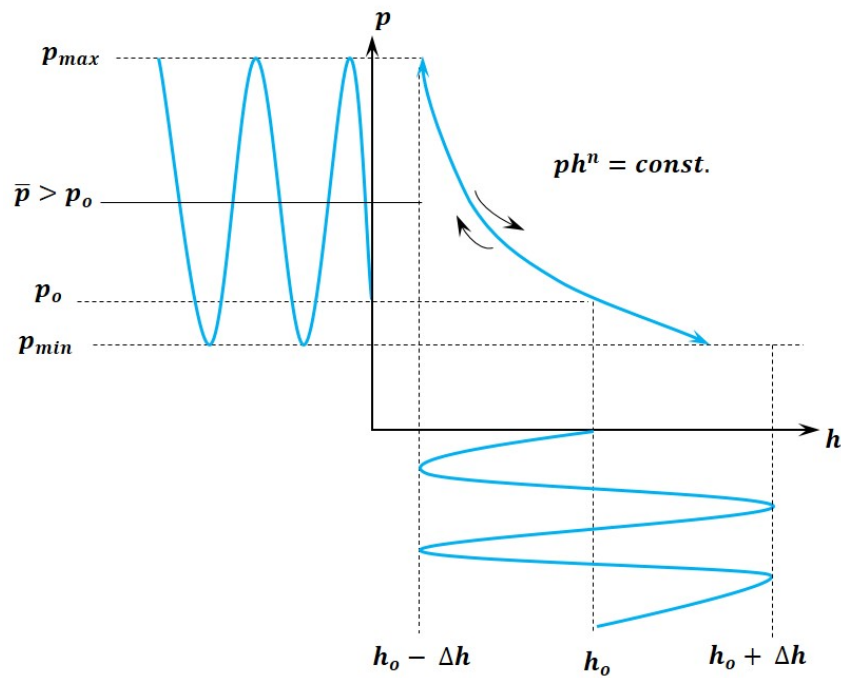


FIGURE 2.5 : The non-harmonic pressure vibration as a result of a harmonic motion

In order to develop a sub-micrometre levitating motion, most OAPL applications that used the SFL technique were advanced with piezoelectric (PZT) components. Many types of PZT devices have been utilised to participate in the generation of SFL. For example, some OAPL applications have involved using transducers, tube PZT, stacked actuators, while other researchers have used single layer PZT, which is the type that has been utilised for the current work. Clearly, PZT is available in many types, shapes and sizes depending on the application. Moreover, to drive the PZT, it is necessary to build suitable electrical circuitry in order to provide an appropriate voltage. Despite SFL designs being restricted through the size and design of the PZT elements, many systems amplifying the PZT response have been created. Hashimoto et al, (1996) reported that instant acoustic energy pressure can lead to steadily levitating objects with a weight of many kilograms regardless of the material. Moreover, the author stated that the surface of object subjected to NFAL must be flat in order to levitate stably. The essential features of NFAL with a one

of plate modal shapes excitation (flexural) were experimentally investigated. Additionally, theoretical illustration was made for the levitation design through plate modal shape investigations. Furthermore, the study acquired important results: a- the size of levitating object needs to be more than  $3/2$  wavelengths of the flexural oscillation to levitate the object steadily; b-a linear relationship between the levitating displacement and the excitation amplitude was discovered; c-an association between the levitating displacement and area density represented by the mass to area of the levitating item was elicited (ibid).

### 2.3 Levitating Characteristics of OAPL Bearing

Stolarski and Chai, 2006, theoretically considered squeeze-film influence on a linear sliding bearing with self-carrying ability. It was established that this kind of technique can work at a varied series of frequencies and load circumstances. An air film with a thickness of a few microns can be developed at a frequency of up to 4 kHz, lifting a mass of up to 0.8 kg. A modification to the compressible Reynolds equation by eliminating the air inertia force effect was proposed. The equation was solved numerically in order to explain an ultra-thin gas film problem, which the flow induced by the air inertia influence and this was found to be insignificant, thus being safely neglected. Stolarski and Woolliscroft, 2007, presented another enhanced bearing design using elastic hinges in a bearing (Figure 2.6). The design utilised a pair of stack piezoelectric actuators only on two sides of the bearing (top and bottom) to produce an excitation. It was elicited that the piezoelectric actuators and the elastic hinges played an important role in improving the linear bearing design. Based on the elastic hinges, the sides of the bearing can be distorted as a result of driving the actuators by a suitable voltage and frequency, which leads to adequate SFL bearing design. The researchers investigated a suitable operation frequency range to be applied to the design, which they found was between 0.5 kHz and 3 kHz. It emerged that operating the design at one of the natural frequencies leads to a large

squeeze-film thickness, which was verified by the experimental results. Moreover, it was discovered that the bearing levitation can be considered insignificant when the design is driven with non-resonance frequencies. Finally, the experimental results were compared with those predicted by a computer model of the bearing design at various operating parameters (e.g. voltages and range of frequencies).

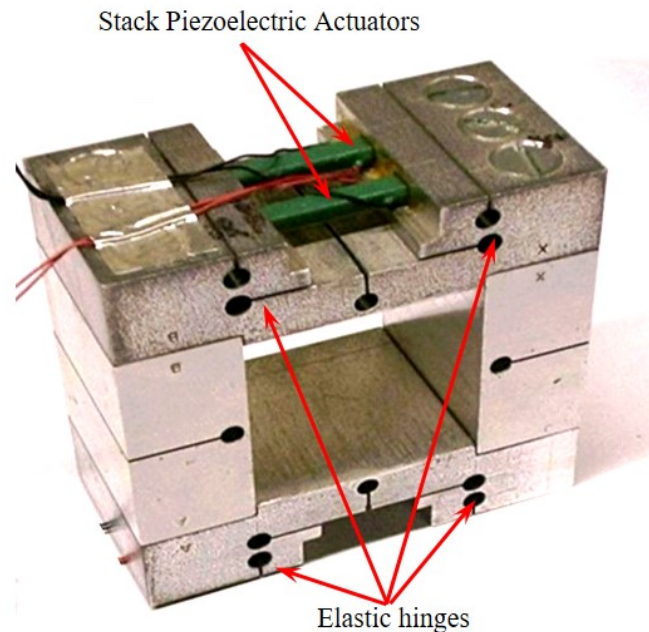


FIGURE 2.6 : Linear SFL bearing with piezoelectric actuators attached (Stolarski and Woolliscroft, 2007).

Stolarski (2010) made a comparison between experimental work for SFL bearing and theoretical results acquired from the Reynolds equation that represented the bearing system. Computational fluid dynamics (CFD) was used to deliver the validity of using the Reynolds equation. The examination revealed that for small vibrating amplitudes the Reynolds equation provides good agreement with CFD system modelling. However, the author found that the theoretical results presented a greater load capacity than those from the experimental results. In other words, the pressure profiles from the experimental results were somewhat smaller than those predicted by the theory. Yoshimoto et al, (2007) revealed a new improved design of squeeze-film linear bearing using ultrasonic vibrations, which comprised

a guide-way, a cartridge and single layer piezoelectric actuators, as shown in Figure 2.7. They focused on the ultrasonic frequency to drive the bearing design in contrast to the study of Stolarski and Woolliscroft (2007) outlined above. An oscillating amplitude was increased to  $1.7 \mu\text{m}$  measured at the edge of the top plate of the bearing. The noise generated during operation could be ignored when the bearing was driven at ultrasonic vibration. Furthermore, simple elastic hinges were added to the design to eliminate the need for complex ones in the SFL bearing structure, which avoided potential damage of the bearing structure in terms of the stress concentration and fatigue in the elastic hinges. Moreover, the design also greatly reduced the industrial cost. Finally, the power consumption was reduced due to the use of the single layer piezoelectric actuators instead of stack ones.

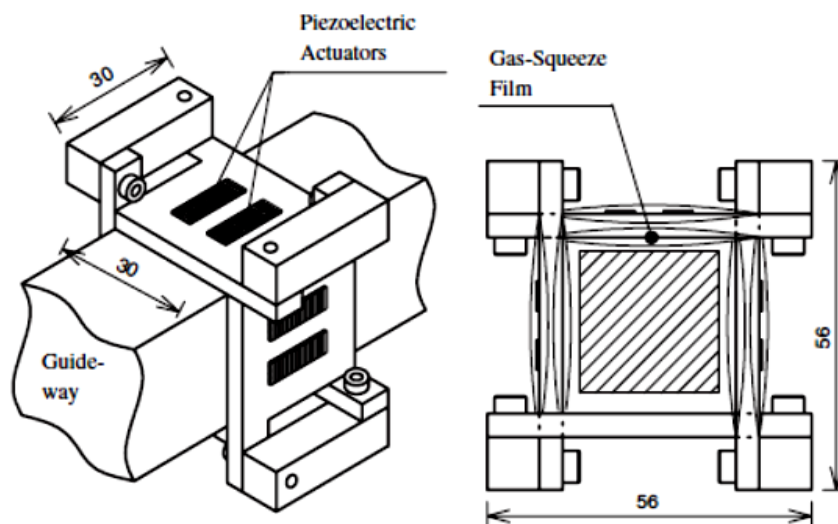


FIGURE 2.7 : Linear SFL bearing design (Yoshimoto, Kobayashi, and Miyatake, 2007).

### 2.3.1 Levitating Features of SFL Journal Bearing

Wang and Au (2011) developed the design of a hollow cylindrical journal bearing made from Aluminium (AL2024-T3), which worked based on the squeeze-film levitation method. The design included three 20-mm long fins mounted on the outer

surface of the bearing, equally spaced, 120° apart (Figure 2.8). Six single layer piezoelectric actuators were attached on the outer surface of the bearing. The casing of this design can be flexed creating a model of triangular shape (Figure 2.8), where the fin structure and position were one of the reasons behind the modal shape. The study was based on rules derived from a CFX and FEA simulation. The authors stated that to achieve a better squeeze-film thickness and to permit the bearing to reach its stable equilibrium quickly, the oscillation frequency setup should be not less than 15 kHz, to ensure that the oscillation amplitude is as large as possible. Hence, these investigations determined that this action can lead to enhancement of the squeeze-film thickness.

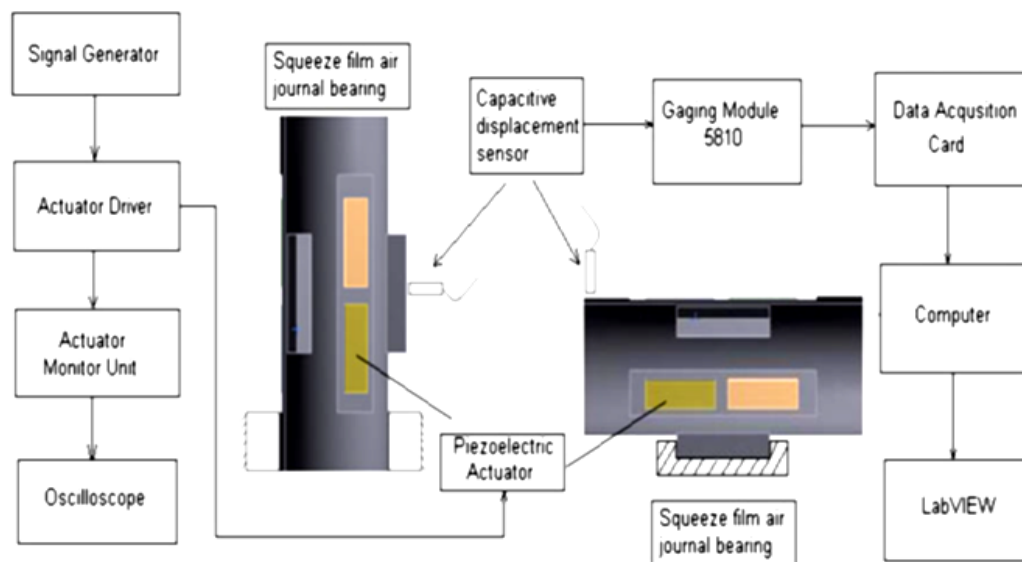


FIGURE 2.8 : Experimental set up of SFL journal bearing (Wang and Au, 2011).

Wang and Au (2012) built upon their previous research by investigating more with the same journal bearing material and size. They theorised that the levitation phenomenon stems from the presence of positive pressure in the SFL bearing design. Different natural frequencies and modal shapes were established for the bearing design by using a finite element program (ANSYS). It recognised two significant modal shapes, the 13<sup>th</sup> and 23<sup>rd</sup>, at the respective theoretical frequencies of 16.37 and 25.64 kHz (Figure 2.9). Moreover, they elicited that bearing levitation can occur with

both of the two modal shapes, but clearly, that the 13<sup>th</sup> mode was able to produce a greater load-carrying capacity. It was believed that the mode shape could produce less pressure leakage or in other words, the squeeze-air film at that modal shape was the thickest.

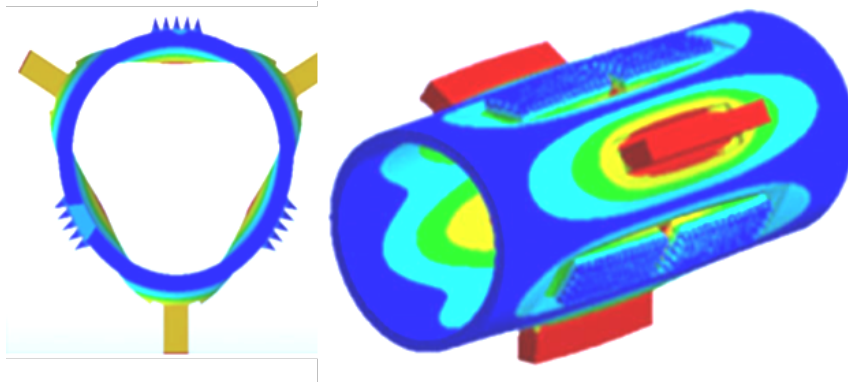


FIGURE 2.9 : Modal shape of squeeze-film journal bearing (Wang and Au, 2012).

Wang et al. (2013) examined the dynamic characteristics of bearing designs driven based on the SFL technique. The bearings were made from two different materials, one from aluminium and the other from copper, with the geometry for both designs being identical. They evaluated the static and dynamic behaviour of the bearings. It was discovered that whilst both bearings levitated a load when excited at the exciting modal shape (mode 13), the aluminium bearing presented better levitating characteristics than the copper one. They concluded that the difference between the bearing design results was because the Aluminium one had a higher modal vibration and a greater deformation response than the copper one as well as this being due to the mechanical material properties. The study involved implementing a CFX model to illuminate the squeeze-film influence, taking in consideration the pressure leakage from the bearing design boundaries. It is worth mentioning that all studies that all the studies carried out by Wang et al. (2011, 2012 and 2013) have been poor in showing the ways to undertake the simulation of the fluid - solid interface to determine the squeeze-film characteristics which are considered the most important factor in research regarding the squeeze-film levitation

phenomenon.

### 2.3.2 SFL characteristics

Minikes and Bucher (2003) investigated theoretically and experimentally an OAPL based on a squeeze-film levitation method. The examined design structure comprises a piezoelectric disc (actuator) type PZT-5A, which is polarised in its thickness and a mass the same size as the piezoelectric disc sited concentrically on top of it (Figure 2.10). It was elicited that there was an association between the elastic distortion and electric field that influenced fluid entrapped between the two surfaces (mass and piezoelectric disc). The authors tackled separately the equations that describe the system coupling that represents the structure-fluid interaction. The mechanical dynamic behaviour of the actuators was simulated through finite element analysis, whereas a numerical description of the fluid flow characteristics was represented by the Reynolds equation, analysed using the finite difference. The ultimate part of the mathematical examination revealed and simulated outcomes of a pressure distribution and some explanations regarding the squeeze-film performance. The researchers conducted a comparison between the results of the physical measurements and mathematical outcomes, which included an inspection of the response and dynamical actions of a freely suspended mass.

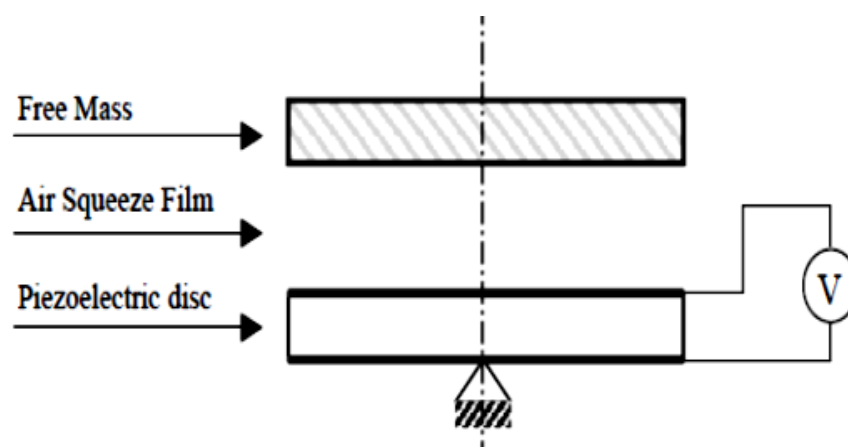


FIGURE 2.10 : Squeeze-film design (Minikes and Bucher, 2003).

Minikes and Bucher (2006) observed the rationality of the compressible Reynolds equation for a model design of squeeze-film levitating. The design consisted of a symmetric half of a flat sample (levitating object) with a width  $L$  and a much larger length, which was located at a height  $Z$  from a flat driving surface (Figure 2.11). The height  $Z$  was of order  $10^{-4}$  m, which was two orders of magnitude less than the width  $L$ . The fluctuating structure compressed a gas that existed at clearance between the levitating object and the oscillating wall, which led to a time averaged pressure greater than the ambient one. The contributions of this study were taking into consideration the effect of the temperature field and the impact of the near-field emission pressure at the boundaries of the levitated sample.

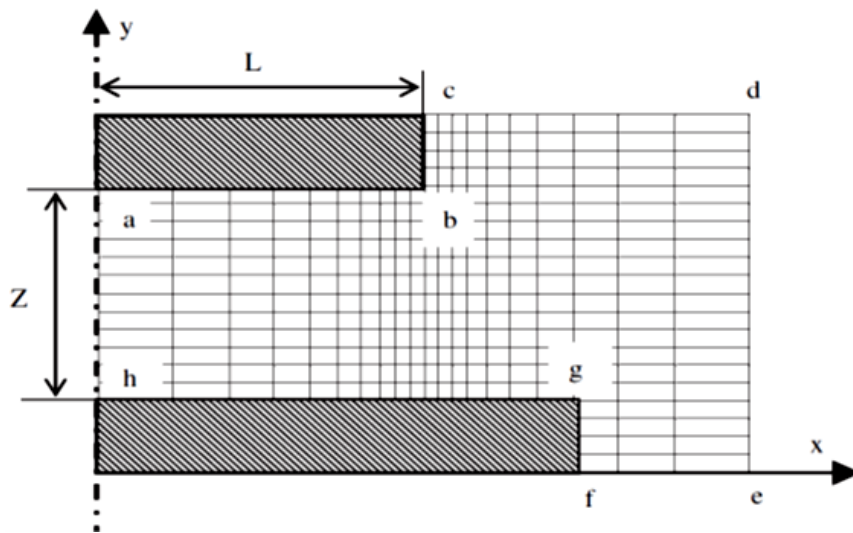


FIGURE 2.11 : Squeeze-film design (Minikes and Bucher, 2006).

It was revealed that the proposing of pressure discharge at the boundaries, included in the Reynolds equation, was insufficient in circumstances where the driving surface is bigger than the levitated surface. Finally, a comparison was made between the numerical calculations and an analytical second-order result of the Reynolds equation with a pressure discharge boundary condition, with the two being found to be well matching. Ilssar et al. (2014) employed optimisation for a levitation system design, which was able to lift a light weight for sub millimetres in



a normal direction or against gravitation. The design comprised an ultrasonic transducer and a rounded plate connected above that transducer. The effect of the design parameters, including geometry design and fluid flow were examined. The main goal was to find a suitable levitating design that could generate high levitating efficiency for a lightweight item and an accurate levitation capability in order to meet the high necessities of microelectronics developments. A mathematical scheme using finite differences was implemented to analyse air film entrapped between the vibrating and levitating surfaces (Figure 2.12). A coupled-field analysis of the reaction of the vibrating plate, which was calculated through finite element analysis (ANSYS) and a squeezed-film, which was a numerical scheme, was undertaken. A mathematical judgement between the optimised and the classical levitating designs was presented. Whilst the authors contended that the levitating happened as a result of NFAL, the analysis of the fluid flow was based on the Navier-Stoke equation and the compressible Reynolds equation.

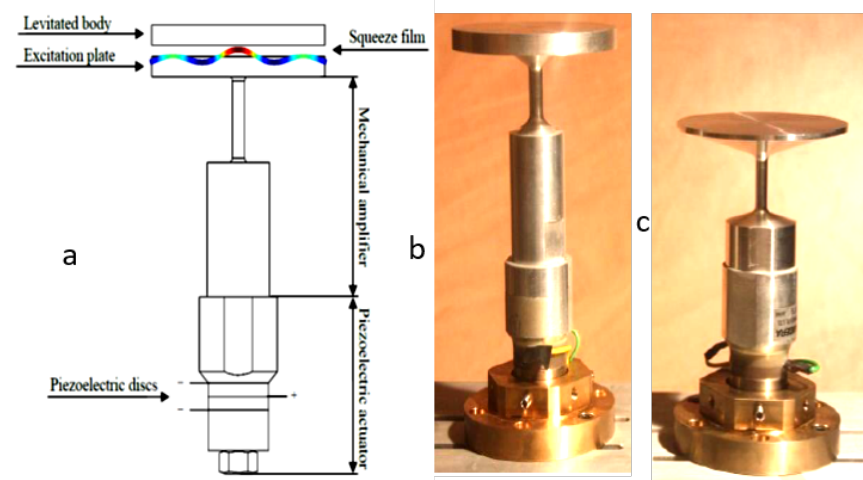


FIGURE 2.12 : a-Schematic layout of transducer design, b-the former transducer design, c-the optimal transducer design (Ilssar, Bucher, and Cohen, 2014)

Bucher et al (2016) (Bucher et al., 2016) worked with a mechatronics rig design system producing a frictionless action that could raise a lightweight object (silicon wafer) over the design for a few micrometres against gravity. It was explained how

the physical structure design involved carrying out a resonance tracking, which was aimed at retaining the design close to its resonance bandwidth and also outlined a closed-loop control for the system elevation. Moreover, the researchers investigated how to develop propulsion for the levitating object. It was generated through the design of a ring actuator. This was driven by three piezoelectric transducers that naturally yielded travelling waves in any wanted path, which created traveling pressure gradients in a clearance (air film) between the system and the levitated object, thereby lifting it with no contact. Furthermore, in the study, they controlled what is called a wafer aligner (Figure 2.13) through an appropriate numerical calculation, thereby effectively driving the system. It was believed that the new design could produce ultrasonic excitation signals able to deliver NFAL and propulsion.

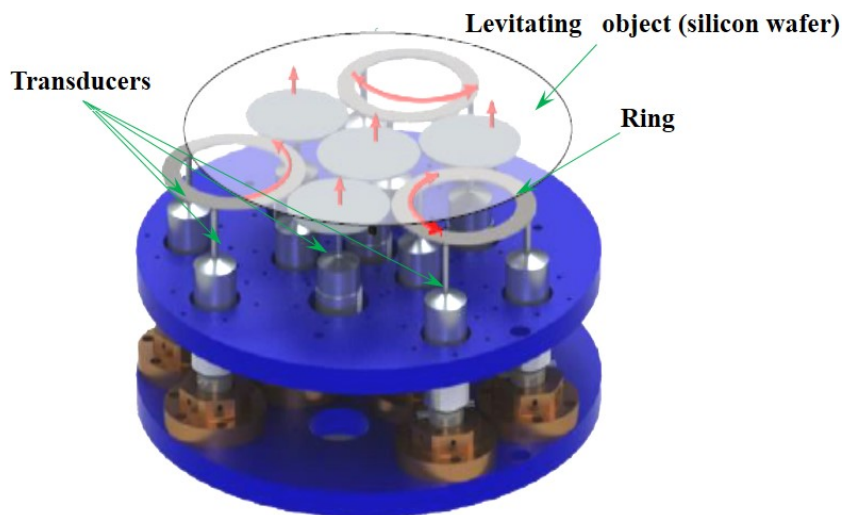


FIGURE 2.13 : Wafer aligner design; arrows show the direction of forces / torques Bucher et al., 2016

In the same field as Hashimoto's (1996) (Hashimoto, Koike, and Ueha, 1996) investigations, Kim and Jeong (2007) (Kim and Ih, 2007) studied the effect of the unsteadiness problem that often occurs with an object is levitated at the micron level. The authors pointed out that with instability in the levitating, difficulties in pick up or moving the levitating object arose. The examined levitation design was operated at ultrasonic frequency of 20.5 kHz with a velocity range of 1 m/s on a normal path.

Various acoustic sources (radiators) of different radius of 25, 30 and 35 [mm] were investigated. A flat aluminium disc (Al 7075) of thickness of 3 [mm] and radius of 10 [mm] was employed as a levitating sample (Figure 2.14).

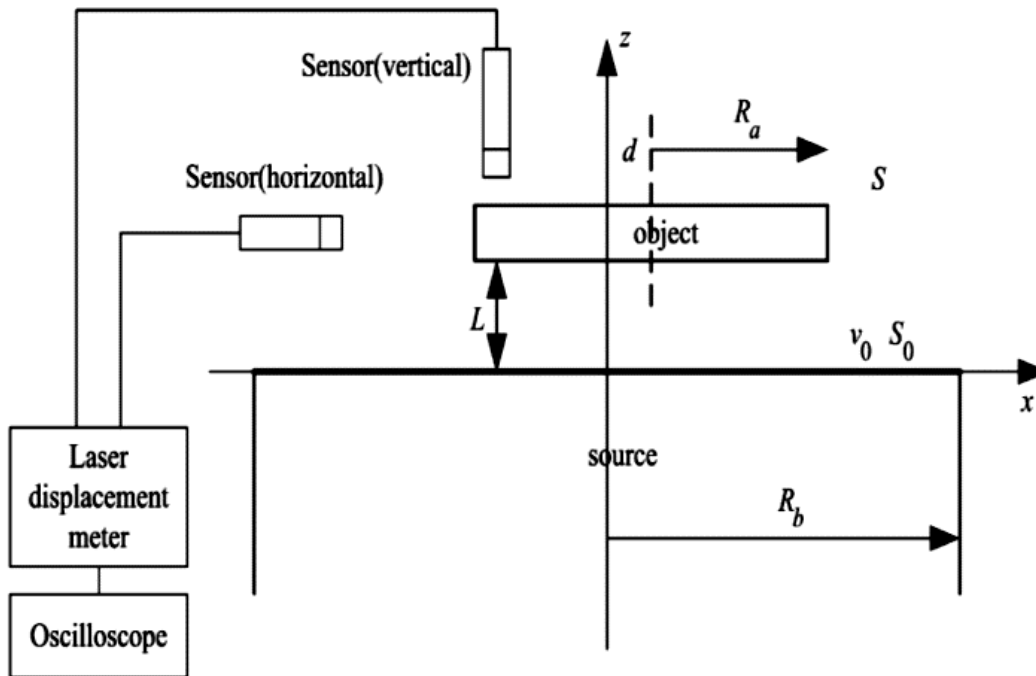


FIGURE 2.14 : Setup diagram of NFAL Kim and Ih, 2007.

The investigations were based on the phenomenon of NFAL. It was observed that when shifting between the acoustic source midpoint and the levitated object centre, the latter can wobble in a lateral direction. The time averaged potential was utilised to detect the transporting direction of the levitating sample when its centre shifted from the acoustic source midpoint. The researchers verified this through calculation for a swaying frequency and analysing the non-linear oscillation motion of a levitating sample. Additionally, a safe zone to avoid unbalanced conveying of the sample was proposed.

### 2.3.3 NFAL Influence and Load-Carrying Capacity

Stolarski and Woolliscroft (2007) demonstrated how a vibrating plate design can be used to create OAPL for an object placed on a plate. The design consisted of

a rectangular flat plate fixed at both ends, with piezoelectric actuators glued underneath to generate an excitation when driven by a certain voltage and frequency. Self-levitation for the object was established and hence, the outcomes justified the design. The authors discovered that there is an association between the levitating distance and the weights of the objects that can be levitated on the vibrating plate design. Moreover, the study findings illustrated that the arrangement and location of the piezoelectric actuator can affect the levitating distance, whereby the levitating is totally reliant upon the width wise attached PZTs, whereas the length wise attached ones participate in NFAL influence. Additionally, through finite element modelling using the ANSYS software, the predicted natural frequencies and modal shapes of the excitation plates provided good agreement when compared with the measured outcomes. The researchers concluded that the material of the excitation plate could affect the levitating distance. However, they could not explain the fluid-solid interaction or illustrate the fluid flow performance that impacts on the levitating. To suppress contamination, (Liu et al., 2009) carried out OAPL for a lightweight object depending on the occurrence of NFAL, They utilised the modal shape analysis, which determines the natural frequency of a desired mode and then, calculated the levitation force in terms of the levitation distance relying on the squeeze-film phenomenon through the benefit of a physical measured amplitude and a pressure distribution on the vibrator surface. The researchers deployed the Reynolds equation as the main equation to model the pressure distribution in the squeeze-film, under the assumptions that the flow was laminar, isothermal, and that there was a compressible thin film of fluid (air). They implemented theoretical observations based on a non-uniform exciting surface to compute the levitation force formed by the SFL and the outcomes were more efficient as the utilised a driving surface as uniform piston motion, in particular, with the experimental measurements, to represent the structure–fluid interaction. However, the study led to confusion by describing the levitating as being based on two different circumstances. First, it was proposed that NFAL technique was behind the levitating effect, and then, it was assumed the

investigation was based on the SFL method. Ishii et al. (2014) assumed that a weight (loading plate) can be statically levitated at a place where its gravity and the acoustic radiation influence are stabilised. They demonstrated a plate-shaped design to create a friction-less transporter for the weight throughout utilising the method of NFAL. The transporter design comprised four flexural aluminium vibrating plates and a loading plate, which they linked via supporting posts (Figure 2.15).

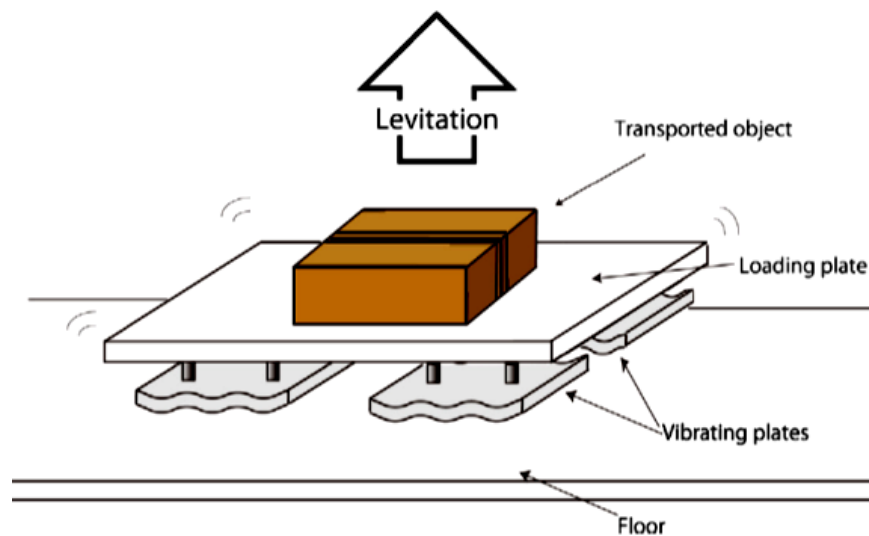


FIGURE 2.15 : Design of NFAL (Ishii et al., 2014).

The benefit from these posts was the minimisation of the deflection effect made by heavy loads. In addition, the design included four piezoelectric actuator (PZT) elements glued to each one of the vibrating plates, with these being driven at an ultrasonic frequency of (22.3 kHz). The study revealed that the levitation load was achieved as a result of transferring the acoustic radiation force from the vibrating plates to the loading plate. It was elicited that the maximum levitating height created by this design was 256 micrometres. Moreover, it was found that a weight of (4.0 kgf) can be levitated when the design used for two exciting plates is joined to a loading plate. Ilssar and Bucher (2015) developed a new approach based on NFA through the superposition of an equation regarding the motion of a levitating object and a compressible fluid flow equation that describes the squeeze-film, where system coupling (fluid-structure interaction) was achieved. The researchers

created NFAL design comprising an oscillating structure for making the essential vibration (driving surface) and a freely levitated flat sample, which were both cylindrical (discs) with matching diameters (Figure 2.16). The levitated sample was exposed only to the gravity and to the pressure influenced by the ambient fluid.

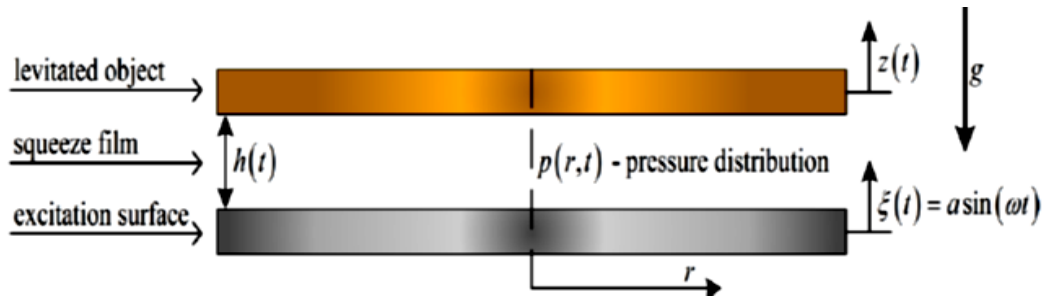


FIGURE 2.16 : SFL design (Ilssar and Bucher, 2015).

Furthermore, for the analysis, it was assumed that a vibrating surface fluctuates uniformly as a rigid piston. The study involved, firstly, investigating the levitation by modelling the system in the absence of damping characteristics and then, this was advanced to include a damping force. The action of the SFL was based on the compressible Reynolds equation, which was adapted under the assumption of isothermal conditions and only the vertical motion of the levitating surface was considered. However, the study led to confusion by describing the analysis as being based on the NFAL, while the modelling involved dealing with the Reynolds equation instead of the pressure radiation one and the velocity of the sound, as recommended in the literature. In addition, the authors assumed the driving surface moves like a piston, which does not hold in reality. Ilssar et al. (2017) carried out a new case study based on NFAL, which built upon the previous investigation (Ilssar and Bucher, 2015) in which it was anticipated that the driving surface fluctuates as a non-uniform standing wave (Figure 2.17). The investigation was accomplished by creating a calibration procedure that was employed to regulate the height of levitating, being reliant on carrying a load through a precise form of driving. The approach outcomes can be achieved numerically based on a finite difference modelling of the Reynolds equation. However, the authors mixed-up the SWAL and NFAL

methods. In addition, they used the Reynolds equation to describe the squeeze-film action.

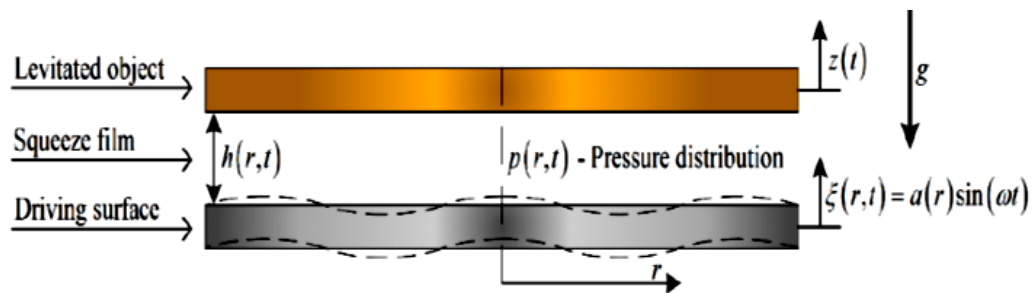


FIGURE 2.17 : NFAL design (Ilssar, Bucher, and Flashner, 2017).

Wei et al. (2018) designed a new contactless prototype levitating system for weights, which consisted of two actuator transducers, vibrating plate and a levitating sample of the same size as the vibrating plate, as shown in Figure 2.18. The levitating characteristic was based on an NFAL approach driven by standing waves and using a reverse hydrodynamic effect. The authors discovered that this effect acted as a pressure gradient and deflection angle to attain passive force and velocity on a driving plate. In addition, in the study, the levitation was deemed to have happened as a result of non-parallel squeeze-film. The authors stated that, the conveying of the sample occurred as a result of viscous fluid mechanics and a dynamic lubrication approach. The bearing and pushing capability is calculated through numerical estimation of the compressible Reynolds equation and a CFX model. However, the study did not reveal a levitation performance with time. In addition, the study led to confusion by describing the influence of the levitation as being based on acoustic, standing wave and SFL.

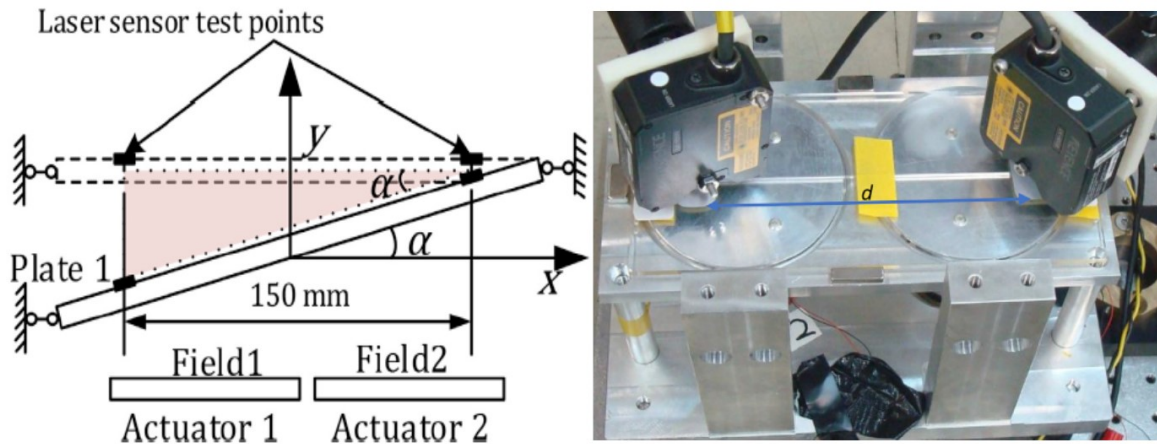


FIGURE 2.18 : **Left**-deflection angle; **Right**- Experimental set up for a non-parallel SFL design (Wei, Shaham, and Bucher, 2018).

Li et al. (2017) introduced a new idea regarding an improvement in load-levitating capability by making engraved grooves on a bottom surface of levitating plates. The levitating design comprised actuators, transducers, a vibrating plate connected to the transducer and different rounded levitating samples (Figure 2.19).

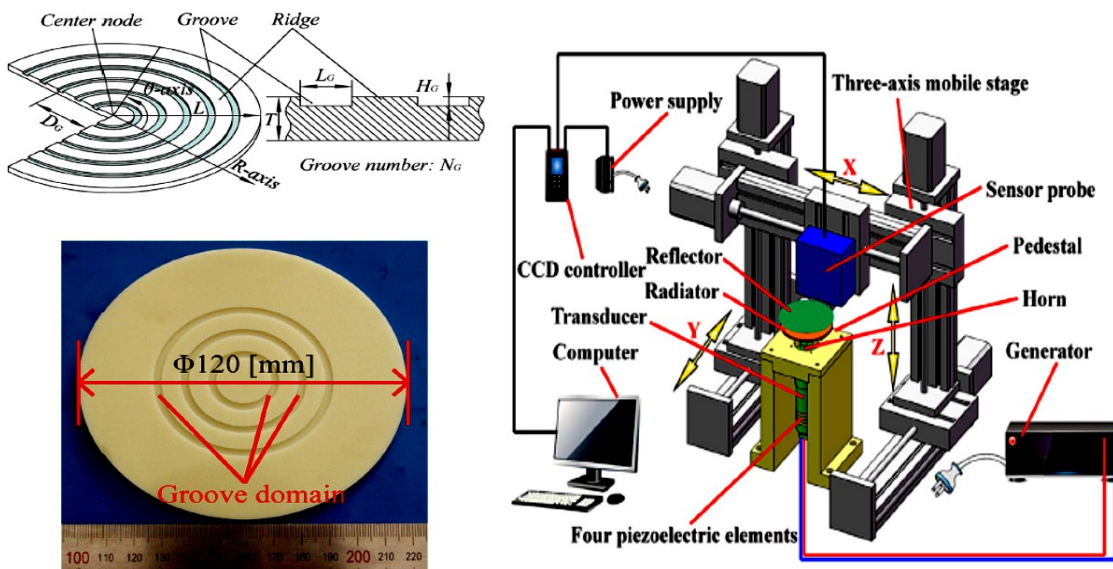


FIGURE 2.19 : **Left**-engraved levitating disc configuration; **Right**- Experimental set up (Li, Liu, and Feng, 2017).

The analysis of the study was based on NFAL method. The compressible Reynolds equation, combined with the driving plate mode shape, was utilised to determine



air pressure distribution in a pressurised gas (air) layer and accordingly, to find out the levitation force. An association between levitating distance and oscillation amplitude under various levitating surface situations was determined and compared with the measured outcomes.

### 2.3.4 Conclusion

The studies regarding OAPL comprise three main categories according to the reason for the effect. That is frictionless movement of an object levitated over a vibrating surfaces can occur as a result of: SWAL, NFAL and SFL. In this chapter, many parameters highlighted by the literature have been described and the shortcomings of some investigations have also been covered. Regarding the previous work, Hashimoto, in 1969, achieved important results that improved the steady levitating of an object steadily, whereby the size of the levitation object needed be greater than  $3/2$  wavelengths compared to the flexural vibration. Stolarski and Woolliscroft (2007) offered an enhanced design called 'elastic hinges' in the SFL bearing for a linear motion guide. Yoshimoto, et al. exhibited a new design of squeeze-film linear bearing using ultrasonic vibrations to avoid the noise generated during operation. Wang and Au (Wang and Au, 2011; Wang and Au, 2012; Wang and Au, 2013), when studying the effect of SFL on a journal bearing, found that air film at high vibration amplitude leads to an increase air-film thickness within the micrometre scale and thus, journal bearing design reaches stable levitating when the air-film vibrates with a range of ultrasonic frequency. However, for the simulation to find the SFL performance with time and Fluid – Solid Interaction (FSI), they did not explain the way to implement that calculation. Stolarski and Woolliscroft illustrated how the arrangement and location of the piezoelectric actuator fixed to the underside of a plate can improve the levitating distance. However, they did not simulate the levitation circumstances or evaluate the important features of squeeze-film levitation, such as pressure distribution and separation distance. Hence, one of the

objectives in the current study is to simulate the SFL and to calculate the essential characteristics of SFL. Some of the literature fostered confusion when describing the method of levitating operation. For example, in some investigations it was assumed that the levitating happened as a result of NFAL, whilst utilising the compressible Reynolds equation to describe the levitation action. This work will be based on SFL and will involve the levitating for a lightweight object placed on a forced displacement plate design. Specifically, to these ends, various types of material for the plate designs, several plate dimensions, various types of single layer piezoelectric actuators (PZTs), different dynamic distortion or modes of PZTs as well as different positions and arrangements of PZTs have been studied.

## Chapter 3

# Driving Unit – Piezoelectric Actuators

### 3.1 Introduction

This chapter illustrates the fundamentals and the basics of piezoelectric actuators as well as transducer design. The knowledge is essential to understand the context in the later chapters regarding SFL systems. The chapter begins with a short history of piezoelectricity and review of piezoelectric substances. In addition, an overview of piezoelectric actuators, their work and function, is provided, with their benefits and drawbacks also being described. Moreover, the piezoelectric coefficients, their finite elements, their mathematical description and various piezoelectric material properties are presented. Finally, various modes of piezoelectric actuators based on polarisation orientation, applied electric field and electrode location are demonstrated. To conclude, the accomplished outcomes are summarised and proposals for future works provided.

#### **Piezoelectric History**

The occurrence of piezoelectricity was explored in 1880 by the French physicist brothers Pierre and Jacques Curie. They discovered that, some crystals, when a load is applied in a specified direction display different charges (positive and negative) on some parts of the surface. Later, in 1881, Gabriel Lippmann mathematically

made a significant contribution to piezoelectricity by predicting the reverse influence and that when a piezoelectric entity is subjected to an electric source a deformation is experienced, which was subsequently experimentally confirmed by the brothers Curie. They mechanically connected two piezoelectric objects, by altering the mechanical effect created from one of them into an electric signal collected from the other.

## 3.2 Piezoelectric ceramics overview

Piezoelectric ceramics are used in multi-purpose materials (smart materials) for various implementations due to their reliability, sensitivity, fast response and low energy consumption. They can be glued onto the surface of the structure or implanted into the structure itself. They can be used as sensors and transducers, to change many physical parameters into electrical indications. Furthermore, they can do the reverse: change the energy from electrical into mechanical vibration. That is, piezoelectric ceramics can be used as actuators, altering a voltage into an accurate physical movement (Qin, 2012). Based on the statement that all equipment that has moving components may oscillate, the excitation forces transported to neighbouring mechanisms within it can produce the motion; displacement with various amplitude and frequency. There are occasions, though not many, when oscillation can be put to good use. The previous chapters have explained the parts that comprise the design of the squeeze film levitation in which the piezoelectric actuators are an important part, as the performance of such a levitation system will largely be based on them. Hence, acknowledgement of the operating principle and the fundamental design approaches is crucial when exploring the squeeze film levitation system. In this chapter, piezoelectric actuators are used as a forced source when they are attached to a thin plate structure and an electric field is applied to them. A distortion of the plate can take place as a result of the contraction and expansion of these actuators when a sufficient voltage and a certain signal waveform are exerted. The

plate design (plate and actuators) defamation has the important role of delivering the levitating for an object placed on it. The objects created for squeeze film levitation (SFL) designs have been widely implemented using piezoelectric actuators as driving components. A piezoelectric actuator generally comprises two main parts: a mechanical one, which has an elastic structure and an electrical one, which is the piezoelectric material block (Shah, 2011).

### 3.3 Dynamics of Piezoelectricity

#### Introduction

There are many modes of deformation that can be constructed through a piezoelectric material. In order to understand these, some piezoelectric coefficients must be defined. These coefficients,  $d_{3n}$  and  $g_{3n}$ , representing charge and voltage, respectively, are those most widely used with piezoelectric material properties (Rogacheva, 1994). In addition, most of the coefficients are presented with notations that represent piezoelectric axes (Figure 3.1). The first subscript of the piezoelectric coefficients  $d_{3n}$  or  $g_{3n}$  denotes the electrical axis, while the second refers to the mechanical one. Since a piezoelectric component is thin, the electrodes are only applied to the top and bottom surfaces. Consequently, the electrical axis is always "3", as the charge or voltage is always transferred through the thickness ( $n=3$ ) of the component. The mechanical axis can be either 1, 2, or 3, since the stress can be applied or obtained on any of these axes and the shear about one of them is represented by the subscripts 4, 5, or 6, respectively (Figure 3.1).

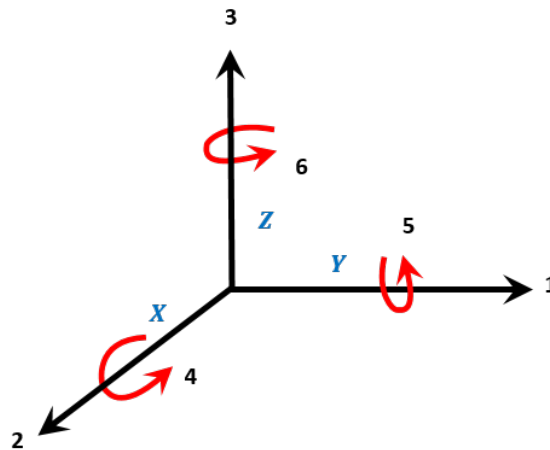


FIGURE 3.1 : Direction of piezoelectric element axes.

Based on electrical field excitation and the distortion of importance, piezoelectric actuators can be employed utilising different modes: longitudinal  $d_{33}$ , transverse  $d_{31}$  and shear  $d_{15}$ . In the next subsections, these modes are explained (Soh, Yang, and Bhalla, 2012).

### Piezoelectric working principles

As above, ceramics have a property called piezoelectricity, whereby when force is exerted on this material, it will create an electric field related to that force, which is known as the direct piezoelectric influence. The opposite of this relationship also is true, when the piezoelectric object is subjected to an electric source, it slightly varies in shape, which is called inverse piezoelectric behaviour. The working principles of the piezoelectric influence and inverse piezoelectric effect are illustrated in Figure 3.2 (Jordan and Ounaies, 2001; Ballas, 2007).

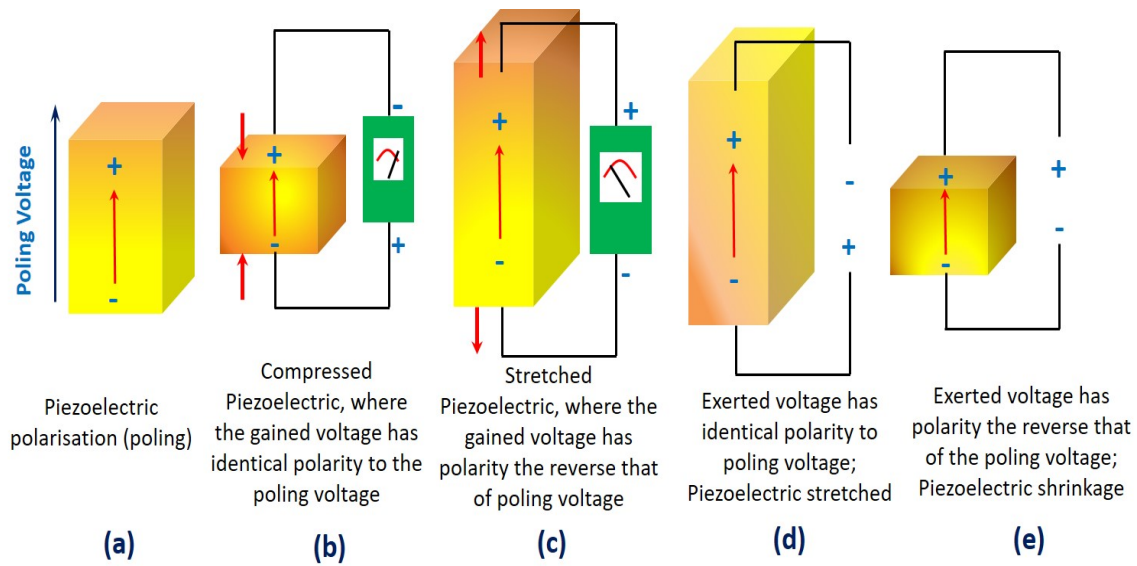


FIGURE 3.2 : Direct and indirect piezoelectric material effects, voltage gained and shape change.

The length of the piezoelectric entity will grow or contract when a voltage is applied along the direction of the polarisation, as shown in Figure 3.2. Moreover, it can be stretched and contracted cyclically when an alternating voltage is applied. An electric field distorts a piezoelectric object in various directions with different strengths. The two most utilised kinds of piezoelectric influence for constructing piezoelectric actuators are the longitudinal and transversal deformation modes (Figure 3.2-d and Figure 3.2-e). The polarisation can be created in one direction, because the piezoelectric materials are anisotropic. It is typically specified as having an index of 3, and the paths normal to that are assigned as index 1 and 2. A piezoelectric component can produce a strain when an electrical field in the direction of polarisation is applied to it and this action can be expressed as:

$$s = E_3 d_{3i} \quad (3.1)$$

Where,  $s$  denotes the strain,  $E_3$  is an applied electrical field and  $d_{3i}$  is a charge constant, which has the unit of  $m/V$ . For actuators utilising the longitudinal influence, the piezoelectricity distorts on a similar path to that of the exerted electric field. As

for the transversal action  $d_{31}$ , the distortion is on a path perpendicular to the direction of the exerted electrical field (Rogacheva, 1994; Vijaya, 2016). A piezoelectric ceramic item can be modified in terms of its composition, form, and size to meet the necessities of a particular function. Larger sensitivity and higher functional temperatures can be found with ceramics built-up from lead Zirconate/lead Titanate group (PZT) than with ceramics made from other chemicals. PZT materials now are the most widely utilised. Piezoelectric actuators have the ability to transform electrical energy into mechanical energy (Figure 3.3) (Qin, 2012). Consistent with the electrical drive technique, they can be separated into two classes based on the driving type: resonant and non-resonant. Resonant ones include ultrasonic motors, ultrasonic transducers and piezoelectric transformers. The non-resonant driven type include many one-stroke piezoelectric actuators. Their working oscillation range is from quasi-static up to approximately half of the fundamental frequency of the mechanical design. Typical strain levels that can be acquired by a piezoelectric element are approximately 0.1%. For quasi-static applications, this strain happens at field strength of magnitude  $1000 \text{ V/mm}$ . This extreme field strength is restricted to around 75% of the magnitude of the coercive field (the capacity of a ferromagnetic material to resist an exterior magnetic field without converting into being demagnetised). So as to raise the whole dynamic distortion ability of a piezoelectric actuator, stack or multilayer piezoelectric actuators are frequently utilised. For resonant driven piezoelectric actuators, an alternative technique to escalate the dynamic deformation is to utilise magnifying tools like boosters or horns (Ballas, 2007).

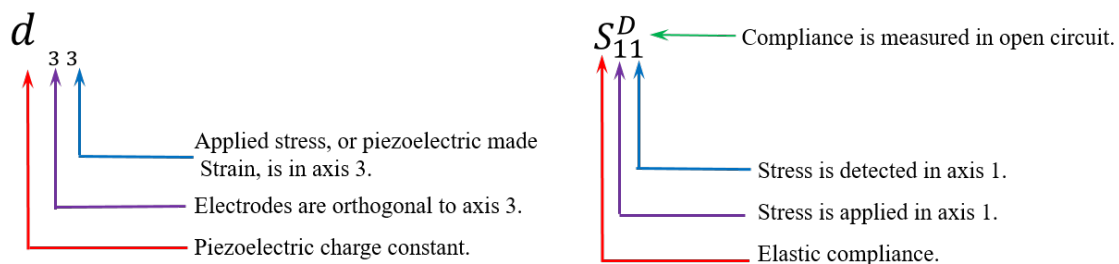
### 3.4 Piezoelectric Coefficients

There are many coefficients for piezoelectric material that must be studied to recognise how various types' work, with the purpose of selecting suitable ones for an application. In addition, their mathematical expressions their mathematical expressions need to be understood so as to be able to simulate them into finite element



package in the right way. In this section, some important piezoelectric coefficients as well as mathematical and finite element expressions are introduced (Jordan and Ounaies, 2001; Vijaya, 2016). Some piezoelectric substance constants are expressed with a superscript, which identifies either an electrical or a mechanical condition. The superscripts are T, E, D, and S, where:

- T is a constant stress corresponding to being mechanically free;
- E is a constant field equivalent to a short circuit;
- D is a constant electrical displacement identical to an open circuit;
- S is a constant strain equivalent to a mechanical clamp.



#### (a) Piezoelectric Strain Coefficient ( $d$ ).

This is considered as an electromechanical parameter of the piezoelectric material, being the suitability constant between displacement and stress or strain and the electric field. It is the degree of electrical polarisation produced per unit of mechanical stress executed to piezoelectric material. Alternatively, it is the mechanical strain generated by material per unit of electric field executed (Kim, 2006).  $d_{33}$  is the induced polarisation in direction 3 per unit of stress exerted in direction 3, or it is the strain induced per unit of electric field in direction 3, as shown in Figure 3.1 and Figure 3.2. Whilst  $d_{31}$  is induced polarisation in direction 3 per unit of stress exerted in direction 1, or it is the mechanical strain in direction 1 per unit of electric field in direction 3.  $d_{15}$  is

induced polarisation in axis 1 per unit of shear stress exerted around direction 2 or induced shear strain about direction 2 per unit of electric field exerted in direction 1. A high magnitude of  $d$  coefficients is advantageous for piezoelectric materials, which are considered beneficial in motional or vibrational devices, such as sonar (Kim, 2006; Vijaya, 2016). In all piezoelectric materials  $d_{31}$  is negative and  $d_{33}$  is positive. Figure 3.3 demonstrates the piezoelectric deformation modes  $d_{33}$  and  $d_{31}$ , when the electric field,  $E$ , is applied parallel to the piezoelectric polarisation,  $P$  (Figure 3.3-a), via the application of a voltage  $V$  between the bottom and top electrodes, which are displayed by the purple area. This action will lead to a vertical strain (thickness-wise), which can be represented by  $\epsilon_{33} = d_{33}V$  and a lateral strain or (in-plane) contractions, which can be represented by  $\epsilon_{31} = d_{31}V$  and  $\epsilon_{32} = d_{32}V$ . In contrast, if the electric field is exerted perpendicular to the direction of piezoelectric polarisation and by electroding the side faces of the piezoelectric component (Figure 3.3-b), the action will be a shear strain, which can be represented by  $\epsilon_{15} = d_{15}V$ . The use of lateral electrodes may not be feasible with a thin piezoelectric. In this situation the, top and bottom electrodes can be used again, but the piezoelectric polarisation must be aligned with an in-plane direction (Giurgiutiu, 2007).

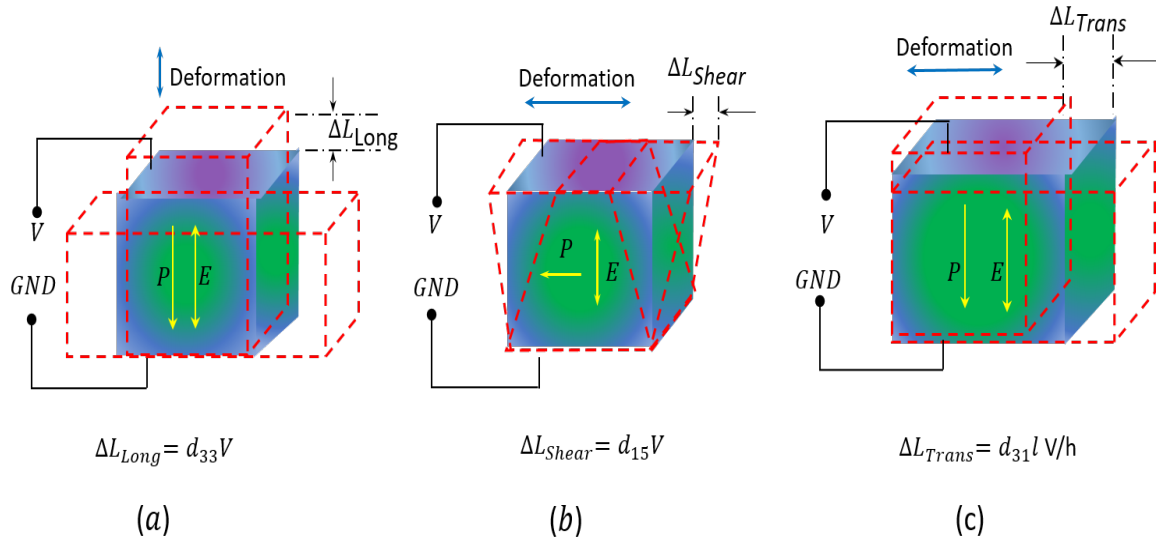


FIGURE 3.3 : Basic Piezoelectric modes: (a) Longitudinal Mode; (b) Shear Mode and (c) Transverse Mode (purple area shows the electrodes).

#### (b) Piezoelectric Voltage Coefficient.

This is described as the electric field promoted in a material per unit of mechanical stress exerted on it. Otherwise, it is the mechanical strain created by the material per unit of electric displacement to execute it. The coefficient is significant for evaluating a material's suitability for sensing utilisation. The first subscript signifies the direction of the electric field produced in the substance, whereas the second refers to the applied stress direction or the induced strain (Kim, 2006). A high magnitude of piezoelectric voltage coefficients is advantageous for piezoelectric materials, which are considered beneficial in harvest voltages in response to mechanical stress (Bowen et al., 2014; Vijaya, 2016).

$$\frac{\text{Field}}{\text{Applied Stress}} = \frac{\text{Strain}}{\text{Applied charge/Electrod area}} \quad (3.2)$$

#### (c) Electromechanical Coupling Factor (K).

This can be utilised to calculate the efficiency of energy transformation in the component (but not the total efficiency of a transducer). It is an indicator of the effectiveness with which a piezoelectric transforms electrical energy into

mechanical energy, or vice versa. The relation of energy alteration can be represented as (Vijaya, 2016):

- For component electrically stressed:

$$K = \frac{\text{Stored electrical energy}}{\text{Applied mechanical energy}} \quad (3.3)$$

- For component mechanically stressed:

$$K = \frac{\text{Stored mechanical energy}}{\text{Applied electrical energy}} \quad (3.4)$$

### 3.5 Piezoelectric Performance

Piezoelectric actuators are sometimes specified in terms of their free deflection and blocked force. Free deflection  $X_f$  refers to displacement attained at the maximum recommended voltage level if the actuator is entirely free to move. Blocked force  $F_b$  refers to the force exerted at the maximum recommended voltage level when the actuator is entirely blocked and not allowed to move. Deflection is at a maximum when the force is zero, and force is at a maximum when the deflection is zero (Figure 3.4). All other values of simultaneous displacement and force are calculated through a line drawn between these points on a force versus deflection line (Figure 3.4).

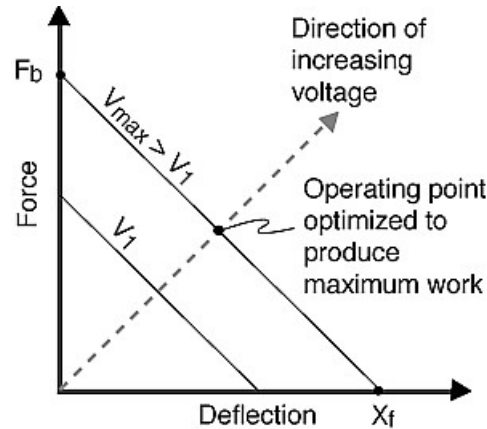


FIGURE 3.4 : Force versus displacement for a piezoelectric actuator (Ghodssi and Lin, 2011).

### 3.6 Piezoelectric Mechanical and Electrical Modelling

In general, the dynamic performance of a linear system exposed to a harmonic movement can be designated with adequate accuracy by combining only a few of the eigenmodes. An individual eigenmode governs the oscillation performance of the system in the range of the corresponding resonant vibrational frequency. Consequently, when a piezoelectric actuator is operated close to one of its resonant frequencies, its performance can be labelled with reasonable accuracy through a representation with only one degree of freedom (1-DOF). Based on electro-mechanical analogies, the dynamic displacement of a transducer working close to one of its resonant frequencies can be illustrated through a corresponding mechanical or electrical model. As can be seen in Figure 3.5 and Figure 3.6, the models comprise a modal mass ( $m$ ), modal stiffness ( $c$ ), modal damping ( $d$ ), electrical capacitance ( $C$ ) and electrical resistance ( $R$ ). The electromechanical conversion parameter ( $\alpha$ ) defines the transmission ratio of the electrical and mechanical amounts. Input voltage, charge, modal displacement, angular frequency and mechanical load are signified by  $U, Q, \Omega, u$  and  $F$  respectively. Along with these models, the dynamics of the system can be expressed as:

$$m\ddot{u} + d\dot{u} + cu = \alpha U + F \quad (3.5)$$

$$\frac{1}{C} (Q - \alpha u) + R (\dot{Q} - \alpha \dot{u}) = U \quad (3.6)$$

In harmonic movement  $U(t) = \text{Re} [Ue^{j\Omega t}]$ , the association between the input and the output excitation can be expressed as:

$$\begin{bmatrix} \widehat{\Gamma} \\ \widehat{\dot{u}} \end{bmatrix} = \begin{bmatrix} Y_{11} & Y_{12} \\ Y_{21} & Y_{22} \end{bmatrix} \begin{bmatrix} \widehat{U} \\ \widehat{F} \end{bmatrix} = \begin{bmatrix} \frac{j\varphi}{jR\varphi + \frac{1}{C}} + \frac{j\varphi\alpha^2}{-m\varphi^2 + jd\varphi + c} & \frac{j\varphi\alpha}{-m\Omega^2 + jd\varphi + c} \\ \frac{j\varphi\alpha}{-m\varphi^2 + d\varphi + c} & \frac{j\Omega}{-m\varphi^2 + jd\varphi + c} \end{bmatrix} \quad (3.7)$$

In which, the current is  $\widehat{\Gamma} = j\Omega\widehat{Q}$ ,  $\widehat{F}$  and  $\widehat{\dot{u}}$  are complex amplitude and the elements of the transfer matrix are defined as:

$$Y_{11} = \frac{\widehat{\Gamma}}{\widehat{U}} = \frac{j\varphi}{jR\varphi + \frac{1}{C}} + \frac{j\varphi\alpha^2}{-m\varphi^2 + jd\varphi + c} \quad (3.8)$$

the short-circuit input admittance

$$Y_{21} = \frac{\widehat{\dot{u}}}{\widehat{U}} = \frac{j\varphi\alpha}{-m\varphi^2 + d\varphi + c} \quad (3.9)$$

the short-circuit core admittance (forward)

$$Y_{12} = \frac{\widehat{\Gamma}}{\widehat{F}} = \frac{j\varphi\alpha}{-m\varphi^2 + jd\varphi + c} \quad (3.10)$$

the short-circuit core admittance (backward)

$$Y_{22} = \frac{\widehat{\dot{u}}}{\widehat{F}} = \frac{j\varphi}{-m\varphi^2 + jd\varphi + c} \quad (3.11)$$

the short-circuit output admittance.

The model factors can be determined from the measurement outcomes of the admittances.

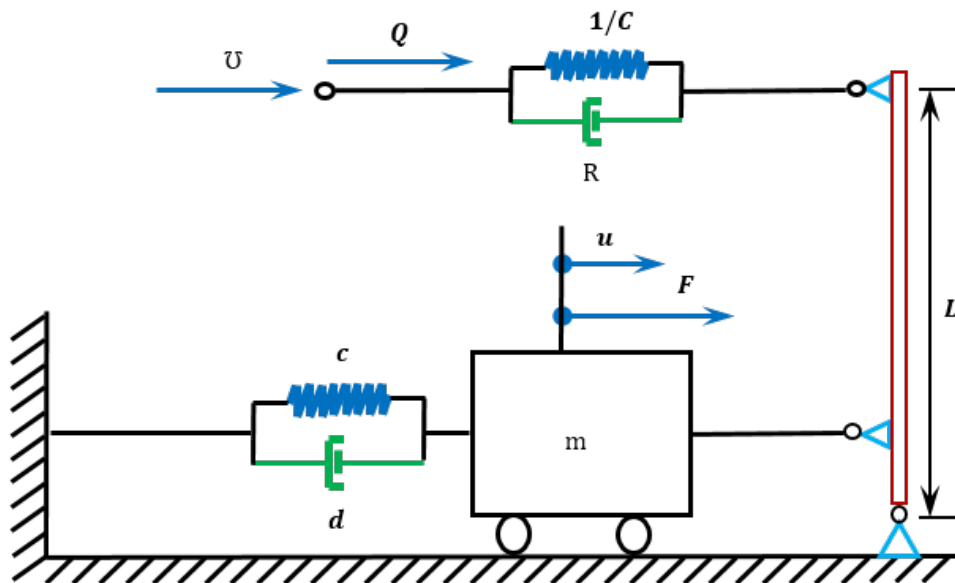


FIGURE 3.5 : Equivalent mechanical state of piezoelectric element.

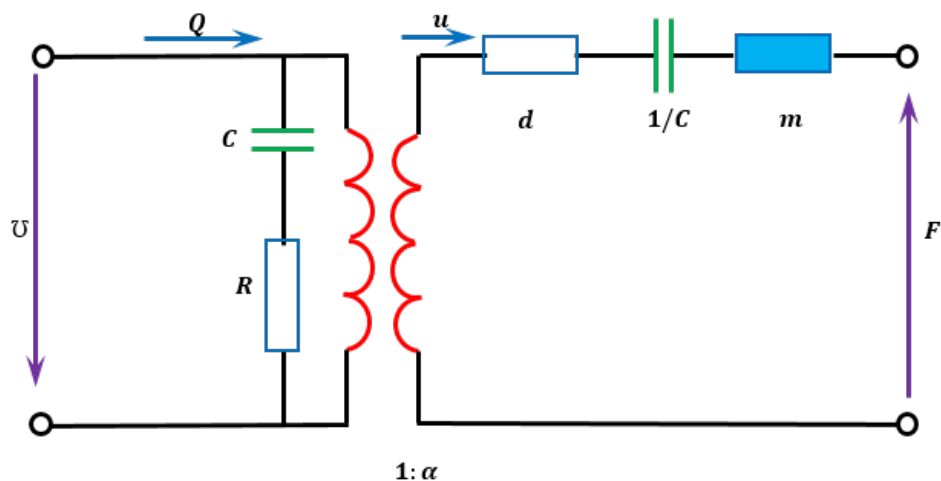


FIGURE 3.6 : Equivalent electrical state of piezoelectric element.

### Piezoelectric drawbacks

There are three main problems associated with piezoelectric performance (Gomis-Bellmunt and Campanile, 2009; Gautschi, 2002):

1. Mechanical stability of the piezoelectric material under large AC stresses;
2. Electrical breakdown of the material under high fields;

### 3. Reduction in efficiency due to dielectric losses and depolarisation.

These problems can be overcome by smart piezoelectric design and better material selection. The piezoelectric effect, the types of actuator and the interpretation of a manufacturer's data on the piezoelectric actuator will be illustrated in the next section to demonstrate its working principles.

### **Transducer Design and Performance**

One of important OAPL application designs is a transducer. The operational frequencies to power this design are often between 20 and 100 [kHz], with the high requirements regarding the power, efficiency and oscillation amplitude of operational ultrasonic transducers. For such applications, Langevin (or sandwich) transducers are usually utilised (Figure 3.7). These include front and rear metal masses, piezoelectric actuators rings and a central bolt passed in the middle of the Langevin design to create a pre-stressing effect. There are several advantages of Langevin transducer design, one of these being the effect of pre-stress on the piezoelectric elements through a central bolt or peripheral sleeve leads to an acceptable dynamic stress scale, whereby the maximum power intensity is significantly improved. Another advantage of the design, is that the mechanical connection between the elements (e.g. actuators and metal masses) is enhanced as a result of the pre-stressing and so, the mechanical damping declines. In addition, the metal end sections have a good functionality of heat-sinks and consequently, the transducer can be operated at greater oscillation levels than with other kinds of ultrasonic transducers designs. Finally, as the production of metal is much easier than that of piezoelectric materials, different geometrical configurations of transducers are obtainable, which will contribute to enhancing design performance and accordingly, the levitation effectiveness (Nakamura, 2012).



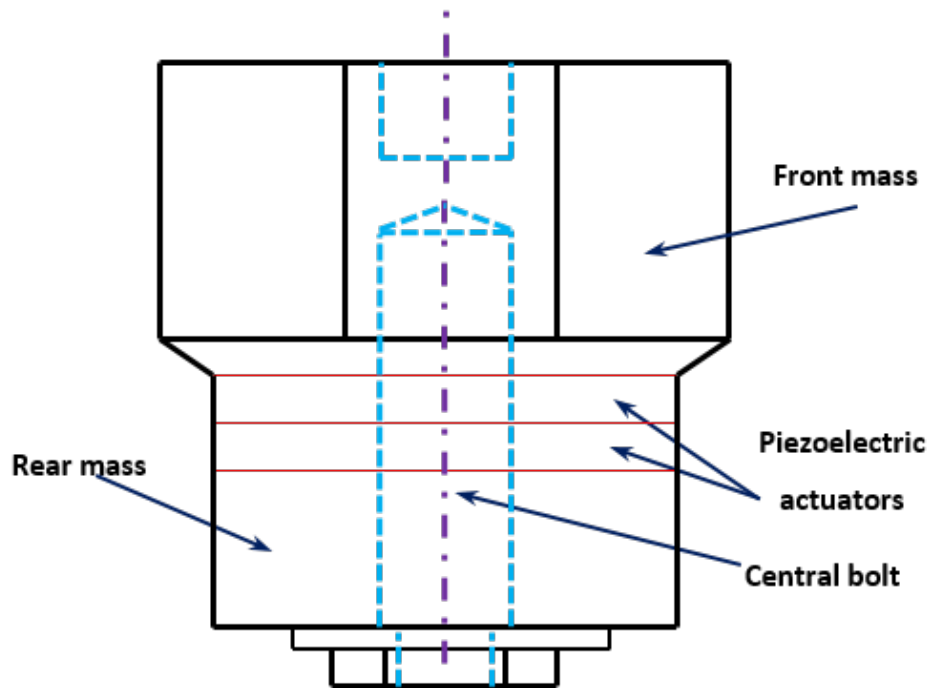


FIGURE 3.7 : Design of a Langevin type ultrasonic transducer.

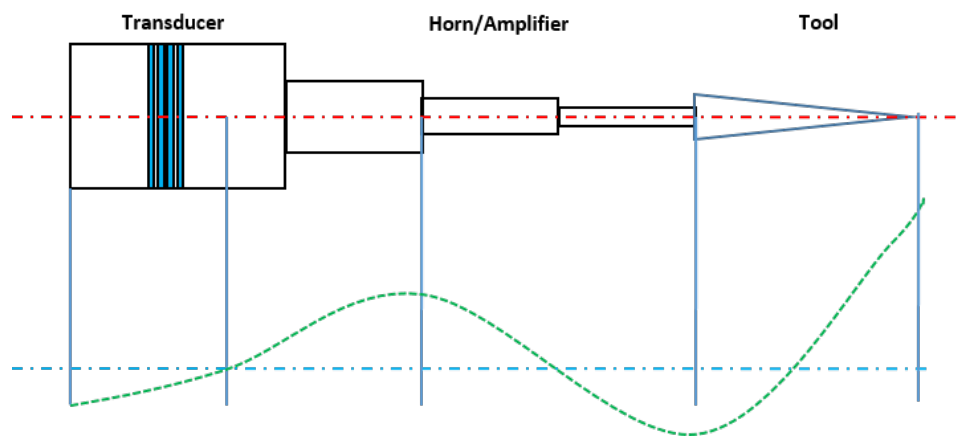


FIGURE 3.8 : Design ultrasonic transducer.

### Transducer Characteristics

The performance of a transducer can be observed according to many criteria for various applications. For ultrasonic transducers, the performance criteria can be itemised as follows (Nakamura, 2012).

- Resonance frequency:

The transducer resonance frequency should match the quantified operating frequency. Usually, this frequency is that of the first longitudinal oscillation mode. Input to Output Power The transducer input power  $p_e(t)$  can be represented as follows:

$$p_e(t) = V(t) \cdot I(t) \quad (3.12)$$

Where  $V(t)$  is an alternative input voltage and  $I(t)$  is the current. The transducer design reveals a capacitive behaviour when it is not operated in a field close to the frequency of resonance. The average effective power is expressed as:

$$\bar{P}_e = \frac{1}{T} \int_0^T V(t) I(t) dt \quad (3.13)$$

In the harmonic case the influential power outcomes can be presented as:

$$\hat{P}_e = \frac{1}{2} \hat{V} \hat{I} \cos \varnothing_e = \hat{P}_a \cos \varnothing_e \quad (3.14)$$

In which  $\hat{P}_e$  is the apparent power,  $\varnothing_e$  is the phase variance between  $V(t)$  and  $I(t)$ .

The electric power device size that is utilised to operate transducers can be evaluated through the apparent power  $\hat{P}_a$ . Minimised apparent power for a specified output condition, such as a specified amplitude or mechanical power can lead to improvement in the electric power device through decreasing its size. The transducer's mechanical output power can be determined as:

$$P_m(t) = F(t) \cdot v(t) \quad (3.15)$$

The influential power for harmonic oscillation can be evaluated through analogy with the electrical one as:

$$\hat{P}_m = \frac{1}{2} \hat{F} \hat{v} \cos \varnothing_m = \hat{P}_a \cos \varnothing_m \quad (3.16)$$

$\phi_m$  is the phase variance between  $F(t)$  and  $v(t)$ .

### Efficiency and power efficiency

Generally, the ratio of output mechanical power to the consumed electrical power is represented the efficiency  $\eta$ , which for the harmonic oscillation of the transducer can be estimated as:

$$\eta = \frac{\widehat{P}_m}{\widehat{P}_a} = \frac{\widehat{F}\widehat{v}\cos\phi_m}{\widehat{V}\widehat{I}\cos\phi_e} \quad (3.17)$$

The ratio of mechanical power transported to the electrical power absorbed through the transducer is described as the power efficiency  $\eta_P$ , which is given as follows:

$$\eta_P = \frac{\widehat{P}_m}{\widehat{P}_e} = \frac{\widehat{F}\widehat{v}\cos\phi_m}{\widehat{V}\widehat{I}} \quad (3.18)$$

Notably, great efficiency  $\eta$  and power efficiency  $\eta_P$  are required for the transducer system.

### Mechanical quality factor

The mechanical quality factor  $Q_m$  is considered as the most significant high power characteristic of piezoelectric performance, which is the transposed mechanical loss parameter,  $\tan\phi$ . Basically, it is a magnification parameter of oscillation of a piezoelectric resonator during resonance. An excellent mechanical quality parameter or "hardness" in PZT (lead zirconate titanate) is accomplished by acceptor doping (a dopant atom, which if compiled with a semiconductor can create a p-type region) the system, thereby producing an internal region, which restricts the motion of a domain wall. This is the central reason a mechanical loss in a piezoelectric substance. A large mechanical  $Q_m$  matches with a large resonant amplitude and high efficiency of the piezoelectric material. The structural damping and material of the

piezoelectric matter is usually calculated by  $Q_m$ .

$$Q_m = 2\pi \frac{\text{Energy stored}}{\text{Energy dissipated per cycle}} = 2\pi \frac{E_s}{\int_V E_{loss} dV} = 2\pi \frac{E_T}{E_{EA}} \quad (3.19)$$

Where,  $E_s$  is the stored energy,  $V$  is the sample volume,  $E_{loss}$  is the losses energy,  $E_T$  is the kinetic energy and  $E_{EA}$  is the dissipated energy (Soh, Yang, and Bhalla, 2012; Jordan and Ounaies, 2001).

### Piezoelectric quality number ( $M$ )

This describes the degree of phase drop or phase rise of the admittance roles and is suitable for categorising piezoelectric actuators in terms of electrical performances. When  $M < 2$ , the resonance frequency (the system has a high oscillation amplitude) and anti-resonance frequency (maximum impedance frequency or minimum admittance) (Figure 3.9) do not occur anymore and the transducer cannot be operated with zero reactive power. In addition, extra apparent power is required which creates a high power electric system and thus, the piezoelectric quality number of the transducer should be greater than two. If  $M < 2$ , it is guaranteed that the frequency of resonance occurs and that the transducer can work with zero reactive power, although the damping of the load could be big (Jordan and Ounaies, 2001; Nakamura, 2012).

### Actuator Operating Approaches

The resonance frequency of every single transducer differs marginally as a result of industrial tolerances. In addition, the resonant frequency also undergoes change when working as a result of changing input power, temperature, and so on. Thus, it is essential to achieve a scheme of resonance tracking that can regulate the operating frequency during operation. This is significant if the design of actuation has a high

mechanical quality factor,  $Q_m$ . There are two commonly utilised resonance tracking techniques, Self-Vibrating Circuit (SVC) and Phase Locked Loop (PLL) tracking control, which are described briefly below.

### **Self-Vibrating Circuit (SVC)**

This principle is about making the entire circuit unbalanced at the preferred oscillation frequency and accordingly, the system advances a limit cycle. To implement this, two settings are required. Firstly, the feedback must be positive, in other words, the whole phase shift in the feedback loop is zero. Additionally, the loop gain is larger than unity, that is, a net magnification within the loop occurs. A self-induced vibration will be persistent when the two conditions or the settings stated above are met at a specified eigenmode (natural frequency). However, when the settings are met at more than one eigenmode, so as to pick the preferred one, a filter located in the feedback route can be deployed during that mission. A simplified layout of the SVC is illustrated in Figure 3.10. There are some disadvantages of the SVC, which make it incompatible for certain approaches, such as squeeze-film levitation. The system efficiency is low. In addition, at high power levels loading circumstances may fluctuate extremely over time, with the system developing a high nonlinearity and as a result, the operation can fail (Nakamura, 2012).

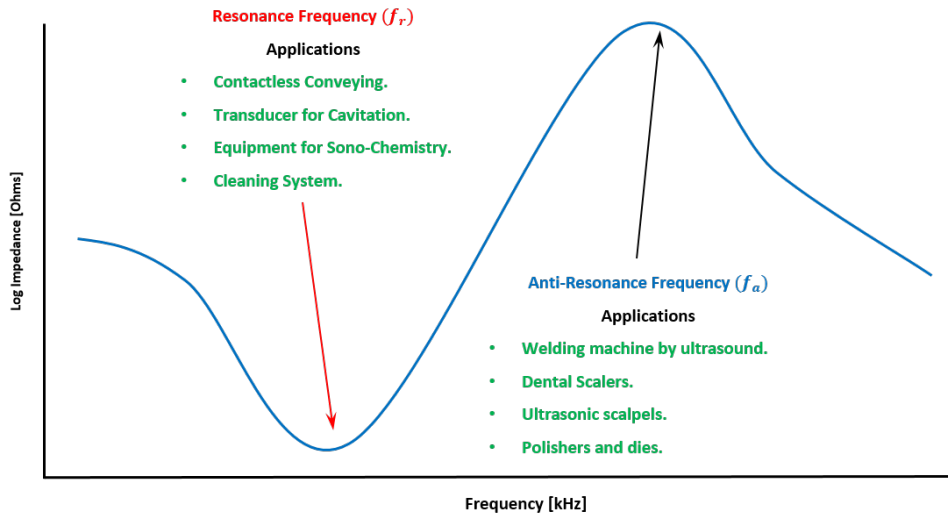


FIGURE 3.9 : Piezoelectric frequency response.

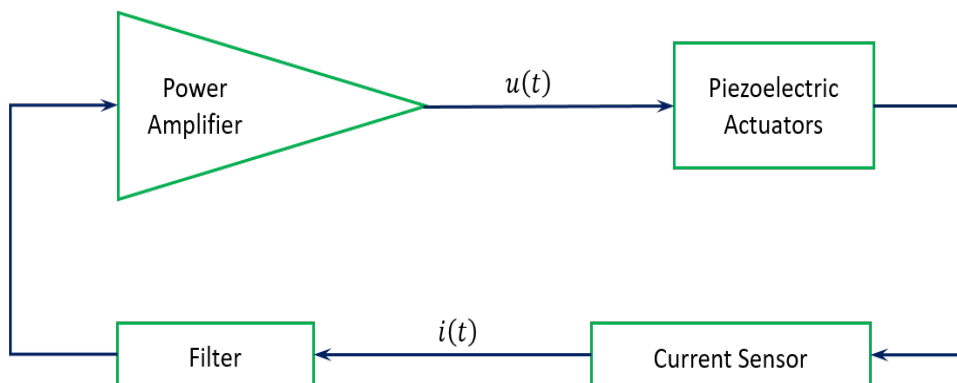


FIGURE 3.10 : Self-vibrating circuit (SVC) layout.

### Phase-Locked-Loop (PLL) Technique

The PLL is a high powerful driving technique for a piezoelectric actuator systems at their resonant frequencies (Figure 3.11). It involves a voltage controlled oscillator (VCO), a filter, a phase inspector, and a current sensor. A power amplifier operates the piezoelectric actuator or what is equivalent to an ultrasonic transducer, whereas the amplifier is activated by the VCO. The output frequency of the VCO is effected by the exerted voltage at the input. The actual operating voltage and current on the transducer is represented by the inputs to the phase inspector. The phase variance between these pair signals must be directed to being zero to preserve the resonance

frequency magnitude. After the filter, the output of the phase inspector is a voltage related to the phase variance between the signals. This voltage is proportional to the error between the resonant frequency and the working frequency, being provided to the VCO, which in turn, leads to the operating frequency being close to the resonance (Smith, 1966).

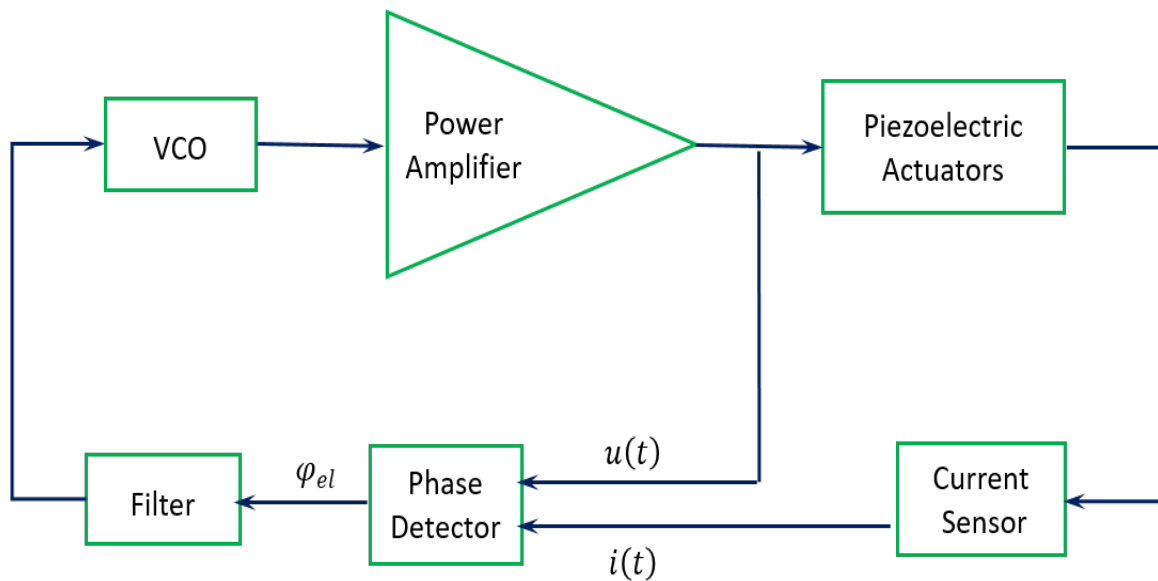


FIGURE 3.11 : Phase-locked-loop.

The preferred working power level is acquired by regulating the power amplifier gain. The PLL controller is much more complex than the self-vibrating circuit (SVC); however, it offers high stability and reliability. Hence, it is highly appropriate for operating piezoelectric transducers in resonance. However, it is challenging for the PLL technique to catch the resonant frequency relying on the phase measurements. That is, a PLL can fail the mission, in particular, when an extremely damped system is utilised, for example, when a transducer is used for the welding of plastics. A damped system denotes a minimum phase magnitude where the admittance between anti-resonance and resonance does not drop to less than the zero-phase line. To solve this challenge, a controller called a load-adaptive phase, such as that developed by can be utilised as an extension to the PLL (Littmann et al., 2003).

### Piezoelectric Mathematical Description

The physical constants for piezoelectric ceramics (elasticity, permittivity, etc.) are tensor magnitudes, because they are considered as anisotropic materials and the magnitudes are governed by the direction of the exerted stress or electric field (Kim, 2006). In reduced tensor representations, the coefficients have two subscripts, which denote the direction of the related amounts and a superscript, which is utilised to point out a quantity that remains constant. The relative expansion or strain of a piezoelectric component is related to the applied field strength. It can be estimated very simply, through the following formula (Al-Budairi, 2012; Vijaya, 2016):

$$\varepsilon = \frac{\Delta l}{l_0} d_{ij} E \quad (3.20)$$

$$E = \frac{U}{w_s} \quad (3.21)$$

where,  $d_{ij}$  is the piezoelectric constant of the material,  $E$  is the electric field strength,  $U$  the applied voltage and finally,  $w_s$  is the thickness of the piezoelectric material in the poling direction. The electric performance of the material is illustrated by:

$$D_e = \varepsilon_\sigma E_e \quad (3.22)$$

where,  $D_e$  is the electric displacement,  $\varepsilon_\sigma$  is permittivity and  $E_e$  is the electric field strength. Similarly, the mechanical properties are defined by Hooke's law:

$$S = S_E \sigma \quad (3.23)$$

Where,  $S$  is strain,  $S_E$  is the compliance matrix and  $\sigma$  is stress. When the two equations are chained together, the coupled piezoelectric equations in the strain charge form can be acquired:

$$S = S_E \sigma + d^T E_e \quad (3.24)$$



$$D_e = d\sigma + \varepsilon_\sigma E_e \quad (3.25)$$

Where,  $d$  characterises the piezoelectric coupling constants, subscript  $E$  indicates zero (or constant) electric field,  $\sigma$  is zero (or constant) stress field and superscript  $T$  represents matrix transposition. Equation (3.24) can be utilised to represent associations for a piezoelectric actuator and likewise equation (3.24) can be deployed to define the action of a piezoelectric sensor. Additionally, these equations can be quantified for poled piezoelectric ceramics, like PZT, in the following form (Rogacheva, 1994):

$$\begin{bmatrix} S_1 \\ S_2 \\ S_3 \\ S_4 \\ S_5 \\ S_6 \end{bmatrix} = \begin{bmatrix} S_{11}^E & S_{12}^E & S_{13}^E & 0 & 0 & 0 \\ S_{12}^E & S_{11}^E & S_{13}^E & 0 & 0 & 0 \\ S_{13}^E & S_{13}^E & S_{33}^E & 0 & 0 & 0 \\ 0 & 0 & 0 & S_{44}^e & 0 & 0 \\ 0 & 0 & 0 & 0 & S_{44}^e & 0 \\ 0 & 0 & 0 & 0 & 0 & S_{66}^e \end{bmatrix} + \begin{bmatrix} \sigma_1 \\ \sigma_2 \\ \sigma_3 \\ \sigma_4 \\ \sigma_5 \\ \sigma_6 \end{bmatrix} + \begin{bmatrix} 0 & 0 & d_{31} \\ 0 & 0 & d_{31} \\ 0 & 0 & d_{31} \\ 0 & d_{15} & 0 \\ d_{15} & 0 & 0 \\ 0 & 0 & 0 \end{bmatrix} \quad (3.26)$$

$$\begin{bmatrix} D_1 \\ D_2 \\ D_3 \end{bmatrix} = \begin{bmatrix} 0 & 0 & 0 & 0 & d_{15} & 0 \\ 0 & 0 & 0 & d_{15} & 0 & 0 \\ d_{31} & d_{31} & d_{33} & 0 & 0 & 0 \end{bmatrix} \begin{bmatrix} \sigma_1 \\ \sigma_2 \\ \sigma_3 \\ \sigma_4 \\ \sigma_5 \\ \sigma_6 \end{bmatrix} + \begin{bmatrix} \varepsilon_{11} & 0 & 0 \\ 0 & \varepsilon_{11} & 0 \\ 0 & 0 & \varepsilon_{33} \\ 0 & 0 & 0 \end{bmatrix} \begin{bmatrix} E_1 \\ E_2 \\ E_3 \end{bmatrix} \quad (3.27)$$

The component  $d_{ij}$  of the matrix  $d$  represents the coupling between the electric field in the  $i$  direction and the strain in the  $j$  direction. In practice, due to crystal symmetries, the coupling matrix  $d$  has only a few non-zero elements.

### Piezoelectric Finite Element Method Formulation

An engineering problem involving piezoelectric objects can be solved by the finite element (FE). The method is akin to the modeling of lumped parameter mechanical systems with both the mechanical and the electrical terms in the equation of motion. Equivalences between the structural damping and dielectric loss, additionally in between the stiffness / permittivity / coupling are made use of when formulating the fundamental set of equations stated in the following matrix arrangement:

$$\begin{bmatrix} M & 0 \\ 0 & 0 \end{bmatrix} \begin{bmatrix} \ddot{q} \\ \ddot{p} \end{bmatrix} + \begin{bmatrix} B_d & 0 \\ 0 & B_p \end{bmatrix} \begin{bmatrix} \dot{q} \\ \dot{p} \end{bmatrix} + \begin{bmatrix} K_s & K_z \\ K_z^T & K_p \end{bmatrix} = \begin{bmatrix} f_e \\ L_e \end{bmatrix} \quad (3.28)$$

where,  $B_d$  is responsible for structural damping,  $B_p$  for dielectric loss and  $M$  is a mass matrix. Terms  $q$  and  $p$  and their first and second order derivatives represent the structural and electrical degrees of freedom,  $K_p$  is anisotropic permittivity,  $K_s$  is the anisotropic stiffness and finally,  $K_z$  is the piezoelectric effect. The above equation construction, associated with lumped parameter exciting systems, can be utilised for piezoelectric scenarios using the stress–charge formula of the piezoelectric equations, which are given by:

$$\sigma = c_E S - e_p E_e \quad (3.29)$$

$$D_e = e_p^T S - \epsilon_S E_e \quad (3.30)$$

where,  $e_p$  is the piezoelectric coupling coefficient in the stress–charge system,  $c_E$  covers stiffness quantities under constant electric field and  $\epsilon_S$  is the electric permittivity matrix under constant stain. As can be seen, equations (3.29) and (3.30) differ considerably from equations (3.24) and (3.25), which are given in the strain–charge form. The linear piezoelectric equations can be illustrated in another form, where the fundamental equations in stress–charge, strain–charge, strain–voltage and stress–voltage can be defined (Rogacheva, 1994). The finite element method (FEM) representation of the piezoelectric influence is grounded on the stress–charge

arrangement utilisation of the  $e_p$  coupling term, whilst the piezoelectric matrix  $d$  can also be directly used and is represented in most FEM packages. For instance, in the ANSYS package,  $d$  is represented in the strain–charge matrix shape. This is, then, internally altered into the piezoelectric stress–charge matrix, using the strain matrix at a constant temperature. Changing between the strain-charge to stress-charge is determined according to (Takács and Rohal'-Ilkiv, 2012; Rogacheva, 1994).

$$\varepsilon_S = \varepsilon_\sigma - d_{SE}^{-1} d^T \quad (3.31)$$

$$e_p = d_{SE}^{-1} \quad (3.32)$$

$$C_E = S_E^{-1} \quad (3.33)$$

where, subscripts  $\sigma, S, E$  represent the values estimated under constant stress, strain and electric field. The elements of the anisotropic elasticity matrix may also be illustrated by the following expressions (Vijaya, 2016; Al-Budairi, 2012):

$$\begin{bmatrix} \frac{1}{E_s} & -\frac{\nu_{xz}}{E_x} & 0 & 0 & 0 & 0 \\ 0 & \frac{1}{E_y} & 0 & 0 & 0 & 0 \\ 0 & 0 & \frac{1}{E_z} & 0 & 0 & 0 \\ 0 & 0 & 0 & 0 & \frac{1}{G_{xz}} & 0 \\ 0 & 0 & 0 & 0 & \frac{1}{G_{yz}} & 0 \\ 0 & 0 & 0 & 0 & 0 & \frac{1}{G_{xz}} \end{bmatrix} \quad (3.34)$$

$$G_{xy} = \frac{1}{2[S_{11}^E] - [S_{11}^E]} \quad (3.35)$$

Where,  $\nu$  is Poisson's ratio in a given direction.

### 3.7 Conclusion

This chapter has provided an overview of piezoelectric actuators, their work and function, with their advantages and disadvantages described. In addition, the piezoelectric coefficients, mathematical description, finite element formulation, and various piezoelectric material properties have been presented. A piezoelectric object can produce a strain or mode deformation in various ways, including elongation, shrinkage and shear mode. Consequently, it will be important to consider polarisation orientation, electric field applied and electrode location in designing the arrangement of actuators on the plate design. If an alternating electric field is applied parallel to the piezoelectric polarisation, expansion and contraction can be created in a controlled manner.

## Chapter 4

# Mathematical Modelling of Thin Plate.

### 4.1 Introduction

In this chapter, the plate structure deformation through piezoelectric component bonding for actuation is presented. It is essential to inspect this issue because of the utilising of piezoelectric substances in oscillation control at micrometre and nanometre scales.

### 4.2 Plate under Concentrated Load

#### 4.2.1 Rectangular Plate Simply Supported

Assume a load distributed over a surface of the plate is given by the expression (Timoshenko and Woinowsky-Krieger, 1959);

$$q = q_{\theta} \sin \frac{\pi x}{a} \sin \frac{\pi y}{b} \quad (4.1)$$

$q_{\theta}$  represents the intensity of the load at the centre of the plate. The differential equation for the deflection surface becomes

$$\frac{\partial^4 w}{\partial x^4} + 2 \frac{\partial^4 w}{\partial x^2 \partial y^2} + \frac{\partial^4 w}{\partial y^4} = \frac{q_0}{D} \sin \frac{\pi x}{a} \sin \frac{\pi y}{b} \quad (4.2)$$

The boundary conditions for simple supported edges are

$$\begin{aligned} (1) \quad w = 0 \quad (2) \quad \frac{\partial^2 w}{\partial x^2} = 0 \quad \text{for } x = 0 \text{ and } x = a \\ (3) \quad w = 0 \quad (4) \quad \frac{\partial^2 w}{\partial y^2} = 0 \quad \text{for } y = 0 \text{ and } y = b \end{aligned} \quad (4.3)$$

All boundary conditions are satisfied with the expressions

$$w = C \sin \frac{\pi x}{a} \sin \frac{\pi y}{b} \quad (4.4)$$

Substituting equation (4.4) into equation (4.2) can lead to

$$\pi^4 \left( \frac{1}{a^2} + \frac{1}{b^2} \right)^2 C = \frac{q_0}{D} \quad (4.5)$$

With the boundary conditions of equation 4.3

$$w = \frac{q_0}{\pi^4 D \left( \frac{1}{a^2} + \frac{1}{b^2} \right)^2} \sin \frac{\pi x}{a} \sin \frac{\pi y}{b} \quad (4.6)$$

At the centre of the plate where  $x = a/2, y = b/2$

$$w_{max} = \frac{q_0}{\pi^4 D \left( \frac{1}{a^2} + \frac{1}{b^2} \right)^2} \quad (4.7)$$

For a square plate where  $a = b$  the deflection of the plate becomes as follows:

$$w_{max} = \frac{q_0 a^4}{4\pi^4 D} \quad (4.8)$$

If the sinusoidal load distribution is given by the equation

$$q = q_0 \sin \frac{m\pi x}{a} \sin \frac{n\pi y}{b} \quad (4.9)$$

Where  $m$  and  $n$  are integer numbers can be proceed as before, the deflection surface can be expressed as follows (Timoshenko and Woinowsky-Krieger, 1959),

$$w = \frac{q_0}{\pi^4 D \left( \frac{m^2}{a^2} + \frac{n^2}{b^2} \right)^2} \sin \frac{m\pi x}{a} \sin \frac{n\pi y}{b} \quad (4.10)$$

### Navier Solution Approach for Simply Supported Rectangular Plates

Navier approach can be used to determine the plate deflection at any kind of load given by the equation (Venstel and Krauthammer, 2001),

$$q = f(x, y) \quad (4.11)$$

For this purpose one can represent equation (4.11) in the form of double trigonometric series:

$$f(x, y) = \sum_{m=1}^{\infty} \sum_{n=1}^{\infty} a_{mn} \sin \frac{m\pi x}{a} \sin \frac{n\pi y}{b} \quad (4.12)$$

The deflection surface can be expressed as follows:

$$w = \frac{1}{\pi^4 D} \sum_{m=1}^{\infty} \sum_{n=1}^{\infty} \frac{a_{mn}}{\left( \frac{m^2}{a^2} + \frac{n^2}{b^2} \right)^2} \sin \frac{m\pi x}{a} \sin \frac{n\pi y}{b} \quad (4.13)$$

In a case of a single load  $P$  uniformly distributed over the area of the rectangular shown in Figure 4.1.

$$\begin{aligned} a_{mn} &= \frac{4P}{abuv} \int_{\xi-u/2}^{\xi+u/2} \int_{\eta-v/2}^{\eta+v/2} \sin \frac{m\pi y}{a} \sin \frac{n\pi y}{b} dx dy \\ a_{mn} &= \frac{16P}{\pi^2 mn uv} \sin \frac{m\pi \xi}{a} \sin \frac{n\pi \eta}{b} \sin \frac{m\pi u}{2a} \sin \frac{n\pi v}{2b} \end{aligned} \quad (4.14)$$

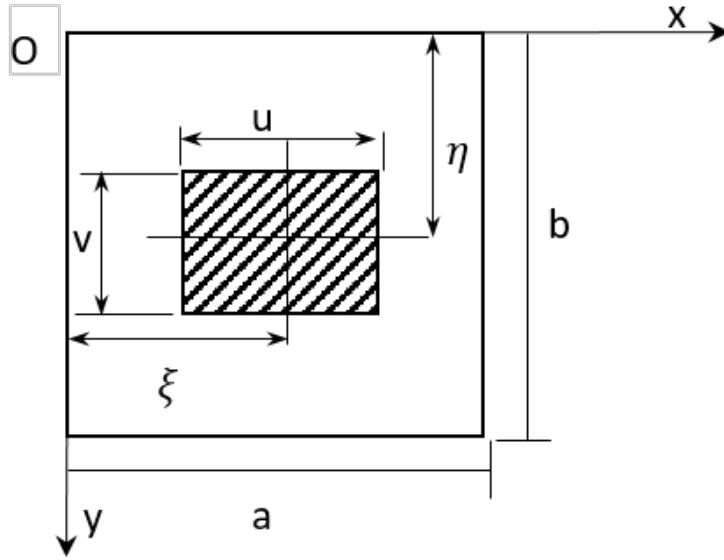


FIGURE 4.1 : Plate under concentrated load distributed as a rectangular.

By substituting  $\zeta = \frac{a}{2}$ ,  $\eta = \frac{b}{2}$ ,  $u = a$  and  $v = b$ .

The case of practical interest is a single load concentrated at any given point  $x = \zeta$ ,  $y = \eta$  of the plate. Using equation (4.14) and letting  $u$  and  $v$  tend to zero that gives the expression of,

$$a_{mn} = \frac{4P}{ab} \sin \frac{m\pi\zeta}{a} \sin \frac{n\pi\eta}{b} \quad (4.15)$$

And by equation (4.13) at the deflection

$$w = \frac{4P}{\pi^4 abD} \sum_{m=1}^{\infty} \sum_{n=1}^{\infty} \frac{\sin \frac{m\pi\zeta}{a} \sin \frac{n\pi\eta}{b}}{\left( \frac{m^2}{a^2} + \frac{n^2}{b^2} \right)^2} \sin \frac{m\pi x}{a} \sin \frac{n\pi y}{b} \quad (4.16)$$

This series converges quickly, and one can attain the deformation at any point of the plate with adequate accuracy by considering only the first few terms of the expression. The expression of plate deflection at the centre when the load applied at middle. Thus,  $\zeta = x = \frac{a}{2}$ ,  $\eta = \frac{b}{2}$  and equation (4.16) yields (Timoshenko and Woinowsky-Krieger, 1959; Venstel and Krauthammer, 2001),

$$w_{max} = \frac{4P}{\pi^4 abD} \sum_{m=1}^{\infty} \sum_{n=1}^{\infty} \frac{1}{\left( \frac{m^2}{a^2} + \frac{n^2}{b^2} \right)^2} \quad (4.17)$$



where  $m = 1, 3, 5, \dots$  and  $n = 1, 3, 5, \dots$ . When the plate considered as a square shape, expression (4.17) can be rewritten as,

$$w_{max} = \frac{4Pa^4}{\pi^4 D} \sum_{m=1}^{\infty} \sum_{n=1}^{\infty} \frac{1}{(m^2 + n^2)^2} \quad (4.18)$$

Considering the first four terms of the equation (4.18) yields,

$$w_{max} = \frac{0.01121 Pa^2}{D} \quad (4.19)$$

### Concentrated Load on a Plate

The deflection of a plate has boundary conditions of a simple supported and a geometry of rectangular can be gained through using Navier's method (Timoshenko and Woinowsky-Krieger, 1959). The single load  $P$  is located at points of  $x = \zeta, y = \eta$ . To get on the solution, equation (4.16) needs to be represented as follows.

$$w = \frac{4Pb^3}{\pi^4 a D} \sum_{m=1}^{\infty} S_m \sin \frac{m\pi\zeta}{a} \sin \frac{m\pi x}{a} \quad (4.20)$$

$$S_m = \sum_{n=1}^{\infty} \frac{\sin \frac{n\pi y}{b} \sin \frac{n\pi \eta}{b}}{\left(\frac{m^2 b^2}{a^2} + n^2\right)^2} \quad (4.21)$$

Introducing the notation

$$S'_m = \sum_{n=1}^{\infty} \frac{\cos \frac{n\pi(y-\eta)}{b}}{\left(\frac{m^2 b^2}{a^2} + n^2\right)^2} \quad (4.22)$$

$$S''_m = \sum_{n=1}^{\infty} \frac{\cos \frac{n\pi(y+\eta)}{b}}{\left(\frac{m^2 b^2}{a^2} + n^2\right)^2}$$

Equation (4.21) can also be represented by

$$S_m = \frac{1}{2} (S'_m - S''_m) \quad (4.23)$$

To evaluate the sums of equation (4.22), one can use the following series;

$$\sum_{n=1}^{\infty} \frac{\cos nz}{\alpha^2 + n^2} = -\frac{1}{2\alpha^2} + \frac{\pi}{2\alpha} \frac{\cosh \alpha (\pi - z)}{\sinh \pi \alpha} \quad (4.24)$$

Which can be implemented for  $0 \leq z < 2\pi$  By Differentiating the left and right-hand sides of equation (4.24) with respect to  $\alpha$  produces,

$$\frac{\partial S(\alpha)}{\partial \alpha} = -2\alpha \sum_{n=1}^{\infty} \frac{\cos nz}{(\alpha^2 + n^2)^2} \quad (4.25)$$

By substituting the result of equation (4.25), one can conclude that

$$\begin{aligned} \sum_{n=1}^{\infty} \frac{\cos nz}{(\alpha^2 + n^2)^2} &= -\frac{1}{2\alpha} \frac{\partial S(\alpha)}{\partial \alpha} \\ &= -\frac{1}{2\alpha^4} + \frac{\pi}{4\alpha^3} \frac{\cosh \alpha (\pi - z)}{\sinh \pi \alpha} \\ &\quad - \frac{\pi (\pi - z) \sinh \alpha (\pi - z)}{4\alpha^2 \sinh \pi \alpha} \\ &\quad + \frac{\pi^2 \cosh \alpha (\pi - z) \cosh \pi \alpha}{4\alpha^2 \sinh^2 \pi \alpha} \end{aligned} \quad (4.26)$$

To acquire the results of sums of equation (4.22), one needs to put in equation (4.26). First  $z = (\pi/b)(y - \eta)$ , then  $z = (\pi/b)(y + \eta)$  and  $\alpha = (m b/a)$ . By means of these terms for substituting in equations (4.23) and (4.20), the following expression for the deflection of the plate can be expressed as follow.

$$w = \frac{Pa^2}{\pi^3 D} \sum_{m=1}^{\infty} \left( 1 + \beta_m \coth \beta_m - \frac{\beta_m y_1}{b} \coth \frac{\beta_m y_1}{b} - \frac{\beta_m \eta}{b} \coth \frac{\beta_m \eta}{b} \right) \frac{\sinh \frac{\beta_m \eta}{b} \sinh \frac{\beta_m y_1}{b} \sin \frac{m\pi \zeta}{a} \sin \frac{m\pi x}{a}}{m^3 \sinh \beta_m} \quad (4.27)$$

Where  $\beta_m = \frac{m\pi b}{a}$ ,  $y_1 = b - y$  and  $y \geq \eta$

when  $y < \eta$  the value of  $y_1$  must be changed by  $y$  and then the value  $\eta$  by  $\eta_1 = b - \eta$ , in equation (4.27). If a load  $P$  concerted at a point  $A$  on the plate axis symmetry, which may be utilised as the  $x$  axis (Figure 4.2). By substituting  $\eta = \frac{b}{2}$  and the notation  $\alpha_m = \frac{m\pi b}{2a} = \frac{\beta_m}{2}$  in equation (4.27), the deflection of the plate

rewritten as

$$w = \frac{Pa^2}{2\pi^3 D} \sum_{m=1}^{\infty} \left[ (1 + \alpha_m \tanh \alpha_m) \sinh \frac{\alpha_m}{b} (b - 2y) - \frac{\alpha_m}{b} (b - 2y) \cosh \frac{\alpha_m}{b} (b - 2y) \right] \times \frac{\sin \frac{m\pi\xi}{a} \sin \frac{m\pi x}{a}}{m^3 \cosh \alpha_m} \quad (4.28)$$

Which is valid for  $y \geq 0$ , that is, below the  $x$  axis (Figure 4.2). Putting,  $y = 0$ , one can acquire the plate deflection along the  $x$  axis in the expression of,

$$w_{y=0} = \frac{Pa^2}{2\pi^3 D} \sum_{m=1}^{\infty} \left( \tanh \alpha_m - \frac{\alpha_m}{\cosh^2 \alpha_m} \right) \frac{\sin \frac{m\pi\xi}{a} \sin \frac{m\pi x}{a}}{m^3} \quad (4.29)$$

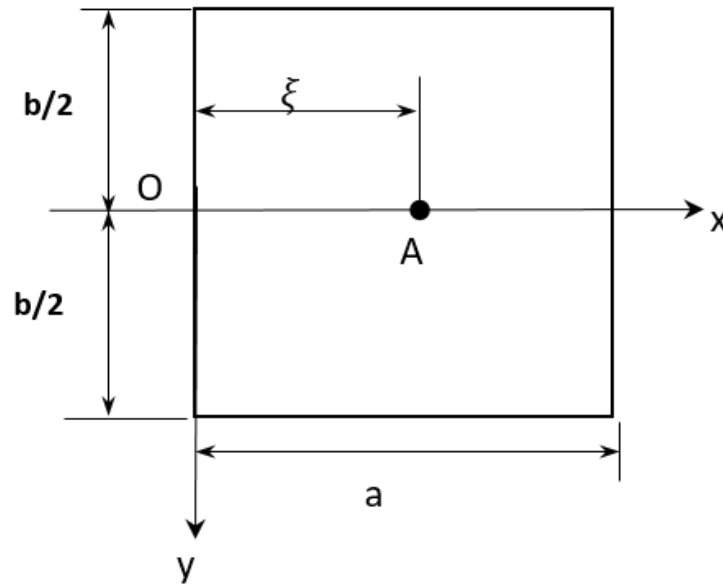


FIGURE 4.2 : Plate under concentrated load and axis of deformation

IF a load  $P$  exerted at the centre of the plate, the maximum deflection is gained through substituting  $x = \xi = a/2$  in equation (4.29) as (Timoshenko and Woinowsky-Krieger, 1959),

$$w_{Max} = \frac{Pa^2}{2\pi^3 D} \sum_{m=1}^{\infty} \frac{1}{m^3} \left( \tanh \alpha_m - \frac{\alpha_m}{\cosh^2 \alpha_m} \right) = \alpha \frac{Pa^2}{D} \quad (4.30)$$

TABLE 4.1 : Factor  $\alpha$  values for different ratio of  $b/a$ .

$b/a$	1	1.1	1.2	1.4	1.6	1.8	2	3	$\infty$
$\alpha$	0.0116	0.01265	0.01353	0.01484	0.0157	0.0162	0.01651	0.0169	0.01695

## 4.2.2 Dynamic Plate Theory

The small transverse displacement  $w$  of a thin plate is governed by the Classical Plate Equation. The differential equation of thin plate bending has the form of (Venstel and Krauthammer, 2001; Leissa, 1969).

$$\Delta^4 w = \frac{F(x, y)}{D} \quad (4.31)$$

$$\Delta^4 w = \frac{\partial^4 w}{\partial x^4} + 2 \frac{\partial^4 w}{\partial x^2 \partial y^2} + \frac{\partial^4 w}{\partial y^4}$$

$$D = \frac{E t^3}{[12 (1 - \nu^2)]}$$

In which  $E$  is the Young's modulus,  $\nu$  is the Poisson's ratio of the plate material and  $t$  is the thickness of the plate.  $F(x, y)$  is the applied load acting on the plate, and  $D$  is plate stiffness coefficient, bending or flexural rigidity of plate which it is a measure of the resistance of the bending deformation of a plate. Furthermore, the differential operator  $\Delta$  is called the laplacian differential operator. As can be seen from the plate equation that is the plate bending coefficient  $D$  highly effects on the displacement of the plate. Moreover, Plate bending coefficient or flexural rigidity coefficient of a plate  $D$  is a function of frequency parameters are expressed in terms of  $\omega a^2 \sqrt{\frac{\rho}{D}}$  Where  $a$  is a length dimension, and do not depend upon Poisson's ratio unless at least one of the edges of the plate is free. However, because  $D$  contains  $\nu$ , the frequencies themselves depend upon  $\nu$  for all cases of boundary conditions of the plate (Leissa, 1969). Assume that the load acting on a plate is normal to its surface and that the deflections are small in comparison with the thickness of the plate, thin plate deformation equation at different boundary condition can be represented as follow;

For the case where two sides of the plate are simply supported and the other two are free, the deformation equation can be obtained as follows (Timoshenko and Woinowsky-Krieger, 1959).

$$w = \frac{q a^4}{D} \sum_{m=1,3,5}^{\infty} \left( \frac{4}{\pi^5 m^5} + A_m \cosh \frac{m\pi y}{a} + B_m \frac{m\pi y}{a} \sinh \frac{m\pi y}{a} \right) \sin \frac{m\pi x}{a}$$

$$A_m = \frac{4}{\pi^5 m^5} \frac{v(1+v) \sinh \alpha_m - v(1-v) \alpha_m \cosh \alpha_m}{(3+v)(1-v) \sinh \alpha_m \cosh \alpha_m - \alpha_m(1-v)^2}$$

$$B_m = \frac{4}{\pi^5 m^5} \frac{v(1-v) \sinh \alpha_m}{(3+v)(1-v) \sinh \alpha_m \cosh \alpha_m - \alpha_m(1-v)^2}$$

$$y = \pm b/2, \quad \alpha_m = \frac{m\pi b}{2a}$$
(4.32)

where  $q$  is the intensity of the load

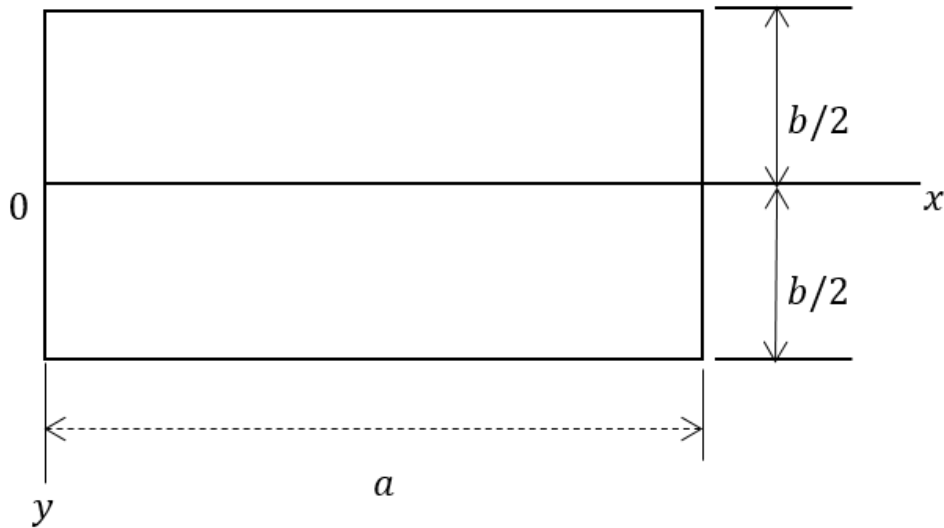


FIGURE 4.3 : Plate coordinates and dimensions.

For the case where the plate with two opposite edges simply supported and the other two edges clamped. The deflection at the centre can be represented by the formula (Timoshenko and Woinowsky-Krieger, 1959).

$$w = \alpha \frac{q a^4}{D}$$
(4.33)

TABLE 4.2 : The numerical values of  $\alpha$  at various plate dimensions (Timoshenko and Woinowsky-Krieger, 1959).

$a/b$	$\alpha$	$b/a$	$\alpha$
$\infty$	0.00260	1	0.00192
2	0.00260	1.1	0.00251
1.5	0.00247	1.2	0.00319
1.4	0.00240	1.3	0.00388
1.3	0.00234	1.4	0.00460
1.2	0.00223	1.5	0.00531
1.1	0.00209	1.6	0.00603

There are 21 combinations of simple boundary conditions (i.e., either clamped ( $C$ ), simply supported ( $SS$ ), or free ( $F$ )) for rectangular plates. Frequency parameters are expressed in terms of  $w = \alpha \frac{q a^4}{D}$  where  $a$  is a length dimension, and do not depend upon Poisson's ratio unless at least one of the edges of the plate is free. However, because  $D$  contains  $\nu$ , the frequencies themselves depend upon  $\nu$  for all cases. The first comprehensive collection of solutions for rectangular plates, presented by the Rayleigh method with deformation functions as the product of beam functions; that is (Timoshenko and Woinowsky-Krieger, 1959),

$$w(x, y) = X(x) Y(y) \quad (4.34)$$

where  $X(x)$  and  $Y(y)$  are chosen as the fundamental mode shapes of beams having the boundary conditions of the plate. This choice of function then exactly satisfies all boundary conditions for the plate, except in the case of the free edge, where the shear condition is approximately satisfied. The six possible distinct sets of boundary conditions along the edges  $x = 0$  and  $x = a$  are satisfied by the following mode shapes: Simply Supported at  $x = 0$  and  $x = a$ :

$$X(x) = \sin \frac{(m-1)\pi x}{a} \quad (m = 2, 3, 4, \dots) \quad (4.35)$$

Clamped at  $x = 0$  and  $x = a$ :

$$X(x) = \cos \gamma_1 \left( \frac{x}{a} - \frac{1}{2} \right) + \frac{\sin(\gamma_1/2)}{\sinh(\gamma_1/2)} \cos \gamma_1 \left( \frac{x}{a} - \frac{1}{2} \right) \quad (m = 2, 4, 6, \dots) \quad (4.36)$$

Where the value of  $\gamma_1$  are obtained as a roots of  $\tan(\gamma_1/2) + \tanh(\gamma_1/2)$  and

$$X(x) = \sin \gamma_2 \left( \frac{x}{a} - \frac{1}{2} \right) - \frac{\sin(\gamma_2/2)}{\sinh(\gamma_2/2)} \sinh \gamma_2 \left( \frac{x}{a} - \frac{1}{2} \right) \quad (m = 3, 5, 7, \dots) \quad (4.37)$$

Where the value of  $\gamma_2$  are obtained as a roots of  $\tan(\gamma_2/2) - \tanh(\gamma_2/2)$  Free at  $x = 0$  and  $x = a$ :  $X(x) = 1 \quad (m = 0), \quad X(x) = 1 - \frac{2x}{a} \quad (m = 1)$

$$X(x) = \cos \gamma_1 \left( \frac{x}{a} - \frac{1}{2} \right) - \frac{\sin(\gamma_1/2)}{\sinh(\gamma_1/2)} \cos \gamma_1 \left( \frac{x}{a} - \frac{1}{2} \right) \quad (m = 2, 4, 6, \dots) \quad (4.38)$$

and

$$X(x) = \sin \gamma_2 \left( \frac{x}{a} - \frac{1}{2} \right) + \frac{\sin(\gamma_2/2)}{\sinh(\gamma_2/2)} \sinh \gamma_2 \left( \frac{x}{a} - \frac{1}{2} \right) \quad (m = 3, 5, 7, \dots) \quad (4.39)$$

Clamped at  $x = 0$  and Free at  $x = a$

$$X(x) = \cos \frac{\gamma_3 x}{a} - \cosh \frac{\gamma_3 x}{a} + \left( \frac{\sin \gamma_3 - \sinh \gamma_3}{\cos \gamma_3 - \cosh \gamma_3} \right) \left( \sin \frac{\gamma_3 x}{a} - \sinh \frac{\gamma_3 x}{a} \right) \quad (4.40)$$

where  $\cos \gamma_3 \cosh \gamma_3 = -1 \quad (m = 1, 2, 3, \dots)$

Clamped at  $x = 0$  and Simply support at  $x = a$

$$X(x) = \sin \gamma_2 \left( \frac{x}{2a} - \frac{1}{2} \right) - \frac{\sin(\gamma_2/2)}{\sinh(\gamma_2/2)} \sinh \gamma_2 \left( \frac{x}{2a} - \frac{1}{2} \right) \quad (4.41)$$

$(m = 2, 3, 4, \dots)$

Free at  $x = 0$  and Simply support at  $x = a$

$$X(x) = 1 - \frac{x}{a} \quad (m = 1) \quad X(x) = \sin \gamma_2 \left( \frac{x}{2a} - \frac{1}{2} \right) + \frac{\sin(\gamma_2/2)}{\sinh(\gamma_2/2)} \sinh \gamma_2 \left( \frac{x}{2a} - \frac{1}{2} \right) \quad (4.42)$$

( $m = 2, 3, 4, \dots$ )

The functions  $Y(y)$  are similarly chosen by the conditions at  $y = 0, y = a$  by replacing  $x$  by  $y$ ,  $a$  by  $b$  and  $m$  by  $n$  in equations (4.32) - (4.42). The indicators  $m$  and  $n$  are seen to be the number of nodal lines lying in the  $x$  and  $y$  directions, respectively, including the boundaries as a nodal lines, except when the boundary is free. The frequency  $\omega$  is given by

$$\omega^2 = \frac{\pi^4}{a^4} \frac{D}{\rho} \left\{ G_x^4 + G_y^4 \left(\frac{a}{b}\right)^4 + 2 \left(\frac{a}{b}\right)^2 [\nu H_x H_y + (1 - \nu) J_x J_y] \right\} \quad (4.43)$$

where,  $G_x, H_x$  and  $J_x$  are function determined from table according to the conditions at  $x = 0$  and  $x = a$

The quantities  $G_y, H_y$  and  $J_y$  are obtained from Table by replacing  $x$  by  $y$  and  $m$  by  $n$ .

Fundamental frequencies were obtained for 18 combinations of boundary conditions using Raylieght method, but used simple trigonometric functions which satisfied only the geometric boundary conditions and the mode shapes are given in Table The frequency  $\omega$  is given for  $\nu = 0.25$  by

$$\omega^2 = \frac{\pi^4}{a^4} \frac{D}{\rho} \frac{K}{N} \quad (4.44)$$



TABLE 4.3 : Boundary conditions (B.C) and parameters of Plate in dynamic approaches (Leissa, 1969; Venstel and Krauthammer, 2001).

B.C	$m$	$G_x$	$H_x$	$J_x$
$SS^a$	2, 3, 4, ...	$m - 1$	$(m - 1)^2$	$(m - 1)^2$
$SS^b$	2, 3, 4, ...	$m - 1$	$(m - 1)^2$	$(m - 1)^2$
$C^a$	2	1.506	1.248	1.248
$C^b$	3, 4, 5, ...	$m - \frac{1}{2}$	$\left(m - \frac{1}{2}\right)^2 \left[1 - \frac{2}{(m - \frac{1}{2})\pi}\right]$	$\left(m - \frac{1}{2}\right)^2 \left[1 - \frac{2}{(m - \frac{1}{2})\pi}\right]$
	0	0	0	0
$F^a$	1	0	0	$12/\pi$
	2	1.506	1.248	5.017
$F^b$	3, 4, 5, ...	$m - \frac{1}{2}$	$\left(m - \frac{1}{2}\right)^2 \left[1 - \frac{2}{(m - \frac{1}{2})\pi}\right]$	$\left(m - \frac{1}{2}\right)^2 \left[1 + \frac{6}{(m - \frac{1}{2})\pi}\right]$
$C^a$	2, 3, 4, ...	$m - \frac{3}{4}$	$\left(m - \frac{3}{4}\right)^2 \left[1 - \frac{1}{(m - \frac{3}{4})\pi}\right]$	$\left(m - \frac{3}{4}\right)^2 \left[1 - \frac{1}{(m - \frac{3}{4})\pi}\right]$
$SS^b$	2, 3, 4, ...	$m - \frac{3}{4}$	$\left(m - \frac{3}{4}\right)^2 \left[1 - \frac{1}{(m - \frac{3}{4})\pi}\right]$	$\left(m - \frac{3}{4}\right)^2 \left[1 + \frac{3}{(m - \frac{3}{4})\pi}\right]$
$F^a$	1	0	0	$3/\pi^2$
$SS^b$	2, 3, 4, ...	$m - \frac{3}{4}$	$\left(m - \frac{3}{4}\right)^2 \left[1 - \frac{1}{(m - \frac{3}{4})\pi}\right]$	$\left(m - \frac{3}{4}\right)^2 \left[1 + \frac{3}{(m - \frac{3}{4})\pi}\right]$
$C^a$	1	0.597	-0.0870	0.471
	2	1.494	1.347	3.284
$F^b$	3, 4, 5, ...	$m - \frac{1}{2}$	$\left(m - \frac{1}{2}\right)^2 \left[1 - \frac{2}{(m - \frac{1}{2})\pi}\right]$	$\left(m - \frac{1}{2}\right)^2 \left[1 + \frac{2}{(m - \frac{1}{2})\pi}\right]$

where,  $a$  refers to  $x = 0$  and  $b$  refers to  $x = a$

It is establish that for all thinkable boundary conditions involving of any mixture of Freely-supported, free, and fixed edges, frequencies can be calculated from the formula

$$\lambda^2 = G_x^4 + G_y^4 \frac{a^4}{b^4} + \frac{2 a^2}{b^2} [v H_x H_y + (1 - v) J_x J_y] \quad (4.45)$$

Where the factors  $G_x, G_y, H_x, H_y, J_x$  and  $J_y$  hinge on on the nodal shape and the boundary conditions. Magnitudes of these factors are presented in Table 4.4 for the three pure boundary conditions (Figure 4.4), whereas all the plate edges have the same situation, and for the twelve circumstances whereas few numbers of the plate edges have one circumstance and the rest another. Assume the frequency of a rectangular plate with three edges fixed and one freely-supported (parallel to the Y-axis) is needed for the mode  $m = 2, n = 3$ . Thus from Table 4.3 and equation (4.45) yields:

$$\lambda^2 = 1.25^4 + 2.5^4 \frac{a^4}{b^4} + \frac{2 a^2}{b^2} \left[ v 1.25^2 \left( 1 - \frac{1}{1.25 \pi} \right) 2.5^2 \left( 1 - \frac{1}{2.5 \pi} \right) + (1 - v) 1.25^2 \left( 1 - \frac{1}{1.25 \pi} \right) 2.5^2 \left( 1 - \frac{1}{2.5 \pi} \right) \right]$$

Thus the frequency parameter  $\lambda$  is found for any proportion  $a/b$ ; the frequency is determined as follows.

$$f = \frac{\lambda h \pi}{a^2} \left[ \frac{Eg}{48\rho (1 - v^2)} \right]^{1/2} \quad (4.46)$$

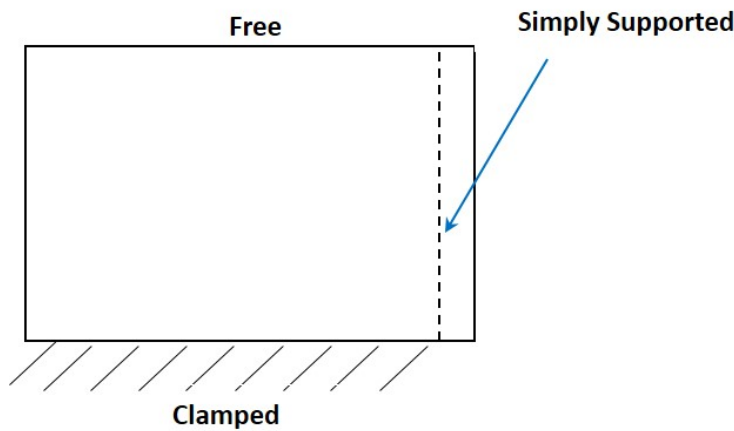
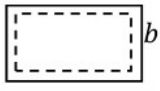

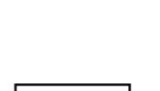

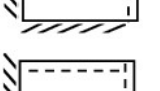

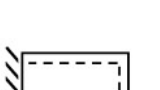
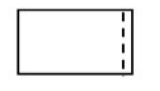






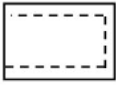



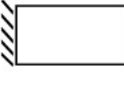


FIGURE 4.4 : Plate boundary conditions signs used in Table 4.3.

TABLE 4.4 : Boundary conditions and parameters under plate dynamic theories (Leissa, 1969).

Boundary conditions	$m$	$G_x$	$H_x$	$J_x$
	2, 3, 4, ...	$m - 1$	$(m - 1)^2$	$(m - 1)^2$
	2	1.506	1.248	1.248
	3, 4, 5, ...	$m - \frac{1}{2}$	$(m - \frac{1}{2})^2 \left[ 1 - \frac{2}{(m - \frac{1}{2})\pi} \right]$	$(m - \frac{1}{2})^2 \left[ 1 - \frac{2}{(m - \frac{1}{2})\pi} \right]$
	0	0	0	0
	1	0	0	$12/\pi^2$
	2	1.506	1.248	5.017
	3, 4, 5, ...	$m - \frac{1}{2}$	$(m - \frac{1}{2})^2 \left[ 1 - \frac{2}{(m - \frac{1}{2})\pi} \right]$	$(m - \frac{1}{2})^2 \left[ 1 - \frac{6}{(m - \frac{1}{2})\pi} \right]$
	2, 3, 4, ...	$m - \frac{3}{4}$	$(m - \frac{3}{4})^2 \left[ 1 - \frac{1}{(m - \frac{3}{4})\pi} \right]$	$(m - \frac{3}{4})^2 \left[ 1 - \frac{1}{(m - \frac{3}{4})\pi} \right]$
	2, 3, 4, ...	$m - \frac{3}{4}$	$(m - \frac{3}{4})^2 \left[ 1 - \frac{1}{(m - \frac{3}{4})\pi} \right]$	$(m - \frac{3}{4})^2 \left[ 1 - \frac{1}{(m - \frac{3}{4})\pi} \right]$
	2	1.506	1.248	1.248
	3, 4, 5, ...	$m - \frac{1}{2}$	$(m - \frac{1}{2})^2 \left[ 1 - \frac{2}{(m - \frac{1}{2})\pi} \right]$	$(m - \frac{1}{2})^2 \left[ 1 - \frac{2}{(m - \frac{1}{2})\pi} \right]$
	2, 3, 4, ...	$m - \frac{3}{4}$	$(m - \frac{3}{4})^2 \left[ 1 - \frac{1}{(m - \frac{3}{4})\pi} \right]$	$(m - \frac{3}{4})^2 \left[ 1 - \frac{1}{(m - \frac{3}{4})\pi} \right]$
	1	0	0	$3/\pi^2$
	2, 3, 4, ...	$m - \frac{3}{4}$	$(m - \frac{3}{4})^2 \left[ 1 - \frac{1}{(m - \frac{3}{4})\pi} \right]$	$(m - \frac{3}{4})^2 \left[ 1 + \frac{1}{(m - \frac{3}{4})\pi} \right]$
	1	0	0	$3/\pi^2$
	2, 3, 4, ...	$m - \frac{3}{4}$	$(m - \frac{3}{4})^2 \left[ 1 - \frac{1}{(m - \frac{3}{4})\pi} \right]$	$(m - \frac{3}{4})^2 \left[ 1 + \frac{3}{(m - \frac{3}{4})\pi} \right]$

Boundary conditions	$m$	$G_x$	$H_x$	$J_x$
	0	0	0	0
	1	0	0	$12/\pi^2$
	2	1.506	1.248	5.017
	3, 4, 5, ...	$m - \frac{1}{2}$	$\left(m - \frac{1}{2}\right)^2 \left[1 - \frac{2}{\left(m - \frac{1}{2}\right)\pi}\right]$	$\left(m - \frac{1}{2}\right)^2 \left[1 + \frac{6}{\left(m - \frac{1}{2}\right)\pi}\right]$
	1	0	0	$3/\pi^2$
	2, 3, 4, ...	$m - \frac{3}{4}$	$\left(m - \frac{3}{4}\right)^2 \left[1 - \frac{1}{\left(m - \frac{3}{4}\right)\pi}\right]$	$\left(m - \frac{3}{4}\right)^2 \left[1 + \frac{3}{\left(m - \frac{3}{4}\right)\pi}\right]$
	1	0.597	-0.0870	0.471
	2	1.494	1.347	3.284
	3, 4, 5, ...	$m - \frac{1}{2}$	$\left(m - \frac{1}{2}\right)^2 \left[1 - \frac{2}{\left(m - \frac{1}{2}\right)\pi}\right]$	$\left(m - \frac{1}{2}\right)^2 \left[1 + \frac{2}{\left(m - \frac{1}{2}\right)\pi}\right]$
	1	0.597	-0.0870	0.471
	2	1.494	1.347	3.284
	2, 3, 4, ...	$m - \frac{1}{2}$	$\left(m - \frac{1}{2}\right)^2 \left[1 - \frac{2}{\left(m - \frac{1}{2}\right)\pi}\right]$	$\left(m - \frac{1}{2}\right)^2 \left[1 + \frac{2}{\left(m - \frac{1}{2}\right)\pi}\right]$
	2	1.506	1.248	1.248
	3, 4, 5, ...	$m - \frac{1}{2}$	$\left(m - \frac{1}{2}\right)^2 \left[1 - \frac{2}{\left(m - \frac{1}{2}\right)\pi}\right]$	$\left(m - \frac{1}{2}\right)^2 \left[1 - \frac{2}{\left(m - \frac{1}{2}\right)\pi}\right]$
	1	0.597	-0.0870	0.471
	2	1.494	1.347	3.284
		$m - \frac{1}{2}$	$\left(m - \frac{1}{2}\right)^2 \left[1 - \frac{2}{\left(m - \frac{1}{2}\right)\pi}\right]$	$\left(m - \frac{1}{2}\right)^2 \left[1 + \frac{2}{\left(m - \frac{1}{2}\right)\pi}\right]$

### 4.3 Plate Deformation Measurements

In order to obtain a scientific relationship between a flat plate deformation and the more interesting material property which is the Poisson's ratio, a rectangular plate

simply supported on all edges for several case studies of plate designs will be experimentally investigated. The aims are to find a proper material for the plate design that positively will influence on a squeeze film levitation (SFL) performance, and also to reveal scientific relationships for the variations of the plate material properties, in particular, Young Modulus and Poisson's Ratio. The measurements have been implemented for the plate of various materials Table 4.5 and subjected to concentrated load of 5 N (Figure 4.5). The outcomes will present the trend of the plate deformation in contrast to the two important material properties which are Poisson's ratio and Young modulus.

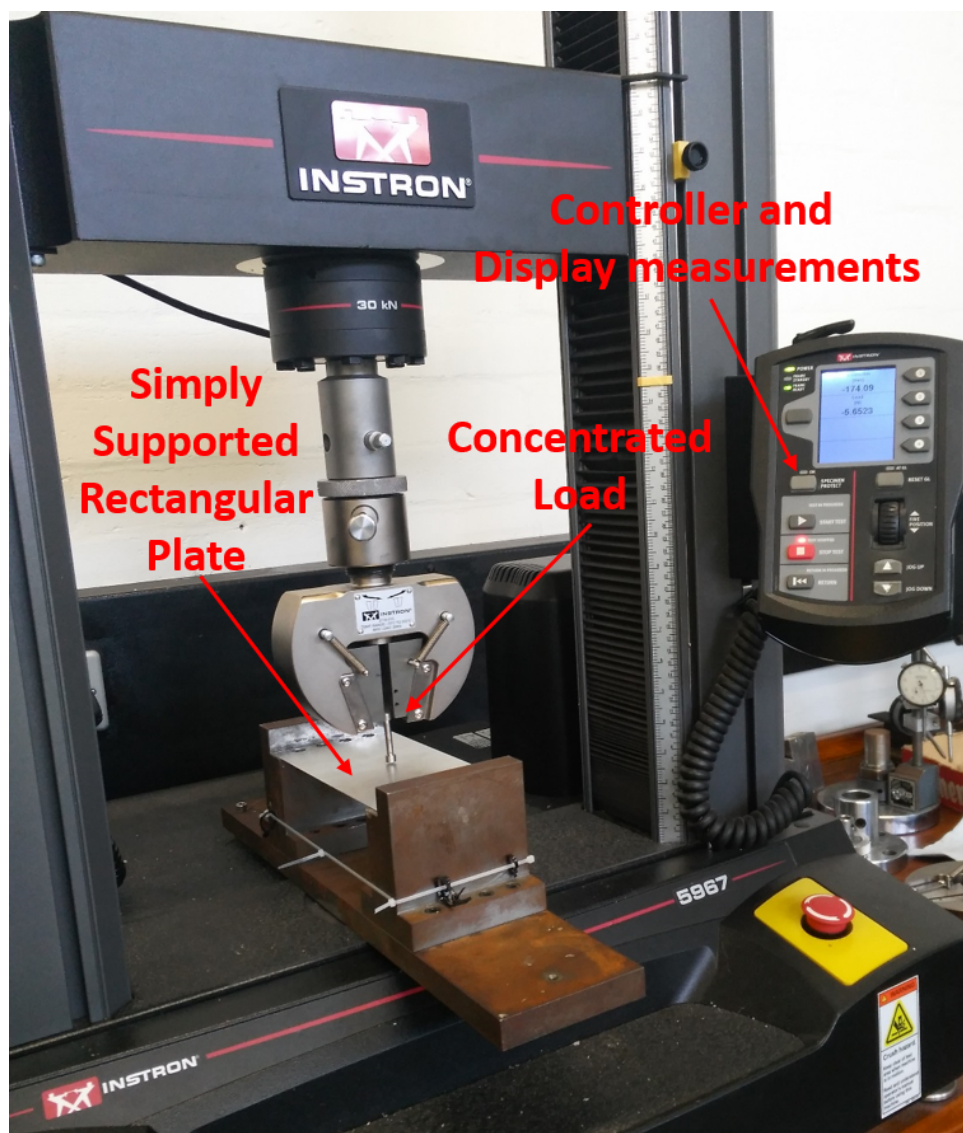


FIGURE 4.5 : INSTRON machine and plate under a concentrated load.

A variety of plate sizes and properties (Young Modulus and Poisson's Ratio) have been experimentally tested (Table 4.5). Some of that material properties have influencing on the forced plate design and consequently on the squeeze film levitation. For example, the material properties of Steel, Aluminium, Copper, Glass, and Polymer have significant variations. Those materials experimentally can be used as forced plate design. As a result, a clear scientific relationship can be drawn to show the behaviour of plate design characteristics.

TABLE 4.5 : Various plate cases, the plate is simply supported and subjected to a central point load of 5 N.

Case No.	Material	Modulus of Elasticity GPa	Poisson's Ratio	Plate Size mm
C1	Steel (St.)	207	0.3	200*100*1
C2	Aluminium (Al.)	69	0.33	200*100*0.5
C3	Aluminium	69	0.33	200*100*1
C4	Aluminium	69	0.33	200*100* 2
C5	Brass (Br.)	97	0.34	200*100*0.5
C6	Polymer HDPE	1.08	0.46	200*100*2
C7	Polymer Acrylic	3	0.36	200*100* 2
C8	Tin	44.3	0.33	200*100*0.23

The association between the deformation measurements and Poisson's ratio plus Young modulus of different plate designs are plotted in Figure 4.6 to Figure 4.8. Many physical parameters influence the forced plate design and accordingly the SFL. The analytical solution of the rectangular plate simply supported on all edges and subjected to a concentrated force illustrates the most effective parameters on the plate deformation.

Figure 4.6 shows the relationship between two important ratios which are  $RatioA = \frac{w t^3}{0.198 p a^2}$  and  $RatioB = \frac{1-\nu^2}{E}$ . These ratios are derived from equation (4.30) It can be

seen that for different plate sizes, the linear trend is that when ratio B increases, ratio A also increases. Figure 4.6 also shows that both polymer materials have the higher Ratio A and Ratio B among the plate materials. Additionally, the relationship between the two ratios (A and B) for the same plate thickness, for example, Aluminium 2 mm thickness, Poly Acryl 2 mm thickness, and Poly HDPE 2 mm thickness all have the ratio A increasing when the ratio B increases.

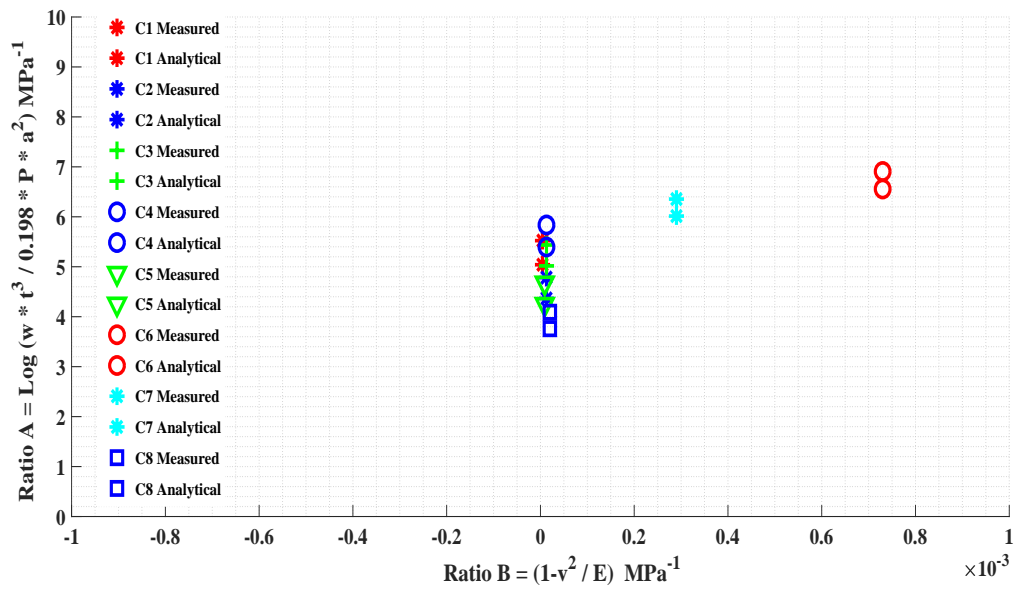


FIGURE 4.6 : Comparison of analytical and measurement results for various plate cases (Table 4.5).

The plate deformation versus plate thickness are presented in Figure 4.8, illustrating that deformation not only depends upon the plate thickness but also on the plate material as expected.

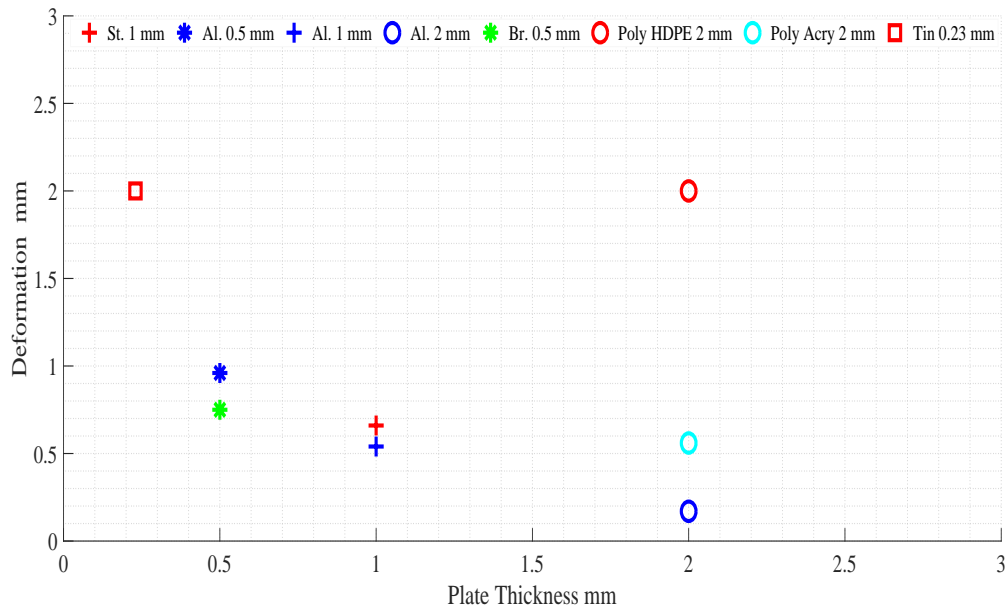


FIGURE 4.7 : Plate deformation measurement result versus plate thickness for various plate cases (Table 4.5).

The relationship between plate deformation under concentrated load and the Poisson's Ratio for various thicknesses is shown in Figure 4.8. Careful inspection of the plot reveals that a higher Poisson's ratio gives a higher deformation for a given thickness. For example, Poly HDPE produces the highest deformation in comparison to other plates of the same thickness.

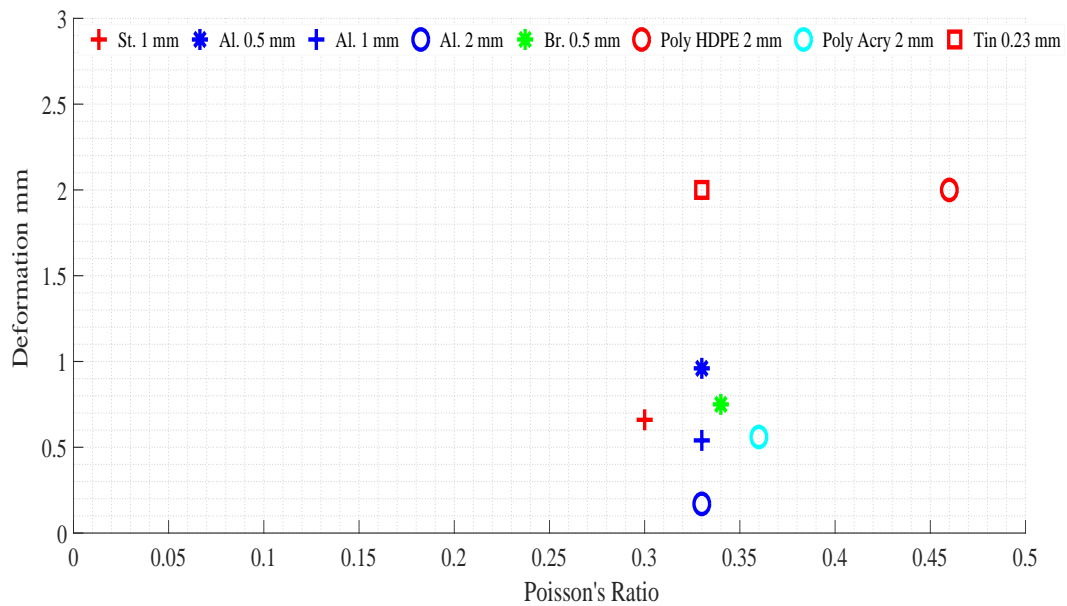


FIGURE 4.8 : Plate deformation measurement result versus Poisson's Ratio for various plate cases (Table 4.5).



## Chapter 5

# Influence of design embodiment on the performance of SFL

### 5.1 Introduction

Conveying and handling of delicate and lightweight objects is currently a significant issue in some industries. Two common contactless movement prototype designs (Table. 5.1), ultrasonic transducer design and actuated plate design, are compared in this chapter. Both designs are based on the method of squeeze-film levitation (SFL) and the aim of this study is to identify the limitations, and challenges of each. The designs are evaluated in terms of levitation capabilities, and characteristics. To this end, physical experimental explorations are made. It is demonstrated that the ultrasonic transducer prototype design is better suited to the terms of levitation capabilities. However, the design has some operating and mechanical designing difficulties. The SFL is considered the best method of OAPL, compared to others, such as magnetic, optical (utilising visible laser light to create radiation pressure), aerodynamic etc., as confirmed by the literature. The advantages of SFL are, firstly, it is suitable for lifting fragile or sensitive components down to a micron-scale. Moreover, contamination encountered with classical production conveying can be avoided. In addition, there is the avoidance of friction for the transporting of delicate and lightweight products during manufacturing. In this study, a

TABLE 5.1 : Plate designs sizes and material properties.

Design	Material	Configuration	Driving Plate size <i>mm</i>	Frequency <i>kHz</i>
A1	Aluminium	Horn-Transducer	200*1	25.8
A2	Aluminium,	Horn-Transducer	200*2	26.4
B	Aluminium	Actuated Plate	200*100*2	0.339

comparison is made of two different prototype SFL designs to achieve a frictionless movement for lightweight objects placed on them. The main aim is to identify an effective non-contact movement design, in terms of the design capability, complexity, and cost. One of the designs (Table 5.1) that has been used in this study is ultrasonic transducer (Design A) which a Langevin of type (FBI 28452 HS) comprises the main part. The measurements related to Design A have been carried out in Mechanical Engineering Department / Tokyo University of Science. Whilst the other (Design B) (Table 5.1), is a actuated plate design, which consists of a plain rectangular plate made of aluminium firmly fastened at both ends. The dynamics of the levitation using the design A and design B physically investigated based on the squeeze film levitation (SFL).

### 5.1.1 Squeeze Film Levitation (SFL) Approach

Squeeze film levitation has been proposed for conveying and holding objects in specific applications. For example, OAPL of glass substrates or silicon wafers can be levitated utilising ultrasonic transducer through that method. The load carrying air film can be produced through the fast oscillation of one of two parallel adjacent flat plates and the phenomenon that pressure is developed in the fluid (air) between the two (clearance or air - gap) is called a squeeze film levitation. When the clearance between the two flat plates is sufficiently wide, and the fluid in it can freely flow

out to the surroundings, then the object falls freely. However, when the distance between the two opposing surfaces becomes significantly smaller than the area of the plate, the influence of the viscous force of the fluid becomes large and the fluid in the clearance is less likely to squeeze out to the surroundings. That is, the situation is such that the fluid is confined within the clearance and the internal pressure  $P$  becomes higher than the ambient pressure  $P_a$ . In order to generate the squeeze effect steadily and to obtain a stable load capacity, thus levitating the object, the oscillating plate is made to vibrate at a high frequency (a squeeze motion). The higher the frequency of vibration, the more viscous the restriction imposed on the fluid in and around the clearance, which means the fluid (air) in the clearance is entrapped, as if there were cylinders around it. If the driving frequency of the squeeze motion sufficiently matches the natural frequency of the system, this will lead to the creation of a spring rigidity of the levitating body-air film. At this time, assuming that the time-averaged height between the two surfaces is  $h_o$ , the ambient pressure is  $p_a$ , the levitating body area is  $A$ , the driving amplitude of the squeeze motion is  $a_o$  and the driving frequency is  $f$ , according to Boyle's law the internal pressure  $P$  is:

$$PA (h_o + a_o \cos 2\pi ft) = p_a Ah_o \quad (5.1)$$

Then, the average time for one cycle in the squeeze movement is:

$$\frac{1}{T} \int_{T=0}^T p dt = \frac{p_o}{\sqrt{1 - \left(\frac{a_o}{h_o}\right)^2}} \quad (5.2)$$

Thus, a light weight item, when placed on the oscillation plate, can be exposed to a normal pressure and consequently, can be levitated above the driving surface at a very small distance (usually below a millimetre). With SFL, a thin air layer with pressure changing as a result of the dynamic deformation of driving surfaces is to be considered. In an OAPL device of small diameter, the vibration surface amplitude is uniform. Also, when very small objects are targeted, their levitation distances are

very small and the Reynolds number ( $Re$ ) is about 10. Hence, the occurrence of the levitation force in an OAPL device of small diameter is assumed to be due to the effect of the squeeze membrane pressure. On the other hand, in the OAPL apparatus for large diameters (e.g. semiconductor wafers), the amplitude of the vibration surface is not uniform, i.e. it has a complex vibration mode. In addition, since a silicon wafer with a diameter of 200 mm is supported with a levitating distance of several hundred Micro-metre, the  $Re$  number exceeds 1000 (Stolarski and Chai, 2006; Minikes, Bucher, and Haber, 2004; Li, Liu, and Feng, 2017).

### 5.1.2 Configuration of Horn-Transducer (Design A)

The ultrasonic transducer used in this experiment, a ring-shaped piezoelectric element (Piezoelectric Ceramics), is sandwiched between two metal blocks and tightened with a bolt to form an integral structure (Figure 5.3), which is also called a bolted Langevin type vibrator. A longitudinal wave (ultrasonic vibration) generated by an ultrasonic vibrator will transmit to a flat circular plate, which is aluminium and has a diameter of 200 mm. Design A includes a horn part (Figure 5.3), located between the Langevin and the circular plate, the function of which is to amplify the vibration of the circular plate (driving structure). Two different driving plate investigated (Table 5.1)

### 5.1.3 Horn Design

In this study, as above, the shape of a horn is selected, as this is an optimum one, according to the required vibration characteristics and usage conditions. Among the horns proposed so far, there are frequently used shapes, such as exponential type, conical type, Catenoidal type and uniform step type (Figure 5.1). In this research, a conical shape has been utilised. (Figure 5.2) shows the conical shape design parameters. The horn is divided into a cylindrical part and one for amplifying the

amplitude, with the length of the cylindrical portion being calculated from the driving frequency and the sound velocity of the longitudinal wave in the material. The cross-sectional area of the horn tip end is defined as the horn narrow end area ( $S_1$ ), the cross sectional area where the cylindrical portion and the amplification portion are connected to the horn's thick end surface area ( $S_2$ ), the cross sectional area of cylindrical portion is notified as ( $S_b$ ).

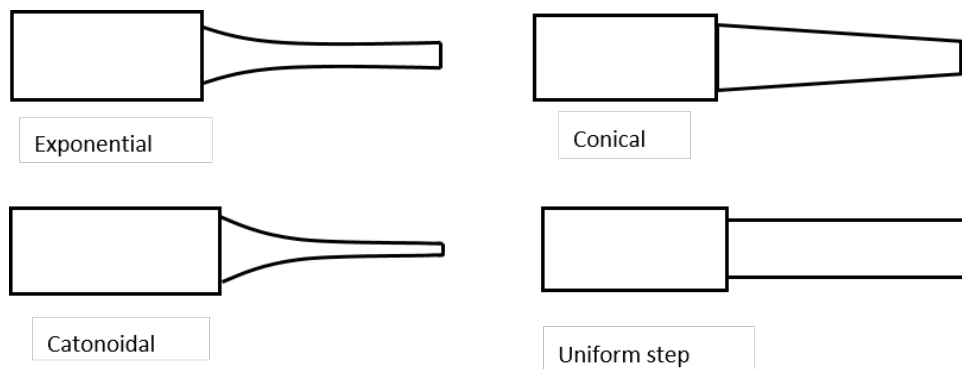


FIGURE 5.1 : Types of horn design.

It is important when designing a horn, first, to determine the cylindrical part area from the transducer to be used and then, finding the thickness end area. If the area ratio with this case is made too large, the step portion becomes too discontinuous, and vibration propagation is obstructed. Experimentally, it should be less than 4:1 and in this experiment, this area ratio was 3:1 in consideration of the balance of the experimental apparatus as a whole. Next, the horn's narrow end area is determined. The smaller the area is, the more the longitudinal wave vibration generated from the vibrator is amplified, but in this experiment, it is necessary to fasten the vibration plate to the tip of the horn by bolts. So, the tip diameter of the horn is set to 10 mm;  $S_1/S_2 = R_2/R_1$ ;  $R_1$  is the radius of the narrow face and  $R_2$  is the radius of the wide face. Wave length constant can be expressed by  $k = \omega/c$ , in which  $\omega$  is driving angular frequency and  $c$  is sound velocity of the material. The full length of the horn can be represented by  $La = \lambda/4 + L$ , in which,  $L$  is the amplification unit (Ensminger and Bond, 2011).

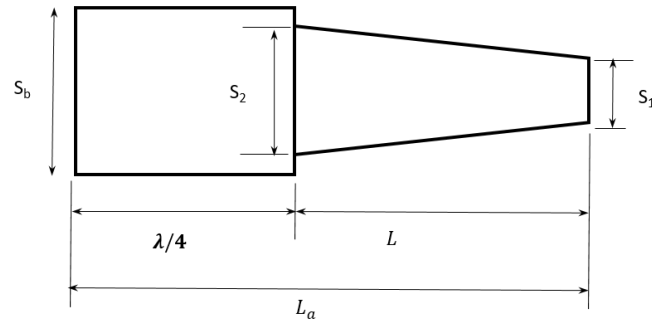


FIGURE 5.2 : Conical horn configuration.

### 5.1.4 Experimental Method for Design A

The principle of the proposed OAPL device is that a sine wave voltage is input to the ultrasonic vibrator, the vibration of which is amplified by the horn, and the vibration plate resonates at a certain natural frequency (Figure 5.3). This creates a squeeze air film and radiated pressure field between the vibrating plate and the levitated object placed on the vibrating plate, whereby a repulsive force acts on the levitated object that is able to lift the object. The experimental equipment that can be used to operate Design A to achieve the levitating and to measure its displacement is briefly described as follows:

Firstly, an output voltage from a function generator is amplified and supplied to the ultrasonic transducer. Secondly, the ultrasonic, vibrates by applying a sinusoidal voltage that gives a vibration displacement after providing a bias voltage, thereby creating a constant displacement. The amplitude voltage and frequency are measured throughout the process by an oscilloscope (Figure 5.3) and (Figure 5.4). A non-contact displacement sensor (model: PHILTEC RC60 - H3) (Figure 5.4) is used for measuring the vibration amplitude of the deformed surface and the separation distance of the levitating object. The sensor is connected to an oscilloscope, which displays the output signal in volts. The voltage corresponds to the dynamic distance of the circular plate and the levitating object's height. The measurements of

the maximum levitation for three different semiconductor wafers of weights 52, 70 and 88 g placed on Design A are taken.

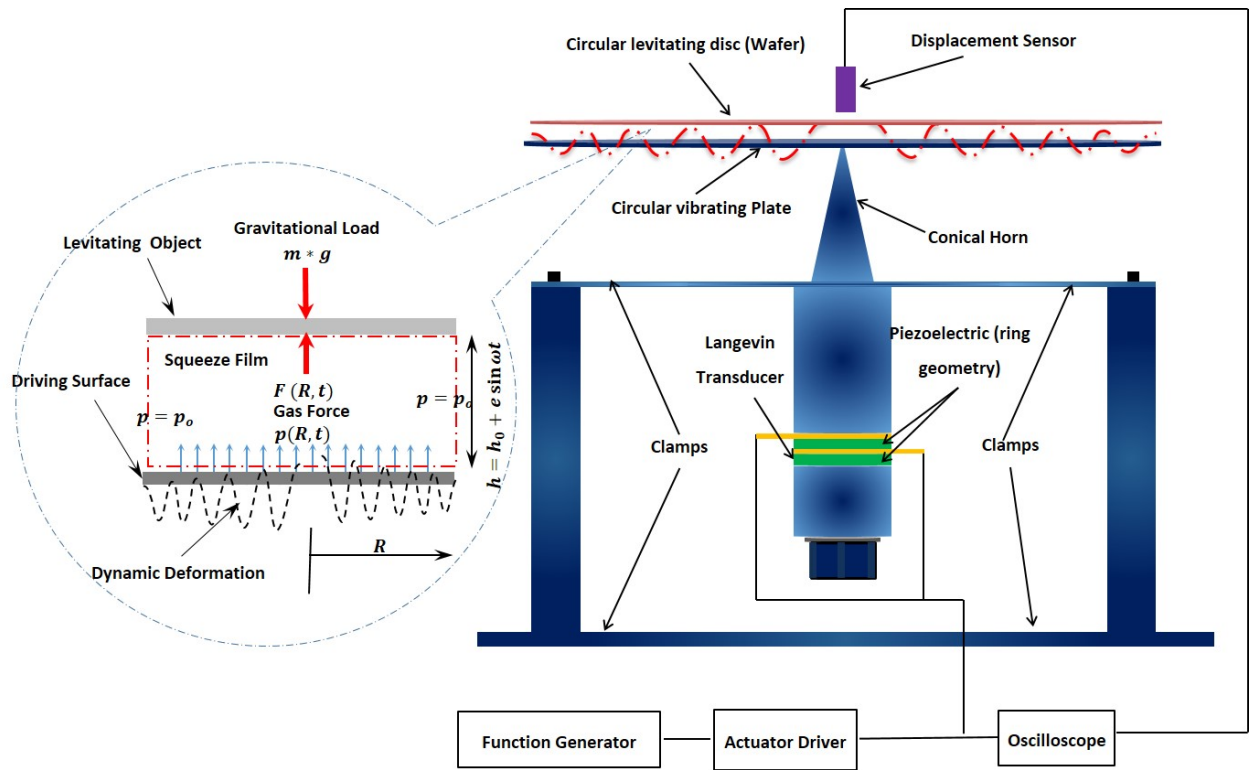


FIGURE 5.3 : Schematic and experimental layout of SFL design A (Tokyo University of Science).

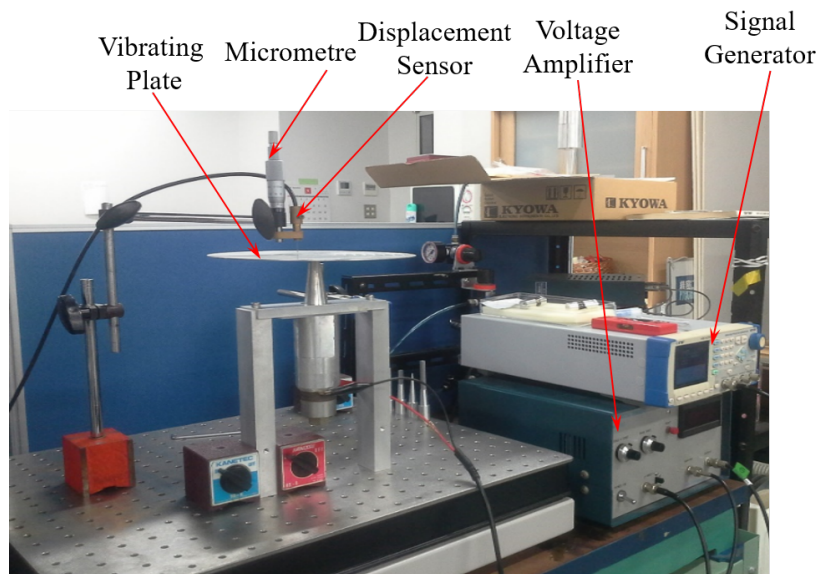


FIGURE 5.4 : Experimental set-up of SFL design A (Tokyo University of Science).

## 5.2 Results and Discussion for Horn-Transducer Designs (A1 and A2)

The vibration mode of the driving plate is visualised by scattering plastic particles on the surface of the plate, while resonating the design (Figure 5.5). From the results, one can predict the nodes and anti-nodes of the vibration. The vibration amplitude of the driving plate and the levitation height of the levitated object are measured utilising a non-contact displacement sensor (Figure 5.5). Measuring the vibration amplitude of the vibrating plate, the voltage applied to the design is the bias voltage  $V_{off}$ , which is 100 V and the alternating voltage  $V_{amp}$  varies from 40 to 90 V. In the same manner as in the case of measuring the vibration amplitude of the vibrating plate, the levitation for three patterns of masses, 52.8, 74.2 and 80 g is measured. The distance between the situation where the object was before inputting the voltage to the ultrasonic transducer (no levitating) and the state at the centre of the supporting object when the object is levitated by inputting the voltage to the ultrasonic transducer is measured, which is the levitating height. First, the voltage when the levitated object is levitating is measured, and immediately after that, the alternating voltage is turned off, and the voltage is measured again with the levitated object set at the centre of the oscillating plate. From the difference between the two voltages measured, the levitating height is calculated.



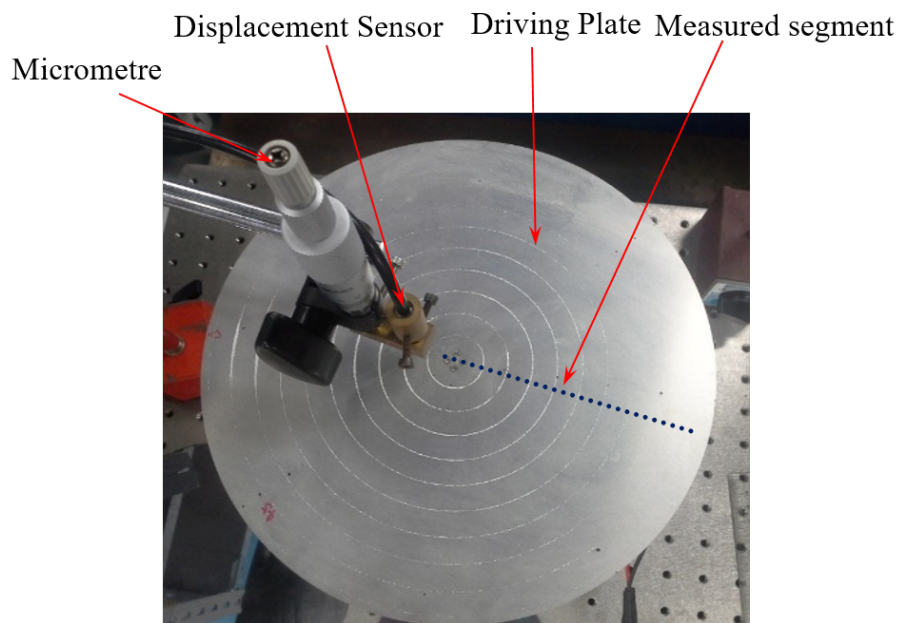


FIGURE 5.5 : Experimental actuated plate set-up design A1 at 26.4 kHz  
(Tokyo University of Science).

Physical measurements for the plate dynamic deformation and load carrying capacity of Designs A1 and A2 (Table 5.1) are made. The dynamic deformation for the segment (Figure 5.6) at a resonance frequency of 26.4 kHz for Design A1, and at resonance frequency of 25.8 kHz for Design A2 (Figure 5.8) are measured.

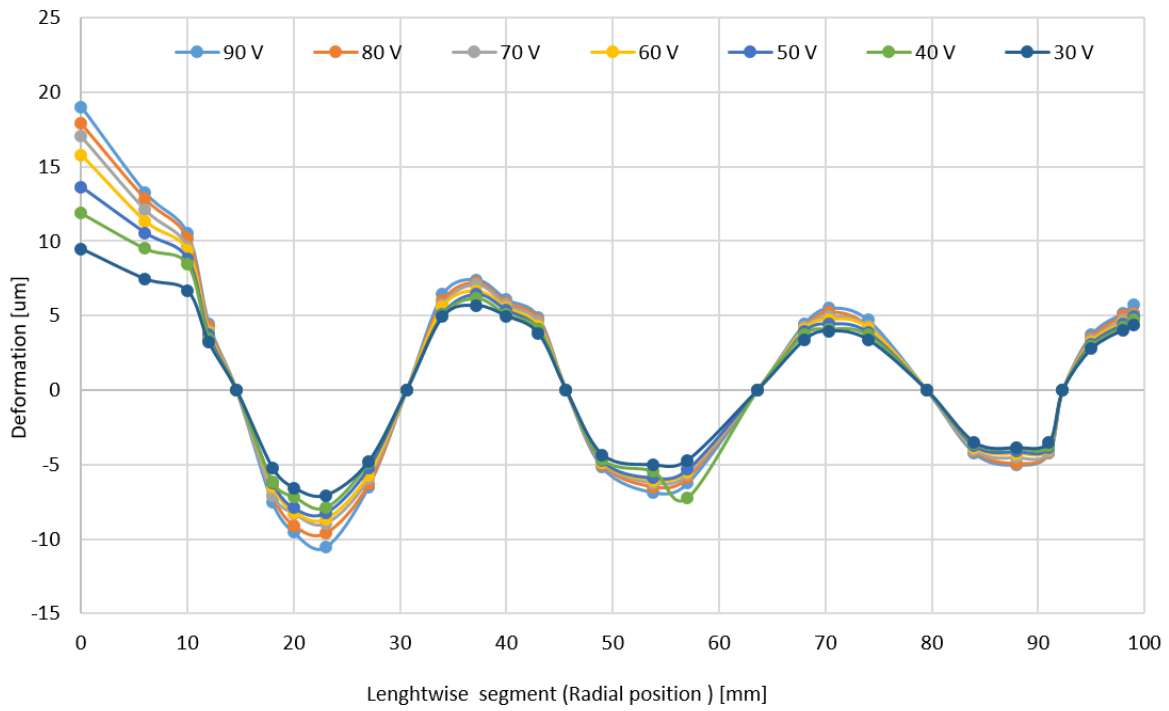


FIGURE 5.6 : Experimental dynamic plate deformation (Design A1) at resonance frequency of 25.8 [kHz].

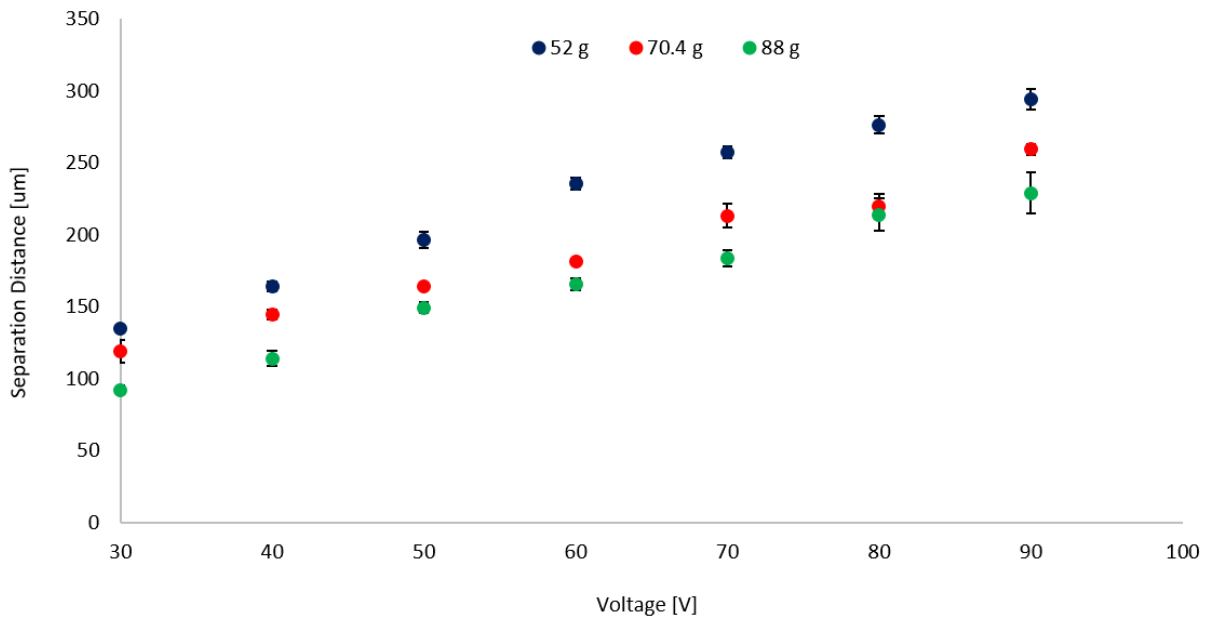


FIGURE 5.7 : Experimental separation distance for various weights (Wafer) at different driving voltages for (Design A1).

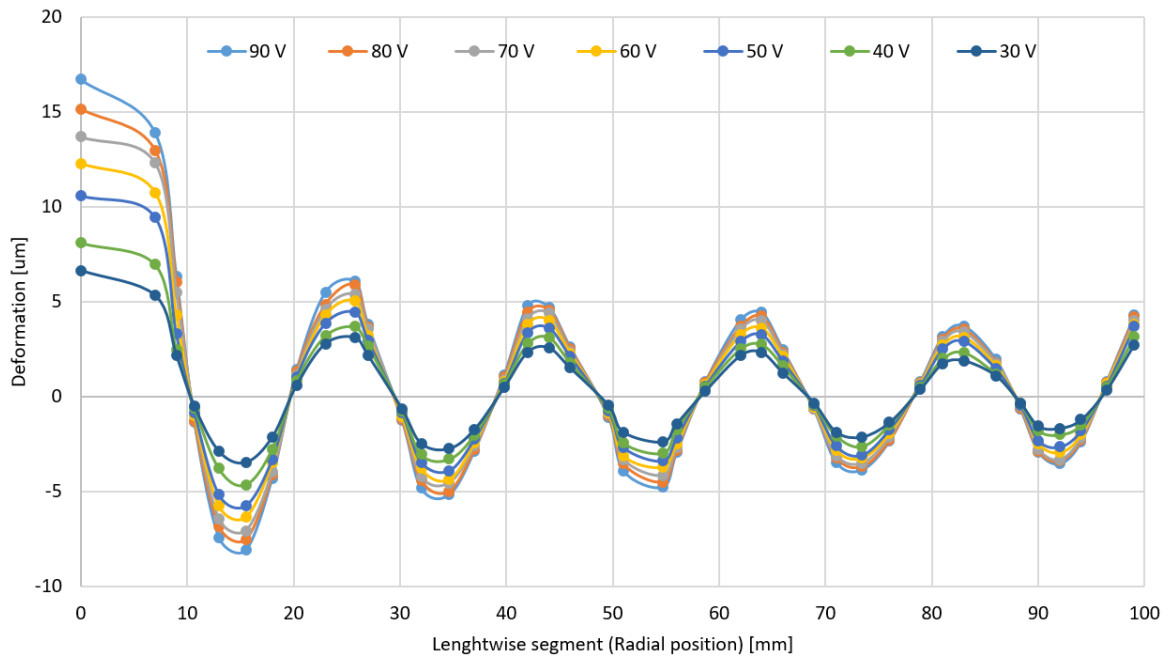


FIGURE 5.8 : Experimental dynamic plate deformation (Design A2) at 26.4 [kHz].

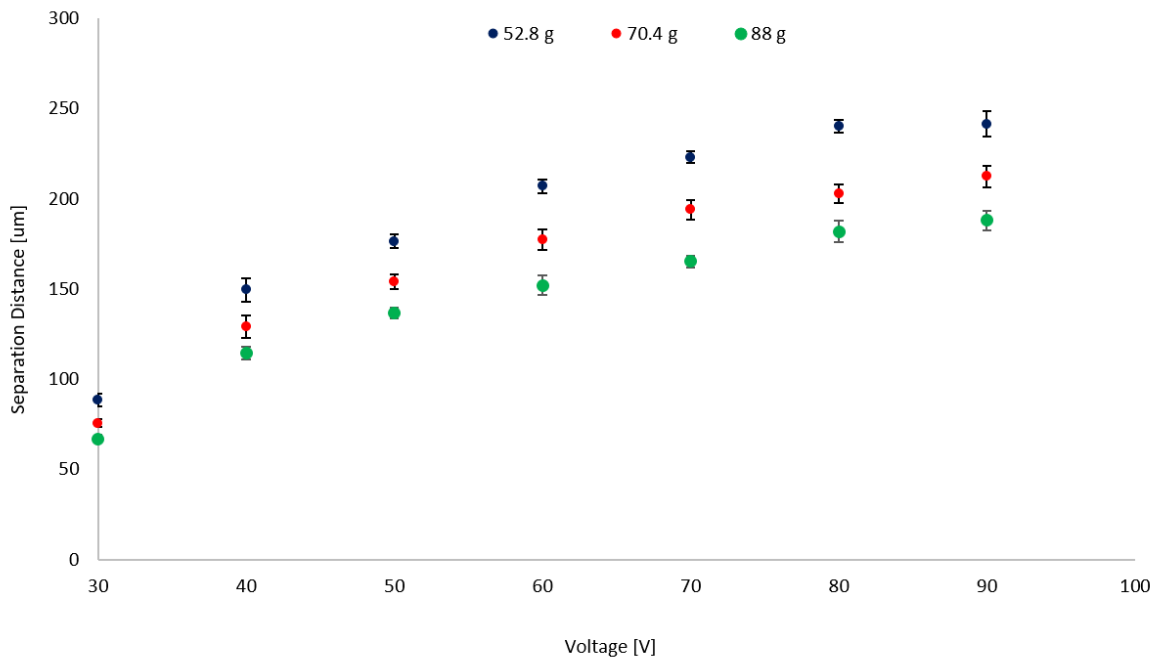


FIGURE 5.9 : Experimental of separation distance for various weights (wafer) at different driving voltages for Design A2.

As can be seen, the dynamic deformation results of Designs A1 and A2 reveal that the deformation is higher at the centre of the designs' plate (Figure 5.6) and (Figure 5.8) and then, become fluctuating at various points of the measured segment. This fluctuation is as a result of the plate modal shape, which is included multi node and anti-node. The plate deformation of design A1 and A2 has a small change during driving the designs at different voltages. This is because the properties of piezoelectric actuators, which are incorporated within the Langiven of the designs, are less sensitive for a small variation of the driving voltages. The measurements reveal that the maximum dynamic deformation of the plate of Design A1 is about  $20 \mu m$ , whereas it is about  $17 \mu m$  for Design A2 at a driving voltage of  $90 V$ . The measurements disclose that the minimum dynamic deformation of the plate of Design A1 and Design A2 (Figure 5.6) and (Figure 5.8) at a driving voltage of  $30 V$  are about  $2.7$  and  $4.5 \mu m$ , respectively. Regarding the load carrying capacity, (Figure 5.7) and (Figure 5.9) show linear relationships with voltage variation as a result of the linear effect stemming from the designs' material properties, in particular, the piezoelectric actuator material properties. Design A1 achieved a higher levitation than Design A2, because the thickness of the plate of Design A1 is thinner, i.e. for the former, it is  $1 mm$ , whilst for the latter, it is  $2 mm$ . The higher levitating happened for the object of weight  $52 g$  placed on Design A1 at a driving voltage of  $90 V$ , which reached to about  $294 \mu m$  (Figure 5.7), whereas the lower levitating occurred for the object of weight  $82 g$  placed on Design A2 at a driving voltage of  $30 V$ , which reached about  $66 \mu m$  (Figure 5.9).

### 5.3 Configuration of Actuated Plate (Design B)

Design B which is compromise from a rectangular plate of size  $200*100*2 mm$ . In addition, four rounded piezoelectric actuators of size  $28 mm$  diameter \*  $0.5 mm$  thickness are glued underside of the plate (Figure 5.10). The actuated plate is clamped at

both ends in the horizontal plane through a steel supporting structure. The investigation includes physical measurements for the actuated plate design through using a digital image correlation system (DIC) from GOM Company.

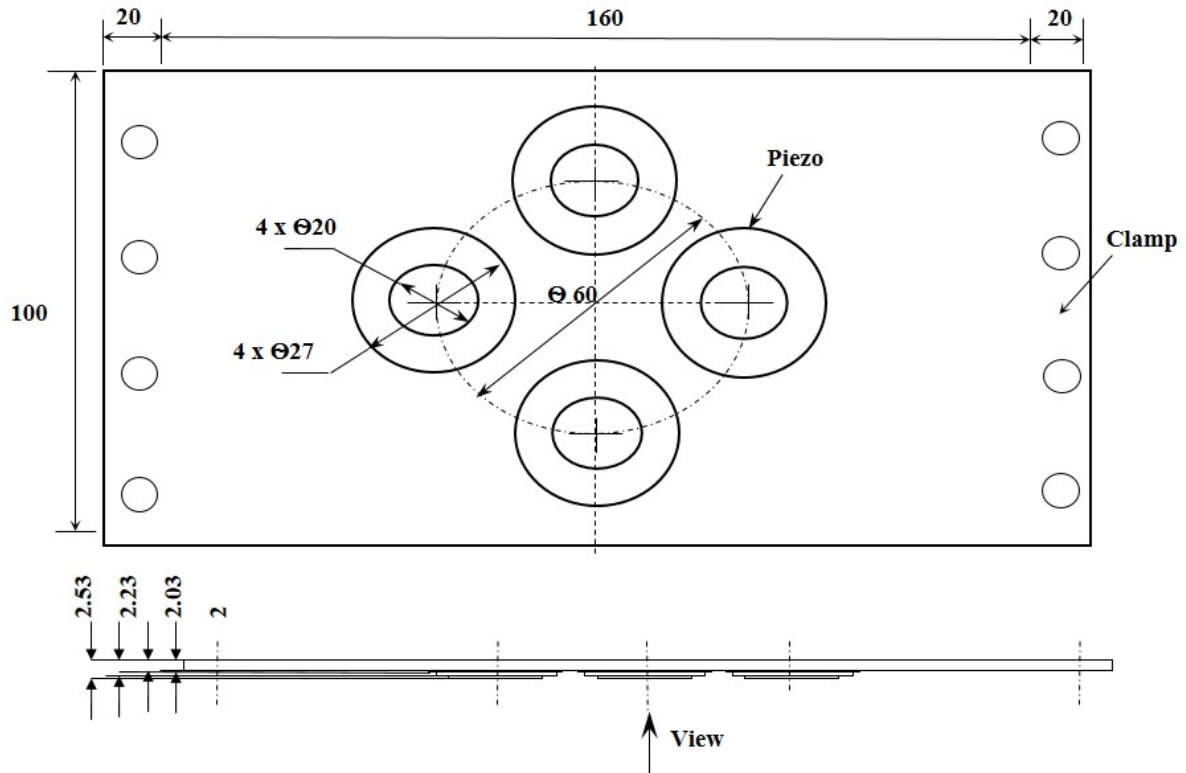
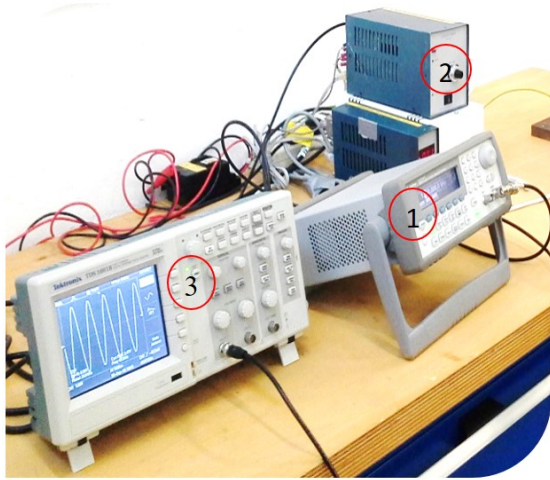


FIGURE 5.10 : CAD model of design B (all units in *mm*).

## 5.4 Experimental Method for Design B

The input apparatus used with Design B consists of a sine wave signal generator connected to an amplifier of type ENP-1-1U (Echo Electronics) (Figure 5.11). The latter has to be utilised to magnify the sine wave voltage produced by the signal generator. The amplified voltage and sinusoidal frequency are supplied to drive the four piezoelectric actuators that are attached to the underside of the plate (Figure 5.10) and (Figure 5.12). The actuators are driven with an AC voltage, which produces a dynamic displacement on the top surface of the plate. The displacement will create a cyclic squeeze-film for the air trapped between the actuated plate and

the object. A decompression and compression process for the air film will suspend the object placed on the vibration plate.



- (1) Signal Generator.
- (2) Voltage Amplifier.
- (3) Oscilloscope.
- (4) High speed camera (ARAMIS - Photron UX50).
- (5) Light (DIC system).
- (6) Vibrating plate design.

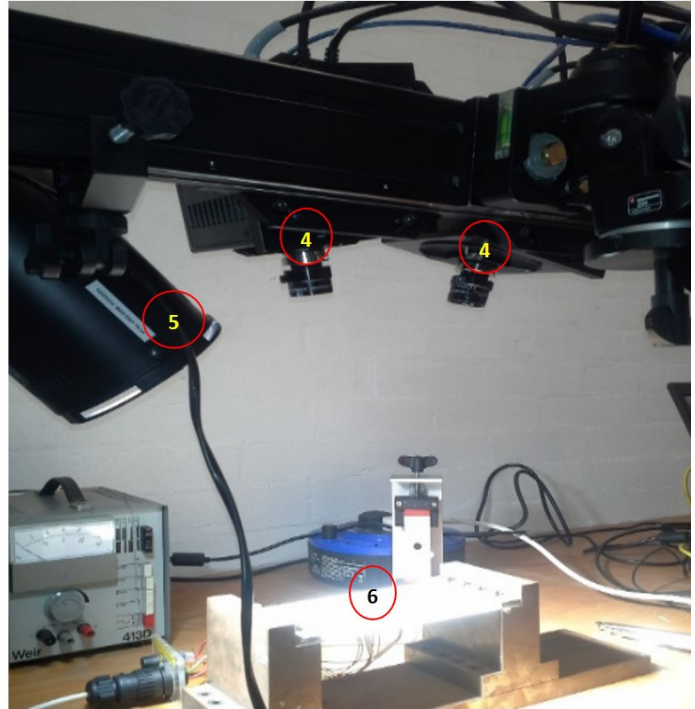


FIGURE 5.11 : Experimental set-up measurements (Design B).

## 5.5 Results and Discussion for Design B

Design B has been detected through DIC system, the system set-up has been illustrated in (Figure 5.12), appendix B shows more details regarding DIC system.

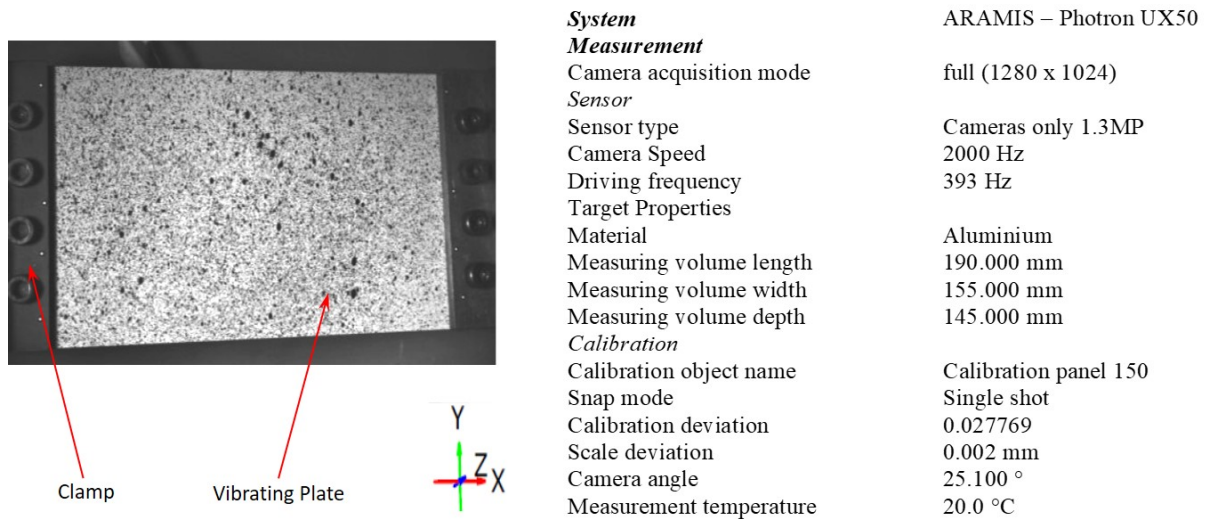


FIGURE 5.12 : Design B and DIC system features and experimental set-up.

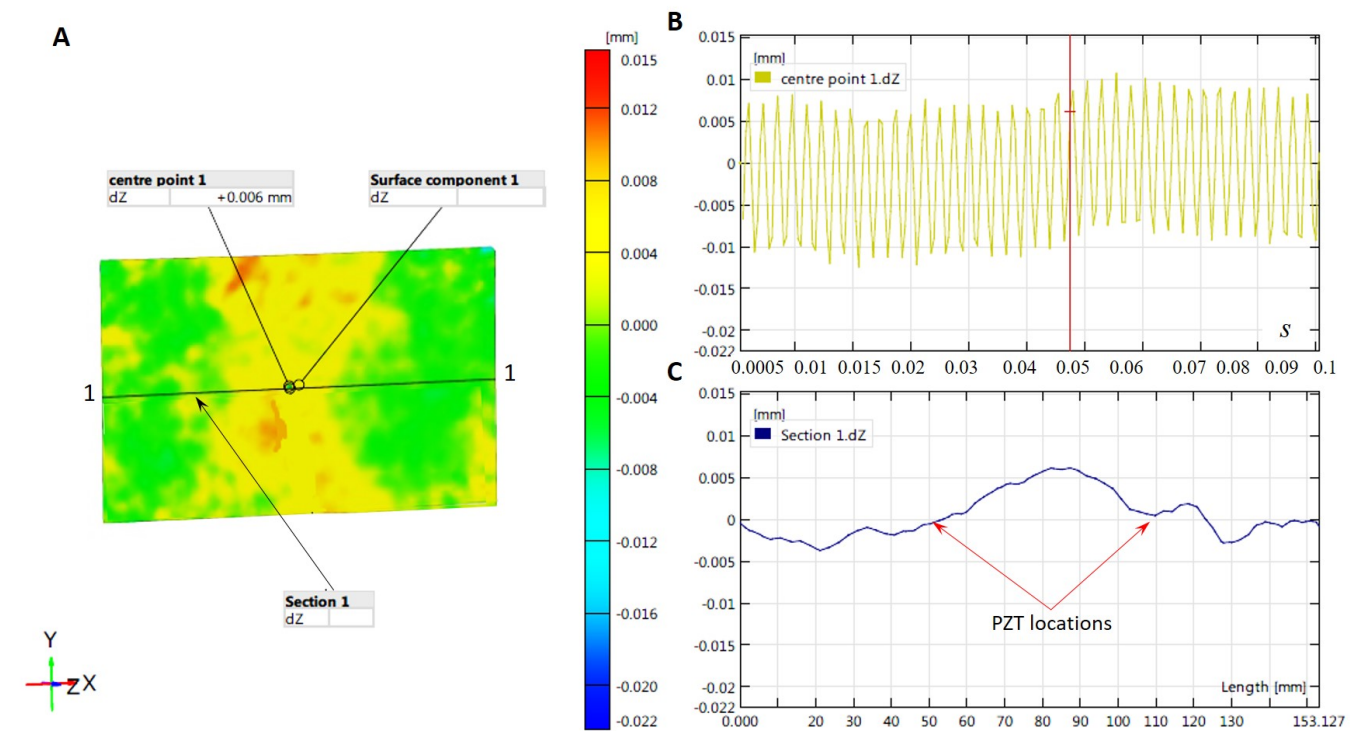


FIGURE 5.13 : Experimental measurements using DIC system for dynamic plate deformation of design B at a resonance frequency of 0.339 kHz: A- plate modal shape; B- plate centre point deformation; C- plate section or lengthwise deformation.

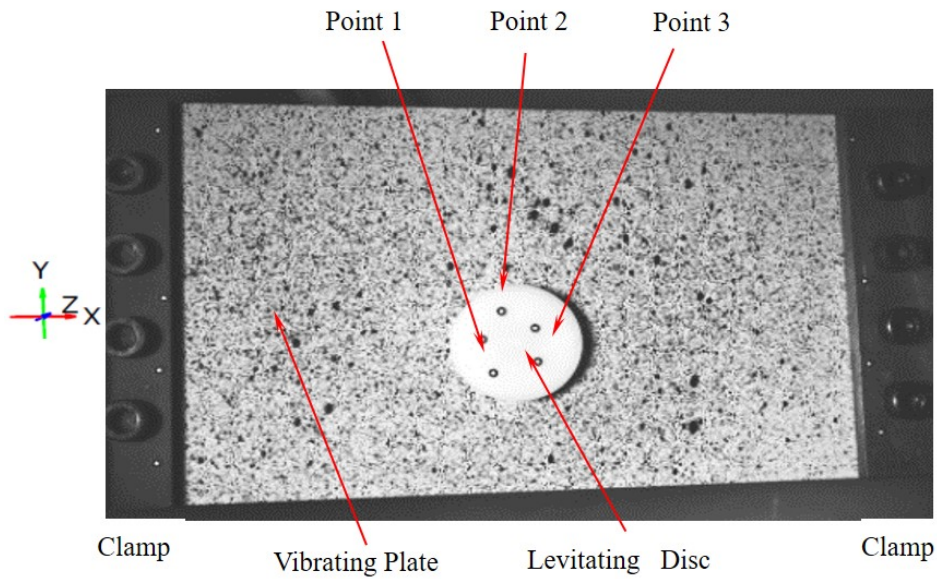


FIGURE 5.14 : Design B and levitating disc under DIC system.

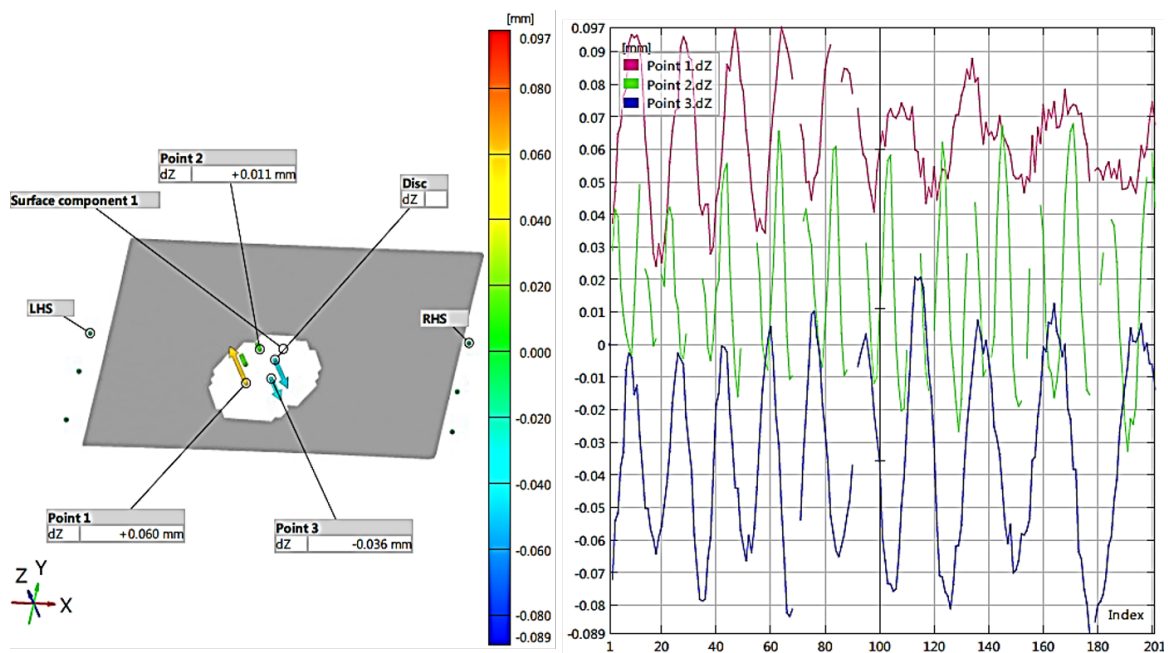


FIGURE 5.15 : Separation distance for a disc of 5 g levitating on Design B at 339 Hz.

The plate modal shape (Figure 5.13) and the dynamic deformation of a plate's centre point and lengthwise segment (Figure 5.13 - B and Figure 5.13 - C) have been detected through the DIC system from GOM Company. The plate's behaviour



shows that there is a symmetry at its central point and the maximum dynamic deformation of approximately  $7 \mu\text{m}$  occurred here due to the boundary conditions, whereby the plate is clamped at both ends, the modal shape of the plate and piezoelectric location at the central area underneath of the plate also has an effect on the plate dynamic deformation. The results for prototype Design B confirm that a weight can be levitated at one of the resonant frequencies of the design (Figure 5.14), which is close from 0.339 kHz. The dynamic levitation distance (Figure 5.15) of the three points on the top surface of the disc, which are selected arbitrarily, show that the disc can tilt/wobble during conveying for Design B. The modal shape of the vibrating plate and consequently the non-uniform distribution of the air-layer pressure that is developed underneath the levitating disc can cause the wobbling (Kim and Ih, 2007). The maximum and minimum levitating distance for a 5 g disc levitated on Design B reach to about 100 and 80  $\mu\text{m}$  respectively, whereas the average separation distance achieves roughly 70  $\mu\text{m}$ .

## 5.6 Conclusion

The study has investigated two different SFL designs that can be used as contactless conveying. The main goal was to compare the designs in terms of load carrying capacity. It is shown that it is possible to hold an object in a non-contact manner. Clearly, the designs are highly affected by the design configuration, in particular, the driving plate characteristics such as the plate size and geometry as well as the driving boundary conditions. Whilst it can be concluded that Design A has a significantly better performance than Design B in terms of load carrying capacity, Design A has a more complicated design, e.g. higher voltages and greater device depth, and therefore is more costly, than Design B. It is for this reason that Design B is more suitable to be utilised as a conveyor for real-world applications.



## Chapter 6

# Alternative Plate Deformation

## Phenomenon for SFL

### 6.1 Introduction

An unconventional method for generating squeeze film levitation (SFL) is investigated using theoretical and experimental measurements of the static and dynamic characteristics of several forced plate designs. A finite element model (ANSYS) is validated by the experimental testing of five different forced plate designs, each of which is excited by an arrangement of two hard piezoelectric actuators glued underneath the plate and driven with DC or AC voltages. It is observed that a repeated distortion of a dimple or crest shape along longitudinal axis in the central area of the plate is created due to the effect of Poisson's ratio rather than vibration mode. This Poisson's effect generates the squeeze-film between the plate and the levitated object. The separation distance between a levitating lightweight object (disc) and the plate is analysed using computational fluid dynamics (ANSYS) and experimentally measured by a laser sensor, with good agreement. This investigation aimed to create a repeated action of a special localised shape of deformation by actuating a driving surface of a thin rectangular plate using a particular arrangement of piezoelectric actuators glued to the underside of the plate. In other words, the aim

is to create a repeated forced dimple deformation in a vertical direction at the centre of the plate, instead of vibrating the plate, which has been widely investigated in previous studies. It is desirable to produce the largest possible displacement at a particular oscillation frequency, as it will produce a greater levitation for objects placed on the forced plate design. Accordingly, different plate materials and sizes are theoretically and experimentally examined in this seeking. This results in the design of a better mechanism for producing the squeeze-film effect that, in turn, improves the levitation of objects. The simulation and measurement procedures for analysing the levitating designs will be explained in this section. First, a theoretical method of modelling the forced plate design, including the static and dynamic analyses, is presented and executed using the finite element method (ANSYS Workbench). Second, a theoretical method for modelling levitating items and calculating their dynamic levitation distance as well as the pressure distribution, using computational fluid dynamic (ANSYS Workbench), is illustrated. Moreover, the method of experimental measurement for the levitating designs is explained.

## 6.2 Method

The simulation and measurement procedures for analysing the levitating designs will be explained in this section. First, a theoretical method of modelling the forced plate design, including the static and dynamic analyses, is presented and executed using a finite element program (ANSYS Workbench). Second, a theoretical method for modelling levitating items and calculating their dynamic levitation distance as well as the pressure distribution, using ANSYS CFD, is illustrated. Moreover, the method of measurement work for the levitating designs is explained.

### 6.2.1 Theoretical Modelling

A basic physical realisation of SFL comprises an elastic plate, piezoelectric actuators and levitated object with air gap; with the actuators vibrating the plate at modes that

deform the plate to squeeze the air (Figure 6.1). SFL depends on the viscosity and compressibility of a thin layer of air that is entrapped between the moving surface and the levitated item. Accordingly, the average pressure in the squeeze-film will be greater than the atmosphere, thus producing a levitating force, which must be greater than the weight of the floating object (Stolarski and Chai, 2008; Atherton, Mares, and Stolarski, 2014; Yoshimoto, Kobayashi, and Miyatake, 2007). This study describes an alternative means of deforming a plate to generate SFL based on a Poisson's Ratio Plate Deformation (Figure 6.3).

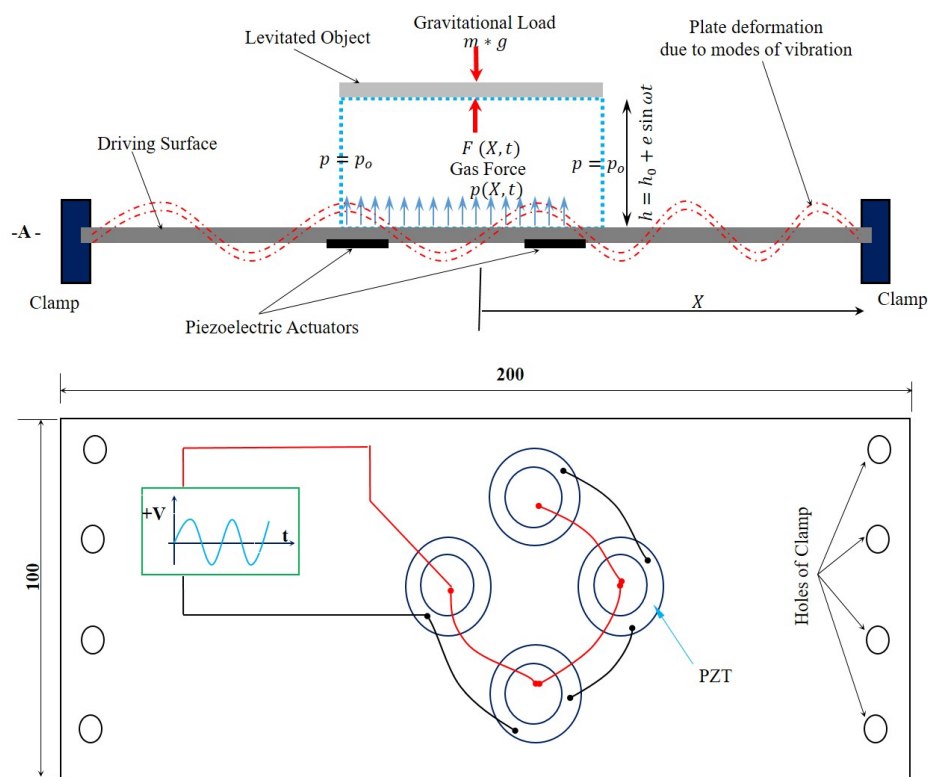


FIGURE 6.1 : A- Side view of SFL schematic design, B- Bottom view of the plate design and Sine wave voltage excitation; all dimensions in [mm].

### 6.2.2 Poisson's Ratio Plate Deformation for SFL

The SFL plate can also be deformed via a different mechanism utilising Poisson expansion/contraction ("Poisson effect"), which is not locked to resonant frequencies of vibration. Exciting a particular arrangement of piezoelectric actuators at many

cycles per second produces cyclic forces elongating the plate which in turn results in a uniaxial state of stress and formation of a dimple in the direction perpendicular to that of the applied uniaxial stress (Figure 6.3 and Figure 6.4).

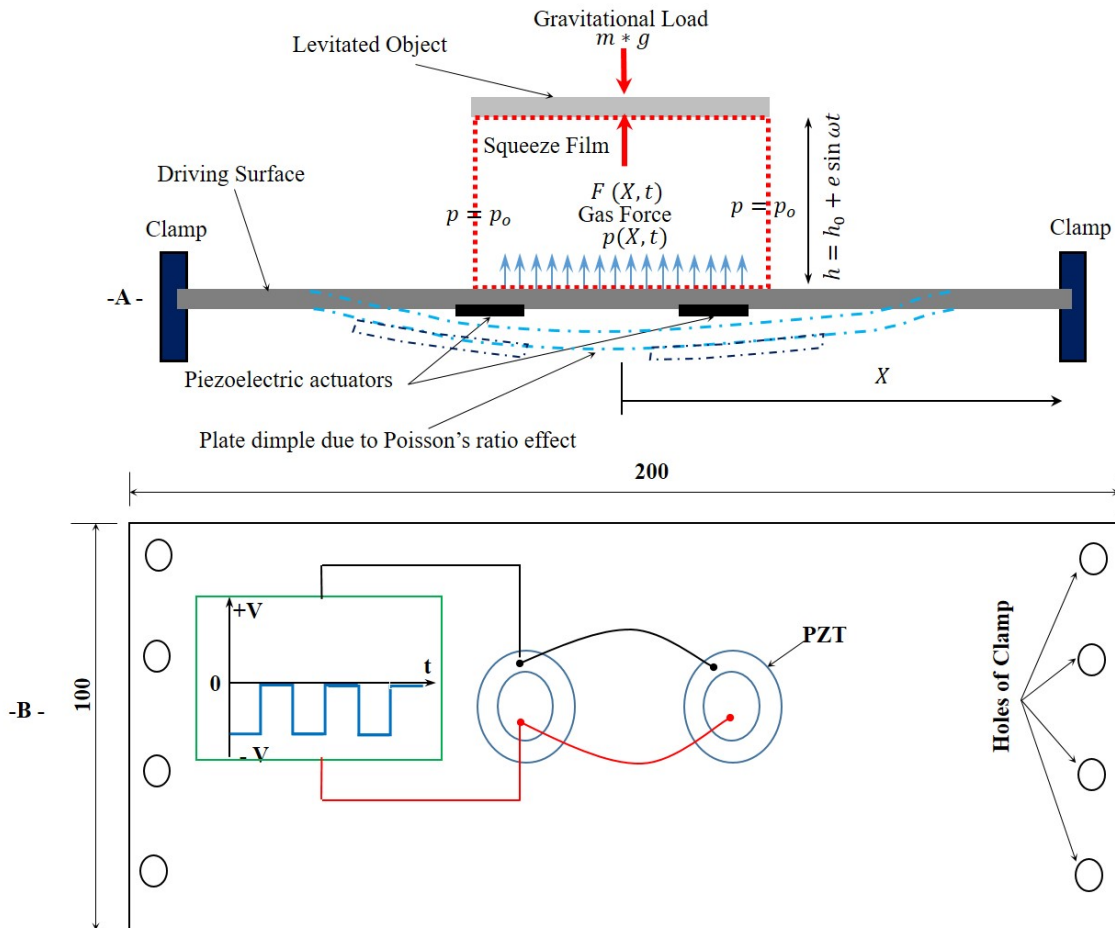


FIGURE 6.2 : A- Side view of SFL generated by oscillating dimple due to Poisson's Ratio effect, B- Bottom view of the plate design and Square wave voltage excitation; all dimensions in [mm].

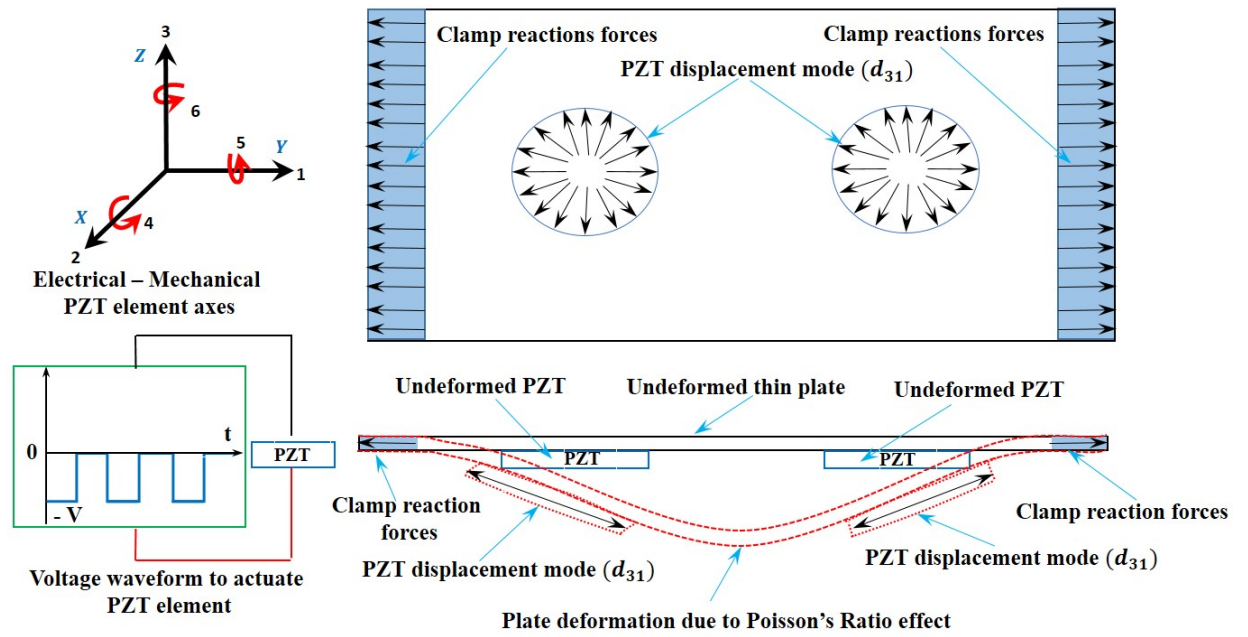


FIGURE 6.3 : Oscillating dimple due to Poisson's Ratio effect based on Square wave voltage excitation

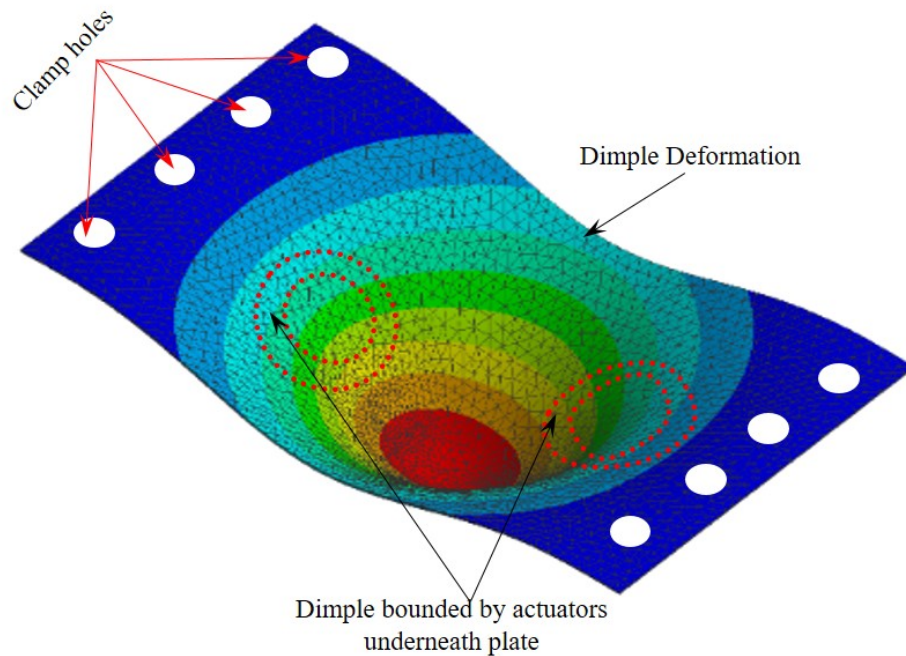


FIGURE 6.4 : Finite element analysis simulation of plate dimple due to Poisson's Ratio effect.

Pulsating with controlled frequency the dimple squeezes the air in the gap between the plate and the object, producing a sustained levitating force (Figure 6.3). In other words, this is not a conventional vibrating plate where the vibration modes deform the plate most at particular frequencies determined by plate geometry, material and boundary characteristics. Therefore, the term 'oscillation' rather than 'vibration' is used here in order to avoid confusing oscillation of forced and localised deformation due to the Poisson's effect with that of modal shapes resulting from vibration of a plate. This investigation aimed to create a repeated action of a specially shaped and localised deformation by actuating a driving surface of a thin rectangular plate using a particular arrangement of piezoelectric generators bonded to the underside of the plate. In other words, the aim is to create a repeated forced dimple deformation in a vertical direction at the centre of the plate, instead of vibrating the plate, which has been widely investigated in previous studies. It is desirable to produce the largest possible displacement at a particular oscillation frequency, as it will produce a greater levitation for objects placed on the plate. Accordingly, different plate materials and sizes are theoretically and experimentally examined in this section. The simulation and measurement procedures for analysing the floating designs will be explained in this section. First, a theoretical method of modelling the forced plate design, including the static and dynamic analyses, is presented and executed using the finite element method (ANSYS Workbench). Second, a theoretical method for modelling floating items and calculating their dynamic levitation height as well as the pressure distribution, using computational fluid dynamic (ANSYS Workbench), is illustrated. Moreover, the method of measurement work for the floating designs is explained.



### 6.2.3 Forced Plate Design and Statement of the Problem

The geometry and main dimensions of the forced plate design are shown in Figure 6.5. Various plate sizes and materials (Table 6.1) have been theoretically and experimentally investigated. A structural design that has been studied comprises a freely suspended flat object lifted as a result of the boosted average pressure created by an actuated surface. It includes a flat plate and two single layer of hard piezoelectric actuators (PZTs) bonded to the underside the plate (Figure 6.5). The actuators utilised were of rounded shape with 35 mm diameter and 0.8 mm thickness and were bonded to the underside of a plate. The plate is firmly fixed at both ends, as shown in Figure 6.5 and can be deformed repeatedly to create a dimple shape or a concave form in the downward direction at the centre of the driving surface (carrier surface). The deformation can be effected by many mechanical and electrical parameters. The most significant factor is the Poisson's ratio that stems from the repeated process of expansion and contraction of the attached piezoelectric actuators on the underside of the carrier surface (thin rectangular plate will be used in this study) when the actuators are driven by a signal of DC (offset voltage) and AC voltage (amplitude voltage).

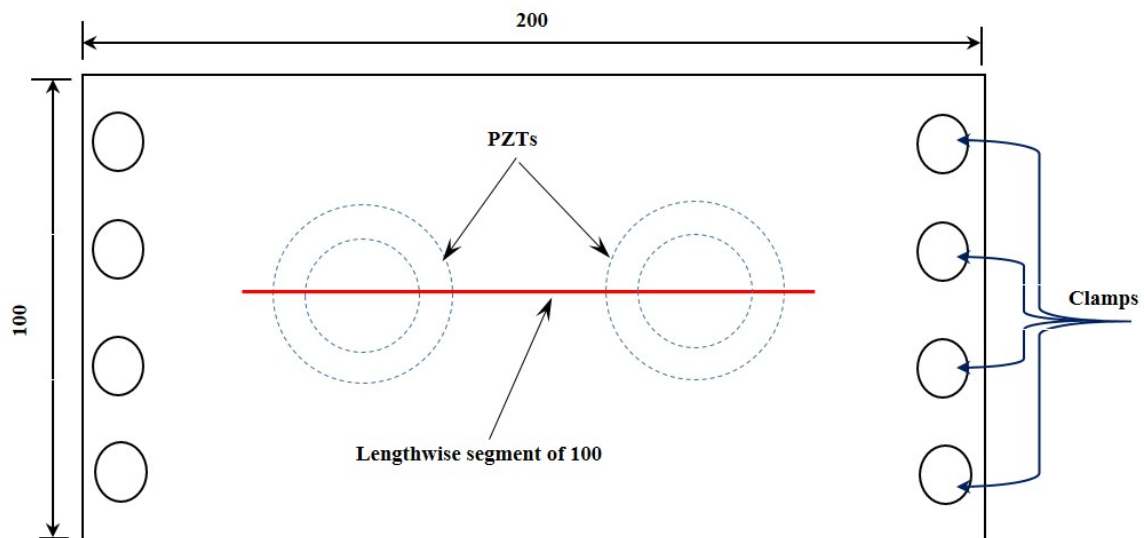


FIGURE 6.5 : Top view of the plate design and lengthwise segment; all dimensions in mm.

TABLE 6.1 : Plates design configurations (Callister Jr and Rethwisch, 2012).

Design No.	Plate size <i>mm</i>	Material	Modulus of Elasticity <i>GPa</i>	Density <i>kg/m<sup>3</sup></i>	Poisson's Ratio
A1	200*100*0.5				
A2	200*100*1	Aluminium	69	2676	0.33
A3	200*100*2				
B	200*100*0.5	Stainless Steel	193	7781	0.33
C	200*100*2	Polyethylene (HDPE)	1.08	970	0.46

#### 6.2.4 Finite Element Modelling (FEM)

A simulation for the forced plate designs (rectangular plate plus two PZTs) was carried out using the ANSYS Workbench transient structural analysis. Commands were written using a trigonometric equation (square wave equation) and implementing them with ANSYS mechanical APDL, and finally exporting them into ANSYS workbench. The purpose of this was to actuate the PZTs with an On/Off time (Figure 6.6) to make a central area of plate design deforming as a dimple in a downward direction or as a concave form. The time step used in ANSYS transient structural analysis simulation is the same as that used in the experimental test, which is 625 microseconds.

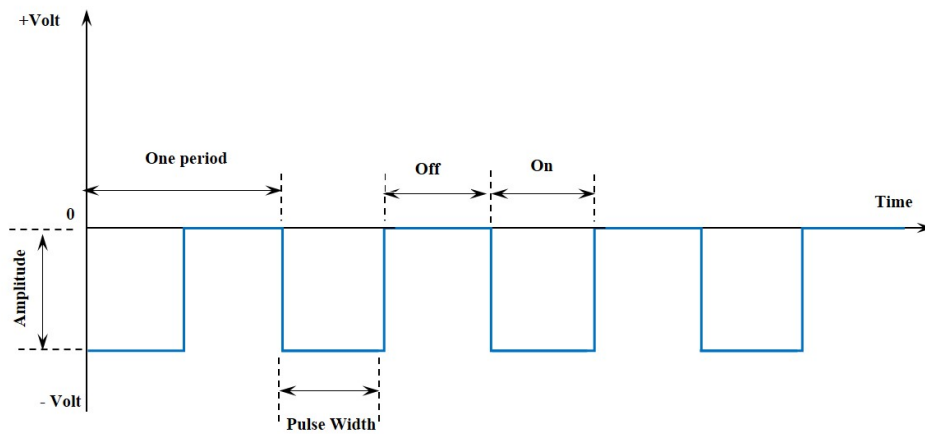


FIGURE 6.6 : Square wave voltage signal to drive the PZTs.

A forced plate design has been simulated throughout the finite element ANSYS workbench. The design consists of a thin flat plate and two rounded piezoelectric actuators type PZT4 bonded to the underside the plate to work as actuators when driven by a voltage. In this study, static and dynamic (transient) analyses have been carried out for various plate designs. The purpose of the static analysis was to calculate the static deformation and to recognise the deformed shape of the plate designs when the piezoelectric actuators are operating a with a DC voltage only. The aim of the dynamic analysis was to calculate the dynamic response of the plate by powering the piezoelectric actuators by an AC voltage. A square wave voltage signal (Figure 6.6) has been executed to drive the actuators that will lead to a dynamic reaction on the plate designs. The purpose of driving the actuators by the square wave amplitude of voltage is to create repeated contraction and elongation of the actuators. In other words, the signal can be used to excite the actuators as a switching on and off. Consequently, the plate will be influenced by that action of mechanical behaviour to generate a repetitive pocket or dimple shaped deformation in the downward direction at the central area of the plate designs. Therefore, it can be said that Poisson's effect has been taking place within the plate. The key aim of this process is to avoid the vibration of the plate design and also to gain a high deformation from the plate design, leading to an enhanced levitation for a load placed

on the plate. The piezoelectric actuator has been modelled with a SOLID227 element, because this has 10 nodes with up to five degrees of freedom per node (UX, UY, UZ, VOLT and TEMP). The structural capabilities include elasticity, plasticity and large strain. It is a coupled-field element and is suitable for three dimensional (3-D) analyses as well as being capable of modelling the piezoelectric actuator. The element of SOLID187 was chosen to mesh the plate. It is a higher order 3-D, with 10 node having three degrees of freedom at each node (translations in the nodal x, y, and z directions). Furthermore, piezoelectric elasticity stiffness and stress matrices have been included in the simulation throughout using Piezo ACT (ANSYS Customization Toolkit) extension. The finite element model (Figure 6.7) and boundary conditions of the forced plate design (Figure 6.5) are presented and the material properties are itemised (Table 6.1). The plate has been modelled with three different materials: aluminium, stainless steel and a polymer (HDPE). In addition, various sizes of plates have been simulated (Table 6.1). The boundary conditions that are implemented in the cases of the current study are fixed boundaries on the both ends of the plate and 150 V difference on each side of the actuators. The finite element mesh for one of the forced plate designs (Design A1) is shown in Figure 6.7. The piezoelectric elasticity stiffness matrix  $[c]N/m^2$  and stress matrix  $[e]C/m^2$  that have been utilised in the simulation as follows:

$$[c] = 10^{10} \star \begin{bmatrix} 13.2 & 7.3 & 7.1 & 0 & 0 & 0 \\ 7.3 & 11.5 & 7.3 & 0 & 0 & 0 \\ 7.1 & 7.3 & 13.2 & 0 & 0 & 0 \\ 0 & 0 & 0 & 2.6 & 0 & 0 \\ 0 & 0 & 0 & 0 & 2.6 & 0 \\ 0 & 0 & 0 & 0 & 0 & 2.6 \end{bmatrix} \quad [e] = \begin{bmatrix} 0 & -4.1 & 0 \\ 0 & 14.1 & 0 \\ 0 & -4.1 & 0 \\ 10.5 & 0 & 0 \\ 0 & 0 & 10.5 \\ 0 & 0 & 0 \end{bmatrix}$$

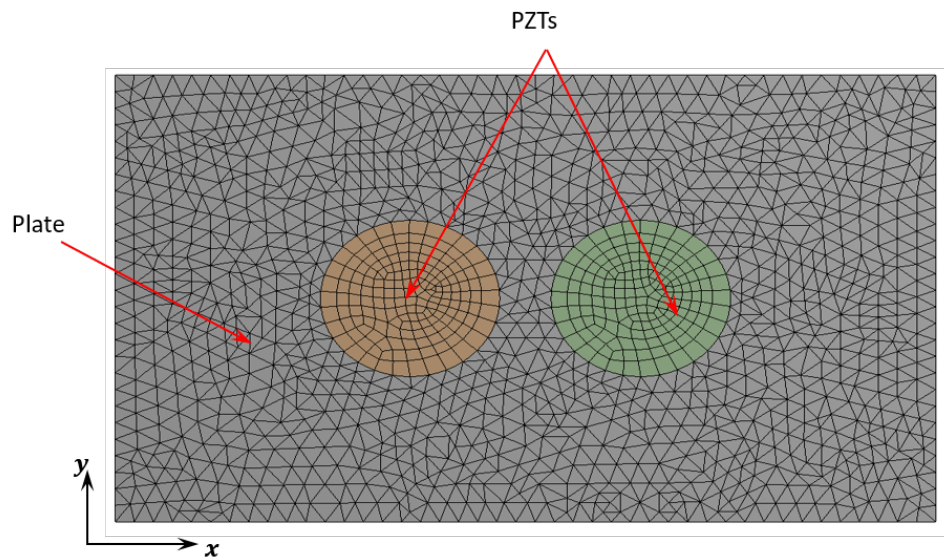


FIGURE 6.7 : Mesh of a forced plate (Design A1), bottom view.

## 6.2.5 Dynamic Analysis

### Structural Dynamics

The function of the dynamic analysis (transient) is to identify the dynamic characteristics of a structure exposed to dynamic driving loads. In this prototype design, the dynamic driving forces stem from the piezoelectric actuators when they are powered by an AC voltage. This is in order to produce sufficient displacement or to realise maximum dynamic reaction and thus, a better levitation can be achieved.

### Squeeze-Film Levitation Modelling

An air film (clearance) that is squeezed between the two surfaces with relative displacement of amplitude ( $e$ ) at a frequency ( $\omega$ ), in the direction of the air film thickness, is proposed (Figure 6.8). The pressure  $p$  at a point in the air-layer is controlled by the Reynolds equation (Langlois, 1962). So the analysis of the squeeze-film dynamics is combined with the Reynolds equation which describes pressure within the air film and the equation of motion which governs the levitated item movement. The Reynolds equation can be expressed in general form as specified by Yoshimoto,

Kobayashi, and Miyatake, 2007; Hamrock, Schmid, and Jacobson, 2004.

$$\frac{\partial}{\partial x} \left( \frac{\rho h^3}{12\mu} \frac{\partial p}{\partial x} \right) + \frac{\partial}{\partial y} \left( \frac{\rho h^3}{12\mu} \frac{\partial p}{\partial y} \right) = \frac{\partial}{\partial x} \left( \frac{\rho h (u_x + u'_x)}{2} \right) + \frac{\partial}{\partial y} \left( \frac{\rho h (u_y + u'_y)}{2} \right) + \frac{\partial (\rho h)}{\partial t} \quad (6.1)$$

Where,  $\rho$  is the air density,  $h$  is the squeeze-film height and  $\mu$  is the fluid viscosity,  $t$  is time. The time dependent term  $\frac{\partial(\rho h)}{\partial t}$  is identified as the “squeeze term” as it signifies squeezing movement of the fluid. In addition,  $u_x, u_y$  and  $u'_x, u'_y$  refer to surface velocity components of bottom and top surfaces in  $x$  and  $y$  direction, respectively. Appendix C shows the SFL force derivation based on Reynolds equation. Langlois, 1962, introduced a perturbation factor for pressure of the order of  $\epsilon$  into the Reynolds equation and obtained the squeeze-film force which represents the one that develops as a result of the pressure variations (squeeze-film pressure and ambient pressure) for a given instant of time.

$$\frac{\partial}{\partial R} \left( R H^3 P \frac{\partial P}{\partial R} \right) = R \sigma \frac{\partial P H}{\partial T} \quad (6.2)$$

The boundary conditions of squeeze-film for circular plates are assumed as

$$P(R, T = 0) = 1 \quad (6.3)$$

The initial pressure between discs is atmospheric. At the outer periphery,

$$P(R = 1, T) = 1 \quad (6.4)$$

$$\sigma = 12\mu R_o^2 \omega / p_o h_o^2 \quad (6.5)$$

Where,  $\sigma$  is the squeeze number. In order to explore the dynamic of squeeze-film approach, it is essential to take into consideration the coupled dynamics of the entire system (fluid and structural domains), which comprises the Reynolds equation and the equation of motion utilising a force equilibrium. Based on the free diagrams

(Figure 6.8-B) the equation of motion can be expressed as;

$$m \frac{d^2 z_t}{dt^2} = F_f - F_m \quad (6.6)$$

$$F_f = \iint (p_i - p_o) r dr d\theta \quad (6.7)$$

$$F_m = mg \quad (6.8)$$

$F_f$  represents the fluid flow force which is evolved as a result of pressure variation and  $F_m$  is the weight of the top surface (circular plate) as employed in the simulation. The following expressions  $z = h_o Z$ ,  $p = p_o P$  and  $\tau = t\omega$  can be used to dimensionless equation (6.5). where,  $h_o$  is initial clearance,  $p_o$  is an ambient pressure,  $\omega$  is an angular velocity of vibration.

$$\frac{d^2 Z}{d\tau^2} = \frac{p_o r_o^2}{m h_o \omega^2} \iint (P_j - 1) R dR d\theta - \frac{mg}{m h_o \omega^2} \quad (6.9)$$

$$z_t = z_l + h \quad (6.10)$$

Through derivation equation (6.10) twice in respect of time yields;

$$\frac{d^2 z_t}{dt^2} = \frac{d^2 z_l}{dt^2} + \frac{d^2 h}{dt^2} \quad (6.11)$$

The levitating height  $z_l$  in terms of motion source can be represented by  $z_l = Z_o \sin \tau$ , thus;

$$\frac{d^2 z_l}{dt^2} = -\omega^2 Z_o \sin \tau \quad (6.12)$$

Equation (6.12) can be rewritten in normalized form as;

$$\frac{d^2 Z}{d\tau^2} = -\omega^2 Z_o \sin \tau + \frac{d^2 H}{d\tau^2} \quad (6.13)$$

By substituting equation (6.13) into equation (6.9) will produce the following expression;

$$-\omega^2 Z_o \sin \tau + \frac{d^2 H}{d\tau^2} = \frac{p_o r_o^2}{m h_o \omega^2} \iint (P_j - 1) R dR d\theta - \frac{m g}{m h_o \omega^2} \quad \text{or} \quad (6.14)$$

$$\frac{d^2 H}{d\tau^2} = \frac{p_o r_o^2}{m h_o \omega^2} \iint (P_j - 1) R dR d\theta + \omega^2 Z_o \sin \tau - \frac{m g}{m h_o \omega^2}$$

Equation (6.14) is a second-order non-linear partial differential equation and its initial conditions ( $t = 0$ ) are given as  $dH/dT = 0$  and  $P_n = 1$ .

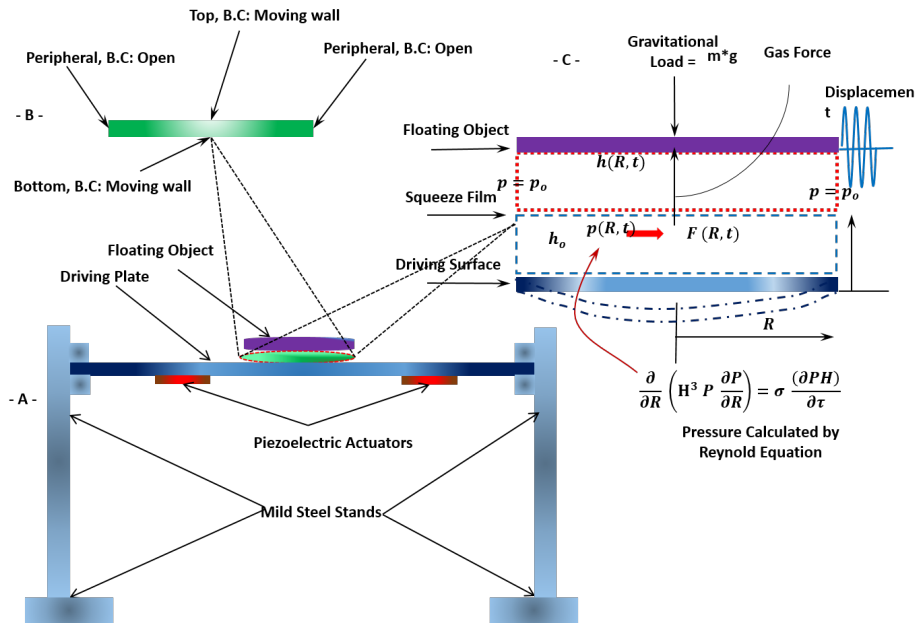


FIGURE 6.8 : Schematic design of the OAPL (SFL); A- Rig design; B- Air film modelling (ANSYS-CFX); C-Design free body diagram.

To understand the floating performance based on the behaviour of squeeze-film, the equation of motion in addition to the Reynold's equation needs to be joined and solved by means of numerical estimation (Minikes and Bucher, 2003; Stolarski and Chai, 2006). The non-dimensional Reynolds equation can be modified into the dimensions (2-D) through proposing the pressure is constant in the Y direction. Newton's Second Law can be applied to represent the equation of motion for the floating surface (Stolarski and Chai, 2006). The levitation force produced through the squeeze film influence must be greater than the levitating load, which indicates its self-weight in order to float the object successfully. The non-contact separation



performance of the design of the forced plate can be inspected depending on the equation of motion coupled to the Reynolds equation with state boundary conditions (B.Cs). Consequently, the performance of the proposed squeeze-film of the forced plate design can be evaluated.

### **Squeeze-Film Action**

An influence of squeeze-film levitation can be generated when an air-layer is entrapped between the two relative displacement surfaces. In fact, average pressure and resulting load carrying capacity that is produced by the cyclic displacement at the layer lead to the production of a complete float for a lightweight object (Figure 6.8-A). In addition, the displacement that is advanced between the surfaces will lead to a rise in the air – film pressure greater than the ambient pressure, which is essential for lifting the object effectively. It is worth mentioning that, the load carrying force can be introduced as a result of layer equilibrium, which is accomplished by a balance between compressibility and viscous forces since the viscous stream cannot not immediately be squeezed (Langlois, 1962; Salbu, 1964). When inertia and the tensional stresses in the fluid are negligible, the Reynolds equation is the main non-linear partial differential equation that defines the pressure distribution in the squeezed air-layer and can be evaluated through the Navier–Stokes and continuity equations. Furthermore, two important, instantaneous and recurrent steps are behind the pressure distribution in the squeezed air–film, which stem from the influence of the boundaries on the flow cycle. Hence, throughout the compression stage, the development in pressure forms an outward flow, while simultaneously, the air-layer between the surfaces reduces, letting only a slight airstream to occur. In contrast, during the decompression period, the pressure falls and the stream alters to begin an inward flow. At this stage, the air-gap rises, letting a superior flow quantity pass in at a slow velocity (Langlois, 1962).

### Model of Squeeze Air-Film in ANSYS CFX

A simulation utilising ANSYS CFD is implemented to examine the performance of a levitated object (freely suspended rigid mass). It is assumed that only one degree of freedom (1-DOF) in the vertical direction is simulated. The instantaneous position of the object is evaluated by the balancing its inertia, the fluid flow force made by pressure distribution and gravity. An air-film that exists between a lightweight object (5 g disc) and a flat, rectangular plate (Figure 6.8) of various designs is simulated. In other words, different case studies are implemented to identify the factors that affect the floating performance. The air film is of thickness ( $20 \mu\text{m}$ ) and it has the same area as the disc (35 mm, diameter) (Figure 6.8-B). Three boundary conditions (named as Top, Bottom and Side) have been used to model the semi-cylindrical shape of the air-layer and to analyse the squeeze film levitation (Figure 6.9). The top boundary condition refers to the bottom surface of the floating object and also represents the mass of the object, which is (5 g). The bottom boundary condition denotes the top surface of the moving plate design and also indicates the bottom plane of the air-layer that it has been modelled as a deformed boundary. It is given an amplitude (displacement) acquired from the forced plate designs that will squeeze the air-layer in the normal direction (Figure 6.10). Finally, the Side boundary condition has been modelled on the periphery of the air-layer as an open boundary, so the flow in this boundary will not be restricted to the stream direction. In other words, the pressure value is identified (atmospheric pressure), but the direction of flow is unknown, see figure 6.8-C and figure 6.9.

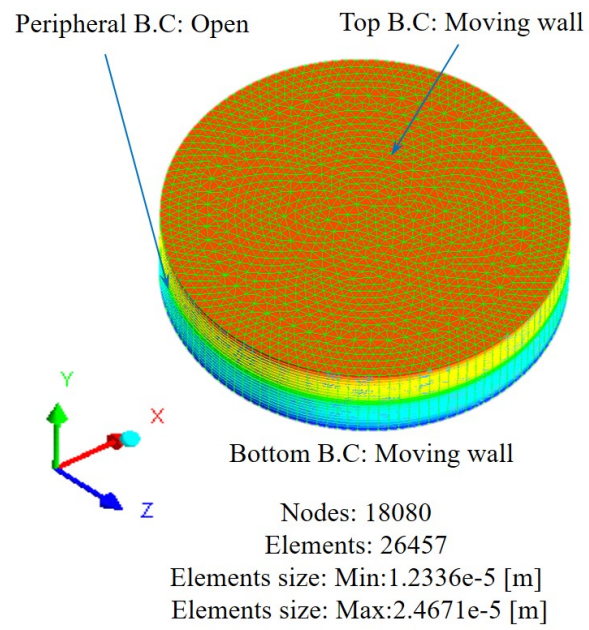


FIGURE 6.9 : Squeeze film Modelling with ANSYS-CFD.

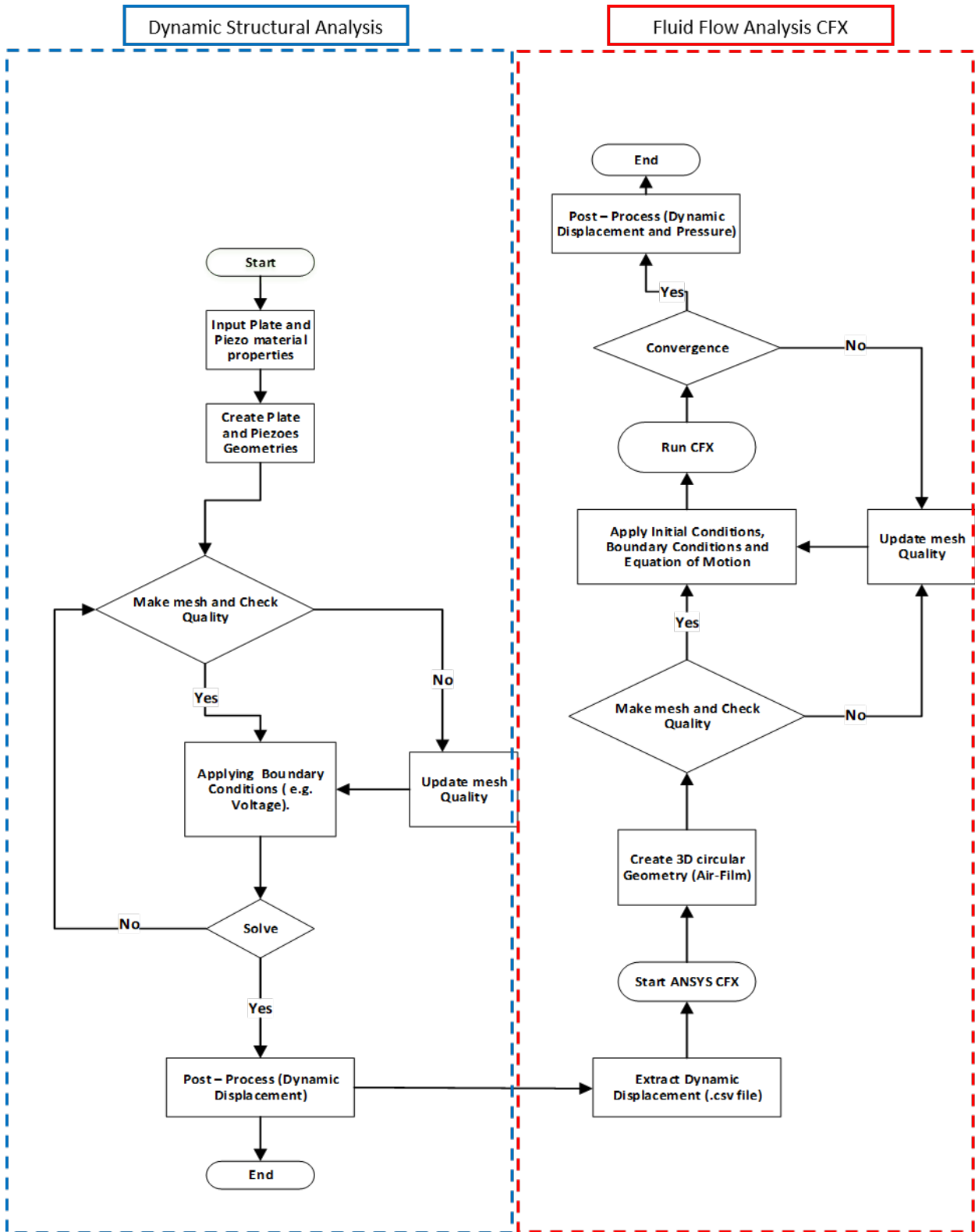


FIGURE 6.10 : Theoretical method flowchart.

## 6.3 Experimental Method

### 6.3.1 Configuration Study

The experimental set-up for the static and dynamic responses is shown in Figure 6.11 -Figure 6.13. The piezoelectric actuators of type PZT-4 are bonded to the bottom of the plate. Piezoelectric actuators, produce a repeated dimple shaped deformation in a downward direction at the central area of the plate design. The aim of this is to induce the squeeze of the air that is entrapped between the plate and the floating object (disc of 5 [g]). Piezoelectric actuators are connected in parallel and their displacement is calculated by the entire capacitances and corresponding inductances. The experimental set-up is shown in Figure 6.11 and comprises of an oscilloscope, DC power supply, AC power supply amplifier, signal generator, laser sensor, plate design rig and piezoelectric actuators. The experiment requires the signal generator to create a regular or arbitrary single voltage. In this study a square form of signal voltage has been employed. The output terminal of the signal generator is connected to the amplifier of type ENP-1-1U (Echo Electronics) and is essential to increase the voltage input from the signal generator. The performance factors of the amplifier are listed in Table (6.2). It can offer a stable 15 magnification for the AC and DC signal inputs. Its operational point can be regulated to gain the appropriate bandwidth for the experimental measurements. The oscilloscope is used in this work to read and display the output signals of the signal generator and the amplifier. The laser triangulation sensor from the Micro-Epsilon Company of type ILD-2300-5 is vertically placed above the plate design. So as to achieve sufficiently accurate measurements from the laser sensor, it has been justified according to the guide setting provided from the company. The sensor captures the static and dynamic deformation of the plate design plus the levitation distance of the floating object (disc of 5 g) without any contact and the output measurements data from it can be displayed on a computer through installing the laser sensor software. The software has more flexibility regarding manipulating the output data. For example, it can capture the

entire output data without averaging, whilst having the ability to view the average estimated data. The goals of the experimental measurements are to observe the dynamic response of the designs and the floating performance. Additionally, the aim is to validate the static and dynamic deformations, which are calculated from the theory of the coupled-field analysis. Moreover, in order to avoid sideways movement of the floating object (disc) (Stolarski and Chai, 2006) and also to measure the normal separation, the disc has been placed inside a suspended metal ring of inner diameter larger than the disc diameter by of 5 mm, (Figure 6.12). Four thin cords are stretched parallel to the ring and connected to a fixed support such that there is no contact between the ring and the plate design. In this way, the disc will only lift inside the ring in a normal direction (1-DOF) when the plate design is driven.

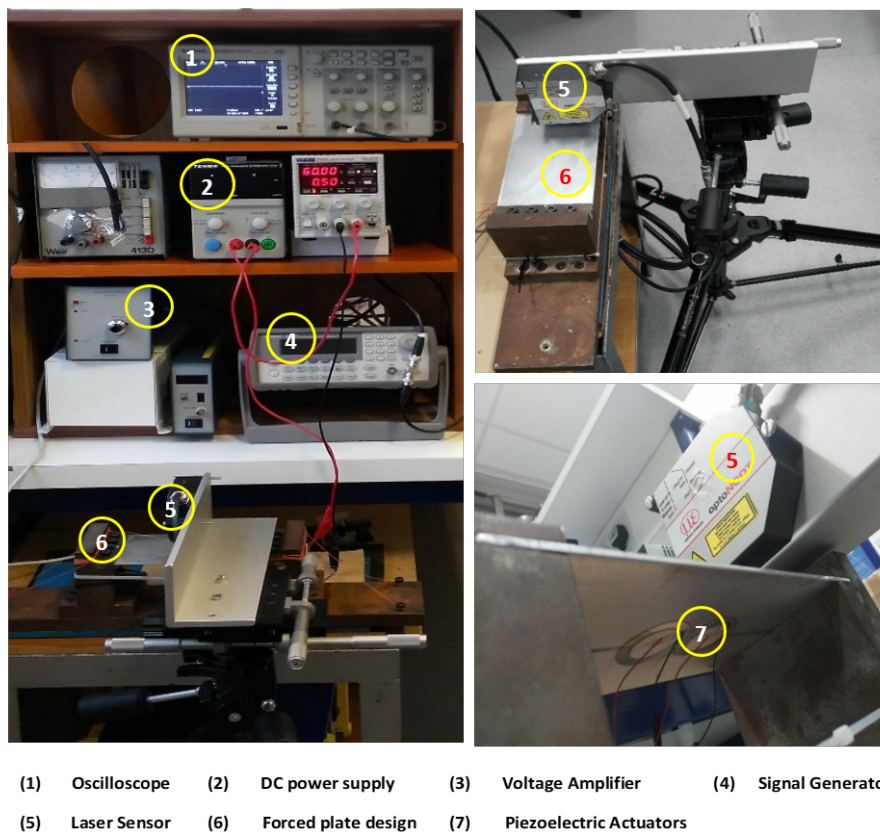


FIGURE 6.11 : Experimental devices used for the measurements.

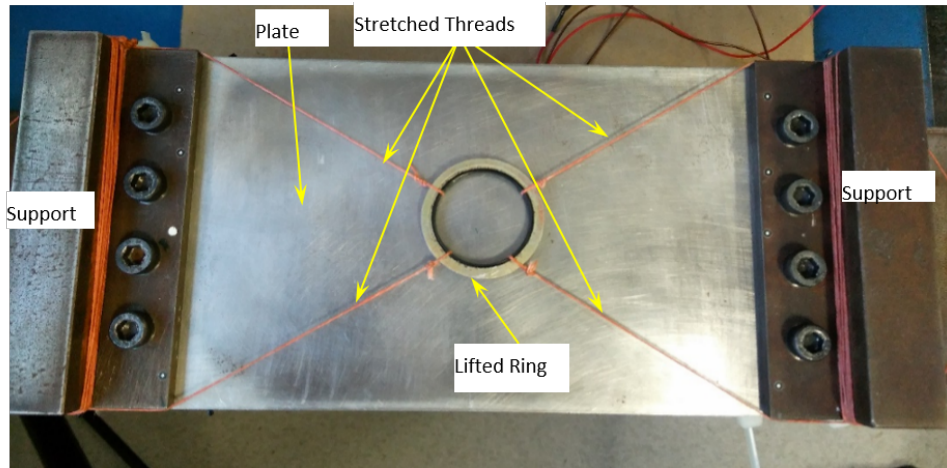


FIGURE 6.12 : Top view for floating design with lifted metal ring.

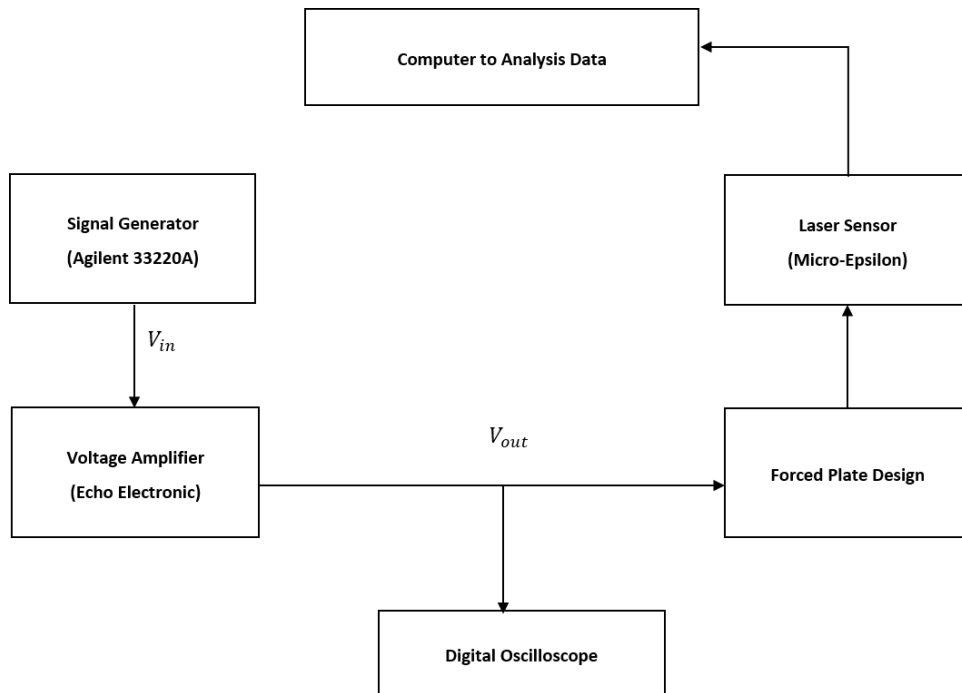


FIGURE 6.13 : Layout of the measurement work.

TABLE 6.2 : AC voltage amplifier specifications.

Performance index	Range
Max. Output voltage	0 – 150 V
Max. Output current	1 A
Bandwidth	DC : 10 kHz
Internal impedance	100 k $\Omega$
Magnification	25 dB (15 times)
Stability with time	$1 \cdot 10^{-4}$ /h
Size	103*124*220 mm
(W * H * L)Weight	4.5 kg

The PZTs, theoretically and experimentally, are excited by an amplitude of square wave voltage (Figure 6.6). The reason for doing so, is firstly to actuate the PZTs with an alternating voltage amplitude, i.e. having an On / Off period of time and secondly, this cyclical action will produce a mechanical behaviour of expansion and contraction for the PZTs. In other words, the forced plate design with that type of excitation can reveal the Poisson's ratio effect. As a result, this can create a time-dependent recurrent deformation at the central area of the plate design in downward direction. Hence, that mode of deformation will lead to levitation of an object placed on the plate without causing vibration of the plate.

## 6.4 Results and Discussion

In this section, the static and dynamic behaviour for the forced plate designs is presented and discussed. Simulations of one of the plate designs (Design A1), which show contour plots for the static and dynamic deformations respectively, are presented in (Figure 6.14) and Figure 6.15). Static and dynamic deformations for a lengthwise segment (Figure 6.16-Figure 6.25) on the central area of the top surface



of the plate have been investigated, theoretically, using ANSYS Workbench and also measured experimentally (Figure 6.16–Figure 6.28) for all five designs (Table 6.1).

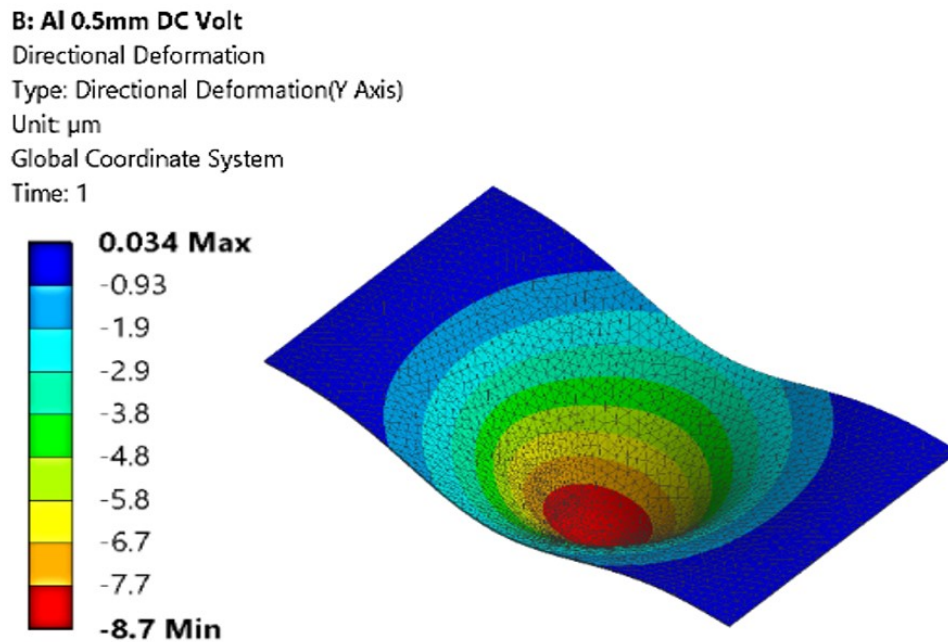


FIGURE 6.14 : Static deformation (Design A1).

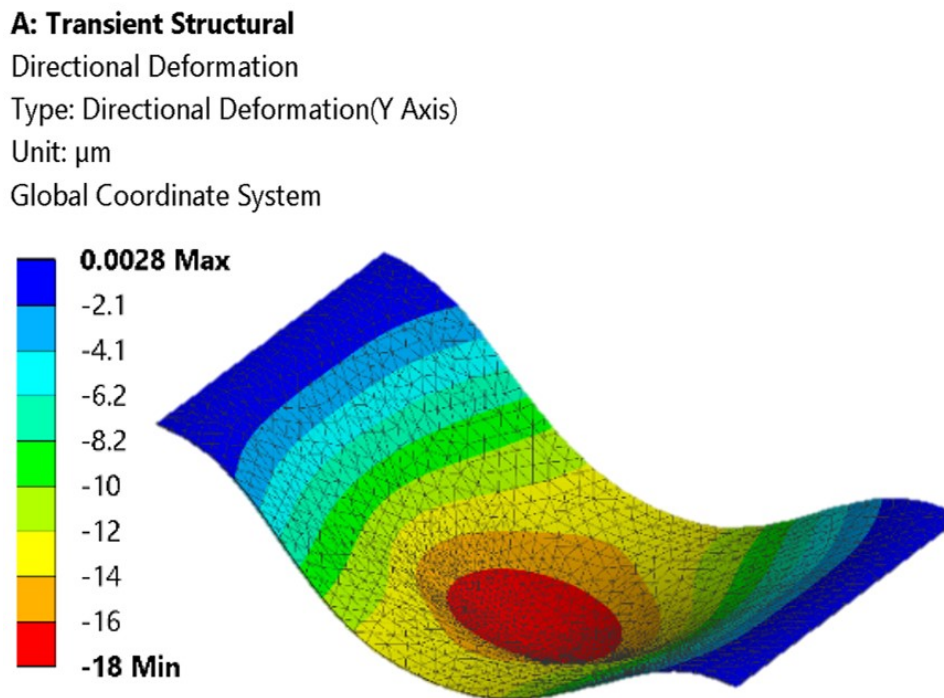


FIGURE 6.15 : Dynamic deformation (Design A1).

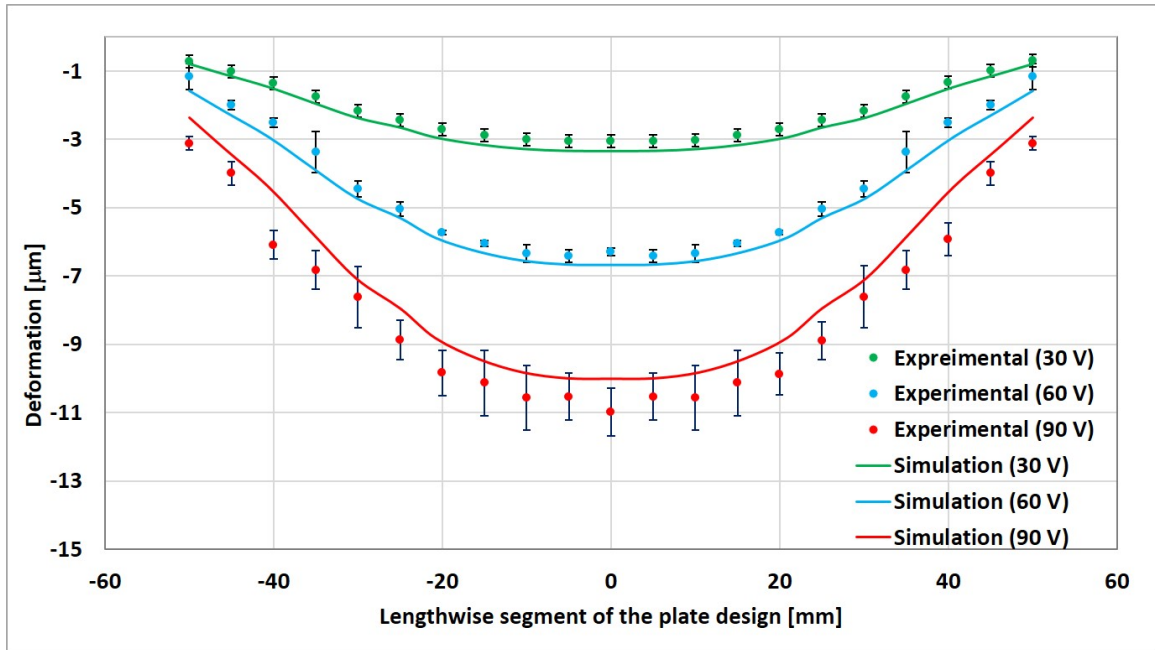


FIGURE 6.16 : Measurement and simulation of static deformation (Design A1).

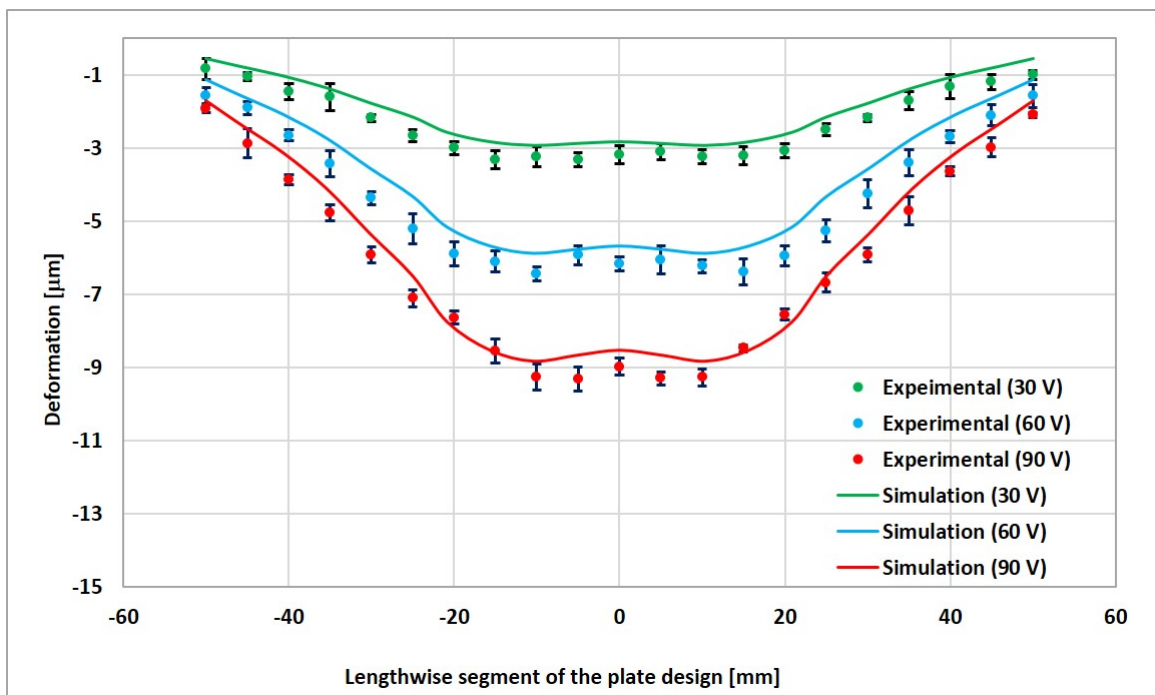


FIGURE 6.17 : Measurement and simulation of static deformation (Design A2).

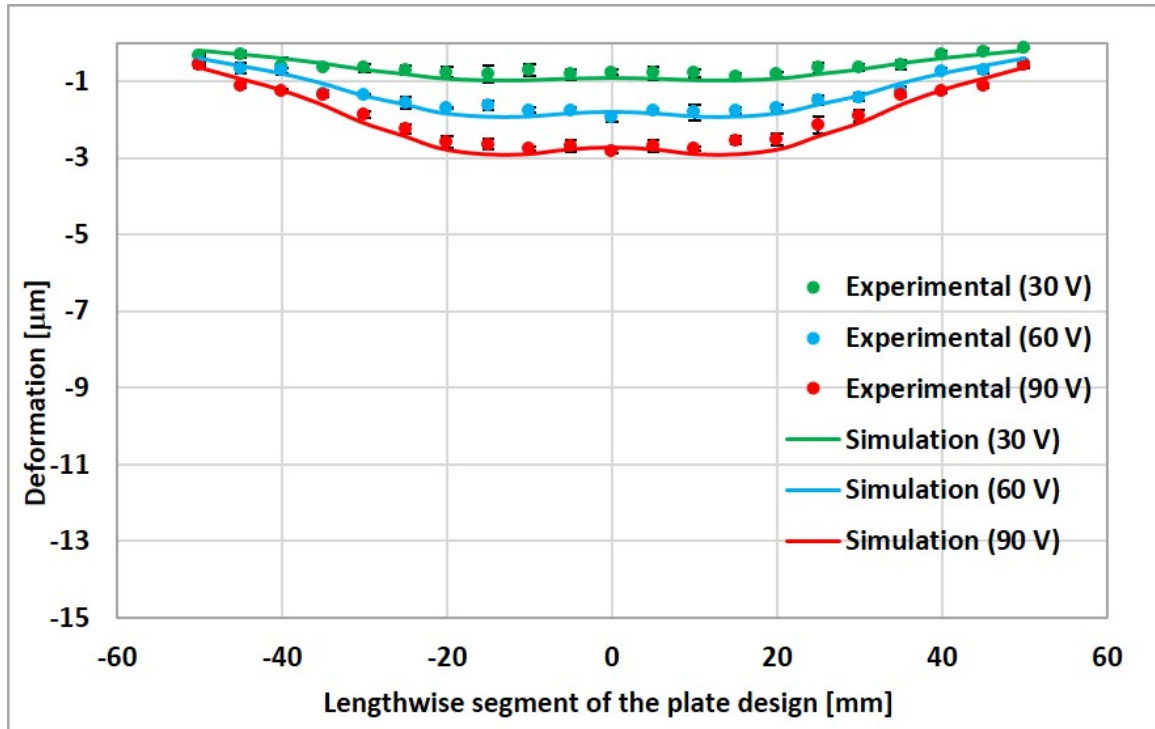


FIGURE 6.18 : Measurement and simulation of static deformation (Design A3).

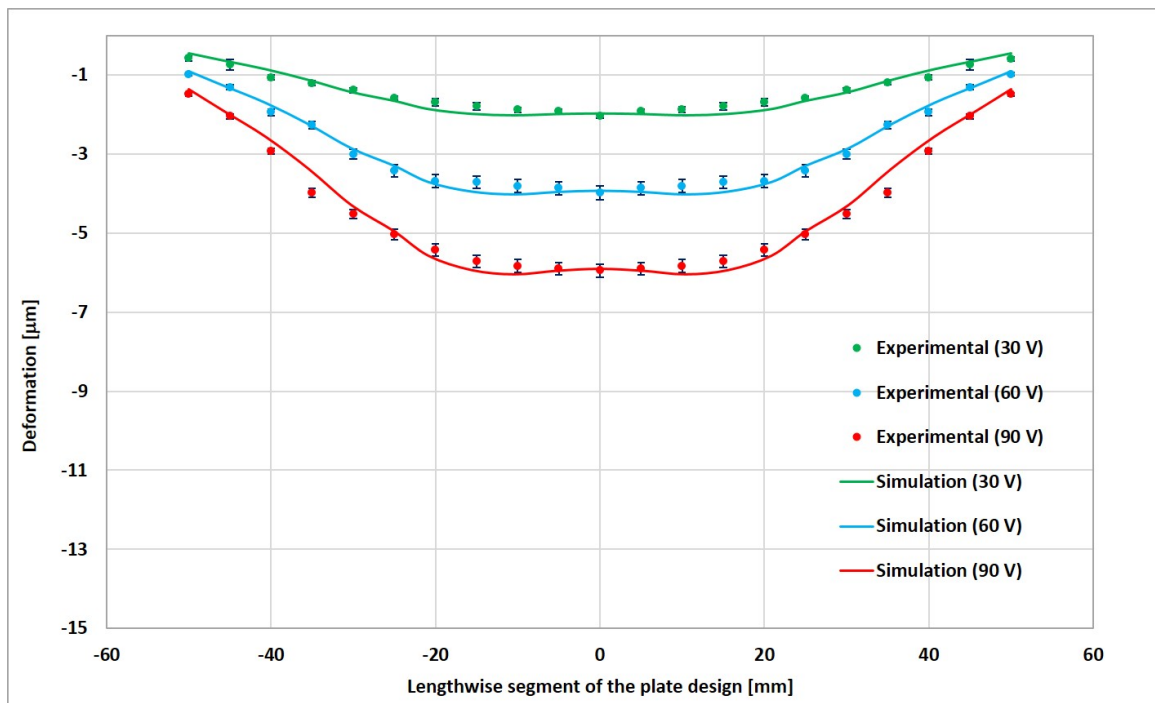


FIGURE 6.19 : Measurement and simulation of static deformation (Design B).

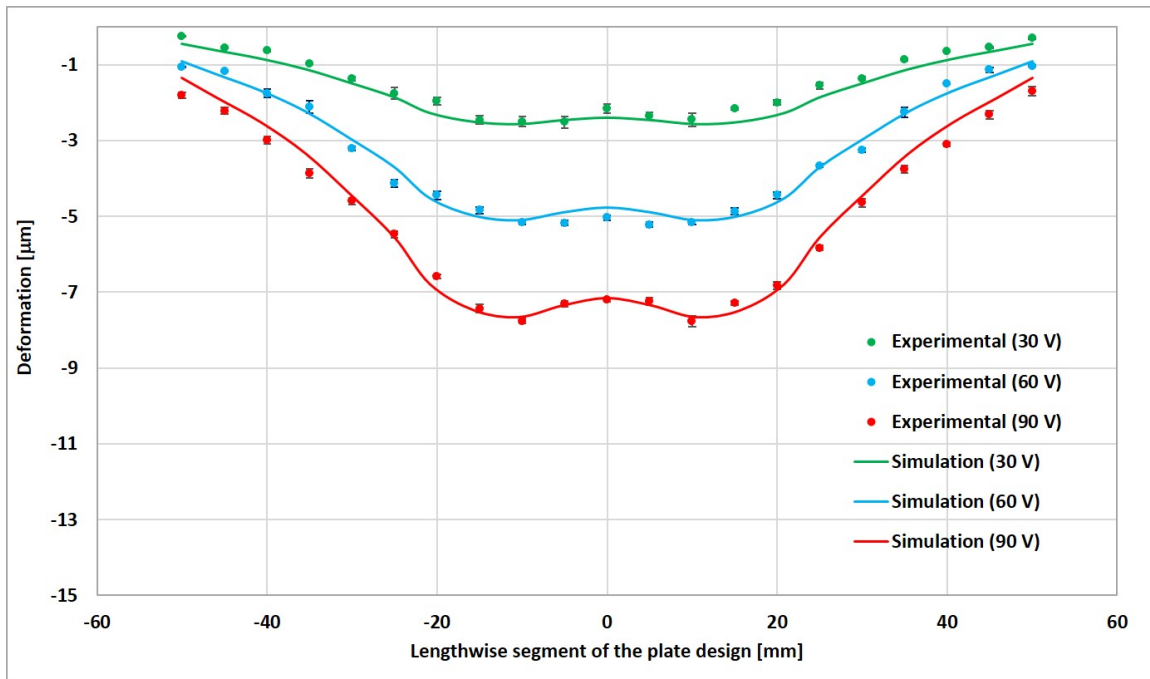


FIGURE 6.20 : Measurement and simulation of static deformation (Design C).

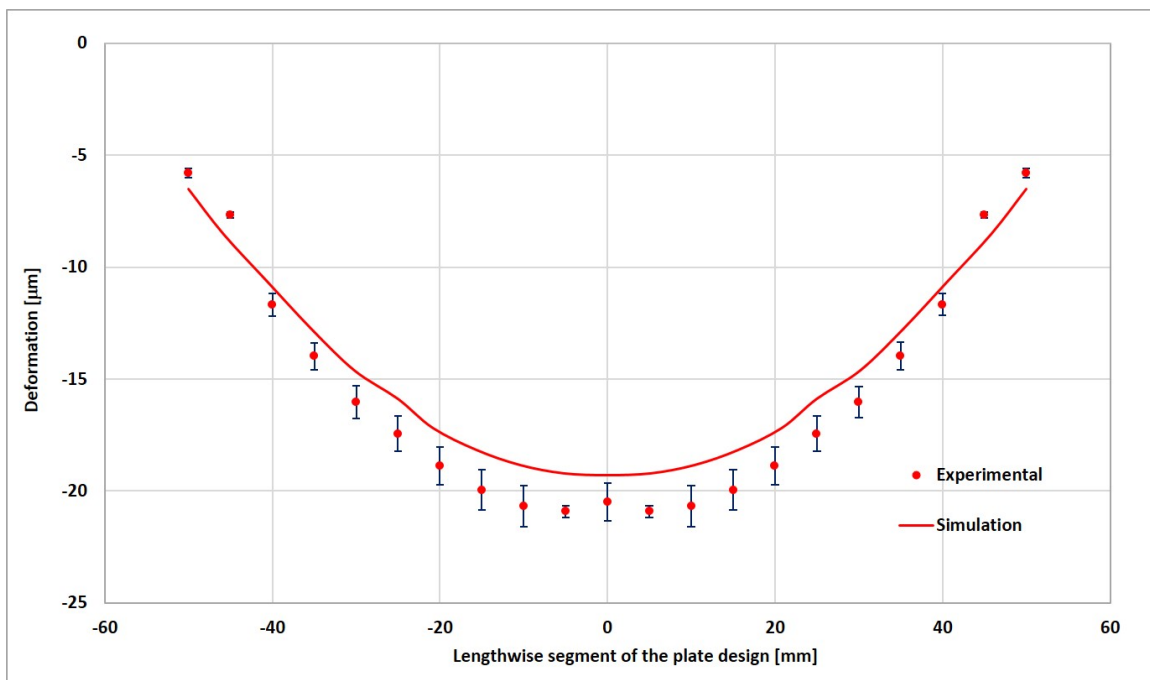


FIGURE 6.21 : Measurement and simulation of dynamic deformation (Design A1).

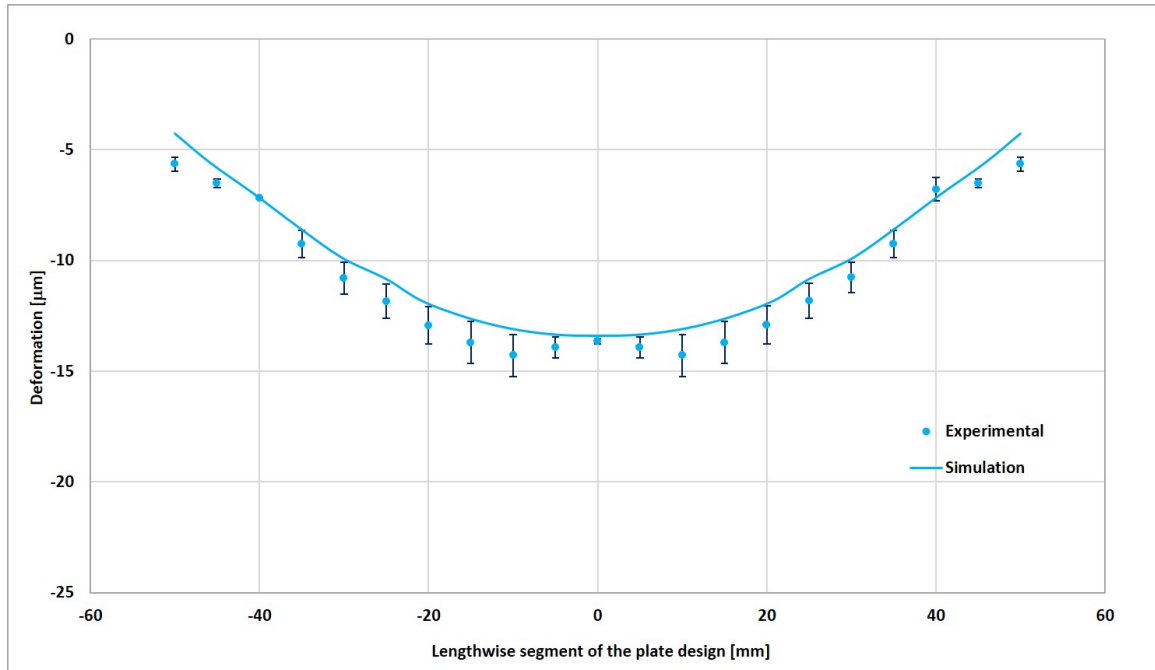


FIGURE 6.22 : Measurement and simulation of dynamic deformation (Design A2).

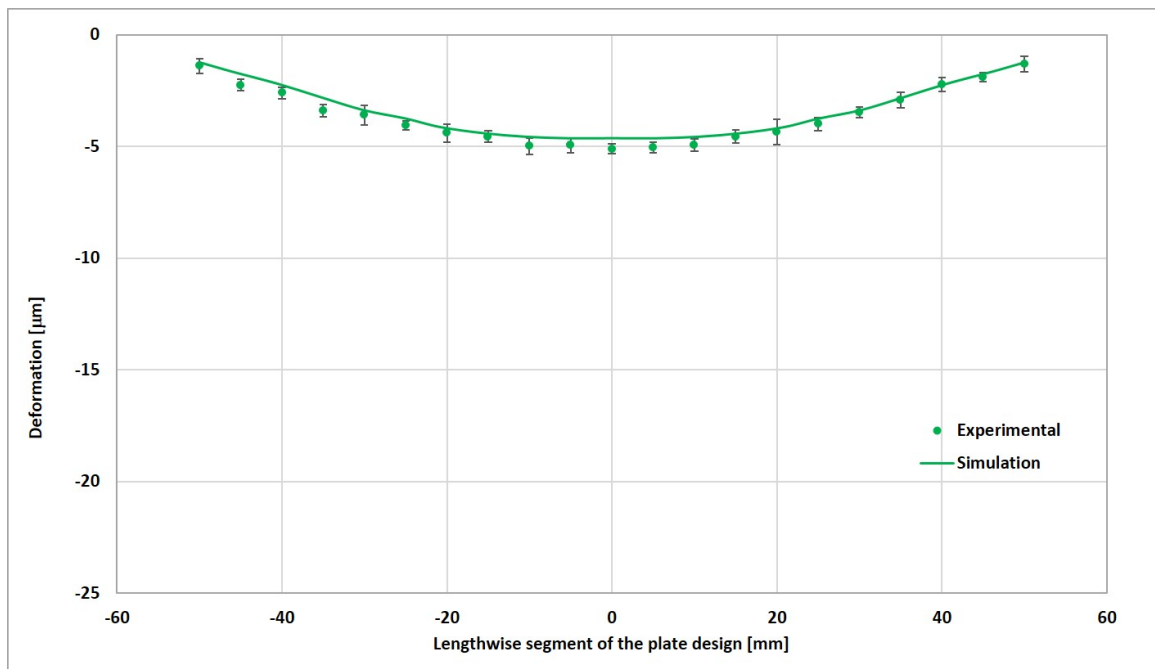


FIGURE 6.23 : Measurement and simulation of dynamic deformation (Design A3).

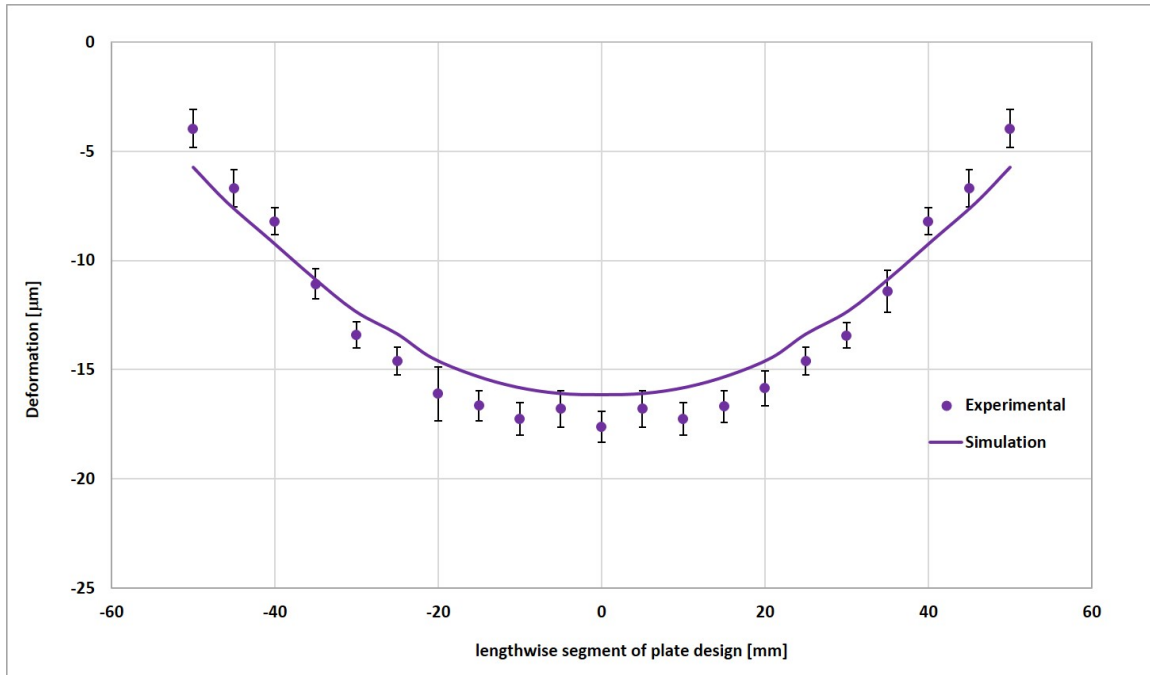


FIGURE 6.24 : Measurement and simulation of dynamic deformation (Design B).

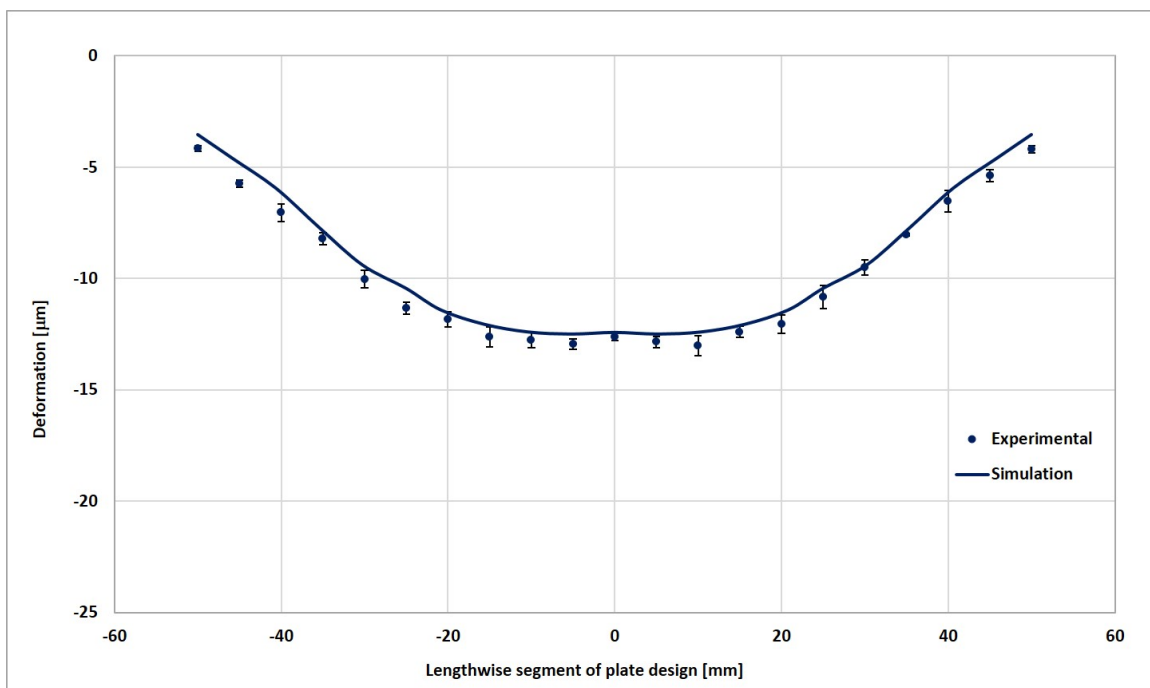


FIGURE 6.25 : Measurement and simulation of dynamic deformation (Design C).

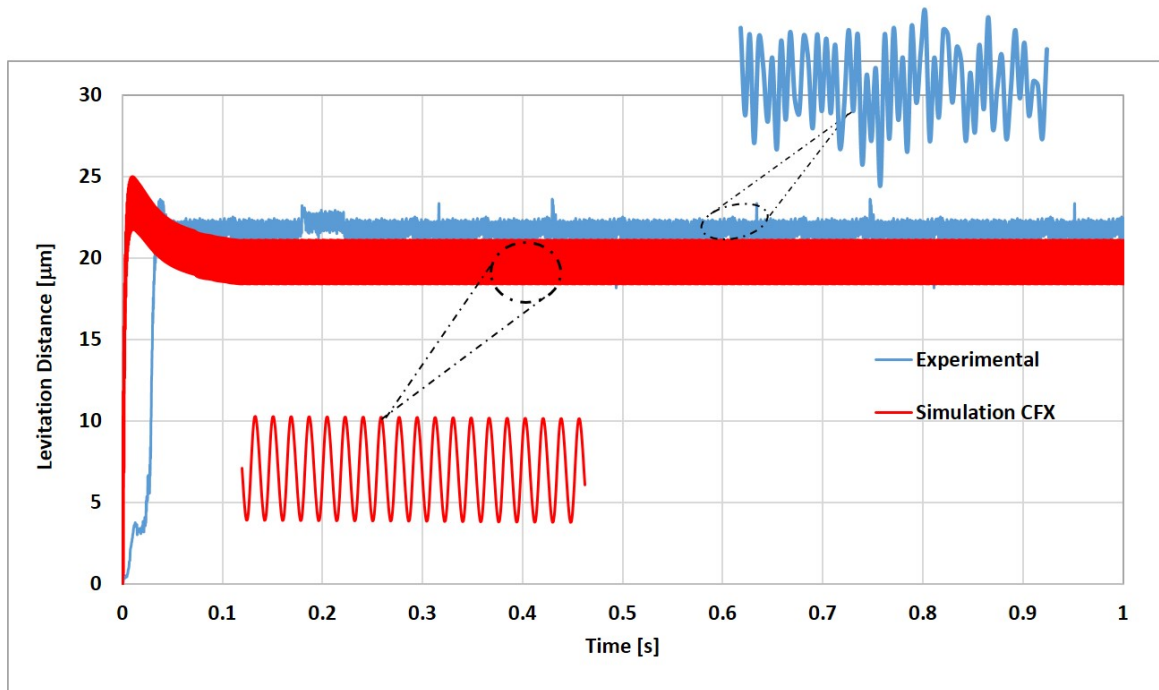


FIGURE 6.26 : Measurement and simulation of dynamic levitation (Design A3).

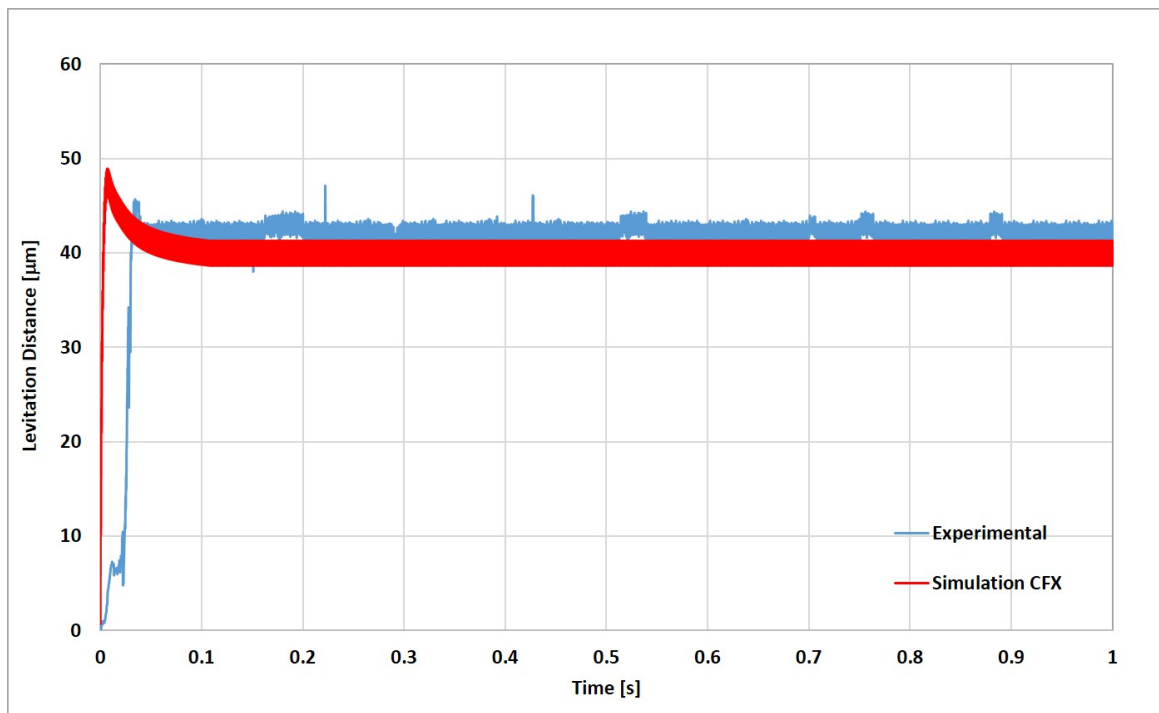


FIGURE 6.27 : Measurement and simulation of dynamic levitation (Design C).

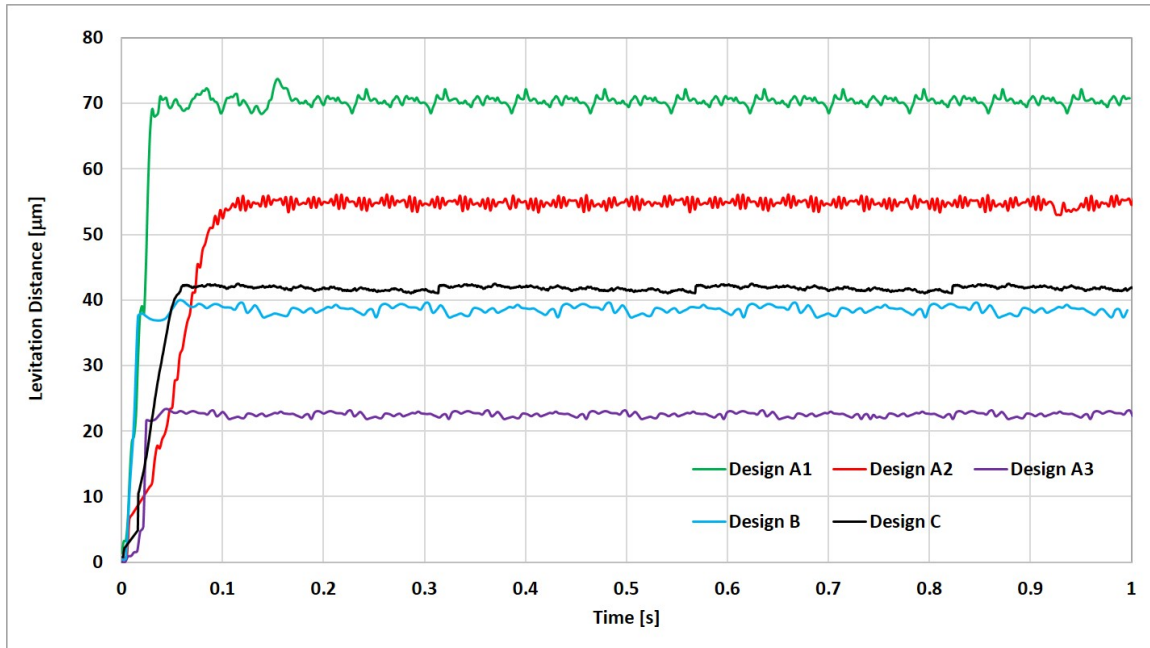


FIGURE 6.28 : Measurement of dynamic levitation for various designs.

As can be seen from Figure 6.14 and Figure 6.15, the effect of Poisson's ratio on the plate design is the formation of a dimple at the central area of the plate. This influence and the shape of deformation stem from the repeated expansions and contractions of the bonded piezoelectric actuators when they are operated by a square wave signal of voltage. The static results show that a high deformation of the plate occurs when high voltages are applied to the actuators and also with a thinner plate design (Figure 6.14 and Figure 6.16) (Hashimoto, Koike, and Ueha, 1996; Stolarski and Woolliscroft, 2007).

The forced plate design A1, made from aluminium and of thinner thickness (0.5 mm) delivers the highest deformation among the five plate designs (Figure 6.16). As long as the operational voltage is in the linear domain of the piezoelectric actuator material, the deformations are directly proportional to the driving voltage, as illustrated in Chapter 3 in Figure 3.4. That is, the plate design deformation increases as the applied voltage is raised. Furthermore, the variations in the measurement results for the plate designs deformation occurred as a result of many factors, such



as the noise of electric devices (voltage amplifier and signal generator), the linearity of the Laser Sensor  $1.5 \mu\text{m}$  and the unforeseen human movement inside and around the laboratory. Meanwhile, it has been estimated that the maximum deformation of the plate in the form of design A3 (aluminium, of size  $(200*100*2 \text{ mm})$  is of the order of 3 and  $5 \mu\text{m}$  under the static and dynamic conditions, respectively. When this is compared to the maximum deformation of design B (polyethylene, of size  $200*100*2 \text{ mm}$ , which is of the order of 7 and  $15 \mu\text{m}$  in the static and dynamic conditions, respectively, one has to conclude that it behaves better than design A3. Hence, the contribution of design B to the SFL can be considered as being significant. Furthermore, there is a good correlation between the measurement and simulation results of the deformation for all the plate designs. The dynamic behaviour of the disc levitation for two designs (Figure 6.26 and Figure 6.27) has been investigated theoretically and experimentally. The simulation of dynamic levitation of the disc is achieved from when the time is equal zero and when the squeeze-film realises a pseudo-steady state (Figure 6.26). A moving mesh technique has been employed to model the squeeze-film motion. The input parameters of levitation distance simulation that have been utilised are film thickness at  $20 \mu\text{m}$ ,  $R=35 \text{ mm}$  and load at the Top B.C of 5 g.

#### 6.4.1 The Dynamic performance of the squeeze-film levitation

As can be seen from Figure 6.26 and Figure 6.27, one can be observed that between time 0 to about  $0.026 \text{ s}$  the surfaces (driving and floating) come in and out of mutual interaction. So, the surfaces can be in contact at the start-up, when the squeeze-film influence is not adequate to accomplish continuous normal separation of the floating object. The measured disc levitation with design A3 (Figure 6.26), is set to create an overshoot of separation of about  $22.4 \mu\text{m}$  at a time of  $0.0792 \text{ s}$ , after which, the separation tends to be at a steady state behaviour of about  $21.1 \mu\text{m}$ . Meanwhile, the theoretical result of design A3 (Figure 6.26) has an overshoot of levitation of about

24.7  $\mu\text{m}$  at 0.0001 s and after about 0.0953 s, the dynamic levitation has established a complete squeeze-film action and tends to be at the steady state behaviour of about 20.8  $\mu\text{m}$ , where it fluctuates at an average squeeze-film elevation (Figure 6.26, enlarged display). Thus, the steady state error for the (measurement and theoretical results accounting for disc levitation obtained with design A3 is about 1.44 %. The results of the theoretical and physical measurements of the floating of the disc with design C, has also been compared (Figure 6.26), between time 0 to about 0.0269 s, within which the surfaces tend to separate. After that, an overshoot of separation of about 44.8  $\mu\text{m}$  develops and then, at a time of 0.047 s, the separation tends to become a steady state behaviour of about 41.829  $\mu\text{m}$ . The theoretical results of design C, have an overshoot of levitation of about 48.95  $\mu\text{m}$  at a time of 0.0001 s and after about 0.0755 s, the dynamic levitation acquires a complete squeeze-film state, which tends to be a steady state behaviour of about 39.723  $\mu\text{m}$ , fluctuating at an average squeeze-film levitation (Figure 6.27). The results (simulation and measurement) show that there is a delay time between them of about 0.0269 s. Accordingly, the steady state error for the outcomes (measurement and simulation) of disc levitation obtained through design C is about 5.31 %. The measurement results for both designs display some spikes due to the data being measured through the laser sensor entirely without averaging them. The levitation of the disc for the various designs has been illustrated as averaged results acquired through the laser sensor (Figure 6.28). As can be seen a steady state disc separation of 70  $\mu\text{m}$  occurs with design A1, which has a thinner plate, whereas a steady state dynamic disc levitation of 22.3  $\mu\text{m}$  happens with design A3, which has a thicker plate. Moreover, design C shows a higher dynamic levitation of 41.85  $\mu\text{m}$  than that produced by design A3. In addition, design B creates a separation for the disc of 38.63  $\mu\text{m}$ . It can be concluded from the results obtained for various plate designs, that the disc separation is affected by the plate material more than the plate dimensions.

## 6.5 Concluding Remarks

An alternative method for accomplishing dynamic levitation for a light object using various plate actuator designs has been investigated. The results of experimental measurements and simulation presented in this paper support the drawing of the following statements. This investigation has shown that a forced plate design with PZT actuators driven by a certain signal voltage will create a cycling dimple deformation at the central area of the plate. Driving the PZT actuators with a square wave voltage signal is found to be effective for squeeze-film levitation, which has been detected both theoretically and experimentally for a lightweight object (disc) placed on the forced plate designs. Moreover, from this investigation, it has been observed that the forced plate design characteristics in addition to the levitation of an object (disc) are affected by several other factors, and in particular, the plate size, material and the boundary conditions. The experimental measurements are consistent with the theoretical results for a one degree of freedom (1-DOF) simulation. This could be advanced by considering multiple degrees of freedom of the floating object.



## Chapter 7

# Summary of Findings and Concluding

### 7.1 Summary of Findings

The squeeze film levitation mechanism has been studied theoretically and experimentally to build non-contact levitation systems. The research introducing the background to the study, the motivation, the aims, the objectives and providing a thesis outline. Accordingly, studies regarding similar non-contact conveying technologies were reviewed covering three main categories depending on the specific mechanism driving oscillating air pressure. That is, it was explained how frictionless conveying of a lightweight object levitated over an oscillating surface can happen as a result of: standing wave (SWAL), acoustic radiation (NFAL) or squeeze film levitation (SFL). The investigations clarified the essential parameters that are influenced on the SFL such as piezoelectric actuators position underside the driving plate, material, size and boundary conditions of the driving structure, coupled-field between the driving structure and the actuators and the fluid-solid interface that is presented between the excited plate and the levitated object. An overview of piezoelectric actuators, their work and function as well as their advantages and disadvantages were provided. In addition, the piezoelectric constants, their finite elements, their mathematical explanations and several piezoelectric material properties were illustrated. Moreover, several modes of piezoelectric actuators based on the polarisation orientation, applied electric field and electrode location were demonstrated. The

transducer design and its performance were demonstrated. In addition, the mathematical modelling of the plate structure deformation throughout the piezoelectric component bonding for actuation was reviewed. It is essential to inspect these issues because of the utilising of piezoelectric elements in oscillation control at micrometre scale.

Moreover, the research work has involved investigating two different designs that can be utilised as contactless conveying systems. One of the designs (Design A), is called the ultrasonic transducer, for which an ultrasonic transducer of a Langevin type represents the main component. The other design (Design B), is in the form of a plain rectangular plate made of Aluminium is used firmly fastened at both ends. In addition, four rounded piezoelectric actuators are attached to the underside of the plate. The central aim was to make a comparison between the designs in terms of load carrying capacity and ease of manufacturing. Experimental investigations have been implemented for both designs to determine their performance in terms of the ability to levitate light objects. Clearly, the designs are greatly influenced by the design configuration, in particular, the driving plate characteristics, such as the plate size and geometry as well as the driving boundary conditions. Based on SFL, a computer model was constructed simulating the levitation process. The analysis of the investigation outcomes signifies that the non-contact levitation offered by Design A is superior to that provided by Design B. The measurements reveal that the maximum dynamic deformation of the disc of Design A is about 20 [ $\mu\text{m}$ ] at a driving voltage of 90 [V]. The measurements disclose that the minimum dynamic deformation of the plate of Design A at a driving voltage of 30 [V] are about 2.7 [ $\mu\text{m}$ ]. Whereas, the average levitating heights for a 5 [g] disk floated on Design B reaches to about 70 [ $\mu\text{m}$ ]. However, the former is more complex than the latter in terms of its manufacturing and use in practical conveying applications.

Furthermore, The SFL plate can also be deformed through a different mechanism utilising Poisson Ratio or due to expansion/contraction processes of the actuators, which is not locked to resonant frequencies of plate vibration or based on particular

and limited cases of modal shapes of the driving structure as carried out with the conventional SFL system. The outcomes of experimental measurements and simulation gained in this investigation indicate that the forced plate designs can respond to a certain signal of voltage in a controlled way. Thus, a new technique has been found for exciting different forced plate designs in such a way that a dimple-shaped elastic deformation at the central area of the plate can be generated. This can be realised through driving the actuators of the designs by the square wave voltage signal. The specific dynamic response in the form of repeating dimple deformation of the forced plate designs can be utilised to deliver effective SFL. This has been verified both theoretically and experimentally for a light disc placed on the plate.

## **7.2 Concluding Remarks**

This chapter provides conclusions drawn from the investigations and their outcomes described in the preceding chapters. Moreover, the contributions to knowledge will be indicated and recommendations for future research aiming at further improvements of squeeze film levitation techniques will be put forward. For this study, levitation of a lightweight object utilising a squeeze-film levitation technique has been the focus. The squeeze-film mechanism was experimentally investigated using specially constructed a test rig equipped with electric driving units to power single layer piezoelectric actuators glued to the underside of thin plate to achieve levitation for the lightweight object. The deformation modes of various oscillating thin plate designs were determined experimentally as well as through simulation of the designs with the finite element program (ANSYS). Accordingly, the effect of Poisson's ratio contraction generated by the actuators on glued to the underside of it the plate and excited by a certain type of signal voltage was studied. This was also simulated for various thin flat plate designs under static and dynamic conditions through ANSYS program. This investigation has shown that a forced plate design with PZT actuators driven by a certain signal voltage will create a cycling dimple

deformation at the central area of the plate. Driving the PZT actuators with a square wave voltage signal is found to be effective for squeeze-film levitation, which has been detected both theoretically and experimentally for a lightweight object (disc) placed on the forced plate designs. Moreover, fluid-solid interaction of an air-layer that is naturally entrapped between the driving surface and the levitating object was simulated. Furthermore, a laser sensor device and high-speed camera (digital image correlation [DIC] system) were utilised to capture the displacement from the driving plate and, to detect the separation distance for the floating object. The results of simulation modelling were validated experimentally for static and dynamic conditions of the plate.

### 7.3 Contributions to Knowledge

The investigations have led to the following contributions:

(a) **Piezoelectric actuator location and operating method.**

The location for mounting piezoelectric actuators of the single layer type is significant since this can affect the deformation of the driving structure (plate). In this investigation, an arrangement of two piezoelectric actuators underneath the driving structure and actuated with a certain periodic waveform voltage (square waveform) were adopted. This arrangement can yield a dynamic deformation of the plate with repeated dimple shape due to the Passion ratio effect. It was subsequently found that this method can contribute to creation of the SFL replacing conventional way of vibrating plate.

(b) **Fluid-Solid Interface for Analysing the SFL Influence.**

An air film that exists between the levitated object and the actuated plate of various designs is modelled. The average pressure and resulting load carrying capacity that is produced by the cyclic displacement at the layer lead to the production of a complete float for a lightweight object. The displacement



that is advanced between the surfaces will lead to a rise in the air – film pressure greater than the ambient pressure, which is essential for lifting the object effectively. A simulation utilising ANSYS CFD is implemented to examine the performance of a levitated object.

**(c) Coupled-field exploration between Piezoelectric Actuators and Driving Structure.**

Piezoelectric actuators and the driving structure (thin flat plate) were modelled using the finite elements with appropriate boundary conditions. The dynamic driving forces stem from the piezoelectric actuators when they are powered by an AC or DC voltage. This is in order to produce sufficient displacement or to realise maximum dynamic reaction and thus, a high levitation can be achieved. It was found that they are the key to accurate modelling outcomes.

**(d) Driving structure material and size.**

The material for the plate of the SFL design is also a significant parameter that can affect the performance of lightweight separation. It has been established that selecting a driving plate with appropriate material properties can create a greater dynamic deformation than that obtainable with other materials for the equivalent load. For example, the forced plate design, made from Aluminium and of thinner thickness delivers the highest deformation among the five plate designs, as long as the operational voltage is in the linear domain of the piezoelectric actuator material.

**(e) Clarification of confusion between three approaches to non-contact levitation based on oscillation air pressure.**

The study clarified confusion in the levitation between three approaches to non-contact levitation through literature review of non-contact levitation and contactless conveying. Noticeable differences between Standing wave levitation (SWL), Near-field acoustic levitation (NFAL) and squeeze film levitation

(SFL). SWAL has a different design to the NFAL technique, whereas the former is only employed for tiny particles, the latter can be used for a heavier levitated object. However, the principle underpinning both methods (SWAL and NFAL) is based on sound radiation. In contrast, the SFL method is fundamentally based on compressing air.

## 7.4 Future Work Recommendations

Despite having investigated a number of significant issues, the study has raised a number of issues that require further exploration. The following future work could prove highly beneficial.

- (a) Using Auxetic material rather than conventional solid material, as they can possess negative Poisson's ratio, in which stretching in one direction leads to expansion in the direction transverse to the loading direction. It follows that if the load is inverted from stretching to compression, the material shrinkages in transverse direction. Thus, the distinctive behaviour of the Auxetic material may improve the SFL design when it is used as a driving structure.
- (b) Further investigations into detecting and analysing the whole levitating object movement, as the levitation of the object is unstable and/or wobbling occurs throughout its movement above the oscillation plate of the SFL design.
- (c) Enhancing the current SFL design based on the findings presented at the beginning of this chapter. For instance, the findings reveal that a big oscillation amplitude for the SFL is desirable. This can be accomplished through creating a SFL design that has alternative boundary conditions. However, the boundary conditions can affect the dynamic deformation and this is in conflict with the other outcomes, for example, the dimple dynamic deformation of the driving structure has to be sufficient to achieve the levitation. The SFL design is

consequently a problem of optimisation and it would be interesting to continue trying to find combinations of design factors that will yield the optimal SFL performance.

- (d) To improve plate driving, instead of utilising the piezoelectric actuators, which are made from a brittle substance that can fracture when the driving structure (plate) deformation is too large, a new sort of material, namely Micro Fibre Composite (MFC), could be a better driving component, because of its higher flexibility.



## References

- Al-Budairi, Hassan Dakhil (2012). "Design and analysis of ultrasonic horns operating in longitudinal and torsional vibration". PhD thesis. University of Glasgow.
- Atherton, MA, C Mares, and TA Stolarski (2014). "Some fundamental aspects of self-levitating sliding contact bearings and their practical implementations". In: *Proceedings of the Institution of Mechanical Engineers, Part J: Journal of Engineering Tribology* 228.9, pp. 916–927.
- Avitabile, Peter, Chris Niezrecki, Mark Helfrick, Chris Warren, and Pawan Pingle (2010). "Noncontact measurement. Techniques for model correlation". In: *Sound and Vibration* 44.1, p. 8.
- Ballas, Rüdiger G (2007). *Piezoelectric multilayer beam bending actuators: Static and dynamic behavior and aspects of sensor integration*. Springer Science & Business Media.
- Bowen, CR, HA Kim, PM Weaver, and S Dunn (2014). "Piezoelectric and ferroelectric materials and structures for energy harvesting applications". In: *Energy & Environmental Science* 7.1, pp. 25–44.
- Brandt, EH (1989). "Levitation in physics". In: *Science* 243.4889, pp. 349–355.
- Bucher, Izhak, Dotan Ilssar, Ran Gabai, Nadav Cohen, Ran Shaham, and Solomon Davis (2016). "Controlled acoustic levitation—physical model and real-time digital implementation". In: *Advanced Intelligent Mechatronics (AIM), 2016 IEEE International Conference on*. IEEE, pp. 452–456.
- Callister Jr, William D and David G Rethwisch (2012). *Fundamentals of materials science and engineering: an integrated approach*. John Wiley & Sons.

- Chu, Boa-Teh and Robert E Apfel (1982). "Acoustic radiation pressure produced by a beam of sound". In: *The Journal of the Acoustical Society of America* 72.6, pp. 1673–1687.
- Ensminger, Dale and Leonard J Bond (2011). *Ultrasonics: fundamentals, technologies, and applications*. CRC press.
- Fayed, Mohammad E and Thomas Skocir (1996). *Mechanical conveyors: selection and operation*. CRC Press.
- Gautschi, Gustav (2002). "Piezoelectric sensors". In: *Piezoelectric Sensorics*. Springer, pp. 73–91.
- Ghodssi, Reza and Pinyen Lin (2011). *MEMS materials and processes handbook*. Vol. 1. Springer Science & Business Media.
- Giurgiutiu, Victor (2007). *Structural Health Monitoring with Piezoelectric Wafer Active Sensors: with Piezoelectric Wafer Active Sensors*. Elsevier.
- Gomis-Bellmunt, Oriol and Lucio Flavio Campanile (2009). *Design rules for actuators in active mechanical systems*. Springer Science & Business Media.
- Hagara, Martin, Róbert Huňady, Pavol Lengvarský, and Jozef Bocko (2014). "Numerical Verification of a Fullfield Deformation Analysis of a Specimen Loaded by Combined Loading". In: *American Journal of Mechanical Engineering* 2.7, pp. 307–311.
- Hamrock, Bernard J, Steven R Schmid, and Bo O Jacobson (2004). *Fundamentals of fluid film lubrication*. CRC press.
- Hashimoto Y., Koike Y. and S. Ueha (1998). "Transporting objects without contact using flexural traveling waves". In: *The Journal of the Acoustical Society of America* 103.6, pp. 3230–3233.
- Hashimoto, Yoshiki, Yoshikazu Koike, and Sadayuki Ueha (1996). "Near-field acoustic levitation of planar specimens using flexural vibration". In: *The Journal of the Acoustical Society of America* 100.4, pp. 2057–2061.

- Ilssar, D, I Bucher, and N Cohen (2014). "Structural Optimization for One Dimensional Acoustic Levitation Devices—Numerical and Experimental Study". In: *International Conference on Noise Vibration Engineering (ISMA), Leuven, Belgium, Sept*, pp. 15–17.
- Ilssar, Dotan and Izhak Bucher (2015). "On the slow dynamics of near-field acoustically levitated objects under High excitation frequencies". In: *Journal of Sound and Vibration* 354, pp. 154–166.
- Ilssar, Dotan, Izhak Bucher, and H Flashner (2017). "Modeling and closed loop control of near-field acoustically levitated objects". In: *Mechanical Systems and Signal Processing* 85, pp. 367–381.
- Ishii, Takahiko, Yosuke Mizuno, Daisuke Koyama, Kentaro Nakamura, Kana Harada, and Yuki Yoshi Uchida (2014). "Plate-shaped non-contact ultrasonic transporter using flexural vibration". In: *Ultrasonics* 54.2, pp. 455–460.
- Jordan, TL and Zoubeida Ounaies (2001). *Piezoelectric ceramics characterization*. Tech. rep. Institute for computer application in science and engineering Hampton VA.
- Jost, P (1976). "Economic impact of tribology". In: *Proc Mechanical Failures Prevention Group*, pp. 117–139.
- Kim, Cheol-Ho and Jeong-Guon Ih (2007). "On the horizontal wobbling of an object levitated by near-field acoustic levitation". In: *Ultrasonics* 46.4, pp. 331–335.
- Kim, Hyeoungwoo (2006). "Impedance adaptation methods of the piezoelectric energy harvesting". In:
- Langlois, WE (1962). "Isothermal squeeze films". In: *Quarterly of Applied Mathematics* 20.2, pp. 131–150.
- Leissa, Arthur W (1969). "Vibration of Plates, Scientific and Technical Information Division". In: *National Aeronautics and Space Administration*.
- Li, Wenjun, Yuanyuan Liu, and Kai Feng (2017). "Modelling and experimental study on the influence of surface grooves on near-field acoustic levitation". In: *Tribology International* 116, pp. 138–146.

- Littmann, Walter, Tobias Hensel, Christopher Kauczor, Jörg Wallaschek, and M Sinha (2003). "Load-adaptive phase-controller for resonant driven piezoelectric devices". In: *World Congress Ultrasonics, Paris*. Vol. 48, p. 64.
- Liu, Pinkuan, Jin Li, Han Ding, and Wenwu Cao (2009). "Modeling and experimental study on near-field acoustic levitation by flexural mode". In: *IEEE transactions on ultrasonics, ferroelectrics, and frequency control* 56.12.
- McGuire, Patrick M. (2009). *Conveyors: application, selection, and integration*. CRC Press.
- Minikes, A and I Bucher (2006). "Comparing numerical and analytical solutions for squeeze-film levitation force". In: *Journal of fluids and structures* 22.5, pp. 713–719.
- Minikes, Adi and Izhak Bucher (2003). "Coupled dynamics of a squeeze-film levitated mass and a vibrating piezoelectric disc: numerical analysis and experimental study". In: *Journal of Sound and Vibration* 263.2, pp. 241–268.
- Minikes, Adi, Izhak Bucher, and Shimon Haber (2004). "Levitation force induced by pressure radiation in gas squeeze films". In: *The Journal of the Acoustical Society of America* 116.1, pp. 217–226.
- Nakamura, Kentaro (2012). *Ultrasonic transducers: Materials and design for sensors, actuators and medical applications*. Elsevier.
- Otsuka, Tetsuro, Kazutaka Higuchi, and Koichiro Seya (1990). "Ultrasonic levitation by stepped circular vibrating plate". In: *Japanese journal of applied physics* 29.S1, p. 170.
- Pan, Bing, Kemao Qian, Huimin Xie, and Anand Asundi (2009). "Two-dimensional digital image correlation for in-plane displacement and strain measurement: a review". In: *Measurement science and technology* 20.6, p. 062001.
- Qin, Qinghua (2012). *Advanced mechanics of piezoelectricity*. Springer Science & Business Media.
- Reinhart, G and J Hoeppepner (2000). "Non-contact handling using high-intensity ultrasonics". In: *CIRP Annals-Manufacturing Technology* 49.1, pp. 5–8.
- Rogacheva, Nellya N (1994). *The theory of piezoelectric shells and plates*. CRC press.



- Salbu, E.O.J. (1964). "Compressible squeeze films and squeeze bearings". In: *Journal of Basic Engineering* 86.2, pp. 355–364.
- Shah, Abid A (2011). "A FEM-BEM interactive coupling for modeling the piezoelectric health monitoring systems". In: *Latin American Journal of Solids and Structures* 8.3, pp. 305–334.
- Siebert, Thorsten, Thomas Becker, Karsten Spilthof, Isabell Neumann, and Rene Krupka (2007). "Error estimations in digital image correlation technique". In: *Applied Mechanics and Materials*. Vol. 7. Trans Tech Publ, pp. 265–270.
- Smith, L Jack (1966). "Use of phase-locked-loop control for driving ultrasonic transducers". In:
- Soh, Chee-Kiong, Yaowen Yang, and Suresh Bhalla (2012). *Smart materials in structural health monitoring, control and biomechanics*. Springer Science & Business Media.
- Stolarski, T.A. and W. Chai (2008). "Inertia effect in squeeze film air contact". In: *Tribology International* 41.8, pp. 716–723.
- Stolarski, TA and Wei Chai (2006). "Self-levitating sliding air contact". In: *International journal of mechanical sciences* 48.6, pp. 601–620.
- Stolarski, TA and CI Woolliscroft (2007). "Use of near-field acoustic levitation in experimental sliding contact". In: *Journal of applied mechanics* 74.4, pp. 816–820.
- Takács, Gergely and Boris Rohal'-Ilkiv (2012). *Model predictive vibration control: efficient constrained MPC vibration control for lightly damped mechanical structures*. Springer Science & Business Media.
- Thangali, Seshadri R (1991). "Noncontact handling of semiconductor wafers". PhD thesis.
- Timoshenko, Stephen P and Sergius Woinowsky-Krieger (1959). *Theory of plates and shells*. McGRAW-HILL.
- Ueha, Sadayuki, Yoshiki Hashimoto, and Yoshikazu Koike (2000). "Non-contact transportation using near-field acoustic levitation". In: *Ultrasonics* 38.1-8, pp. 26–32.

- Vandaele, Vincent, Alain Delchambre, and Pierre Lambert (2011). "Acoustic wave levitation: Handling of components". In: *Journal of applied physics* 109.12, p. 124901.
- Vandaele, Vincent, Pierre Lambert, and Alain Delchambre (2005). "Non-contact handling in microassembly: Acoustical levitation". In: *Precision engineering* 29.4, pp. 491–505.
- Venstel, E and T Krauthammer (2001). *Thin plates and shells, theory, analysis and application*.
- Vijaya, MS (2016). *Piezoelectric materials and devices: applications in engineering and medical sciences*. CRC Press.
- Wang, C. and Y.H.J. Au (2011). "Study of design parameters for squeeze film air journal bearing—excitation frequency and amplitude". In: *Mechanical Sciences* 2.2, pp. 147–155.
- Wang, C. and Y.J. Au (2013). "Comparative performance of squeeze film air journal bearings made of aluminium and copper". In: *The International Journal of Advanced Manufacturing Technology* 65.1-4, pp. 57–66.
- Wang, Chao and YH Joe Au (2012). "Levitation characteristics of a squeeze-film air journal bearing at its normal modes". In: *The International Journal of Advanced Manufacturing Technology* 60.1-4, pp. 1–10.
- Wei, Bin, Ran Shaham, and Izhak Bucher (2018). "Theoretical investigation and prototype design for non-parallel squeeze film movement platform driven by standing waves". In: *Tribology International* 119, pp. 539–548.
- Whymark, RR (1975). "Acoustic field positioning for containerless processing". In: *Ultrasonics* 13.6, pp. 251–261.
- Wiesendanger, Markus (2001). "Squeeze film air bearings using piezoelectric bending elements". PhD thesis. Federal Institute of Technology in Lausanne.
- Yarin, AL, M Pfaffenlehner, and C Tropea (1998). "On the acoustic levitation of droplets". In: *Journal of Fluid Mechanics* 356, pp. 65–91.

---

Yoshimoto, Shigeka, Hiroyuki Kobayashi, and Masaaki Miyatake (2007). "Float characteristics of a squeeze-film air bearing for a linear motion guide using ultrasonic vibration". In: *Tribology international* 40.3, pp. 503–511.



## **Appendix A**

## **Appendix A**

### **A.1 Published Research Paper**

## NFAL Prototype Design and Feasibility Analysis for Self-Levitated Conveying

Xiaoni Chang<sup>a</sup>, Bin Wei<sup>b</sup>, Mark Atherton<sup>c</sup>, Chris Mares<sup>c</sup>, Tadeusz Stolarski<sup>c</sup>, and Ahmed Almurshedi<sup>c</sup>

<sup>a</sup>School of Economic and Management, Beihang University, Beijing, P. R. China; <sup>b</sup>State Key Laboratory of Tribology, Tsinghua University, Beijing, P. R. China; <sup>c</sup>College of Engineering, Design and Physical Sciences, Brunel University, London, UK

### ABSTRACT

In order to avoid friction and scratching when conveying object, an acoustic levitation prototype was designed to verify the feasibility. The modal shapes and the forced harmonic shapes of the prototype are obtained by an ANSYS coupled field computation with a one-quarter symmetry model and the levitation capacity was assessed by the use of groups of simulation and physical testing. The simulation results showed that the pure flexural and mixed flexural wave shapes with different wave numbers existed at some specific frequency. The amplitude in the central point of an aluminum plate having four piezoelectric discs glued to the bottom surface was simulated for a frequency spectrum. The experimental results confirmed the theoretical results and the feasibility of the prototype and confirm that objects can be floated at several resonant frequencies under forced vibrating condition. The system can provide largest bearing capacity when both the piezoelectric disc and the plate resonances coincide.

### ARTICLE HISTORY

Received 20 April 2015  
 Accepted 14 November 2015

### KEYWORDS

NFAL; ANSYS; prototype; resonant; piezoelectric; squeeze-film levitation

### Introduction

The near-field acoustic levitation (NFAL) concept comes from high-frequency gas squeeze theory. The gas squeeze theory was originally proposed by Gross (1) and improved by Langlois (2). Next, Salbu (3) proposed the fixed object squeeze film model and believed that the squeeze film characteristics are similar to the piston exciting situation. The carrying capacity can be obtained by simple calculation. The free levitation theory was first proposed by Beck, et al. (4) and a numerical method is applied in their model. Later, research on squeeze film characteristics that were solved by lubrication dynamic methods was developed (Kuroda and Hirata (5); Jing, et al. (6)). Based on free levitation theory, the modal shapes were considered in Hashimoto's (7) research. The excited shape was a supposed ideal flexural wave and coupled to the film thickness equation. The model was proved to be more stable and had a higher bearing capacity than that in the rigid disk excitation condition. Later, the linearization solution was derived by Minikes and Bucher (8) and the feasibility was verified by Hashimoto's experiments. Stolaski and Chai (9) and Stolarski (10) investigated the characteristics of the designed linear bearing, and a 2D model for the new bearing was established. Liu, et al. (11) and Li, et al. (12) researched the bearing force in experiments and plotted the film thickness curves versus frequencies. Recently, some scholars combined the squeeze film theory with ultrasonic phenomena (Wei and Ma (13), (14); Li, et al. (15); Xie and Wei (16)) and compared the ultrasonic levitation results with squeeze film by numerical computation. Thus, the concept of an ultrasonic squeeze film was proposed and the theory was further developed. Recently, from the point of view

of engineering practice, many researchers have focused on some typical situations of the squeeze film such as the non-Newtonian fluid film, the film with a porous layer, damping effects, and so on (Nabhani, et al. (17); Rao, et al. (18); Bouzidane and Thomas (19)). Research history for Near Field Acoustic Levitation (NFAL) is listed in Table 1.

The table shows different model and solution methods for the NFAL system. Aiming at the model forms, there are three main models for the NFAL system: infinite width model for simple estimation, axial symmetry model for the round exciting disc, and a 2D model for a common exciting plate. All of the modal shapes, including rigid, purely flexible, mixed (true) models, and object status could influence the complex extent of the mathematic models. The solutions corresponding to the models mainly included acoustic radial field and squeeze film methods; however, for the free object the model can only be solved numerically.

In engineering practice, the horn is helpful to the actuator design (Wang and Wei (20)). However, due to space constraints, the horn cannot be used in self levitation conveyor system, so the resonance frequency of the system is difficult to predict and is greatly affected by the layout of the piezodiscs.

### Prototype design

The physical NFAL platform and the levitated samples are shown in Fig. 1. The dimensions and the materials of the piezoelectric discs and the exciting plate are listed in Table 2. The four piezoelectric discs are connected to the output port of the amplifier by the block terminal with a 1 A fuse. The layout of piezoelectric discs is shown in Fig. 2.

**CONTACT** Bin Wei ✉ [buaaweibin@126.com](mailto:buaaweibin@126.com)

Color versions of one or more of the figures in the article can be found online at [www.tandfonline.com/utrb](http://www.tandfonline.com/utrb).

Review led by Benyebka Bou-Said

© 2016 Society of Tribologists and Lubrication Engineers

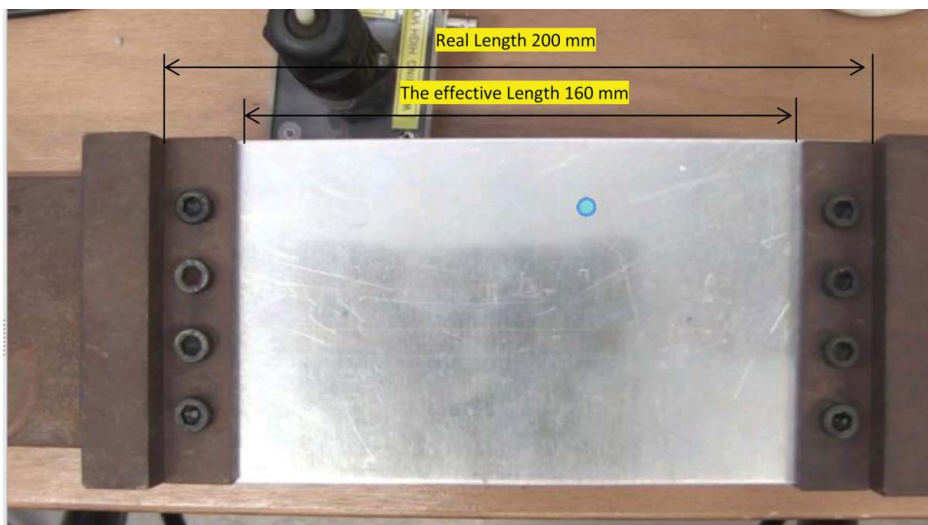
**Nomenclature**

- $F =$  Dimensionless bearing force  $F(T) = \frac{g(T)}{p_0 R_0^2}$
- $f =$  Squeeze frequency
- $g =$  Bearing force (N)
- $H =$  Dimensionless form of  $h$ ,  $H = h/h_0$
- $h =$  Film thickness (m)
- $h_0 =$  Initial film thickness (m)
- $L =$  Width variable (m)
- $m =$  Mass of free levitation object (kg)
- $P =$  Dimensionless form of  $p$ ,  $P = p/p_0$

- $p =$  Squeeze film pressure (Pa)
- $p_0 =$  Atmospheric pressure (Pa)
- $T =$  Dimensionless form of  $t$ ,  $T = \omega t$
- $t =$  Time (s)
- $X =$  Dimensionless form of  $x$ ,  $X = x/L$
- $Y =$  Dimensionless form of  $y$
- $y =$  Width of the plate actuator
- $\mu =$  Dynamic viscosity (Pa s)
- $\sigma =$  Squeeze number  $\sigma = \frac{12\mu\omega b^2}{h_0^2 p_a}$
- $\omega =$  Squeezing angular frequency,  $\omega = 2\pi f$  (rad/s)


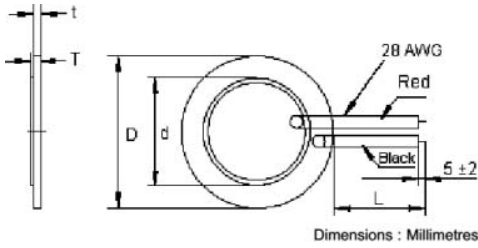

**Table 1.** Research history of the NFAL.

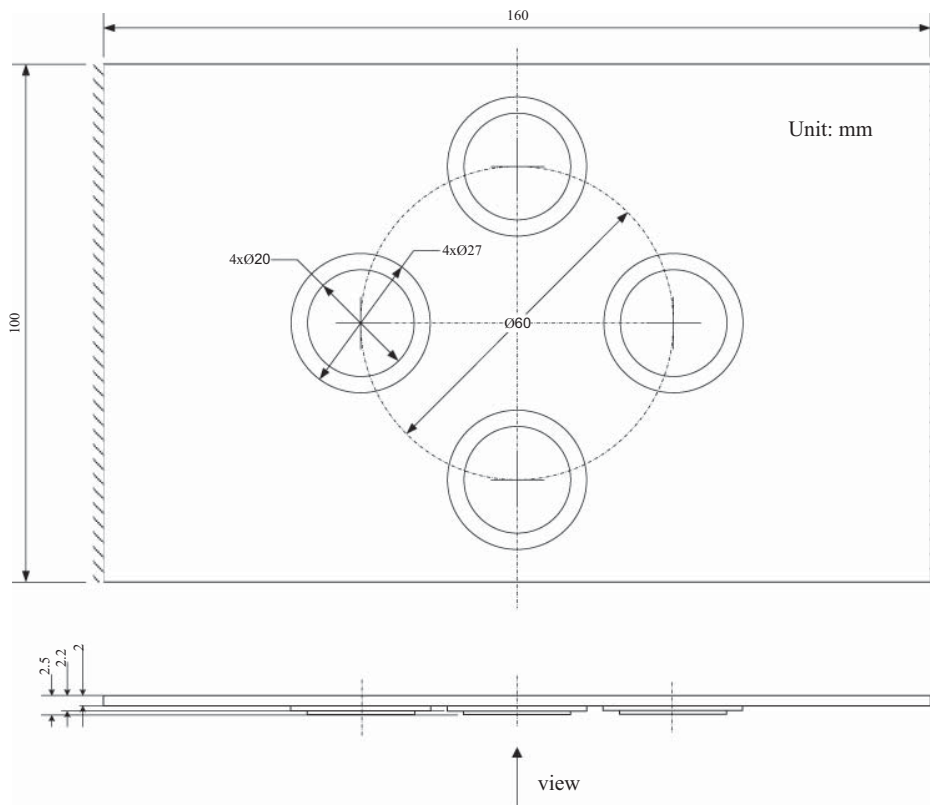
Publication date	First author	Model type	Modal shape of excitation disk	Sample suspended situation	Calculation method
1961	Langlois (2)	Infinite wide Axial symmetry	Not take account	Fixed	Reynolds equation perturbation
1964	Sablu (3)	Axial symmetry	Not take account	Fixed	Reynolds equation numerical method
1968	Diprima (21)	Infinite wide	Not take account	Fixed	Reynolds equation analytic method
1969	Beck, et al. (4)	Axial symmetry	Not take account	Free	Reynolds equation and motion equation perturbation method
1983	Takada and Miura (22)	Infinite wide	Not take account	Fixed	Reynolds equation linearization method
1984	Kuroda and Hirata (23)	Axial symmetry	Not take account	Free	Numerical method
1996	Hashimoto (7)	Infinite wide	Flexible modal shape	Fixed	Ultrasonic analytical theory
1997	Beltman and Vander Hoogt (24)	2D Rectangle	Not take account	Fixed	Finite element method
2003	Minikes and Bucher (25)	Axial symmetry	Flexible modal shape	Fixed	Numerical method
2004	Minikes and Bucher (8)	Infinite wide	Rigid and flexible model	Fixed	Modified Reynolds linearization method
2006	Stolarski and Chai (9)	2D model	Not take account	Fixed	Reynolds equation numerical method
2006	Ha, et al. (26)	2D model	Flexural model	Fixed	Experiment reserch
2007	Yoshimoto, et al. (27)	2D model	Take account	Free	Reynolds equation numerical method ANSYS fluid simulation
2009	Liu, et al. (11)	Axial symmetry	Flexible wave	Fixed	Reynolds equation numerical method
2010	Stolarski and Chia (10)	2D model	Take account	Free	Reynolds equation numerical method ANSYS fluid simulation
2011	Wei, et al. (28)	Axial symmetry	Real modal shape	Fixed	ANSYS ultrasonic simulation
2012	Stolarski, et al. (29)	2D model	take account	Fixed	Reynolds equation numerical method
2014	Wang and Wei (20)	Axial symmetry	Mixed modal shape	Free	Reynolds equation analytic and numerical method
2014	Wang and Wei (30)	Infinite wide	Rigid model	Fixed	Reynolds equation linearization method



**Figure 1.** Designed plate actuator.

**Table 2.** Dimensions and materials of the piezoelectric discs and the plate.

Sort	image	Drawing	Properties
Piezoelectric disc			Materials: Brass and iron Resonant frequency = 4.2 K $D = 27$ mm $d = 20$ mm $t = 0.3$ $T = 0.5$
Plate and layout		As Fig. 2	Materials: Aluminum Real length = 200 mm Effective length = 160 mm Width = 100 mm Height = 2 mm



**Figure 2.** Dimensions of the exciting plate.

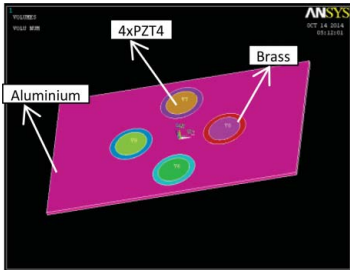
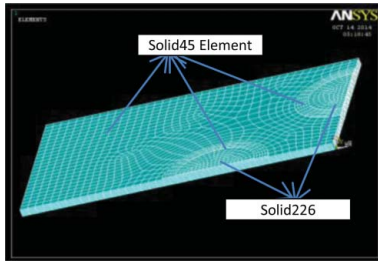
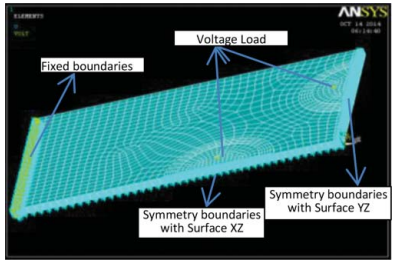


**Figure 3.** Levitation samples.

The piezoelectric discs are fixed at the bottom of the plate with professional adhesive and distressed for 12 h. Therefore, the prototype of the actuator (exciting plate) is made up of the plate and the piezoelectric discs, which can radiate a sonic field and squeeze the gas that is close to the plate surface. In this circuit, the capacitances are parallel connected and their resonant frequency is determined by the total capacitances and equivalent inductances. The system resonance frequency and impedance are more important to the levitation capacity than the individual

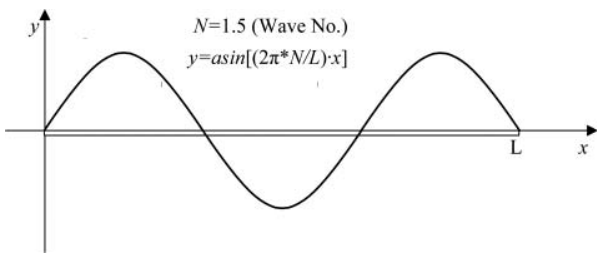


**Table 3.** Finite model and boundary condition of the exciting plate.

Geometry and materials	Hexahedral mesh and element (1/4)	Boundary condition and load (1/4)
		

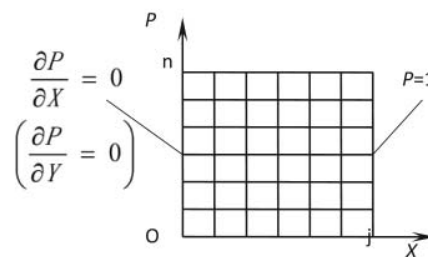
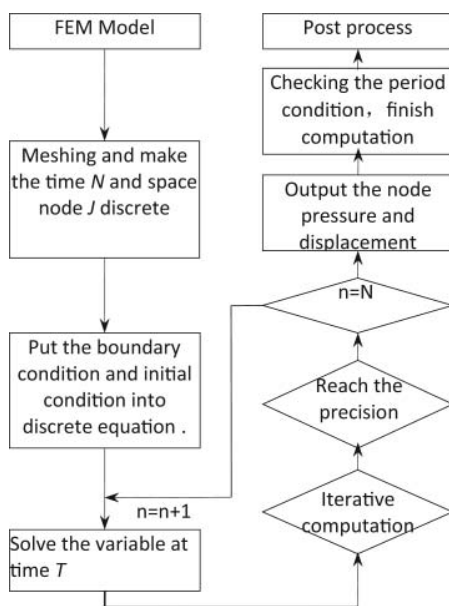
**Table 4.** Materials of the elements.

Materials	Dielectric constants	Young's modulus (GPa)	Poisson ratio	Density (kg/m <sup>3</sup> )	Piezoelectric voltage constants (C/m <sup>2</sup> )
Aluminium	—	69	0.3	2,700	—
Brass	—	110	0.3	6,400	—
PZT4	$\begin{bmatrix} 804.6 & 0 & 0 \\ 0 & 804.6 & 0 \\ 0 & 0 & 659.7 \end{bmatrix}$	$\begin{bmatrix} 132 & 71 & 73 & 0 & 0 \\ & 132 & 73 & 0 & 0 \\ & & 115 & 0 & 0 \\ & & & 30 & 0 \\ & & & & 26 \end{bmatrix}$	—	7,500	$\begin{bmatrix} 0 & 0 & -4.1 \\ 0 & 0 & -4.1 \\ 0 & 0 & 14.1 \\ 0 & 0 & 0 \\ 0 & 10.5 & 0 \\ 10.5 & 0 & 0 \end{bmatrix}$



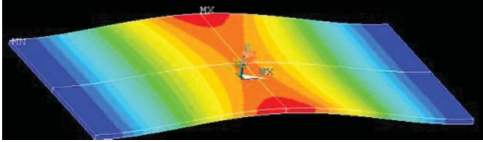
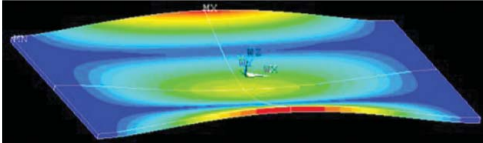
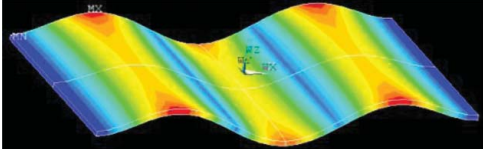
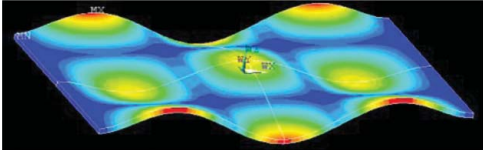
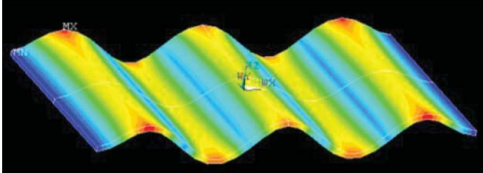
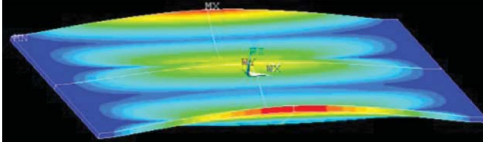
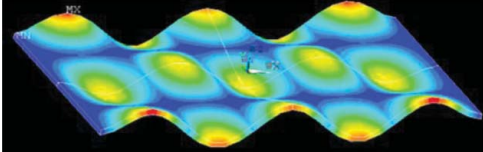
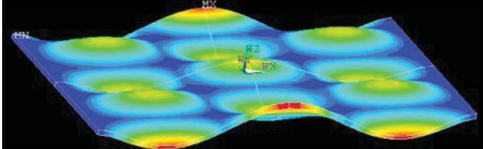
**Figure 4.** Theoretical model of the squeeze film.

properties of the piezoelectric discs. Many kinds of levitation samples including metallic and nonmetallic ones are chosen to test the levitation effects in the experiment shown in Fig. 3. The designed plate actuator is detailed in Fig. 2. The floating objects on the plate can be self-levitated by the effect of NFAL.



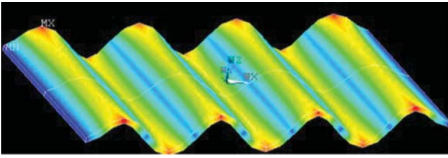
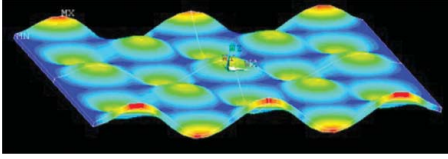
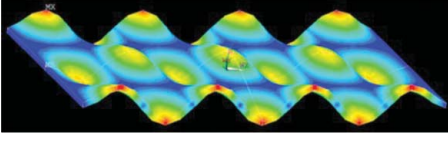
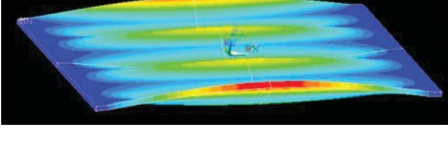
**Figure 5.** Flowchart of the theoretical solution.

**Table 5.** Modal shapes of the exciting plate.

Model frequency	Images Expanded from the 1/4 model	Explanation
1 (417.9)		Pure flexural wave along the x direction
2 (1,461.8)		Pure flexural wave along the y direction
3 (2,291.3)		Pure flexural wave along the x direction
4 (3,632.0)		Mixed modal with both x and y directions (1.5*1)
5 (5,794.0)		Pure flexural wave along x
6 (6,124.5)		Pure flexural wave along y
7 (7,274.8)		Mixed modal with both x and y directions (2.5*1)
8 (8,202.4)		Mixed modal with both x and y directions (2*1.5)

(Continued)

Table 5. (Continued)

Model frequency	Images Expanded from the 1/4 model	Explanation
9 (11,128.9)		Pure flexural wave along x
10 (11,994.3)		Mixed modal with both x and y directions (2.5*2.5)
Was not addressed in experiments (12,662.9)		Mixed modal with both x and y directions (3.5*2)
11 (14,853.8)		Pure flexural wave along y

**Plate finite element and the squeeze film model of the piezoelectric plate actuator**

Because the air pressure boundary condition is neglected in the finite element model (FEM) of the exciting plate, it is reasonable to calculate the modal and harmonic shapes first and then obtain the accurate film thickness equations coupled with the plate shapes, from which the bearing force (nodes pressure) is calculated by the Reynolds equation coupled with the film thickness equation.

**Finite element model of the exciting plate**

The deforming shapes of the plate actuator can be carried out by the FEM. The mathematical model is determined by the geometric dimensions of the plate and the piezoelectric discs (Fig. 2). The FEM vibration model for PZT-4 was researched theoretically and experimentally. The accuracy of the ANSYS FEM model was proven by comparing the results of disc excitation experiments (Wang and Wei (20)). The finite element model and boundary condition of the exciting plate are shown in Table 3 and the material parameters are listed in Table 4. The mechanical mode coupled with an electric field would better simulate the real experiment status. Three materials are included—that is aluminium, brass linings, and PZT4—which are glued to each other in the ANSYS pretreatment. In engineering practice, the symmetry modal shapes (with either an XZ or YZ plane) are available to ensure that the cans are able to steadily self-levitate in the central area on the conveyor belt.

Therefore, only a quarter of the geometry is meshed due to the symmetrical structure, by which some of the irregular modes would be missed but it is beneficial to the main modes extracted from the multiplex ones. The model is divided into different partitions to ensure a hexahedral mesh by the sweeping method. Boundary conditions are applied in this model; that is, fixed boundaries on the left side of the plate, symmetrical

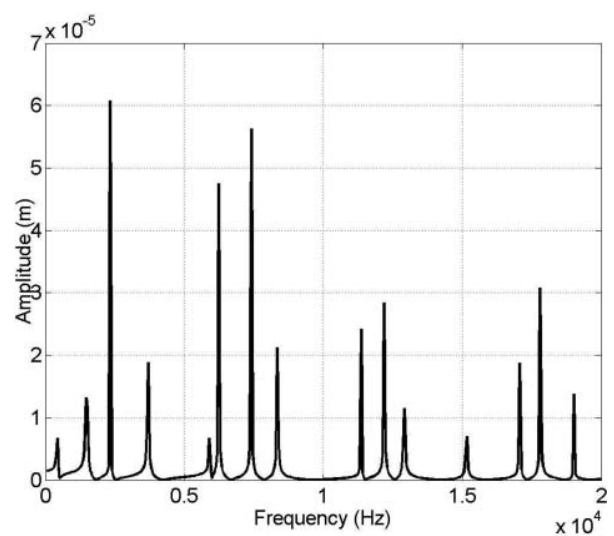


Figure 6. Harmonic analysis results of central point.

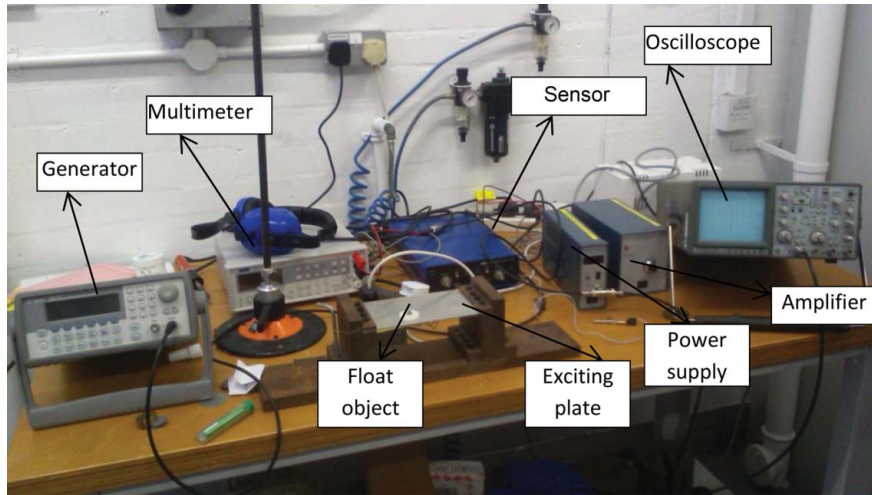


Figure 7. Layout of the experiments.

Table 6. Experiment parameters.

Bandwidth	Acquisition mode	Sample frequency	Resolution	Range
50 kHz	Fast Fourier transform	128 kHz	1.953125 Hz	5 V

boundaries on the XZ and YZ planes, and a 5v INPUT to the amplifier and 75v difference on each side of the piezoelectric disc. The static, modes, and harmonic results of the disk can be obtained by the ANSYS mechanical and electric coupling analysis.

**Squeeze film model of the actuator**

The infinite-width squeeze film governing equations for a fixed floating object consist of the Reynolds equation and film thickness equations defined by the shapes of the plate at a specific frequency. Due to the dimensions of the exciting plate and the actual form of a conveyor, it is reasonable to calculate with infinite wide mode.

The film thickness equations with pure flexural modes are shown in Fig. 4, where N is the wave number, which means the number of wavelengths in the exciting plate, and Y is the modal shapes equation in order to determine the position of the vibration point.

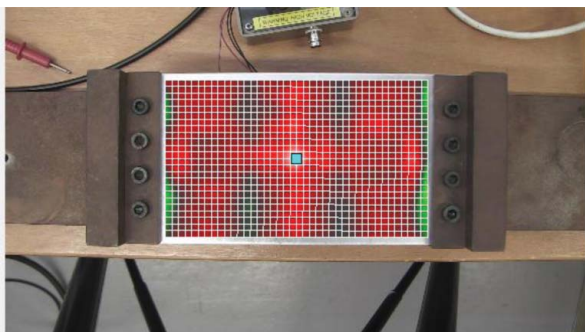


Figure 8. Mesh grid of the modal test.

Therefore, the dimensionless governing equations for the infinite width plate are as follows:

Dimensionless film thickness equation:

$$H(X, T) = 1 - Y(X) \cdot \sin T \tag{1}$$

and the Reynolds equation:

$$\frac{\partial}{\partial X} \left( PH^3 \frac{\partial P}{\partial X} \right) = \sigma \frac{\partial(PH)}{\partial T}, \tag{2}$$

where the dimensionless parameters

$$H = \frac{h}{h_0}, X = \frac{x}{L} \in (0, 1), P = \frac{p}{p_a}, T = \omega t,$$

$$\sigma = \frac{12\mu\omega b^2}{h_0^2 p_a} \text{ (squeeze number)}, Y(X) = a \cdot \sin(2\pi N \cdot X) / h_0.$$

For the square sample, the bearing force can be derived by the pressure integral as follows:

$$f_1(T) = \int_{S_1} \int (p - p_a) dx dy = \int_0^a \int_0^b (p - p_a) dx dy, \tag{3}$$

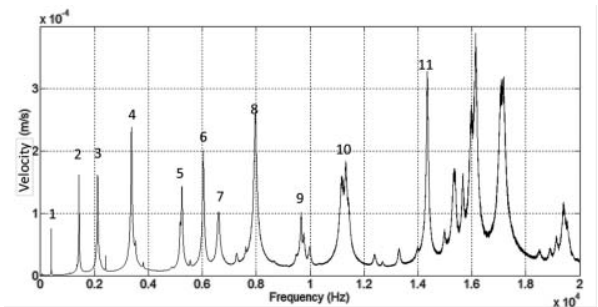
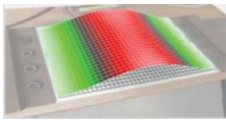
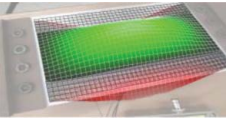
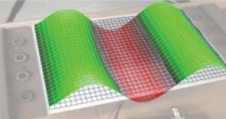
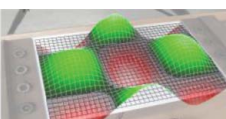
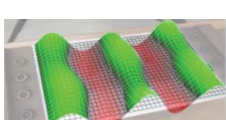
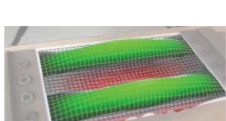
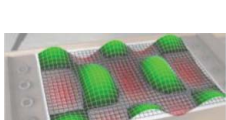
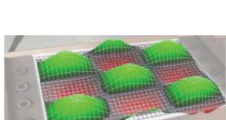
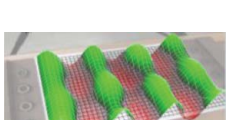


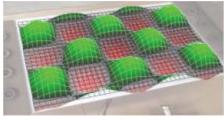
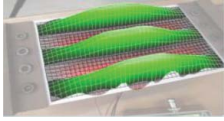
Figure 9. Average velocity values of experimental data.

**Table 7.** Experiment results measured by Polytec laser scanning vibrometer.

Sequence	Frequency	Harmonic shapes	Magnitude ( $\mu\text{m}$ )	Theoretical errors (%)	Floating
1	393.7		75.12	5.8	Unavailable
2	1,425.0		161.4	2.5	Available
3	2,115.6		162.03	7.7	Available
4	3,671.9		238.65	1.1	Unavailable
5	5,240.6		143.04	9.5	Unavailable
6	6,037.5		200.8	1.4	Unavailable
7	6,612.5		102.35	9.1	Available
8	7,965.6		264.42	2.9	Available
9	9,668.8		101.19	13.1	Unavailable

(Continued)

Table 7. (Continued)

Sequence	Frequency	Harmonic shapes	Magnitude ( $\mu\text{m}$ )	Theoretical errors (%)	Floating
10	11,178.1		160.11	6.8	Available
11	14,353.1		327.84	3.3	Unavailable

where  $S_1$  is the square integral area and  $a, b$  are the length and width, respectively.

For the round sample, the pressure integral can be derived as

$$f_2(T) = \iint_{S_2} (p - p_a) r dr d\theta = \int_0^{R_0} \int_0^{2\pi} (p - p_a) r dr d\theta, \quad [4]$$

where  $S_2$  is the round integral area;  $R_0$  is the radial of the sample; and  $x = r \cos\theta, y = r \sin\theta$ .

The program flowchart is shown in Fig. 5. The Reynolds equation was calculated by the means of center difference coupled with the film thickness equation including plate deformation.

### Results and discussion

The modal shapes calculated by ANSYS are listed in Table 5 (below 15 kHz). The symmetry model can explain the basic forms for the exciting plate. There are three kinds of modal shapes. First are the pure flexural modes along the X direction such as modes 1, 3, 5, and so on. Second are the pure flexural modes along the Y direction such as modes 2, 6, 12, and so on.

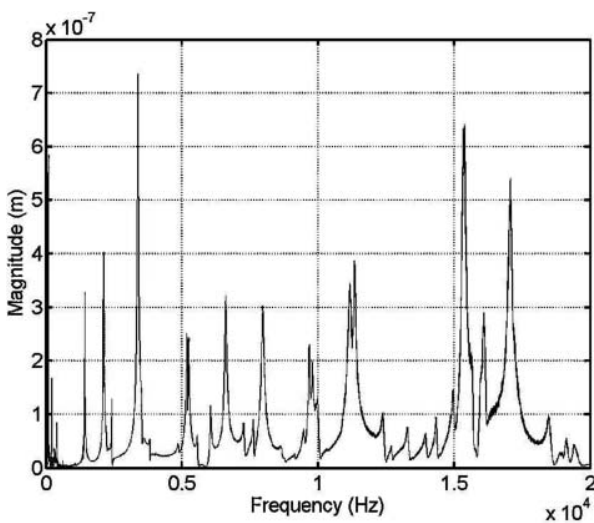


Figure 10. Experimental results of the central point.

The last are mixed wave shapes with different wave numbers along the X and Y directions. For example, the fourth step of modal shapes shows the 1.5\*1 mixed wave shapes.

For the conveyor, a larger amplitude in the central line of the plate is needed. The forced harmonic spectrum at the origin point (central point) is shown in Fig. 6. Not all of the modes can be stimulated well in the forced vibrating condition and not all of the peaks of vibrating amplitude are natural modes; that is, some are harmonic modes. The amplitude–frequency curves show the magnitude of the trend with an increase in frequency. Nearly all of the modal shapes can be excited but with different magnitudes. The harmonic results are corresponding with the modal shapes. However, the resonant frequency is slightly different due partially to the coupling effect of piezoelectric materials.

### Experiments and verification

The experimental instruments are shown in Fig. 7, including a signal generator, power supply amplifier, oscilloscope, capacitive sensor, and multimeter. Some key parameters in the experiments are listed in Table 6.

The harmonic shapes of the plate were measured by the laser scanning vibrometer from Polytec Company. A total of 1,025 nodes,  $41 \times 25$ , are distributed on the plate to collect the velocity in the Z (height) direction as shown in Fig. 8. The sweeping voltage 5v AC, generating an amplifier output of 75v AC.

The average root mean square (RMS) velocity on all surface nodes curves versus frequency is shown in Fig. 9. Due to the symmetry mode in ANSYS, some of the harmonic resonance of

Table 8. Performance parameters of the Fuji amplifier and power supply.

Performance index	Range
Output voltage	0–150 V
Output current	1 A
Voltage range	0 to +150 V
Bandwidth	DC: 100 KHz (100V <sub>p-p</sub> output)
Internal resistance	100 k $\Omega$
Amplification	25 dB (15 times)
Stability with time	$1 \times 10^{-4}$ /h
Stability with current	$1 \times 10^{-4}$
Dimensions	103 mm (W) * 124 mm (H) * 220 mm (D)
Weight	4.5 kg

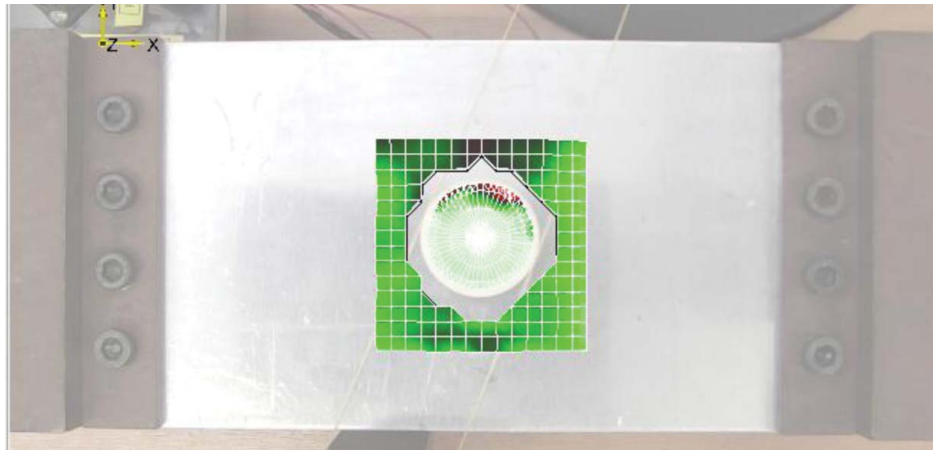


Figure 11. Mesh grid for the levitation height of the object measurement.

the plate could be missing. However, the main levitation point and modal shapes are identifiable in the spectrum. In contrast to the experiment's harmonic spectrum, we found that there are more irregular peaks in the results due to the symmetry model in the theoretical analysis. We extracted the harmonic shapes are measured below 15 KHz frequency from the experiments. The corresponding plate deformations are listed in Table 7.

In contrast to the simulation results in Table 5, from Table 7 we found that the symmetry model can better predict the modal shape of the plates. All of the shapes of the peaks are included in Table 5 (theoretical one) when the frequency is below 15 kHz. The theoretical errors showed that all of the simulation results of one quarter model against the experimental results are below 15%. The largest errors occurred along the X direction (step 3, 5, 9) due to the simplified boundary condition. In contrast, the ones along the Y direction have the best accuracy due to the free boundaries. The experimental results showed that not all of the modal shapes produce make the object self-levitate. The pure ones are appropriate for lower frequency, whereas the mixed ones are appropriate for higher frequency. This is because some researchers have different optimization modal shapes for the self-levitation of different structures and this result provided significant guidance for the prototype design.

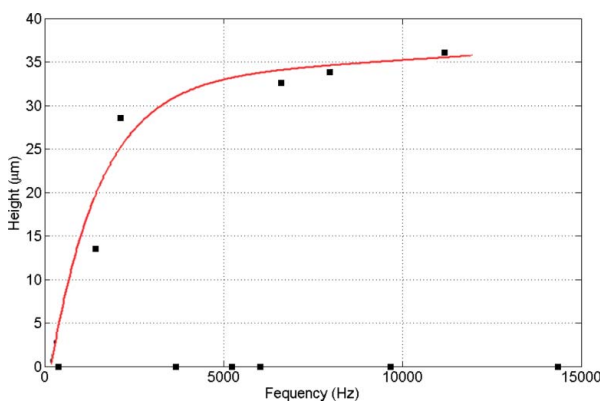


Figure 12. Levitation experiment results.

The results for displacement of the central point are shown in Fig. 10. It is different from the RMS curves but show the same trend. In contrast to the harmonic simulation results (Fig. 6), the results implied that the amplitude of the central point represented the whole vibrating status to a certain extent.

The levitation experiment needs the amplifier to enlarge the energy input. The performance parameters of the Fuji amplifier are listed in Table 8. It can provide a fixed 15× magnification for the DC and AC signal inputs. Its working point can be adjusted for obtaining the largest bandwidth for the experiments. The levitation height of the object was measured by the laser scanning vibrometer (see Fig. 11). The levitation object is made of nylon, with dimensions of  $\Phi 25 \text{ mm} \times 3 \text{ mm}$  and a weight of 6 g. For the highest energy output, the work point should be adjusted in the amplifier. The 7 V offset (before amplification) generated the largest amplitude and avoided clipping, as observed on oscilloscope.

The levitation experimental results and fitting curves are shown in Fig. 12. All of the experimental points correspond to the modal results in Table 7 (black square). The results implied that the levitation can be achieved at six points in the frequency band, whilst points failed. The failed experimental points showed that the pure flexible wave is appropriate to achieve levitation at low frequencies. In contrast, the mixed shapes are appropriate at higher frequencies. This principle can guide and optimize the design of an NFAL platform that works in different frequency bands.

The fitting curve expression is an exponential function with 95% confidence bounds:

$$F(x) = 32.2 * \exp(8.416e - 6 * x) - 44.86$$

$$* \exp(-7.764e - 4 * x). \quad [5]$$

This expression can provide an estimated levitation height of the object; the trend of the levitation curve is reasonable and corresponds to the theoretical results (Hashimoto (7); Wang and Wei (20)) and is comparable with experimental results reported by Atherton (31).

## Conclusion

1. The plate actuator with four piezoelectric discs has significant bearing force that can be used for the conveying of objects.
2. Almost all of the harmonic shapes can be expressed by one quarter simulation models. The symmetry shapes have larger bearing force and the levitated object is more stable.
3. The most appropriate mode is determined by the range of the work band; for the lower band, pure flexural modes are appropriate. In contrast, the mixed modes are beneficial at higher frequency range.
4. To acquire more energy from the amplifier, the working point should be set up to guarantee the largest amplitude and avoiding amplifier clipping.
5. The levitation height is an exponential function of frequency in general, which is consistent with the theoretical results.

## References

- (1) Gross, W. A. (1962), *Gas Film Lubrication*, Wiley: New York.
- (2) Langlois, W. E. (1962), "Isothermal Squeeze Films," *Quarterly of Applied Mathematics*, **20**(2), pp 131–150.
- (3) Salbu, E. O. J. (1964), "Compressible Squeeze Films and Squeeze Bearings," *Journal of Basic Engineering*, **86**(3), pp 355–366.
- (4) Beck, J. V., Holiday, W. G., and Strodtman, C. L. (1969), "Experimental and Analysis of a Flat Disk Squeeze-Film Bearing Including Effects of Supported Mass Motion," *Journal of Lubrication*, **91**(1), pp 138–148.
- (5) Kuroda, S. and Hirata, N. (1984), "Near Field Acoustic Levitation of Planar Specimens Using Flexural Vibration," *Journal of Lubrication*, **50**(459), pp 2727–2731.
- (6) Jing, M. Q., Liu, H., Shen, Y., and Yu, L. (2008), "New Style Squeeze Film Air Bearing," *Journal of Xi'an Jiaotong University*, **42**(7), pp 799–802.
- (7) Hashimoto, Y. (1996), "Near Field Acoustic Levitation of Planar Specimens Using Flexural Vibration," *Journal of the Acoustic Society*, **100**(4), pp 2057–2061.
- (8) Minikes, A. and Bucher, I. (2004), "Levitation Force Induced by Pressure Radiation in Gas Squeeze Films," *Journal of the Acoustic Society*, **116**(1), pp 217–226.
- (9) Stolarski, T. A. and Chai, W. (2006), "Load-Carrying Capacity Generation in Squeeze Film Action," *International Journal of Mechanical Sciences*, **48**(7), pp 736–741.
- (10) Stolarski, T. A. (2010), "Numerical Modelling and Experimental Verification of Compressible Squeeze Film Pressure," *Tribology International*, **43**(1), pp 356–360.
- (11) Liu, P., Li, J., and Ding, H. (2009), "Modeling and Experimental Study on Near-Field Acoustic Levitation by flexural Mode," *IEEE Transactions on Ultrasonics, Ferroelectrics, and Frequency Control*, **56**(12), pp 2679–2685.
- (12) Li, J., Liu, P., Ding, H., and Cao, W. (2011), "Modeling Characterization and Optimization Design for PZT Transducer Used in Near Field Acoustic Levitation," *Sensors and Actuators A*, **171**(2), pp 260–265.
- (13) Wei, B. and Ma X. (2010), "Research on the Characteristic of the Floating Guide Way with Squeeze Film," *Lubrication Engineering*, **35**(8), pp 54–58.
- (14) Wei, B. and Ma, X. (2010), "Research on the Characteristics of Squeeze Film Floating Guide Way including the Model Effect," *Lubrication Engineering*, **35**(2), pp 33–35.
- (15) Li, J., Cao, W., Liu, P., and Ding, H. (2010), "Influence of Gas Inertia and Edge Effect on Squeeze Film in Near Field Acoustic Levitation," *Applied Physics Letters*, **96**(24), pp 1–8.
- (16) Xie, W. J. and Wei, B. (2012), "Parametric Study of Single-Axis Acoustic Levitation," *Applied Physics Letters*, **79**(4), pp 881–886.
- (17) Nabhani, M., El Khelifi, M., and Bou-said, B. (2012) "Combined Non-Newtonian and Viscous Shear Effects on Porous Squeeze Film Behavior," *Tribology Transactions*, **55**(4), pp 491–502.
- (18) Rao, T. V. V. L. N., Rani, A. M. A., and Nagarajan, T. (2013), "Analysis of Journal Bearing with Double-Layer Porous Lubricant Film: Influence of Surface Porous Layer Configuration," *Tribology Transactions*, **56**(5), pp 841–847.
- (19) Bouzidane, A. and Thomas, M. (2013), "Nonlinear Dynamic Analysis of a Rigid Rotor Supported by a Three-Pad Hydrostatic Squeeze Film Dampers," *Tribology Transactions*, **56**(5), pp 717–727.
- (20) Wang, Y. Z. and Wei, B. (2013), "Mixed-Modal Disk Gas Squeeze Film Theoretical and Experimental Analysis," *International Journal of Modern Physics*, **27**(25), pp 1–20.
- (21) Diprima, R. C. (1968), "Asymptotic Methods for an Infinitely Long Slider Squeeze-Film Bearing," *Journal of Tribology*, **90**(1), pp 173–183.
- (22) Takada, H. and Miura, H. (1983), "Characteristics of Squeeze Air Film between Nonparallel Plates," *Journal of Lubrication Technology*, **105**(1), pp 147–151.
- (23) Kuroda, S. and Hirata, N. (1984), "The Characteristic of Motion of a Round Plate Supported on Squeeze Air Film," *Journal of Lubrication*, **50**(459), pp 2727–2731.
- (24) Beltman, W. M. and Vander Hoogt, P. J. M. (1997), "Air Loads on a Rigid Plate Oscillating Normal to Fixed Surface," *Journal of Sound and Vibration*, **206**(2), pp 217–241.
- (25) Minikes, A. and Bucher, I. (2003), "Coupled Dynamics of a Squeeze-Film Levitated Mass and a Vibrating Piezoelectric Disc: Numerical Analysis and Experimental Study," *Journal of Sound and Vibration*, **263**(2), pp 241–268.
- (26) Ha, D. N., Stolarski, T. A., and Yoshimoto, S. (2005), "An Aerodynamic Bearing with Adjustable Geometry and Self-Lifting Capacity. Part 1: Self-Lift Capacity by Squeeze Film," *Proceedings of the Institution of Mechanical Engineers - Part J: Journal of Engineering Tribology*, **219**(1), pp 33–39.
- (27) Yoshimoto, S., Kobayashi, H., and Miyatake, M. (2007), "A Non-Contact Chuck Using Ultrasonic Vibration: Analysis of the Primary Cause of the Holding Force Acting on a Floating Object," *Tribology International*, **40**(3), pp 503–511.
- (28) Wei, B., Ma, X., and Tang, W. (2011), "Study on Characteristics of Ultrasonic Levitation with Piezo-Ceramics Exciting," *Piezoelectrics Acousto-optics*, **33**(1), pp 71–78.
- (29) Stolarski, T. A., Xue, Y., and Yoshimoto, S. (2011), "Air Journal Bearing Utilizing Near-Field Acoustic Levitation Stationary Shaft Case," *Proceedings of the Institution of Mechanical Engineers - Part J: Journal of Engineering Tribology*, **225**(3), pp 120–127.
- (30) Wang, Y. Z. and Wei, B. (2013), "A Linear Solution for Gas Squeeze Film Characteristics in Ultrasonic Excitation Condition,"



## Appendix B

## Appendix B

### B.1 Digital Image Correlation system overview

A comparatively new measurement technique that is now gradually utilized within investigations is digital image correlation (DIC). This is a non-contact photosensitive technique that utilizes one or more camera to capture a sequence of images throughout the investigation. These images can then be visualised to provide full field deformation data permitting the strain domain to be determined (Pan et al., 2009). To recognize usefulness image fineness an arbitrary grey dots of high contrast spot is executed on the exterior region of the item of importance (Fig. B.1).

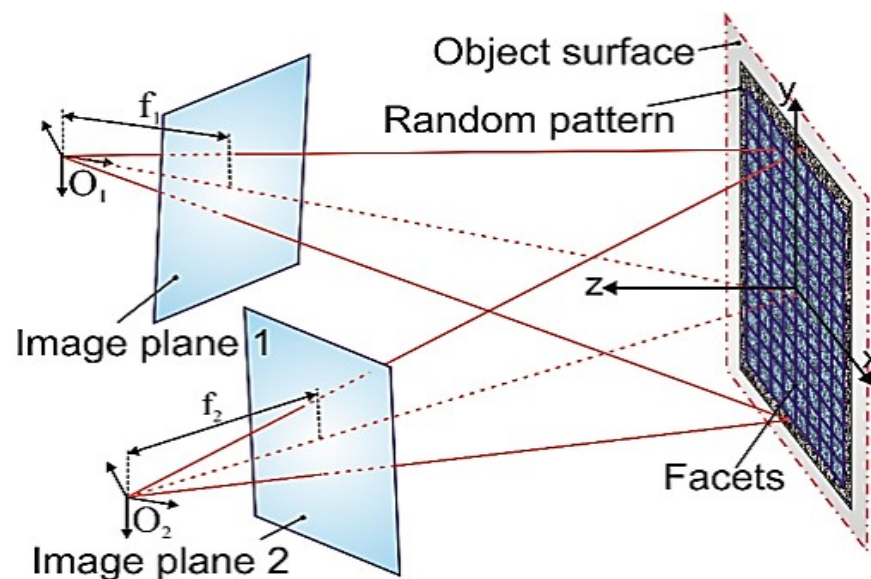


FIGURE B.1 : Photogrammetric standard and calculation of 3-D translation vector (Hagara et al., 2014).

The photo gained by a two of camera are separated into intersecting facets with the greyscale light strength magnitudes. The reference facets are compared with the intersecting facets and the translation vector for each facet is determined. An association algorithm to approach the grey magnitude models in a tiny local neighbourhoods is utilized by the DIC system to correlate matching points from the cameras. The DIC system principle work depends on the photos that are accomplished sequentially. As the load is applied or when a distortion occurs, the comparative location of the points are seized by one camera or more. Practicing of one camera permits the calculation of object distortion in a level parallel to the photo level of the camera (Avitabile et al., 2010). Utilizing for two cameras comparative to each other permits to take of precise pixel in that camera's photos plane. Two cameras from varied directions are necessary in order to implement a 3-dimension calculation for a location of any dot on the item surface. When the location of each camera, intensification of the lenses and all photos parameters are recognised; the complete three-dimension coordinates of any exterior point in the domain can be determined (Dantec Dynamic, 2016). Consequentially, a three-dimension plane contour of the sample can be calculated. When the three- dimension contour is specified, the association of the images captured by the cameras with the reference area photos of the exterior item permits 3-dimension distortions to be determined.

### **B.1.1 Calibration of Cameras**

The aim from implement the calibration for the cameras is to calculate the intrinsic parameters such as focal distance of the lenses, standard dot of the lenses, radial deformation of the lenses, lateral deformation of the lenses and extrinsic parameters which are represented by translation vector and rotation matrix (Dantec Dynamic, 2016). When the camera or cameras is adjusted throughout ISTR- 4D software the whole system will be ready to achieve a good measurement. The calibration can be done by using a calibration plate (Fig. B.2) which is supplied by Dantec. Throughout

change the location of the plate calibration in front of camera or cameras at various angles and position by hand, the ISTR4-4D software records that locations and will seize the various photos automatically.

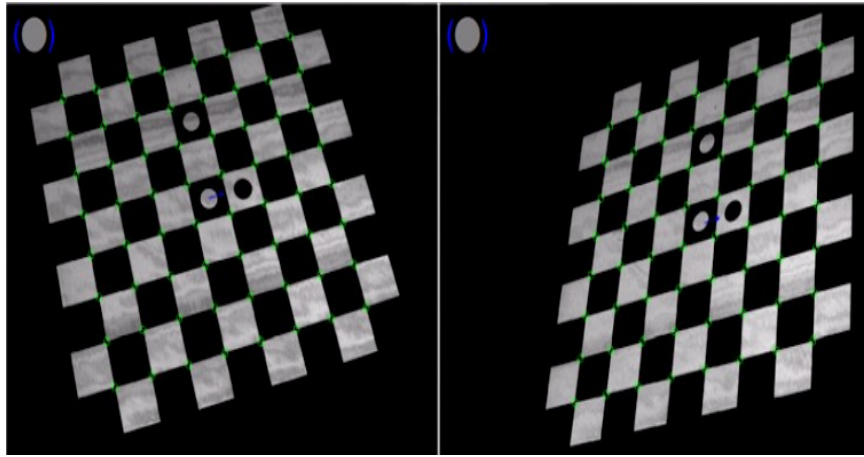


FIGURE B.2 : Calibration Live Image (Dantec Dynamic 2016).

Series of images that are taken by the camera(s) for the tested item which is placed in front of the camera(s) then the ISTR4-4D can manipulate the captured images and correlated alongside the pre-set calibration plate sizes and the parameters are utilized for calculating the intrinsic magnitudes. Achievement of the calibration makes the system ready for evaluation and visualisation for the result data.

### B.1.2 Utilize of Digital Image Correlation and Restrictions

digital image correlation is broadly used in the investigation for calculating of surface deformation and strain. Conversely, there are restrictions to utilize it. In section will explain a short information of causes of slips, uncertainties in the testing methods and accuracy levels of the digital image correlation system. The paint for a region of a test sample is used to recognize patterns essential for camera or cameras. The region of concern on the sample is completely cleaned then a white colour is primary implemented on that interested area and when the white colour is dried, spots of black dots are executed on the tested sample. The fine spots shaped by the executed paint before load applied is utilized as reference dots and the result

are calculated depended on the translation of that dots on the exterior region of the sample begin from the reference location throughout loading. The cameras utilized for monitoring are adjusted, calibrated and the dots tested for excellence by the ISTR4-4D software. The DIC system views an easy calibration instrument with an online feedback of calibration feature. The integral algorithm is proficient of valuing the indecisions of the measuring calibration parameters. The expected miscalculation from the feature check must tend to be less than 0.001 of a millimetre. Conversely, the monitoring achieved by the camera(s) is effected by the miscalculations and it modifies the measures results like contours, displacement and strain. The miscalculations from the DIC system are integral noise of the picked up photos, arithmetical and miscalculations presented by the system calibration, sub-pixel influences causing from the restricted camera resolution and integral indecisions of correlation algorithm (Pan et al. 2009). The miscalculations presented throughout the inaccurate system calibration will not be condensed by the evaluation or visualisations processes. Therefore when a systematic slips is taken place that will lead to hard restrict the system resolution and growth the miscalculation. The miscalculations are categorised into two classifications regarding to their influence on the calculation method (Siebert et al., 2007).

- Correlation errors – define indecisions for the association of corresponding facet locations in various photo borders. Correlation errors can be classified as a statistical error and systematically error or miscalculation. Statistical error happens as a result of the restricted amount of pixels and equivalent grey amount in each facet. In addition, potential error origins can be considered as statistical noise of the grey amounts, several lighting circumstances for the camera(s), image disparity and dimensions of the spot dot or pattern on the sample region. Moreover, systematically errors are presented by subpixel influences. Consequently, the Correlation errors effect the accuracy of photo correlation.

- Three – dimension rebuilding errors – this restriction leads to a direct action on rebuilding of the 3-dimension coordinates of the associated photo facets. The calibration Uncertainties factors produce errors if rebuilding of the three-dimension coordinates from associated facets of the camera or cameras.

The algorithm of the system will automatically specify the accuracy levels of each sample patterns after calibration is conducted. The appropriateness of the spot pattern is one where adequate information points are recognised to describe a displacement. Throughout this procedure, high contrast spot should not go beyond the resolution of the imaging cameras. In this work the ISTR4-4D software was used to recognise good spot pattern for the investigation work. It is challenging to separate one error cause from the others, so the actions of some parameters, for example; spot pattern, out- of- plane displacement, image distortion or lens distortion, noises (shot noise, thermal noise, cut-off noise), sub-pixel recording algorithm, shape function (the second-order shape function produces lower methodical error than the linear shape function at roughly the identical levels of random error) and interpolation scheme. Subset size (the investigators can choice a subset size changing from some pixels to even more than a hundred pixels before the DIC examination) (Pan et al., 2009). In order to achieve high accuracy in displacement measurement utilizing the DIC system the following Experimental settings procedures are highly recommended to be processed.

- Rise the contrast of the spot pattern.
- Ensure parallelism between the digital image sensor target and the sample region.
- utilize a Telecentric lens.
- Employ a high-quality low noise digital image sensor camera and keep stable and even lighting throughout loading.



## Appendix C

# Appendix C

### C.1 Reynolds Equation:

The non-dimensional parameters of Reynolds Eq. for the above assumptions are as follows;

$$P = \frac{p}{p_a}, H = \frac{h}{h_0}, X = \frac{x}{L}, T = \omega t, \varepsilon = \frac{a}{h_0}, \sigma = \frac{12\omega\mu L^2}{p_a h_0^2}$$

$p_a$  is the ambient pressure,  $P$ ,  $H$ ,  $X$ ,  $\varepsilon$  and  $T$  are the dimensionless pressure, mean clearance, lateral coordinate, amplitude, and time, respectively, and  $\sigma$  stands for the squeeze number (Langlois, 1962).

$$\Pi = 1 + \sigma P \quad (\text{C.1})$$

$$\frac{\partial}{\partial x} \left( H^3 \frac{\partial \Pi}{\partial x} \right) = \sigma \frac{\partial H}{\partial T} \quad (\text{C.2})$$

$$\frac{\partial}{\partial x} \left( H^3 P \frac{\partial P}{\partial x} \right) = \sigma \frac{\partial PH}{\partial T} \quad (\text{C.3})$$

Considering that the planes of the levitation are parallel surfaces and that the gap between them behave as, (Langlois, 1962),

$$h = h_0 (1 + \delta \cos \omega t)$$

Or

$$H(T) = 1 + \varepsilon \cos(T) \quad (\text{C.4})$$

Where the constant  $\delta$  is small compared with unity, the studies predicted that the deviation of pressure from surrounding will be of order of  $\delta$ .

Equation C.3 has been solved by (Langlois, 1962), assuming that the pressure field can be expanded as a regular perturbation series in  $\varepsilon$ .

$$p = p_o [(1 + \delta \Pi) + O(\delta^2)] \quad \text{Or}$$

$$P(X, T) = 1 + \varepsilon \Pi(X, T) + O(\varepsilon^2) \quad (\text{C.5})$$

By inserting equation C.4 and equation C.5 into equation C.3 and ignoring the terms of the second degree or higher in  $\varepsilon$ . Therefore in shape of non-dimensional variables that will yield the following equation (Langlois, 1962).

$$\frac{\partial^2 \Pi}{\partial X^2} = \sigma \frac{\partial \Pi}{\partial T} - \sigma \sin T \quad (\text{C.6})$$

$$\Pi(\pm 1/2), T = 0 \quad (\text{C.7})$$

Assume the solution has the form of,

$$\Pi(X, T) = \Pi_1(X) \cos T + \Pi_2(X) \sin T \quad (\text{C.8})$$

$$\frac{\partial \Pi}{\partial X} = -\Pi_1(X) \sin T + \Pi_2(X) \cos T \quad (\text{C.9})$$

By substituting equation C.9 in equation C.6 yields

$$\frac{\partial^2}{\partial X^2} (\Pi_1(X) \cos T + \Pi_2(X) \sin T) = \sigma (-\Pi_1(X) \sin T + \Pi_2(X) \cos T) - \sigma \sin T \quad (\text{C.10})$$

$$\left( \sigma \Pi_2 - \frac{\partial^2 \Pi_1}{\partial X^2} \right) \cos T = \left( \sigma + \sigma \Pi_1 + \frac{\partial^2 \Pi_2}{\partial X^2} \right) \sin T \quad (\text{C.11})$$



$$\frac{\partial^2 \Pi_1}{\partial X^2} - \sigma \Pi_2 = 0 \quad (\text{C.12})$$

$$\frac{\partial^2 \Pi_1}{\partial X^2} + \sigma \Pi_1 + \sigma = 0 \quad (\text{C.13})$$

$$\Pi_1 (\pm 1/2) = \Pi_2 (\pm 1/2) = 0 \quad (\text{C.14})$$

A variety of elementary methods exist for solving this system. The route entailing the least manipulation probably results from combining equation C.12 and equation C.13 into one second order equation for the complex variable  $(\Pi_1 - i\Pi_2)$ , (Langlois, 1962). Carrying out the details leads us to

$$\Pi_1 (X) = \frac{2}{\cos hk + \cos k} \left( \cosh \frac{k}{2} \cos \frac{k}{2} \cosh kX \cos kX + \sinh \frac{k}{2} \sin \frac{k}{2} \sinh kX \sin kX \right) \quad (\text{C.15})$$

$$\Pi_2 (X) = \frac{2}{\cos hk + \cos k} \left( \sinh \frac{k}{2} \sin \frac{k}{2} \cosh kX \cos kX - \cosh \frac{k}{2} \cos \frac{k}{2} \sinh kX \sin kX \right) \quad (\text{C.16})$$

Where,  $k = \sqrt{\frac{\sigma}{2}}$

### C.1.1 Analytical solution for Force and Pressure

The system force can be calculated from the following equation (Langlois, 1962).

$$F = \int_{-1/2}^{1/2} (P - 1) dX \quad (\text{C.17})$$

Where  $F$  and  $P$  are the normalized force and pressure respectively.

At any specific time, the magnitude of  $F$  is the average loading pressure in atmospheric (Langlois, 1962). Thus, with equation C.5 and C.8,

$$F/\delta = \cos T \int_{-1/2}^{1/2} \Pi_1 (X) dX + \sin T \int_{-1/2}^{1/2} \Pi_2 (X) dX \quad (\text{C.18})$$

With Equations C.12 and C.13

$$F/\delta = -f_1(\sigma) \cos T + f_2(\sigma) \sin T \quad (\text{C.19})$$

$$f_1(\sigma) = 1 - \frac{1 \sinh k + \sin k}{k \cosh k + \cos k}$$

$$f_2(\sigma) = \frac{1 \sinh k - \sin k}{k \cosh k + \cos k}$$

At high squeeze numbers, virtually no flow occurs at the peripheries of the wall, and the system mimics that of a piston in a closed channel. In such a case and under the isothermal condition assumption, mass conservation yields  $PH = C$  (Salbu, 1964). Integrating both sides of equation C.3.

$$\frac{\partial}{\partial X} \left( H^3 P \frac{\partial P}{\partial X} \right) = \sigma \frac{\partial(PH)}{\partial T}$$

$$\int_0^{2\pi} \frac{\partial}{\partial X} \left( H^3 P \frac{\partial P}{\partial X} \right) dT = \sigma \int_0^{2\pi} \frac{\partial(PH)}{\partial T} dT = 0 \quad (\text{C.20})$$

Further integrating with respect to  $X$  (from  $X$  to  $X = 0$ ) reduces the equation to

$$\left[ \int_0^{2\pi} H^3 P \frac{\partial P}{\partial X} dT \right]_x = \left[ \int_0^{2\pi} H^3 P \frac{\partial P}{\partial X} dT \right]_{x=0} = \text{const.} \quad (\text{C.21})$$

The equation C.21 holds for all values of  $X$ . Owing to system's symmetry, the pressure gradient at the centre of the wall satisfies the condition  $\frac{\partial P}{\partial X} = 0$  and, thereby, the constant in the equation C.21 must vanish. Integrating the equation C.21 once again with respect to  $X$  (from  $X$  to  $X = 1/2$ ) yields,

$$\left[ \int_0^{2\pi} H^3 P^2 dT \right]_x = \left[ \int_0^{2\pi} H^3 P^2 dT \right]_{x=1/2} = \text{const.} \quad (\text{C.22})$$

Since practically no flow occurs at the boundaries of the wall, the statement of non-leakage of energy leads to utilize a pressure release boundary condition ( $P = 1$ ),

and the constant on the right hand side of the above equation C.22 becomes,

$$Const = \int_0^{2\pi} H^3 dT = \int_0^{2\pi} [1 + \varepsilon \cos T]^3 dT = \pi (2 + 3\varepsilon^2) \quad (C.23)$$

Since  $PH = C$ , where  $C$  is determined from equation C.22 by solving the  $C^2 \int_0^{2\pi} HdT = \pi (2 + 3\varepsilon^2)$  pressure owns the formula of,

$$P = \frac{C}{H} = \frac{(1 + \frac{3}{2}\varepsilon^2)^{1/2}}{1 + \varepsilon \cos T} \quad (C.24)$$

This mass conservation solution found by (Salbu, 1964) is not only free of the squeeze number but also does not include the pressure distribution along the wall. Therefore (Minikes, Bucher, and Haber, 2004) suggested correcting the (Salbu, 1964) solution in the following manner:

$$P = 1 + \left( \frac{(1 + \frac{3}{2}\varepsilon^2)^{1/2}}{1 + \varepsilon \cos T} - 1 \right) MAX [\Pi (X, T)] \quad (C.25)$$

The operator  $MAX$  refers to that one should take the largest enveloped shape within the time period. In order to find this enveloped shape, one must find the time  $T_{max}$ , where the pressure amplitude is maximal. It appears that for squeeze numbers greater than 20 the two solutions are in phase, therefore the time  $T_{max}$  can be found by solving the following (Minikes, Bucher, and Haber, 2004);

$$\frac{\partial}{\partial T} P(T) = \frac{\partial}{\partial T} \left( \frac{(1 + \frac{3}{2}\varepsilon^2)^{1/2}}{1 + \varepsilon \cos T} \right) = 0 \Rightarrow T_{max} = \pi \quad (C.26)$$

Substituting  $T_{max} = \pi$  into equation C.5 which is  $\Pi (X, T) = \Pi_1 (X) \cos T + \Pi_2 (X) \sin T$  yields the maximum enveloped shape and accordingly the resolved mass conservation suggested has the following form Minikes, Bucher, and Haber, 2004,

$$P = 1 + \left( \frac{(1 + \frac{3}{2}\varepsilon^2)^{1/2}}{1 + \varepsilon \cos T} - 1 \right) \left( 1 - 2 \frac{\cosh \frac{\beta}{2} \cos \frac{\beta}{2} \cosh \beta X \cos \beta X + \sinh \frac{\beta}{2} \sin \frac{\beta}{2} \sinh \beta X \sin \beta X}{\cosh \beta X + \cos \beta X} \right) \quad (C.27)$$

Minikes, Bucher, and Haber, 2004 proposed correction allows solving analytically the levitation force for a larger range of squeeze numbers than was initially offered by (Langlois, 1962). The dimensionless time averaged levitation force  $F$  per unit depth at steady state can be expressed by

$$F = \frac{1}{2\pi} \int_0^{2\pi} \int_{-1/2}^{1/2} (P - 1) dXdT \quad (\text{C.28})$$

Where  $F$  can be normalized by  $p_a L$

$$F = \frac{5\epsilon^2}{4\beta} \left( \frac{\beta \cos \beta + \beta \cosh \beta - \sinh \beta - \sin \beta}{\cos \beta + \cosh \beta} \right) \quad (\text{C.29})$$